OPTICAL AND THERMAL FENESTRATION MODELS FOR BUILDING COOLING LOAD CALCULATIONS

By

CHANVIT CHANTRASRISALAI

Bachelor of Engineering in Mechanical Engineering
Chulalongkorn University
Bangkok, Thailand
1992

Master of Science in Architectural Engineering
University of Kansas
Lawrence, Kansas
2000

Submitted to the Faculty of the
Graduate College of the
Oklahoma State University
in partial fulfillment of
the requirements for
the Degree of
DOCTOR OF PHILOSOPHY
May, 2007

OPTICAL AND THERMAL FENESTRATION MODELS FOR BUILDING COOLING LOAD CALCULATIONS

Dissertation Approved:

Dr. Daniel E. Fisher
Dissertation Adviser

Dr. Jeffrey D. Spitler

Dr. Afshin J. Ghajar

Dr. Khaled Mansy

Dr. A. Gordon Emslie
Dean of the Graduate College

ACKNOWLEDGEMENTS

First, I would like to express my sincere gratitude to my research advisor, Dr. Daniel E. Fisher, for his continuous guidance and constant support throughout the course of my Ph.D. study. His constructive advice and positive criticism have helped me become a better researcher.

Next, I would like to thank Dr. Jeffrey D. Spitler, Dr. Afshin J. Ghajar, and Dr. Khaled Mansy for their time serving as members of the advisory committee. I am also grateful to Dr. Lorenzo Cremaschi who served as an unofficial committee for my final defense.

In addition, I am greatly indebted to Dr. Brian A. Rock, my former advisor at the University of Kansas. Without his encouragement, I would not have pursued this doctoral degree in the first place.

Then, I would like to acknowledge the financial support given to me by several organizations during the seven years of my study here. These organizations include the American Society of Heating, Refrigerating and Air-Conditioning Engineers (ASHRAE), the U.S. Department of Energy's National Energy Technology Laboratory (USDOE's NETL), the Federal Highway Administration (FHWA), and the U.S. Army Construction Engineering Lab (USACERL). Additional funding provided by Dr. Spitler is also appreciated.

Moreover, my thanks go to all my friends and colleagues. I frankly appreciate their genuine friendship, generous support and constant help.

Finally, I wish to express my appreciation to all my family members for their unconditional love, patience and understanding. Special thanks go to my parents who always support my pursuit of knowledge and wisdom and to whom I would like to dedicate this hard earned work.

TABLE OF CONTENTS

Chapter Page

LIST OF TABLES

Page

LIST OF FIGURES

Page

Page

Page

NOMENCLATURE

A = area (m^2, ft^2)

c = thermal conductance ($W/m^2 \cdot K$, $Btu/hr \cdot ft^2 \cdot {}^\circ F$)

C_p = specific heat ($J/kg \cdot K$, $Btu/lb_m \cdot {}^\circ F$)

F = view factor (dimensionless), or
fraction of heat transfer rate (dimensionless)

h = heat transfer coefficient ($W/m^2 \cdot K$, $Btu/hr \cdot ft^2 \cdot {}^\circ F$)

I = incident solar radiation (W/m^2, $Btu/hr \cdot ft^2$)

IAC = interior solar attenuation coefficient (dimensionless)

IC = influence coefficient

J = radiosity (W/m^2, $Btu/hr \cdot ft^2$)

k = thermal conductivity ($W/m \cdot K$, $Btu/hr \cdot ft \cdot {}^\circ F$)

$\dot{m}$ = mass flow rate (kg/s, lb_m/hr)

Ni = inward flowing fraction (dimensionless)

$\dot{q}$ = heat transfer rate (W, Btu/hr)

q'' = heat flux (W/m^2, $Btu/hr \cdot ft^2$)

R = reflected solar radiation (W/m^2, $Btu/hr \cdot ft^2$), or
slat curvature radius (mm, in.)

S = slat spacing (mm, in.)

$SHGC$ = solar heat gain coefficient (dimensionless)

$\overline{SS}$ = Hottel's total exchange area (m^2, ft^2)

T = transmitted solar radiation (W/m^2, $Btu/hr \cdot ft^2$), or
temperature (°C, °F), or
slat thickness (mm, in.)

t = thickness (m, ft)

U = overall heat transfer coefficient ($\mathrm{W/m^2\cdot K}$, $\mathrm{Btu/hr\cdot ft^2\cdot{}^\circ F}$)

u = uncertainty

W = slat width (mm, in.)

Symbols

α = solar absorptance (dimensionless)

β = solar altitude angle (deg)

γ = solar azimuth angle (deg)

ε = longwave emittance (dimensionless)

ξ = surface facing (azimuth) angle (deg)

ρ = solar reflectance (dimensionless)

σ = Stefan-Boltzmann constant (5.669×10^{-8} $\mathrm{W/m^2\cdot K^4}$, 0.1714×10^{-8} $\mathrm{Btu/h\cdot ft^2\cdot{}^\circ R^4}$)

Σ = surface tilt angle (deg)

τ = solar transmittance (dimensionless)

ϕ = profile angle (deg)

ψ = slat angle (deg)

CHAPTER 1

INTRODUCTION

1.1 Building Load and Energy Calculations

1.1.1 Importance of Building Energy Simulation

"Given the limitation of traditional design methods, is it surprising that buildings often fail to attain their expected performance? The integrated simulation approach provides a solution to this dilemma by enabling comprehensive appraisals of alternative designs under realistic operating conditions. By allowing practitioners to explore a building's life cycle performance at the design stage, problems can be identified and corrected before they arise. Simulation is a powerful tool in the search for design solutions that ensure occupant well-being, reduce energy consumption, meet sustainability aspirations, mitigate environmental impact and contribute to climate change abatement." [Clarke 2001]

According to the Energy Information Agency (EIA), buildings in the U.S. have consumed more than 30 quadrillion Btu annually in the past decade [EIA 2000]. For residential buildings alone, the total energy use excluding primary electricity and wood was about 10.3 quadrillion Btu, costing American nearly $ 140 billion in 1997 [EIA 1999]. Space heating, space air-conditioning, and lighting accounted for more than half of total energy consumption in both residential and commercial buildings [EIA 1998, 1999]. Although a number of energy saving building components, such as Trombe walls, advanced windows, and radiant systems, have been developed over the last thirty years, only a handful of low energy buildings have been properly constructed due to a lack of knowledge of their thermal behavior. Consequently, low energy building technologies have had relatively little impact on overall energy use.

Several researchers, however, believe that more than 50% of energy savings can be achieved through the optimal design of new buildings and the use of improved building components [Clarke 2001; Rousseau and Mathews 1993; Todesco 1996]. The optimal design requires proper attention to the unique problems associated with a building's location, orientation, climate, and application. Therefore, the full potential savings will require the so-called integrated whole-building design approach to assess the building energy performance and optimize its heating, ventilating, and air-conditioning (HVAC) and lighting systems. The integrated approach not only considers form, function, lighting, and space conditioning criteria, but also actively considers low energy options to meet these criteria. Thermal capacity, shading, daylighting, as well as advanced lighting systems and low energy space conditioning systems are considered thoroughly for the whole design process.

Predicting energy performance of the buildings involves understanding not only complicated thermal heat transfer processes in the buildings but also interactions between various building systems, such as lighting and space-conditioning systems. Due to rapid advances in building technologies, the design and evaluation of the environmental conditions in contemporary buildings have become increasingly complex. Traditional design and energy analysis methods using simplified manual calculation techniques (e.g. the Cooling Load Temperature Difference/Cooling Load Factor (CLTD/CLF) method for design purposes and the Bin Methods for energy analysis purposes) have become inadequate to provide accurate thermal interactions in such buildings. Poor understanding of their thermal behaviors can lead to negative energy impact on a building design. The poor design can also result in uncomfortable spaces. In order to overcome such complexity and provide effective design decision support, building energy simulation has become a clear and emerging solution to shortcomings in the traditional methods [Clarke 2001].

1.1.2 Building Energy Simulation and Thermal Load Calculations

At present, overall solution techniques commonly used in detailed building energy simulation programs may be divided into two categories: sequential and simultaneous approaches. The sequential approach is usually referred to as the Load, System and Plant (LSP) approach [ASHRAE 2001]. In the sequential technique, the simulation of building and HVAC systems are split into three sequential steps. In the first step, the building loads are calculated for the entire period, often one-year period. Then, the simulation of HVAC distribution systems is followed using the building loads as its inputs. The system simulation is also run for the whole period. Finally, the results from the system simulation are applied as inputs to the simulation of the HVAC central plants. The sequential nature of the LSP approach neglects the interactions between building loads, HVAC distribution systems and central plants. Consequently, this approach may yield questionable results for the situation in which there is strong coupling between the building envelope and its space-conditioning systems.

The simultaneous solution technique is an alternative approach that accounts for such load-system-plant interactions. In this technique, the models of building loads, HVAC distribution systems and central plants are solved simultaneously at each time step. This solution technique likely improves the accuracy of the predicted results. However, the simultaneous approach is more prone to numerical instabilities and requires more computation time than the sequential approach.

In detailed building energy simulation, regardless of the solution technique, determining building thermal loads is an important part of the simulation. Two commonly employed approaches for predicting building thermal loads are the Weighting Factor Method (WFM) and Heat Balance Method (HBM) [ASHRAE 2001]. The HBM is based on the law of conservation of energy. The WFM, sometimes called the Transfer Function Method (TFM), utilizes room heat balance calculations for generating the so-called weighting factors; hence, it may be considered to be a simplified, heat balance based load calculation method. The WFM requires simpler input data and less computation time than the HBM does.

The WFM utilizes the principle of superposition to divide complex non-linear room heat transfer processes into a summation of thermal responses of various heat transfer components. In the WFM, pre-calculated weighting factors, sometimes referred to as room response factors, are used to convert instantaneous heat gains/losses into the building thermal loads. According to Kerrisk et al. [1981], two general assumptions are made in the use of the weighting factors. The first assumption is that heat transfer processes are independent of one another and can be represented by linear equations. With this assumption, nonlinear heat transfer processes, such as radiation heat transfer, must be approximated linearly. The other assumption is that system characteristics, such as heat transfer coefficients and the distribution of transmitted solar radiation, are fixed. This means that these system characteristics are independent of time and temperature. Consequently, the weighting factors can be pre-calculated and only one set (for one zone) of weighting factors can be used for the entire simulation period.

On the other hand, the HBM has been perceived as the more accurate method because it is formulated from a consideration of fundamental physical principles. A set of energy balance equations for the enclosed space is solved simultaneously for unknown surface and air temperatures. The HBM allows all heat transfer processes in the building to be treated in a more fundamental form. As a result, such significant assumptions required in the WFM, such as the linearity of heat transfer processes and time-variant system characteristics, are not necessary in the HBM. Since cooling loads are quite sensitive to interior convection, the accuracy of the HBM is largely dependent on its interior convection coefficient model. Without inherent limitations as in the WFM (e.g. constant convection coefficients), the HBM can provide accurate cooling load results when interior convection correlations are appropriately utilized [Fisher et al. 2002]. Although the heat balance equations require simultaneous solution and the HBM arguably requires more computational effort, this disadvantage has been largely negated by advances in desktop computing power.

1.2 Improving the HBM Fenestration Models

The inability of the HBM to accurately model the impact of the simplest interior shading device on the cooling load has long been a source of frustration for building mechanical and architectural engineers. Although many studies have developed detailed fenestration models and measured optical properties of window systems, very little has been done to cast models and input data in a format that is conducive to thermal load calculations. At the root of the problem is a fundamentally and potentially flawed assumption that has never been tested. Currently, the thermal performance of fenestration systems are evaluated by means of two separate but related models: an optical and a thermal model. In virtually every available model and every available experimental data set, it is assumed that the thermal model is dominated by material properties; the impact of the indoor environment in particular is assumed to be inconsequential. This assumption has led to the universal specification of natural convection correlations between the glazing and the interior shading device and between the shading device and the room. An additional problem related to load calculation procedures arise from this assumption. The simpler models that might be tractable in load calculation procedures tend to combine the convection coefficient with the radiation coefficient. For the HBM, the convection coefficient must be treated separately in the computational algorithm, and, for heat balance based load calculation procedures (including the HBM, the WFM and the RTSM), the convection coefficient must be available in order to estimate the magnitude of the heat gain and/or the radiative/convective split.

In the past, extensive studies [Breitenbach et al. 2001; Collins and Harrison 1999; Collins et al. 2002; Collins and Harrison 2004; Duarte et al. 2001; Farber et al. 1963; Jordan and Threlkeld 1959; Klems et al. 1995; Machin et al. 1998; Ozisik and Schutrum 1959; 1960a; 1960b; Parmelee and Aubele 1952; Parmelee and Vild 1953; Pennington et al. 1964; Phillips et al. 2001;

Rheault and Bilgen 1989; Rosenfeld et al. 2000; Yahoda and Wright 2004a; 2004b] have been conducted to analyze and quantify the optical and thermal performance of the fenestration system containing shading devices, sometimes called the complex fenestration system. However, these studies have mostly emphasized product-rating methods. They usually employ specific assumptions and environmental conditions suitable for product rating in developing mathematical models and/or correlation data. For building thermal load calculations, these models and data may not be adequate for several reasons. First, they usually assume that room surfaces are black and have the same temperature as the average room air temperature. This assumption neglects interactions between the fenestration system and the room. In addition, the room air flow field, the thermal radiation exchange between the fenestration system and other surfaces, and the re-radiation of transmitted solar radiation are commonly not accounted for. Finally, most of the studies are only concerned with instantaneous heat gain, which is different from the instantaneous space cooling load due to thermal storage effect. In order to estimate the cooling load, the transmitted solar radiation, the inward flow heat transfer rate of absorbed solar radiation (i.e. the absorbed solar heat gain), and the convective/radiative split of the absorbed solar heat gain are all needed (separately). In most product rating studies, the convective/radiative split of the absorbed solar heat gain is neglected. Also, the transmitted solar heat gain and the absorbed solar heat gain are normally combined as in the use of the solar heat gain coefficient (SHGC) to predict the total solar heat gain. Typically, most existing data and models were not developed with heat balance based thermal load and energy calculations in mind. As a result, these data and models are usually not consistent with heat balance based approaches. This suggests the need to provide accurate load and energy calculation procedures that can handle the fenestration system containing shading devices.

1.3 Research Objective and Scope of Work

The current study addresses the need to overcome the previously described shortcomings by developing improved models specifically aimed at building thermal load calculations. The primary objective of the investigation is therefore to enhance the modeling of fenestration systems containing shading devices for building thermal load and energy calculations. As previously discussed, existing fenestration models are primarily suited for product-rating purposes, and typically are not adequate for implementing in a load calculation scheme. To achieve the research objective, the models considered in this study are therefore within the context of the load calculation scheme and compatible with the HBM and the Radiant Time Series Method (RTSM), which are the currently endorsed ASHRAE cooling load calculation methods. In addition, the models are suitable for incorporating in a building energy simulation tool.

A vast number of shading devices exist in practice including blinds, drapes, roller shades, and shade screens. Of these shading devices, slat-type shading devices, such as Venetian blinds, are popular because they can provide occupant privacy. They are also relatively inexpensive and can be used to provide glare control to improve visual comfort. As stated by Littlefair [1992], "The standard Venetian blinds represent conventional window management practice, and are hence the benchmark against which innovative daylighting systems should be judged." This statement implies the importance of the simulation of slat-type blinds. For the current research, therefore, the focus is on the simulation of the fenestration system containing the slat-type blind.

To enhance the simulation of the fenestration system containing shading devices for load calculation purposes, the present research is divided into two parts: optical and thermal studies. The optical modeling approach is based on the so-called multi-layer optical calculation approach [DOE 2006; ISO 2000; Klems 2002; Rosenfeld et al. 2000; van Dijk and Goulding 1996] where overall optical properties of the fenestration system containing a slat-type blind are determined as a function of the optical properties of glazing and blind layers. The current study emphasizes only the optical models for predicting blind and overall optical properties since existing models [Finlayson et al. 1993; Rubin et al. 1998; Wright 1998] and computer programs [LBL 1994, 2001; van Dijk and Goulding 1996; Wright and Sullivan 1995] for predicting glazing optical properties have been well developed. In this study, two optical models are developed: one for predicting blind optical properties and one for predicting overall optical properties of the fenestration system containing a slat-type blind.

For the thermal study, two thermal models are also developed: one for the HBM and one for the RTSM. The thermal model for the HBM is based on the one-dimensional multi-layer heat balance approach; the thermal model for the RTSM is based on the so-called solar-thermal separation concept [Klems et al. 1995; Klems and Kelly 1996; Klems et al. 1996; Klems and Warner 1997]. The thermal model for the HBM can be used to generate thermal parameters, such as the inward flowing fraction and the total thermal resistance, required by the thermal model for the RTSM. The thermal model for the HBM requires two thermal parameters, which must be experimentally determined. Therefore, an experimental method is also developed to support the thermal model for the HBM. The experimental method can also be used to determine the radiative/convective splits required by the thermal model for the RTSM.

Although the feasibility of the experimental method was demonstrated with a small set of experiments, the full parametric set of experiments necessary to develop empirical correlations for the thermal parameters required by the thermal model for the HBM is beyond the scope of this investigation. Future studies with full parametric experiments are deemed essential to develop the empirical correlations.

1.4 Outline of the Thesis

This thesis is organized into seven chapters. The summary of each chapter is given below.

- Chapter 2 first provides an overview of the simulation of the fenestration system containing shading devices. The chapter then reviews previous studies relating to the fenestration system with shading devices. Finally, the chapter presents the methodology used in the current study to enhance the simulation of the fenestration system containing shading devices.
- Chapter 3 presents a comparative analysis of existing optical models for a slat-type blind. The chapter illustrates the influence of input parameters on optical properties of the blind and the effect of the blind on building thermal loads. Also, the chapter identifies strengths and weaknesses in the existing optical blind models. In addition, the chapter proposes a new comprehensive optical blind model and presents the inter-model comparison of the new model.
- Chapter 4 presents a newly developed comprehensive optical blind model based on previous investigations [Chantrasrisalai and Fisher 2004; 2006]. The chapter provides a technical description of the model and discusses the modeling techniques employed in the model. Detailed calculations of the model are given in Appendices A to C. The chapter also provides suggestions for the model implementation in a building energy simulation tool.
- Chapter 5 presents an experimental validation of the new optical blind model. The chapter first presents an in situ experimental method for measuring solar-optical properties of a fenestration system containing a slat-type blind. The in situ experimental method includes in situ experimental measurements of total solar transmittance of the fenestration system and an estimation of slat solar reflectance of the blind assembly (an

input required by the optical blind model) from field measurements The chapter then illustrates the validity of the new optical blind model by comparing the new model with measured solar transmittance obtained by the in situ experimental method.

- Chapter 6 presents two newly developed thermal fenestration models suitable for load calculations: one for the HBM and one for the RTSM. The chapter also presents a calculation procedure used by the thermal model for the HBM to generate thermal parameters required by the thermal model for the RTSM. In addition, the chapter presents an experimental method developed to support the new thermal models. The chapter then discusses preliminary experimental investigation and provides suggestions for future thermal model studies based on experimental findings.
- Chapter 7 summarizes the findings of the current study and recommends additional research.

In summary, Chapter 2 provides a technical overview of the current research. Chapters 3 to 5 discuss the optical study while Chapter 6 discusses the thermal study. Detailed calculations and supporting information are presented in Appendices. Chapters 3 and 5 include some materials from previous publications [Chantrasrisalai and Fisher 2004; 2006].

CHAPTER 2

SIMULATION OF FENESTRATION SYSTEM CONTAINING SHADING DEVICES

2.1 Energy Transport through Fenestration System and Its Modeling

Because the fenestration system is translucent, energy transport through/from the fenestration system includes both conduction and solar heat gains. Conduction heat gain (or loss) is normally referred to as energy transport due to a temperature difference between outdoor and indoor environmental conditions whereas solar heat gain is typically referred to as energy transport due to solar radiation incident on the fenestration system.

The heat transfer mechanism for the conduction heat gain (or loss) actually involves all three modes of heat transfer: conduction, convection, and radiation. The longwave radiative exchanges occur both externally between the outermost layer(s) of the fenestration system and building surroundings, and internally between the innermost layer(s) and other inside surfaces. The longwave exchanges also occur between layers of the fenestration system itself. At the same time, conduction and convection heat transfer take place due to temperature differences between surfaces and adjacent air. Commonly, the modeling of these heat transfer mechanisms is termed the ‘thermal’ model of the fenestration system.

The solar heat gain includes both solar radiation directly transmitted through the fenestration system and some portion of solar radiation absorbed by the fenestration system's layers. Figure 2.1 conceptually illustrates the fundamental mechanism involved in the solar heat gain. As shown, some of the incident solar radiation can be transmitted directly through the space. The ratio of transmitted solar radiation to incident solar radiation is usually referred to as the solar transmittance of the fenestration system. As also shown in the figure, the rest of the incident solar radiation is either reflected back outside or absorbed by the fenestration system's layers. The ratio of the reflected and absorbed solar radiation fluxes to the incident solar radiation flux is called the reflectance (of the system) and the absorptance (of each layer), respectively. Commonly, these ratios are considered to be 'pure' optical properties due to no appreciable overlap between the solar radiation band and the longwave radiation band by which the radiant heat transfer occurs. In other word, these properties are independent of temperature. Therefore, the calculation procedure used to determine the optical properties is normally termed the 'solar' or 'optical' model of the fenestration system.

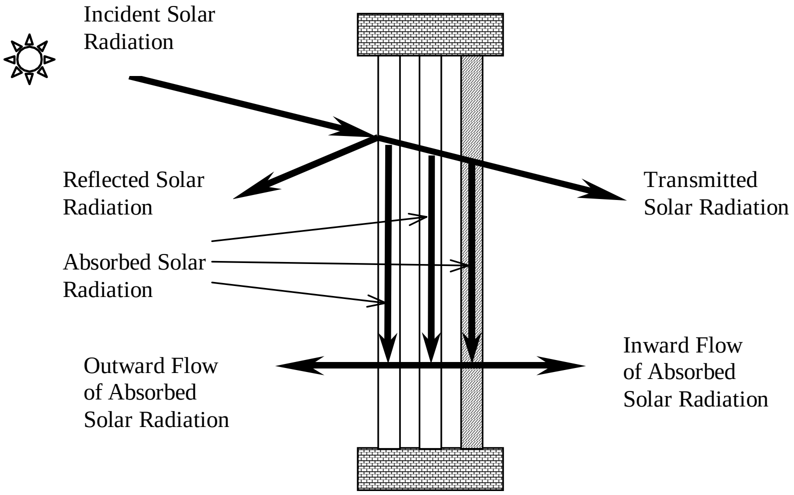

Figure 2-1 Illustration of Solar Heat Gain Components for a Fenestration System Containing Two Glazing Layers and One Shading Layer

Solar radiation absorbed by layers of the fenestration system is transformed into heat energy. As conceptually illustrated in Figure 2-1, some portion of absorbed solar radiation enters into the space while the rest goes back outside. Commonly, the fraction entering the room is called the inward flowing fraction while the fraction leaving the room is called the outward flowing fraction. The propagation mechanism for the inward and outward flowing fractions includes conduction, convection and radiation heat transfer processes and take places at the same time as the heat conduction gain (or loss) occurs. Therefore, the calculation procedure to determine these fractions would naturally and fundamentally be included in the thermal model of the fenestration although the heat conduction gain/loss and inward/outward flowing fractions are often treated separately[1] [ASHRAE 2001]. The next section presents a literature review of previous studies relating to the energy transport through the fenestration system containing shading devices. Then, a technical overview of the current research is given.

2.2 Literature Review

Energy transport through the fenestration system containing shading devices have been studied for more than half a century, and a number of theoretical models to evaluate the performance of the fenestration system have been introduced. Earlier investigations [Farber et al. 1963; Ozisik and Schutrum 1959; 1960a; 1960b; Parmelee and Aubele 1952; Parmelee and Vild 1953; Pennington et al. 1964] provided much of the initial insight into the problem whereas later investigations [Klems et al. 1995; Rosenfeld et al. 2000] attempted to generalize the problem in order to deal with increasing varieties of fenestration products on the market in recent years. Previous investigations of the fenestration system having shading devices are reviewed here.

---

[1] For performance rating purposes, heat conduction loss is normally determined using the overall heat transfer coefficient (U-value) based on winter conditions but solar heat gain is commonly determined using the inward flowing fraction(s) based on summer conditions.

2.2.1 Early Studies of Fenestration System Containing Shading Devices

The earliest attempt to understand the energy performance of the fenestration system containing shading devices was possibly made by Parmelee and his colleagues. In their first paper, Parmelee and Aubele [1952] presented two theoretical models to predict optical properties of a slat-type blind: one for specular-reflecting slat surface and one for diffuse-reflecting slat surface. They also presented mathematical expressions to determine optical properties of a combination of the single glazing and the blind for both external and internal blind. Their model for a diffuse-reflecting slat surface is discussed in detail in Chapter 3. In their subsequent paper, Parmelee et al. [1953] compared their models with experimental data obtained by means of the solar calorimeter. They found that while their models agreed with measured data quite well for direct solar radiation, discrepancies between predicted and measured results for diffuse solar radiation were quite noticeable. They reasoned that the discrepancies were caused by the uncertainty in determining the distribution of diffuse solar radiation. In their last paper [Parmelee and Vild 1953], the authors provided design data for use in determining the solar heat gain. To determine the solar heat gain, they introduced the shading factor defined as the total solar gain from a fenestration system with shading device(s) minus the convection and radiation gain from a single unshaded glazing divided by the solar radiation transmitted through the single unshaded glazing. The shading factor was mathematically expressed as a function of optical properties of the shade-glass combination, optical properties of the single unshaded glazing, incident solar radiation and an experimentally determined constant. This shading factor later became widely known as the shading coefficient (SC)[1]. In their last paper, the authors also presented a refined optical blind model for a diffuse-reflecting slat surface based on the one presented in their first

---

[1] Actually, the definitions of shading factor and shading coefficient are slightly different.

paper. With the refined model, the distribution of transmitted solar radiation onto inside room surfaces can be determined based on view factors between slat surfaces and inside room surfaces.

Later, Jordan and Threlkeld [1959] conducted an experimental study to determine the effectiveness of interior shades on the reduction of solar heat gain. The experimental shade transmission factor, defined as the ratio of collected solar heat to solar radiation incident on the solar collector plate with a correction for the reduction in incident energy as it passes through the cover glass, was used as an indicator for the shade effectiveness. In their paper, they presented equations for calculating the experimental shade transmission factor as a function of experimentally determined optical properties and heat transfer coefficients. They showed that calculated and measured shade transmission factors agreed well for tested shade samples. Although materials of the shades used in the study were similar to those of roller shades, the shades were installed in the calorimeter with the edges sealed as opposed to a conventional installation of roller shades in which air could circulates between the air gap and the room. As a result, they also presented corrected equations of the shade transmission factor for the installation of the shades in an actual room. Since their analysis and experiment only considered an ordinary single glazed window with the interior shades similar to roller shades, their equations and data are quite limited in applications.

In the meantime, Ozisik and Schutrum [1959] also conducted an experiment to investigate the energy performance of the fenestration system containing a roller shade. Unlike Jordan and Threlkeld' work, the shades were installed in the solar calorimeter in a conventional manner. In the paper, Ozisik and Schutrum showed mathematical expressions for use in the determination of convection and radiation gain into the room due to absorbed solar radiation (i.e. inward flowing fraction) and overall heat transfer coefficient (U value). To facilitate design practitioners, they also introduced the K factor for use in the calculation of total heat gain through the fenestration system. This K factor is essentially identical to the currently well-known solar heat gain coefficient (SHGC). Based on calorimeter results, design data (K factor and U value) for various roller shades combined with either regular or heat absorbing glass were also given in the paper. Later, Ozisik and Schutrum also experimentally investigated thermal performance of the fenestration system containing a drape [1960a] or a slat-type blind placed between two layers of glass [1960b]. Similar experimental and theoretical analyses were used to develop design data for use in determining total heat gain through the fenestration system containing either a drape or a between-pane blind. For the fenestration system with a drape, Ozisik and Schutrum [1960a] demonstrated that the K factor was substantially dependent on solar reflectance of the drape whereas solar transmittance and solar absorptance of the drape were quite trivial. Optical properties for various drapes were determined experimentally and presented for normal incidence. For the fenestration system with a between-pane blind, Ozisik and Schutrum [1960b] presented mathematical expressions for effective optical properties as a function of layer optical properties. Models presented by Parmelee et al. [1952] were used to determine optical properties of the blind layer. Similar to previous investigations, data and models developed were limited in scope and applicability because they considered only the single glazing fenestration systems.

To extend the scope of previous studies, Farber et al. [1963] and Pennington et al. [1964] performed both theoretical and experimental studies for a double-glazing fenestration system containing an inside shading device, either slat-type blind or drapery. Similar to previous studies, they presented mathematical expressions for effective optical properties of the fenestration system assuming that optical properties of individual layers were already known. For the fenestration system with the blind, optical models presented by Parmelee et al. [1952] again were used. For the fenestration system with the drape, Farber et al. [1963] attempted to develop a theoretical model to predict optical properties of the drape based on a simple geometry. Possibly, the model is the only existing theoretical model since other studies on the drape [Moore and Pennington 1967; Ozisik and Schutrum 1960a; Van Dyck and Konen 1982; Yellott 1965] all relied on experimental results for predicting the optical properties of the drape. To determine inward flowing of absorbed solar radiation, Farber et al. [1963] also presented models based on a system of heat balance equations. In order to use their models, the knowledge of all heat transfer coefficients (including heat transfer coefficients between glazing layers, between the inner glazing layer and the shading layer, and the shading layer and the room) is needed. In their studies, they assumed that convection heat transfer from the inner glazing layer with the presence of the shading device was the same as convection heat transfer from the inner glazing layer without the shading device. To determine convection from the shading layer, they used the same convection correlation as for convection from the glazing layer by taking into account the increase in the total surface area. Although their approach appeared to be questionable, they showed that the model had reasonable agreements with experimental results obtained by means of a solar calorimeter [Pennington et al. 1964].

Yellott [1965] conducted an experiment to determine the effectiveness of the drape to control solar heat gain. To determine solar heat gain through the fenestration system with the drape, the shading coefficient was utilized. Based on experimental results, the author presented shading coefficients for various combinations of the windows and drapes as a function of solar reflectance of the drape. The author also provided a classification of the drapery fabrics for estimating the shading coefficient based on the so-called openness factor, defined as the ratio of the open area between the fibers to the total area of the fabric [ASHRAE 2001]. Later, Keyes [1967] provided the analysis for classifying drapery fabrics in more detail and Moore and Pennington [1967] described various types of measuring devices and measurement procedures for accurately determining solar-optical properties of the drape.

Van Dyck and Konen [1982] showed a theoretical model for analyzing a fenestration system consisting of a single glazing and a shading device. They investigated various shading devices including blind, roller shade and drapery. Optical properties of the shading device were experimentally determined and then used in the model for predicting the overall optical properties of the fenestrations systems. To determine solar heat gain, it was assumed that solar radiation absorbed by any internal shading device would all remain in the room. This means that the inward flowing fraction of the internal shading layer was assumed to be one. Along with this assumption, it was also assumed that the presence of the internal shading device had no effect on the inward flowing fraction of the glazing layer. Therefore, the same formula as that of the unshaded glazing system was utilized to determine the inward flowing fraction of the glazing layer of the glazing/shading combinations. Although these assumptions greatly simplify the analysis, they are unlikely to be valid for the fenestration system under realistic conditions. In a later study, McCluney and Mills [1993] also employed similar assumptions and developed a similar equation for determining the shading coefficient of the single glazing with an interior shade.

Rheault and Bilgen [1989] presented a theoretical analysis of the heat transfer through a fenestration system with Venetian blinds installed and sealed between two glass panes. Their analysis considered both convection and radiation heat transfer but neglected heat conduction due to the assumption that both the blind and glazing are isothermal. Their analysis was divided into 3 parts: solar radiation, longwave radiation, and convection heat transfer. For the solar radiation exchange, although their model accounted for diffuse solar radiation from both the sky and ground, it was unclear how view factors between slat surfaces and the sky/ground were determined. For both solar and longwave radiation exchanges, it was assumed that the blind had diffuse-reflecting slats; hence, the net radiation method was used to find solar and infrared radiosities and irradiances on surfaces. For convection heat transfer, it was assumed that the presence of the blind had no effect on the convection phenomena in the window cavity due to the large distance from the end of the slats to the glass; thus, a convection correlation for buoyancy driven flow in a vertical cavity was used. The total heat transfer was determined by solving energy balances on the outside glass, the slats, and the inside glass. Rheault and Bilgen [1990] later compared their theoretical model with experimental data obtained using a variable temperature calorimeter and found that their model agreed quite well with measure results. On average, discrepancies between predicted and measured results were only 6% and 7% for total transmitted solar radiation and temperatures of glass panes and room, respectively.

2.2.2 Recent Studies of Fenestration System Containing Shading Devices

Due to advancements in window technologies in the late 1980s to early 1990s, previous models and data obtained by means of solar calorimeters became increasingly obsolete for use in determining optical and thermal characteristics of fenestration systems that can be a combination of a variety of glazing and shading products. Consequently, Klems et al. [Klems 1994a; 1994b; Klems et al. 1995] developed a detailed model in an attempt to generalize the procedure for predicting the solar heat gain through a complex fenestration system, commonly defined as a system that contains one or more non-specular optical components, such as slat-type blinds, drapes, and honeycomb [ASHRAE 2001]. The model was termed the solar-thermal separation and layer method due to its two main concepts. The first basic concept of the model was that the fenestration system consists of a series of plane-parallel layers and the overall optical characteristics of the system could be described as a function of optical properties of individual layers. The so-called layer method was then used to determine overall optical properties of the system from the knowledge of optical properties of each separate layer. Although the authors proposed that the optical properties of individual layers be determined by bi-directional optical property measurements, theoretical models for glazing and/or shading layers might also be used to predict individual layer optical properties. The other main concept of the model was that the inward flowing fractions of the individual layers are purely thermal properties and thus are independent of optical properties of the layers. Similarly, the authors also proposed that the inward flowing fractions be determined by calorimetric measurements although a general thermal model might be utilized as well. Subsequent studies by the same group of researchers [Klems and Warner 1995; Klems and Kelly 1996; Klems et al. 1996; Klems and Warner 1997] were done to support their model. However, these studies only produced limited data [ASHRAE 2001]. A lack of database and/or sub-models for predicting optical and thermal properties of individual layers prevented the model from becoming widely used as visualized by the authors [Klems 2002] even though there was an attempt by other researchers to extend the solar-thermal separation concept by developing a correlation for the inward flowing fraction of the interior blind [Collins and Harrison 1999].

Pfrommer et al. [1996] developed an optical model for the fenestration system containing either external or internal slat-type blinds. Since the model was intended for implementing directly in a building simulation program, analytical formulations were given for most calculations. Unlike other existing models, the model is applicable to a blind having partially specular-reflecting and partially diffuse-reflecting slats. The model is discussed in more detail in Chapter 3 along with the EnergyPlus and Parmelee models [DOE 2002; Parmelee and Aubele 1952]. Analytical and numerical comparisons of the three optical blind models are thoroughly discussed in Chapter 3.

A number of recent studies [Collins et al. 2002; Collins and Harrison 2004; Collins 2004; Duarte et al. 2001; Machin et al. 1998; Oosthuizen et al. 2005; Phillips et al. 1999; Phillips et al. 2001; Ye et al. 1999] have primarily focused on the effect of an internal slat-type blind on convection heat transfer from the glazing layer. Machin et al. [1998] and Duarte et al. [2001] conducted experimental studies to investigate the influence of the horizontal-slat blind on free convection for nighttime and daytime conditions (with and without the presence of solar radiation), respectively. The convection heat transfer rate from a vertical isothermal surface representing the interior-glazing layer was measured using a Mach-Zehnder interferometer. An unheated aluminum blind located adjacent to the glazing was used for the nighttime condition while a heated blind was used for the daytime condition. Various parameters were investigated including the spacing between the blind and the vertical plate, slat angle, and the amount of absorbed solar radiation (represented by the flux used to heat the blind). For both conditions, experimental results showed that the presence of the blind caused a strong periodic variation in the local convection heat transfer rate. For the nighttime condition, the average convection heat transfer rate tended to be slightly lower due to the presence of the blind, except for the completely closed blind case. For the daytime condition, the average convection heat transfer rate showed a strong dependency on the amount of absorbed solar flux. The absorbed solar flux also had an influence on the effect of the blind-to-glazing spacing and the slat angle on the average convection heat transfer rate. In related studies [Collins et al. 2002; Collins and Harrison 2004; Collins 2004; Oosthuizen et al. 2005; Phillips et al. 1999; Phillips et al. 2001; Ye et al. 1999], numerical models based on the computational fluid dynamics (CFD) method were developed to extend the scope of the study on the effect of the Venetian blind on free convection at the interior glazing. Ye et al. [1999] first developed a two-dimensional model using the finite element technique. On the room side, the room air temperature was used as a boundary condition. The model neglected effects of thermal radiation and conduction within the slats of the blind. The model was then validated with Machin's experimental results for the nighttime condition. The study showed that discrepancies between numerical and experimental results were quite significant. The authors suggested that the discrepancies were caused by the heat conduction within the blind. Subsequently, Phillips et al. [1999] extended the model to include the effect of heat conduction. However, the numerical results were still low compared to the experimental results. Phillips et al. [2001] later included the effect of thermal radiation in the model and found that the improved model had good agreements with measured data. Collins et al. [Collins et al. 2002; Collins and Harrison 2004; Collins 2004] extended the numerical model to include the effect of solar radiation absorbed in the blind so that the model could be used for the daytime condition as well as the nighttime condition. Once they validated the model with experimental results for both conditions, they used the model to investigate the influence of various parameters on convection and radiation heat transfer rates from the glazing having an adjacent slat-type blind. Using numerical results, Collins and Harrison [2004] presented correlations in the form of radiative and convective heat flux from the glazing surface. Collins and Harrison [2004] pointed out that their correlations are not practical due to their complexity. Consequently, Collins [2004] has been attempting to develop more usable correlations but has not yet been able to produce one. Oosthuizen et al. [2005] gave a summary of main results obtained from these experimental and numerical studies on the effect of the Venetian blind on free convection at the interior glazing. In addition, Oosthuizen et al. [2005] reported results from numerical studies on the effect of other blind types (the vertical blind and the roller blind) on free convection at the interior glazing. It is worth noting that Collins' correlations [Collins and Harrison 2004] are only applicable for free convection. This means that the correlations are not applicable to most building systems. Moreover, the correlations might not be valid for load calculation purposes since the numerical model used to develop the correlations neglected interactions between the fenestration system and the room.

Meanwhile, Rosenfeld et al. [2000] gave an overview of recent developments in modeling the optical and thermal properties of the complex fenestration system occurring in Europe. For optical properties, the basic concept is similar to the layer method proposed by Klems et al. [1995] such that overall optical properties of the fenestration system are dependent on optical properties of individual layers of the system. In the paper, two models for predicting optical properties of the slat-type blind are discussed. The first model, called the WIS model [van Dijk and Goulding 1996], is conceptually similar to the EnergyPlus model [DOE 2002] described in detail in Chapter 3. The only difference between the two models is probably that slat surfaces are divided into more elements in the WIS model than in the EnergyPlus model (5 elements versus 2 elements). The model is currently incorporated in the ISO standard [ISO 2000]. The other model, called the "simple model", is based on the observation that, for the blind under the consideration, the distribution of radiation reflected from the slat is not uniform and the peak occurs at the specular-reflecting direction. Rosenfeld et al. [2000] showed that the simple model, which accounts for the quasi-specular behavior of the blind, had better agreement with experimental results than the WIS model, which assumes that slat surfaces are purely diffuse. In another paper, Breitenbach et al. [2001] presented mathematical formulations for the simple model. For thermal properties, Rosenfeld et al. [2000] presented an equation for predicting the inward flowing fraction, often called the secondary internal heat transfer factor by European researchers, as a function of outside film resistance, the thermal resistance across the fenestration system, and the inside film resistance. As commonly used for performance rating purposes, outside and inside film resistances were assumed to be constant for some specified boundary conditions (depending on the standards used in each particular country). The thermal resistance across the fenestration system was considered to be an intrinsic thermal property of the fenestration system and considered constant regardless of angle of incidence, level of solar radiation, or environmental conditions. This means that the thermal resistance across the fenestration system only needs to be measured once. To support this idea, they also demonstrated that an error in the thermal resistance across the system as large as 50% would only cause errors of less than 16% and 8% in the inward flowing fraction and the solar heat gain coefficient, respectively. They then also showed that the predicted solar heat gain coefficient agreed well with measured results. Although their demonstration seemed to imply that the thermal fenestration model may be trivial, it is not clear if their assessment is applicable to various other situations, besides the specific conditions required by their performance rating method. Like other studies, they neglected thermal interactions between the fenestration system and the room. More importantly, they also neglected the convective/radiative split of the absorbed solar heat gain and/or the inside convection coefficient, which are needed for estimating the space thermal load.

Recently, Yahoda and Wright [2004a] presented a model for predicting ‘effective’ longwave radiative properties. The model assumes that blind slats are flat, have uniform and temperature-independent properties, and are opaque to longwave radiation. The model also assumes gray and diffuse slat surfaces with respect to longwave radiation. The model is fundamentally similar to a sub-model in EnergyPlus used to predict solar-optical properties of diffuse solar radiation [DOE 2002]. By modeling the longwave radiation in the same way as the shortwave radiation, the blind assembly can be treated as a planar and homogeneous layer that allows the blind assembly to be handled in a fenestration thermal model conventionally used for a glazing system [Yahoda and Wright 2004b]. Yahoda and Wright [2005] also presented an optical model for direct solar radiation. Like Pfrommer's model [Pfrommer et al. 1996], Yahoda's model combined their sub-models into a single model that can describe slat surfaces that are neither purely specular nor purely diffuse. Their sub-model for a specular-reflecting slat surface is an enhanced version of Rosenfeld's simple model [Rosenfeld et al. 2000] that is not restricted to normal incident light. In addition, Yahoda's model has enhanced features by allowing different radiative characteristics for each slat surface (i.e. the upper and lower slat surfaces can have different slat optical properties and different shining factors). The model is only applicable to a blind having flat slats with negligible slat thickness. Yahoda and Wright [Yahoda and Wright 2005] showed that their model predicted nearly identical results as Parmelee's models did for both blinds having purely diffuse-reflecting slats and blinds having purely specular-reflecting slats.

In parallel with the current study, an ongoing ASHRAE research [Collins and Wright 2006; Huang et al. 2006; Wright and Kotey 2006] is attempting to enhance fenestration system simulation for load calculations. Wright and Kotey [2006] presented an optical model for a fenestration system containing shading layers. Similar to the optical fenestration model presented in Appendix D, Wright's model is based on a multi-layer optical calculation, which requires optical properties of individual fenestration layers as inputs. The main difference[1] between Wright's model and the optical fenestration model presented in Appendix D is that the optical fenestration model presented in Appendix D was developed specifically for the fenestration

---

[1] The author used Wright's technical approach (i.e. the matrix solution technique) to derive a model equivalent to Wright's model but consistent with the optical blind model presented in Chapter 5. The author then compared the model with the optical fenestration model presented in Appendix D and found no difference in the predicted results.

system containing a slat-type blind. The optical fenestration model is consistent with the newly developed optical blind model presented in Chapter 4 whereas Wright's model is not. The reason for the development of the optical fenestration model is discussed in detail in Section 2.3.2.2. In addition to Wright's model, Huang et al. [Huang et al. 2006] presented the measured thermal resistance of a fenestration system containing a between-pane blind using a guarded heater plate apparatus while Collins and Wright [Collins and Wright 2006] presented a calculation procedure to predict U-value and inward flowing fractions of a fenestration system containing a diathermanous layer (e.g. a blind layer). According to its primary objective, the ongoing ASHRAE research should result in an enhanced fenestration simulation suitable for load calculations. However, models and data that have been presented as of this writing appeared to be more suitable to product rating than load calculations.

2.3 Methodology for Enhancing Fenestration System Simulation

Typically, the energy performance of a fenestration system is evaluated by means of two separate but related models: an optical model and a thermal model. The optical model is used to handle shortwave phenomena of the fenestration system while the thermal model is used to handle thermal (conduction, convection, and longwave radiation) phenomena of the fenestration system. Therefore, the methodology for enhancing the simulation of the fenestration system is essentially divided into two parts: optical and thermal studies. The optical modeling can be divided into 3 parts: blind, glazing, and fenestration models. The optical blind, glazing, and fenestration models are used to predict optical properties of the blind layer, the glazing layer, and the fenestration system, respectively. Interactions of the models in the current study are illustrated in Figure 2-2. An arrow is used to indicate the flow of information between the models. A single-ended arrow indicates information flow in one direction only and a double-ended arrow indicates information flow in both directions.

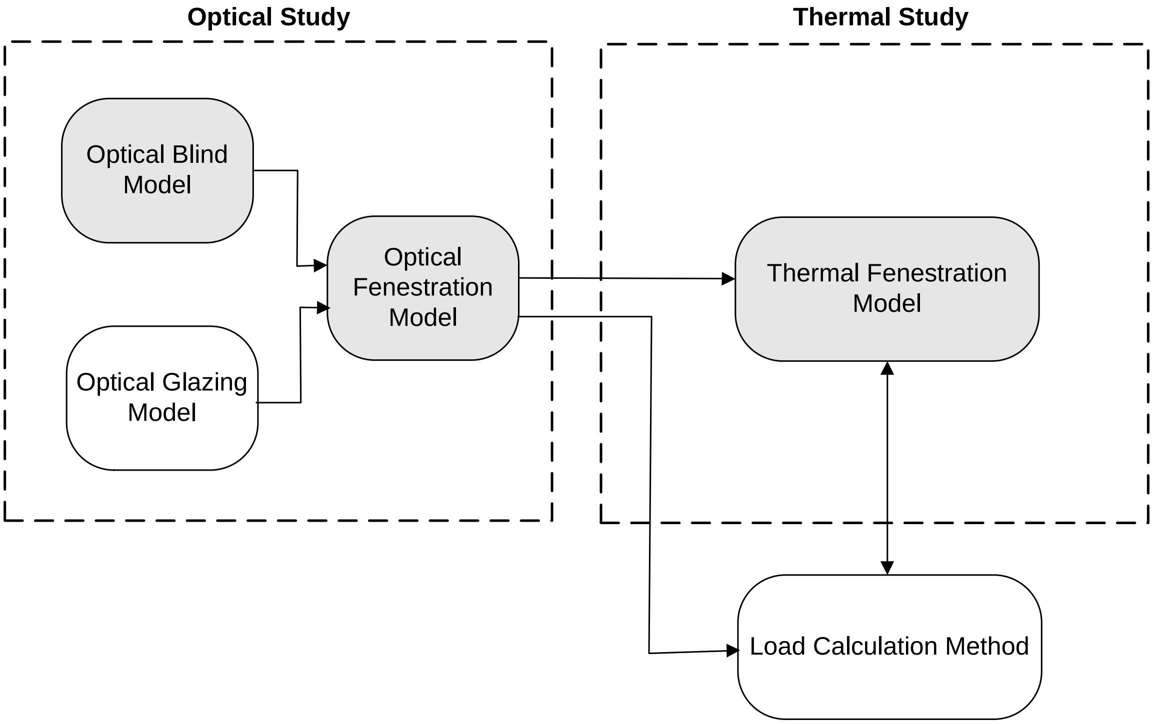

Figure 2-2 Interactions of Optical Models, Thermal Model, and Load Calculation Method

As shown in Figure 2-2, the optical blind and the optical glazing models provide required inputs for the optical fenestration model. Then, the optical fenestration model provides inputs required by the thermal fenestration model and the load calculation method. The thermal fenestration model and the load calculation method interact with each other since the thermal fenestration model is inherently a part of the load calculation method. For the current study, the focus is on the optical blind model, the optical fenestration model, and the thermal fenestration model, which are shown in gray boxes.

Since the objective of the study is to enhance the modeling of the fenestration system for building thermal load and energy calculations, models considered (both optical and thermal) are those compatible with building thermal load calculation procedures. In the next section, model compatibility with building thermal load calculation methods is discussed. Then, an overview of the optical study is presented. Finally, an overview of the thermal study is given.

2.3.1 Model Compatibility with Building Thermal Load Calculation Methods

This section describes criteria used for considering models suitable for the current research. Since currently endorsed ASHRAE cooling load calculation methods include the HBM and the RTSM, the models considered in this study are those compatible with these two methods. To be compatible with the HBM, optical (shortwave radiation) models should distinguish between transmitted beam and transmitted diffuse solar radiation. This distinction is essential for modeling consistency required by the internal solar radiation distribution model used in the HBM since the internal solar radiation model typically treats beam and diffuse radiation differently. Therefore, for instance, an optical blind model should predict both direct-to-direct and direct-to-diffuse blind transmittances, and an optical fenestration model should predict both direct-to-direct and direct-to-diffuse effective (or overall) transmittances. To be compatible with the HBM, thermal models must treat longwave radiation and convection effects separately. Specifically, convection coefficients for surfaces of the fenestration system must be handled separately in the computation algorithms. For load calculations, in general, thermal models should account for the room air flow field and thermal radiation exchanges between the fenestration system and the other room surfaces.

To be compatible with the RTSM, models (both optical and thermal) using explicit calculations are preferable to models using iterative calculations. In general, models developed for the HBM can be used to generate optical and thermal parameters required by the RTSM to predict the transmitted solar heat gains, the absorbed solar heat gain, and the conduction heat gain of the fenestration system. In the RTSM, the solar radiant time factors (Solar RTF) are used to convert the 'beam portion' of the transmitted solar heat gain into the cooling load while the Non-

Solar RTF is used to convert all other radiant heat gains into the cooling load. Similar to the HBM, the RTSM therefore distinguishes between transmitted beam and diffuse solar radiation. This means that the RTSM requires both direct-to-direct and direct-to-diffuse effective transmittances to predict transmitted beam and transmitted diffuse solar heat gains, respectively.

2.3.2 Overview of Optical Study

To deal with a variety of fenestration products, McCluney [2002] suggests the generalized optical modeling approach to determine optical properties of the fenestration system. With the generalized optical modeling approach, bi-conical[1] optical properties of materials that make up the fenestration system must be measured and stored in an optical property database. Then, to determine optical properties of the fenestration system, a three-dimensional (3-D) ray-tracing procedure is used along with the knowledge of the fenestration system's 3-D geometry and the measured optical properties of the fenestration system's components. Although this approach would probably provide the most accurate results, the 3-D ray-tracing technique is computationally intensive and not yet suitable for incorporating into a heat balance based building simulation program, let alone a load calculation procedure.

The more suitable approach for optical calculations in heat balance based load calculations is based on the so-called multi-layer approach. With this approach, optical properties of the fenestration system can be determined as a function of the optical properties of its individual components. Presently, this approach is accepted as a worldwide standard [DOE 2006; ISO 2000; Klems 2002; Rosenfeld et al. 2000; van Dijk and Goulding 1996; Wright and Kotey 2006]. With the multi-layer optical calculation approach, the optical properties of individual components of the fenestration system must be available as inputs, either as a result of direct measurement or as a result of measurements combined with detailed mathematical models.

---

[1] According to McCluney [2002], the term "conical" is used to indicate a nominally conical (pencil point shaped) solid angle whereas the term "directional" is used to refer to an infinitesimally small solid angle. This means that the "conical" term refers to measurable optical properties while the "directional" term refers to theoretical optical properties. Nonetheless, these two terms are often used interchangeably in the literature [Breitenbach et al. 2001; Klems and Warner 1995].

Although the approach is applicable for determining spectral optical properties of the fenestration system, spectrally-averaged optical properties are normally adequate for building load and energy calculations. Therefore, an optical fenestration model is based on multi-layer, spectrally-averaged optical calculations for this research.

The focus of the optical study was on the modeling of the fenestration system containing a slat-type blind. Using the multi-layer optical calculation approach, the optical modeling may be subdivided into 3 parts: glazing, blind, and fenestration. The optical glazing model refers to calculation procedures for determining optical properties of the glazing layer. The optical blind model refers to calculation procedures for predicting optical properties of the blind layer. The optical fenestration model refers to calculation procedures for calculating overall (or effective) optical properties of the combined glazing and shading layers. At present, existing glazing models [Rubin et al. 1998; Wright 1998] and window computer programs [LBL 1994, 2001; van Dijk and Goulding 1996; Wright and Sullivan 1995] have been well developed to deal with a variety of unshaded glazing systems. Therefore, this study was only concerned with the optical blind and optical fenestration models.

2.3.2.1 Investigation of Existing Optical Blind Models

Several models exist for predicting optical properties of the slat-type blind layer [Parmelee and Aubele 1952; Pfrommer et al. 1996; Simmler et al. 1996; Yahoda and Wright 2005]. These models are suitable for incorporating in a building energy simulation tool. The first step in the optical study was therefore to investigate capabilities and accuracy of these existing models. The existing models including the Parmelee model [Parmelee and Aubele 1952], the Pfrommer model [Pfrommer et al. 1996], and the EnergyPlus model [DOE 2002; Simmler et al. 1996] were analytically and numerically investigated. Strengths and weaknesses of the models were also identified. This comparative analysis of existing optical blind models has been published as a SimBuild-2004 conference paper [Chantrasrisalai and Fisher 2004]. Some materials from the paper are also presented in Chapter 3.

2.3.2.2 Development of New Optical Blind and Fenestration Models

The investigation of existing optical blind models discussed in the previous section identified various strengths and weaknesses in the existing models. The study indicated the need for an improved optical blind model. Consequently, a new optical blind model, referred to here as the comprehensive blind model, has been developed. Capabilities of the comprehensive blind model surpass those of existing models in various aspects. The comprehensive blind model takes into account slat thickness as well as slat curvature. The model also accounts for slat surfaces being non-perfect reflectors (i.e. partially diffuse and partially specular-reflecting surfaces). Technical aspects of the comprehensive blind model are summarized below.

- The model is applicable to both blinds having non-zero-thickness flat slats and blinds having zero-thickness curved slats.
- The model is applicable to both blinds having horizontal slats (e.g. Venetian blinds, mini blinds, etc.) and blinds having vertical slats (commonly called vertical blinds).
- The model is applicable to blinds having purely diffuse-reflecting slats, blinds having purely specular-reflecting slats, as well as blinds having partially diffuse and partially specular-reflecting slats.
- The model is applicable to blinds having either opaque, translucent, or perforated slat surfaces.
- The model allows different radiative characteristics on different sides of the blind slats.
- The model treats direct and diffuse components of incident solar radiation separately.
- The model treats diffuse solar radiation from the sky and the ground separately.

The technical description of the comprehensive blind model is presented in Chapter 4. Detailed calculations of the comprehensive blind model are given in Appendices A to C.

In addition to developing the comprehensive blind model, a new optical fenestration model has also been developed. The new optical fenestration model is based on the multi-layer, spectrally-averaged optical calculations that predict the overall optical properties of the fenestration system as a function of the optical properties of individual components. The development of this optical fenestration model is deemed essential since available optical fenestration models [Klems 2002; Wright and Kotey 2006] are often not consistent with existing blind models. For example, blind models typically characterize transmitted direct solar radiation as two components resulting in direct-to-direct and direct-to-diffuse transmittances. These two components are usually combined in the fenestration models and treated as a single component even though they have different characteristics. Fenestration models typically do not distinguish between diffuse solar radiation from the sky and from the ground. Since the newly developed blind model differentiates between these two diffuse solar radiation sources, a multi-layer fenestration model consistent with the new blind model is also needed. Detailed calculations of the newly developed optical fenestration model are presented in Appendix D.

2.3.2.3 Experimental Validation of the Comprehensive Blind Model

In order to validate the comprehensive blind model, an in situ experimental method has been developed. In situ measurements of total solar transmittance for a west-facing fenestration system containing an interior blind were performed for various blind types and configurations. In situ measurements of slat solar reflectance of a slat-type blind were also conducted. The total solar transmittance is a primary metric commonly used to evaluate the optical blind model and the slat solar reflectance is an input required by the optical blind model. Then, the comparison between measured total solar transmittance and predicted results was used to illustrate the validity of the comprehensive blind model. This investigation is discussed in detail in Chapter 5.

2.3.3 Overview of Thermal Study

Although the analysis of optical characteristics of the fenestration system is quite complicated, it is not as difficult as that of its thermal counterpart. To determine heat transfer through the fenestration system, one must rely on experimental results. There are several correlations available in the literature for convection heat transfer in the air gap between (smooth) vertical planes but they often give different results [Rosenfeld et al. 2000]. The presence of the shading device layer adds complexity to the problem. Due to the open nature of the shading device, not only solar (shortwave) radiation but also longwave radiation can pass through the device. Therefore, longwave exchanges with other inside room surfaces occur for both the glazing and the shading device. Also, the airflow from the gap between the glazing and the internal shading device to the room usually occurs depending on the installation of the shading device (i.e. outside or inside mounting) and the room air flow field (i.e. natural, mixed, or forced convection flow field). This means that convective heat transfer from the fenestration system with an interior shading device is certainly not the same as that from the fenestration system without an interior shading device.

At present, no accepted standard thermal model is available to deal with the problem. A thermal fenestration model implemented in the EnergyPlus building simulation program [DOE 2006] is currently the most fundamental model suitable for load calculations. The EnergyPlus thermal model is based on a one-dimensional multi-layer heat balance approach. The model is certainly applicable for the HBM, but is not for the RTSM. The model considers fenestration components separately and directly performs an energy balance at each surface of the individual layers of the fenestration system. The EnergyPlus thermal fenestration model is basically based on two thermal models: one for glazing layers [Arasteh et al. 1989] and one for shading layers [ISO 2000; van Dijk and Goulding 1996]. The thermal model for shading layers is presently incorporated in the ISO standard [ISO 2000]. Unfortunately, the model has not yet been validated [van Dijk and Oversloot 2003]. The model is quite complicated and requires various parameters including convection coefficients in the air gap between the glazing layers and the shading layer, a convection coefficient for convection from the (inside) shading layer to the room air, the air permeability between the air gap and the room, etc. Presently, no existing standard is available to measure these parameters [ISO 2000].

There are two possible paths for enhancing the thermal fenestration simulation. The first path is to develop an experimental method for determining and validating the aforementioned parameters required by the EnergyPlus thermal fenestration model. For thermal load calculation purposes, experiments must be conducted in a full-scale test room in order to account for thermal interactions between the fenestration system and the room (i.e. room air flow field and thermal radiation exchanges with room surfaces). This means that an experimental method employing a small-scale calorimeter or a guarded hot box is likely invalid since the thermal interactions in the small-scale calorimeter do not necessarily reflect those of a realistic building environment. The second path is to develop a new thermal model for the HBM and develop an experimental method to support the new model. For this study, the second path was considered to be a better option. As discussed in the following sections, the new thermal model for the HBM simplifies calculations of the thermal interactions between the fenestration system and the room by combining the innermost glazing layer and an interior blind into a single layer. Consequently, it is feasible to conduct the experiments in a full-scale test room to measure thermal parameters (used to account for the room-fenestration thermal interactions) required by the new model.

For the current research, the focus of the thermal study was on the modeling of the fenestration system containing an interior slat-type blind. A small number of experimental tests were performed to demonstrate the feasibility of the experimental method. Future studies with full parametric experiments are deemed essential to develop empirical correlations in order to fully support the new model. In the following sections, developments of the thermal models and the experimental method are discussed.

2.3.3.1 Development of New Thermal Models

Two thermal fenestration models have been developed: one suitable for the HBM (called the HB thermal fenestration model) and one suitable for the RTSM (called the RTS thermal fenestration model). Similar to the EnergyPlus thermal fenestration model, the HB thermal fenestration model is based on a multi-layer heat balance approach. Like the EnergyPlus model, the HB thermal fenestration model also employs a thermal glazing model (i.e. a thermal model for a fenestration system without shading devices [Arasteh et al. 1989; Wright 1998]) for the glazing layers, except the innermost glazing layer. However, for a fenestration system with an interior blind, the HB thermal fenestration model treats the innermost glazing layer and the blind layer as a single layer. The HB thermal fenestration model requires two thermal parameters for the combined glazing and blind layer that represent thermal interactions within the layer and between the layer and the room. These two parameters are referred to here as the equivalent thermal conductance within the combined layer and the equivalent inside convection coefficient of the inside (fictitious) surface of the combined layer. An experimental method described in the next section is essential for determining these two parameters.

The RTS thermal fenestration model is based on the so-called solar-thermal separation concept [Klems et al. 1995; Klems and Kelly 1996; Klems et al. 1996; Klems and Warner 1997]. Essentially, the RTS thermal fenestration model represents thermal calculations for determining fenestration heat gains and converting heat gains into cooling loads. The model requires various parameters as inputs. These parameters include total (beam and diffuse) solar transmittances, layer-specific solar absorptances, layer-specific inward flowing fractions, total thermal resistance, and radiative/convective splits. Optical models discussed in previous sections can be used to obtain the solar transmittances and absorptances. The ‘complete’ HB thermal fenestration model (when empirical correlations for the two aforementioned thermal parameters are available) can be used to obtain the inward flowing fractions and the thermal resistance. The experimental method described in the next section can be used to obtain the radiative/convective split of the absorbed solar heat gain and the conduction heat gain. Detailed thermal calculations are all presented in Chapter 6.

2.3.3.2 Development of Experiment Method for Thermal Models

Thermal interactions of the fenestration system containing an interior blind in a room are very complicated. Figure 2-3a illustrates thermal interactions between the fenestration system and the room, and Figure 2-3b shows thermal interactions within the gap between the innermost glazing layer and the interior blind. The thermal interactions between the fenestration system and the room include convection from the blind to the room air, longwave radiation between the blind and the room surfaces, bulk convection between the air gap and the room, and longwave radiation between the innermost glazing and the room surfaces. The thermal interactions within the gap include convection from both the glazing and the blind to the air in the gap, and the longwave radiation between the glazing and the blind. Although the sub-model of the EnergyPlus thermal fenestration model for the shading layers fundamentally uses various thermal parameters (including convection coefficients in the air gap between the glazing layer and the blind layer, a convection coefficient for convection from the blind to the room air, the air permeability between the air gap and the room, etc.) to separately handle these thermal interactions, the model has not yet been validated [van Dijk and Oversloot 2003]. According to *ISO Standard 15099* [2000], a feasible experimental method to measure various thermal parameters used in the model is not available. This indicates that the model was developed without considering the level of effort required to measure these parameters. Though these parameters may be measured by an experimental method employing a small-scale calorimeter, thermal interactions in the calorimeter do not necessarily reflect those of a realistic building environment. The replication of a realistic room airflow field (that accounts for both air jet from the supply diffuser and buoyant air flow around the fenestration system as illustrated in Figure 2-3) in the small-scale calorimeter is hard to achieve.

For the current study, a tractable experimental method has been developed along with the new thermal fenestration models. As a result, experimental measurements of thermal parameters required by the new thermal models are feasible. As discussed in the previous section, these thermal parameters include the equivalent thermal conductance and the equivalent inside convection coefficient of the inside surface of the combined layer (required by the HB thermal fenestration model), and the radiative/convective split of the absorbed solar and the conduction heat gains (required by the RTS thermal fenestration model). The experimental method is based on the measurement of the radiative heat gain from the fenestration system at steady-state. The experimental method, which requires that experimental tests be performed in a full-scale test room, is described in detail in Chapter 6.

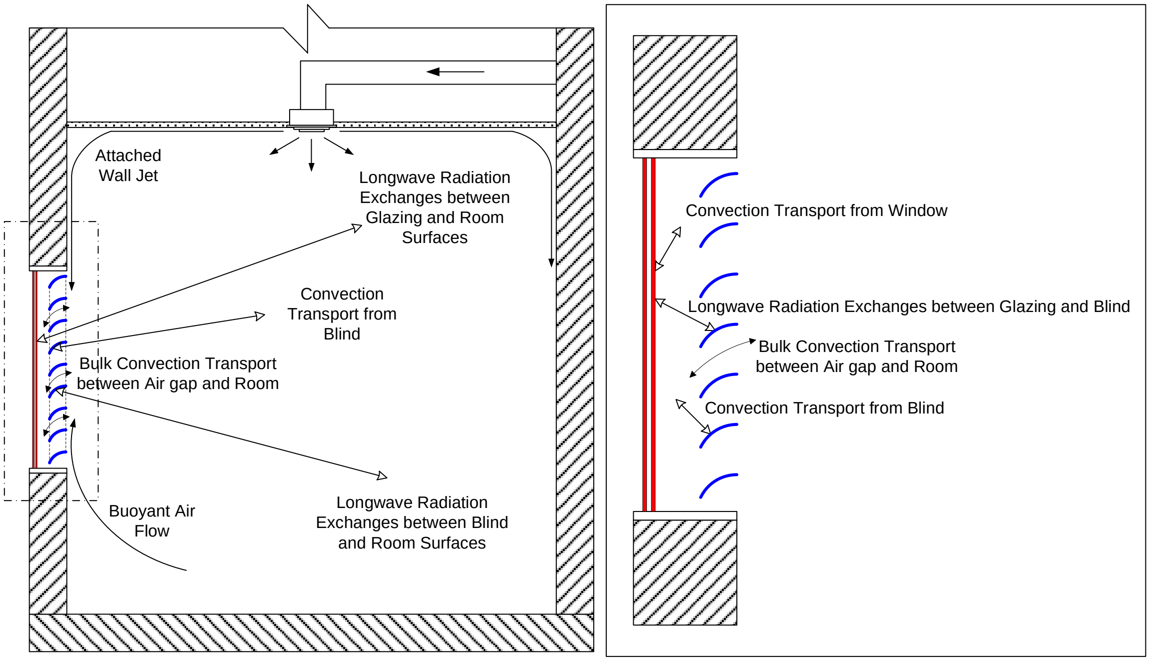

a) Thermal Interactions between the Fenestration System and the Room

b) Thermal Interactions in the Gap between the Window and the Blind

Figure 2-3 Thermal Interactions of the Fenestration System Containing an Interior Blind

CHAPTER 3

COMPARATIVE ANALYSIS OF EXISING OPTICAL BLIND MODELS

3.1 Introduction

The use of solar shading devices is an important strategy in energy conscious building design. Correctly designed shading systems can optimally provide natural light as well as effectively reduce building heat gains and cooling requirements. However, a detailed knowledge of the optical and thermal properties of the shading devices is an essential prerequisite of optimal fenestration system design. It is therefore necessary to have detailed simulation models that can reliably predict and quantify the performance of shading devices for all locations and seasons.

Slat-type shading devices, such as Venetian blinds, are popular because they are relatively inexpensive and can provide occupant privacy. They can also be used to provide glare control to improve visual comfort. Typically, two models are used to characterize the performance of the fenestration system containing slat-type blinds: an optical and a thermal model. The optical (or solar) model handles shortwave phenomena of the fenestration system while the thermal model deals with thermal (conduction, convection, and longwave radiation) phenomena of the fenestration system.

To estimate optical properties of the fenestration system, the current standard approach is based on the so-call multi-layer approach [Klems et al. 1995; Rosenfeld et al. 2000; van Dijk and Goulding 1996]. With this approach, optical properties of the fenestration system can be determined as a function of optical properties of its individual components. The optical properties of individual components of the fenestration system are inputs to the optical fenestration model and can be determined by measurements and/or detailed mathematical models. Mathematical models are preferable since they can easily be used to study the effect of input parameters on fenestration components over a range of conditions [Rosenfeld et al. 2000].

This chapter focuses on models used to predict solar-optical properties of slat-type blinds. The main objective is to investigate and identify weaknesses in existing optical blind models suitable for incorporating into a building simulation tool. The study compares three one-dimensional, optical blind models suitable for building load calculations [Parmelee and Aubele 1952; Pfrommer et al. 1996; Simmler et al. 1996] – and investigates the influence of input parameters on the solar transmittance. A new optical blind model is then proposed. An inter-model comparison of the new model is also presented.

3.2 Existing Optical Slat-Type Blind Models

The earliest attempt to analyze optical characteristics of slat-type blinds was possibly made by Parmelee and Aubele [1952]. They presented two optical blind models: one for a specular-reflecting slat surface and one for a diffuse-reflecting slat surface. Their models are discussed in detail in the next section. In their subsequent paper, Parmelee et al. [1953] validated their models with experimental data obtained by means of the solar calorimeter. They later used their models to develop design data for use in determining the solar heat gain [Parmelee and Vild 1953]. Several researchers [Collins and Harrison 2004; Farber et al. 1963; Ozisik and Schutrum 1960] utilized Parmelee's models to study energy performance of various fenestration systems containing slat-type blinds.

Like Parmelee and Aubele, Pfrommer et al. [1996] developed optical blind models for both specular- and diffuse-reflecting slat surfaces. However, they combined their two models into a single model that can describe slat surfaces that are neither purely specular nor purely diffuse. Their models are discussed in detail in the next section.

Rosenfeld et al. [2000] discussed two optical blind models recently developed by European researchers. The first model, called the WIS model developed by van Dijk and Goulding [1996], is an optical model applicable only for blinds with a diffuse-reflecting slat surface. The WIS model is conceptually similar to Simmler's model [1996], which is described in detail in the next section. The only significant difference between the two models is that slat surfaces are divided into more elements in the WIS model than in Simmler's model (i.e. 5 elements versus 2 elements). The WIS model is currently incorporated in the ISO standard [ISO 2000]. The other model, called the simple model developed by Breitenbach et al. [2001], is based on the observation that the distribution of radiation reflected from the slat is not uniform and the peak occurs at the specular-reflecting direction. Rosenfeld et al. [2000] showed that the simple model, which accounts for the quasi-specular behavior of the blind, had a better agreement with experimental results than the WIS model, which assumes purely diffuse slat surfaces. The simple model, however, was developed specifically for product-rating purposes; hence, the model only predicts blind optical properties for direct solar radiation (e.g. the directional-hemispherical blind transmittance) and is only applicable for normal incident light. The model is therefore not suitable for incorporating in a building simulation tool.

Recently, Yahoda and Wright [2005] presented an optical model for direct solar radiation. Like Pfrommer's direct model, Yahoda's model combined their sub-models into a single model that can describe slat surfaces that are neither purely specular nor purely diffuse. Their sub-model for a specular-reflecting slat surface is an enhanced version of Rosenfeld's simple model that is not restricted to normal incident light. In addition, Yahoda's model has enhanced features by allowing different radiative characteristics for each slat surface (i.e. the upper and lower slat surfaces can have different slat optical properties and different shining factors). The model is only applicable to a blind having flat slats with negligible slat thickness. Yahoda and Wright [2005] showed that their model predicted nearly identical results as Parmelee's models did for both blinds having purely diffuse-reflecting slats and blinds having purely specular-reflecting slats. Yahoda's model is not included in the comparative analysis since the model was not available at the time of the investigation.

3.3 Comparative Analysis

This study investigates three selected optical slat-type blind models – the Parmelee, Pfrommer, and EnergyPlus models [DOE 2002; Parmelee and Aubele 1952; Pfrommer et al. 1996] – that are suitable for use in a building energy simulation program. A brief overview of the Parmelee and Pfrommer models is given in the previous section. The EnergyPlus model was originally developed by Simmler et al. [1996] for the DOE-2 building energy calculation program [Winkelmann et al. 1993]. The EnergyPlus model is only applicable to blinds with diffuse-reflecting slat surfaces. In this section, fundamental calculations of the three models are compared in detail.

3.3.1 Common Basic Assumptions

All three models consider the blind assembly as a series of equidistant slats. The slats are assumed to be of infinite length. Then, in a theoretical analysis, the whole blind assembly is represented by two consecutive slats. The models are considered to be one-dimensional optical blind models since the models predict the amount of solar radiation transmitted through the blind assembly, but do not determine where the transmitted solar radiation falls in the room, which would require a three-dimensional ray tracing technique.

3.3.2 Calculation Procedures for Direct Solar Radiation

All three models similarly divide the calculation procedure for direct solar radiation into two parts. The first part of the calculation procedure deals with directly transmitted radiation and is purely a geometry problem. The ratio of the unobstructed solar radiation passing through the blind to the incident solar radiation is called the opening ratio by Parmelee and Aubele [1952]. This opening ratio is generally referred to as the ‘direct-to-direct transmittance’ of the blind [DOE 2002; Pfrommer et al. 1996]. For flat slats of negligible thickness, all three models predict exactly the same direct-to-direct blind transmittance. However, when either slat thickness or slat curvature is accounted for, the predicted results are slightly different. Later sections discuss how the three models apply corrections to take into account slat thickness and slat curvature.

The second part of the calculation procedure deals with reflected radiation. The EnergyPlus model [DOE 2002] assumes that the slat surface is purely diffuse. Parmelee and Aubele [1952] present two optical blind models: one for a specular reflecting surface and one for a diffuse reflecting surface. Pfrommer et al. [1996] also present algorithms for both specular and diffuse reflecting surfaces but they combined the algorithms into a single model that can describe surfaces that are neither purely specular nor purely diffuse. The Pfrommer model uses a “shining factor” [Pfrommer et al. 1996], defined as the ratio between the diffuse-reflected and the total-reflected components, to specify the diffuseness of the blind slat. The shining factor is one for purely diffuse surfaces and zero for purely specular surfaces.

Both the Parmelee and Pfrommer models consider infinite reflections between slats in calculating the reflected solar radiation for purely specular slat surfaces. Parmelee and Aubele [1952] and Pfrommer et al. [1996] utilize the 2-D ray tracing technique to obtain analytical solutions for specular reflecting surfaces. A preliminary investigation showed that although the Parmelee and Pfrommer models use different formulations, the results predicted by Parmelee’s specular reflecting model and Pfrommer’s model using a shining factor of zero were exactly the same. In this study, the effect of specularly reflecting surfaces was not further investigated.

Using the 2-D ray tracing technique, Parmelee and Aubele [1952] and Pfrommer et al. [1996] also present their diffuse reflecting surface models in an analytical form. However, Parmelee and Aubele consider infinite reflections between slats whereas Pfrommer et al. consider only two reflections. To determine optical properties due to reflected solar radiation, the EnergyPlus model [DOE 2002] employs the net radiation method to solve (solar) radiative energy exchange within an enclosure formed by the outside opening, two slats and the inside opening. Each slat is divided into two elements (illuminated and shaded elements), which vary depending on sunlit area due to incident direct sunlight. To solve radiative energy exchange within the enclosure, only the illuminated element emits energy while all other surfaces have zero emissive power. As previously mentioned, the EnergyPlus model is conceptually similar to the WIS model [van Dijk and Goulding 1996], except that the WIS model divides each slat into five elements.

3.3.3 Predicted Direct Solar Transmission

In this investigation, direct-to-direct transmittance is defined as the fraction of beam solar radiation passing directly through the blind assembly without hitting the slats. Direct-to-diffuse transmittance is defined as the fraction of beam solar radiation passing indirectly through the blind assembly by reflections between the slats. Both direct-to-direct and direct-to-diffuse transmittances are mainly dependent on the profile angle defined as the angle between a plane perpendicular to the blind assembly (the normal plane) and a plane coincident with the line of sight to the sun (the line of sight plane) [Parmelee and Aubele 1952]. Figure 3-1 illustrates the profile angle along with slat geometry. As shown, the slat angle is defined as the angle between the slat and the normal plane. The figure shows a downward facing blind with a positive slat angle. The slat spacing is defined as the distance from the upper surface of the upper slat to the upper surface of the lower slat while the slat width is defined as the distance of a straight line from one end of the slat to the other end as shown in Figure 3-1. Using these conventions, the following analysis is for blinds having horizontal slats.

Overall optical characteristics of the blind assembly are primarily dependent on the slat angle. Other parameters including slat spacing, slat width, slat reflectance, slat thickness, and slat curvature have a secondary effect on the overall optical characteristics of the blind. Figure 3-2 illustrates the influence of the slat angle on the blind transmittances. The different profiles for direct-to-direct and direct-to-diffuse transmittances are characteristic of upward facing, downward facing and fully open (horizontal) blinds.

As shown in Figure 3-2a for 0° (fully open) and –45° (upward facing) slat angle cases, the peak value of the direct-to-direct transmittance (for the blind having flat slats with zero thickness) is equal to one occurring when the sum of the profile angle and the slat angle is zero. At the same profile angle, the direct-to-diffuse transmittance is then equal to zero as shown in Figure 3-2b. Conversely, the peak value of the direct-to-diffuse transmittance occurs at the same profile angle when the direct-to-direct transmittance becomes zero for all three slat angles.

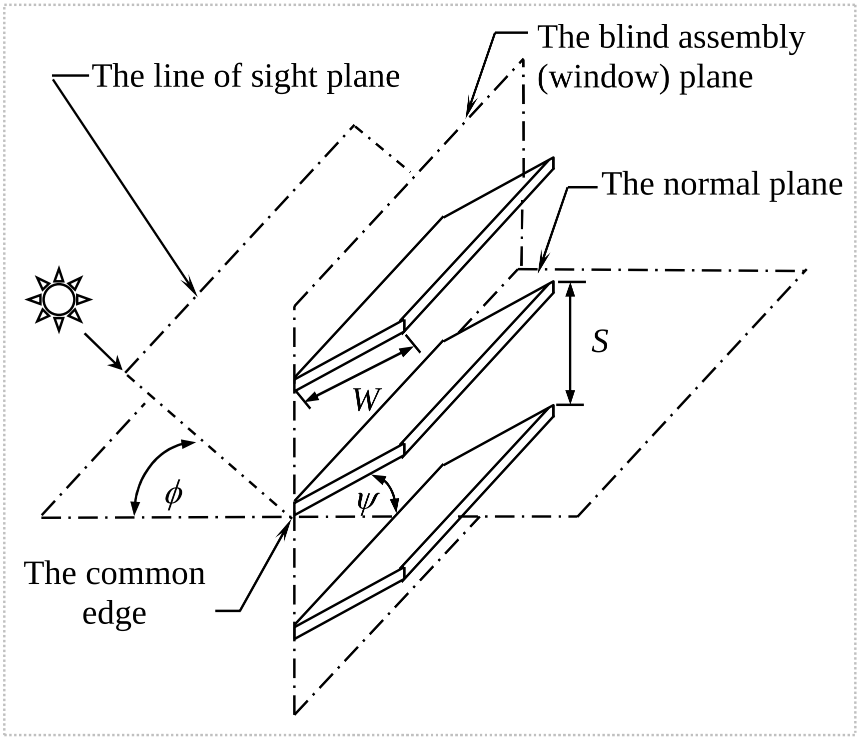

Figure 3-1 Profile Angle and Slat Geometry (ϕ = the profile angle, ψ = the slat angle, S = the slat spacing, W = the slat width)

(a) Direct-to-Direct Transmittance

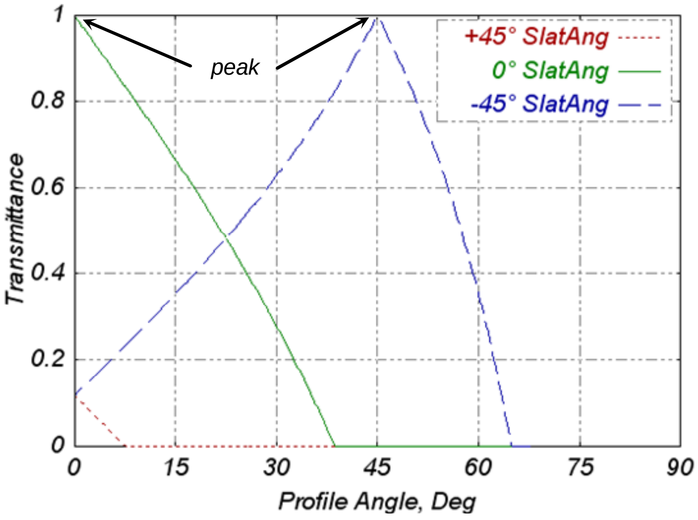

(b) Direct-to-Diffuse Transmittance

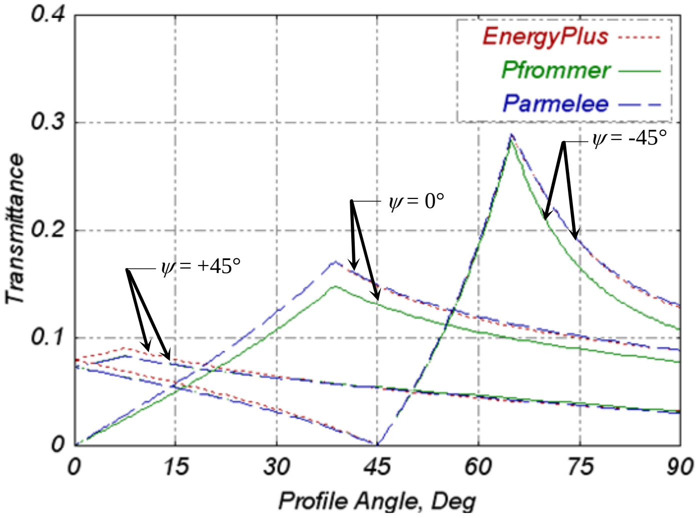

Figure 3-2 Effect of Slat Angle (for Flat Slat with Zero Thickness, and Slat Reflectance of 0.5): (a) Direct-to-Direct Transmittance, (b) Direct-to-Diffuse Transmittance

Since all three models predict the same direct-to-direct transmittance, only one set of results is presented in Figure 3-2a. As shown in Figure 3-2b, the Pfrommer model tends to predict a lower direct-to-diffuse transmittance than the other two models for all slat angles. This is due to the fact that the Pfrommer model considers only two reflections between the slats. On the other hand, both the EnergyPlus and Parmelee models predict nearly identical results for all slat angles indicating that the net radiation method employed in the EnergyPlus model and the 2-D ray tracing technique with infinite reflections between slats used in the Parmelee model are equivalent.

As the slat reflectance increases, the effect of the two-reflection treatment in the Pfrommer model becomes more pronounced. Figure 3-3 shows that there is little difference between the models for a reflectance of 0.1, but a peak error of nearly 25% in the direct-to-diffuse transmittance for a reflectance of 0.9.

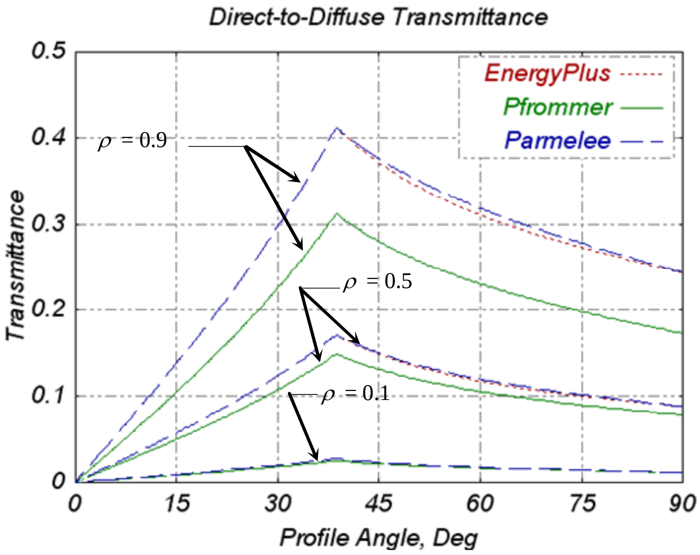

Figure 3-3 Effect of Slat Reflectance on Direct-to-Diffuse Transmittance (for Flat Slat with Zero Thickness, and Slat Angle of 0°)

3.3.4 Calculation Procedures for Diffuse Solar Radiation

Two primary sources are usually treated in the calculation of diffuse solar radiation: the sky and the ground. In the Parmelee model, a hemisphere in front of the blind assembly is used to represent the sky and ground. The upper half of the hemisphere represents the sky while the lower half of the hemisphere represents the ground. Both the sky and the ground are subdivided into a number of small patches. The diffuse radiation leaving each patch is then treated as direct radiation emitted from the center of the patch to the center of the hemisphere where the blind assembly is located. Consequently, the same procedure used to calculate the direct solar radiation is used to calculate diffuse radiation from each patch. The blind transmittances of the sky (or ground) diffuse solar radiation can thus be determined as the ratio of the total solar radiation transmitted through the blind assembly to the total insolation from the sky (or ground) patches

The sky and ground are also considered as separate sources of diffuse solar radiation in the Pfrommer model. Unlike the Parmelee model, however, the hemisphere representing the sky and ground is divided into horizontal slices instead of patches. The diffuse radiation leaving each slice is treated as the direct radiation emitted from the center of the slice to the center of the hemisphere. A uniform radiance from the sky and ground slices is used in the Pfrommer model to calculate blind transmittances for diffuse solar radiation. It is important to note that the Pfrommer model was developed for blinds with horizontal slats only. For horizontal slats, all points on the same horizontal sky (or ground) slice have the same profile angle [Pfrommer et al. 1996]. The blind transmittance of diffuse solar radiation can then be determined by integrating along the profile angle. Pfrommer [1995] provides analytical solutions for their diffuse solar radiation model.

Unlike the other two models, the EnergyPlus model does not differentiate between the diffuse solar radiation from the sky and the ground[1]. The EnergyPlus model uses the net radiation method for both direct and diffuse solar radiation by specifying energy sources of different magnitudes and at different locations [DOE 2002]. For diffuse solar radiation, each slat is equally divided into two segments. A unit energy source is only applied to the fictitious

---

[1] This statement is valid only at the time of this investigation. Currently, the optical blind model implemented in the EnergyPlus program [DOE 2006] is modified to improve its calculations for diffuse solar radiation according to a suggestion resulted from this study.

outside surface while a zero energy source is applied to all other surfaces. The net radiation method is then used to solve diffuse radiative energy balance within the enclosure.

3.3.5 Predicted Diffuse Solar Transmission

To compare the models in this study, all three models predict two blind transmittances for diffuse solar radiation: sky-diffuse and ground-diffuse transmittances. The sky-diffuse transmittance is defined as a fraction of diffuse solar radiation from the sky passing directly and indirectly through the blind assembly. The ground-diffuse transmittance is defined as a fraction of diffuse solar radiation from the ground passing directly and indirectly through the blind assembly. Because the EnergyPlus model does not differentiate between the diffuse solar radiation from the sky and ground, values of sky-diffuse and ground-diffuse transmittances predicted by the EnergyPlus model are always the same.

Diffuse transmittances are plotted as a function of the slat angle in Figure 3-4. As shown, the EnergyPlus model predicts a single diffuse transmittance curve because it does not differentiate between the sky-diffuse and the ground-diffuse transmittances. On the other hand, the Parmelee and Pfrommer models predict two curves: one for the sky-diffuse transmittance and one for the ground-diffuse transmittance. As expected, both the Parmelee and Pfrommer models predict higher ground-diffuse transmittance for the blind opened downward (positive slat angle) and higher sky-diffuse transmittance for the blind opened upward (negative slat angle). The three models predict the same sky-diffuse and ground-diffuse transmittances only for fully opened blinds (slat angle of 0°) when the slat opening's view to the sky and ground are equal.

The effect of slat reflectance on diffuse transmittance is shown in Figure 3-5. The results are shown for fully opened blinds (slat angle of 0°). As shown, the three models predict similar values of diffuse transmittance for low slat reflectance. Similar to previous results, the two-reflection algorithm used in the Pfrommer model results in a 10% under-prediction of the diffuse transmittance relative to other models at high values of slat reflectance.

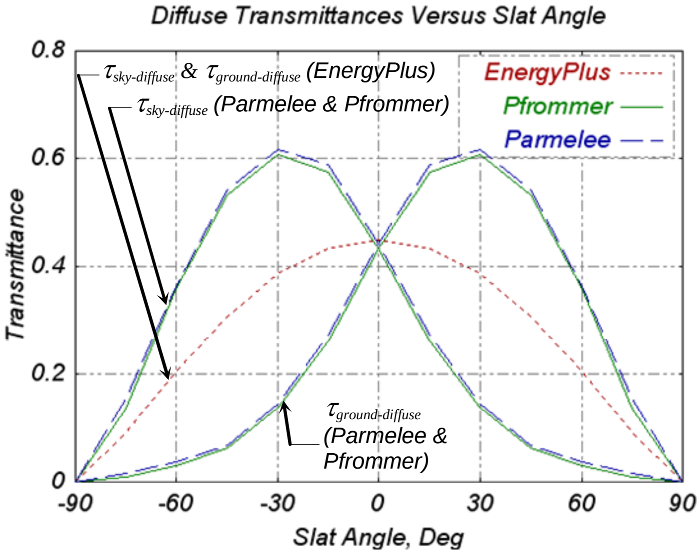

Figure 3-4 Effect of Slat Angle on Diffuse Transmittance(s) (for Flat Slat with Zero Thickness, and Slat Reflectance of 0.5)

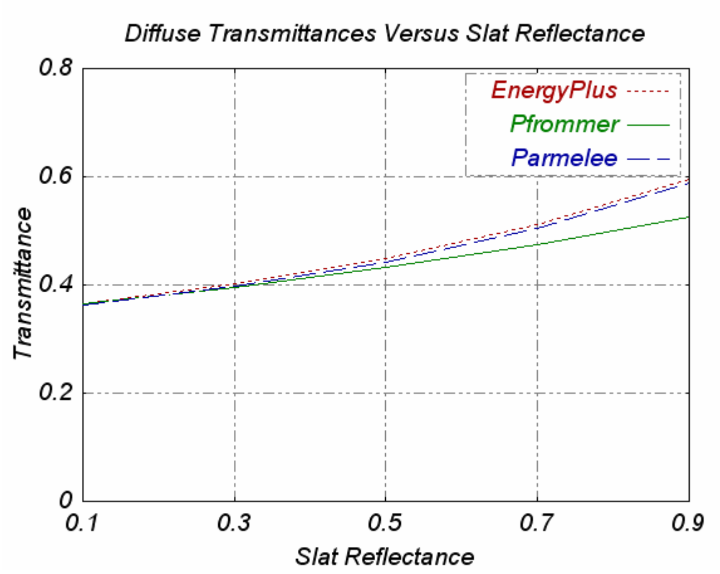

Figure 3-5 Effect of Slat Reflectance on Diffuse Transmittance(s) (for Flat Slat with Zero Thickness, and Slat Angle of 0°)

3.3.6 Corrections for Slat Thickness

In previous sections, the calculation procedures assume flat slats with zero thickness. This assumption may introduce a non-trivial error in the results, especially for wood blinds. Only the Parmelee and EnergyPlus models have corrections to take slat thickness into account. Both models define the correction factor for slat thickness as a fraction of the shaded area due to slat thickness. The Parmelee model [Parmelee and Aubele 1952] applies the correction factor only to direct-to-direct and direct-to-diffuse transmittances. Since the calculation procedures for direct solar radiation are utilized to determine blind transmittances for diffuse solar radiation in the Parmelee model, slat thickness is implicitly accounted for without applying any additional correction to the diffuse transmittances. On the other hand, the EnergyPlus model applies the correction factor to all blind transmittances [DOE 2002].

Figure 3-6 compares flat, zero thickness slats with flat slats having a slat thickness to slat spacing (T/S) ratio of 0.1. The error associated with neglecting the slat thickness can be as high as 15% for the peak direct-to-direct transmittance. As shown in Figure 3-6a, both the Parmelee and EnergyPlus models predict exactly the same direct-to-direct transmittances for the 0° slat angle case, but they predict different results for other slat angles depending on the profile angle (the EnergyPlus correction predicts zero direct-to-direct transmittance at all profile angles for the +45° slat angle case). Likewise, the two models predict almost identical direct-to-diffuse transmittances for the 0° slat angle case, but they predict quite different results for other slat angle cases as illustrated in Figure 3-6b.

(a) Direct-to-Direct Transmittance

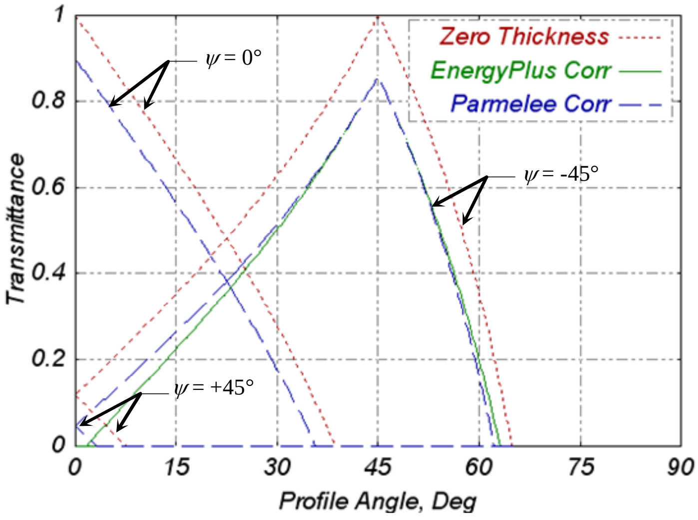

(b) Direct-to-Diffuse Transmittance

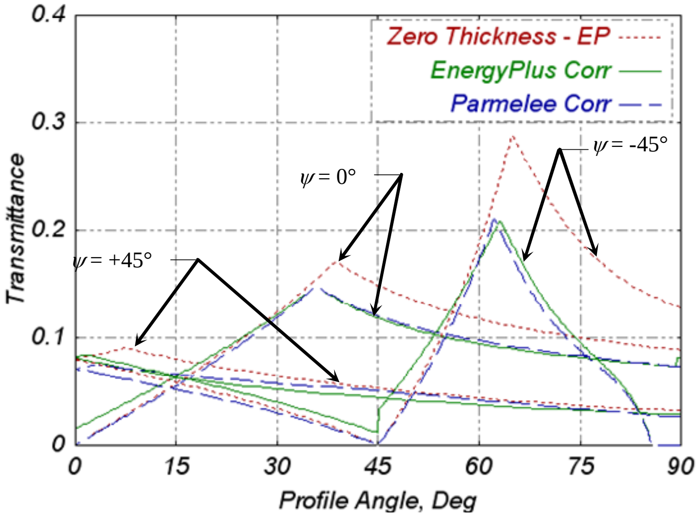

Figure 3-6 Effect of Slat Thickness (for Flat Slat with T/S Ratio of 0.1 and Slat Reflectance of 0.5): (a) Direct-to-Direct Transmittance, (b) Direct-to-Diffuse Transmittance

3.3.7 Corrections for Slat Curvature

As previously mentioned, the flat slat assumption is used in all three models. Only the Pfrommer model has corrections to account for the effect of slat curvature, and those corrections are only applied to the direct-to-direct and direct-to-diffuse transmittances [Pfrommer 1995].

Figure 3-7 compares flat, zero thickness slats with curved slats having a slat curvature radius to slat width (R/W) ratio of 1.0.

(a) Direct-to-Direct Transmittance

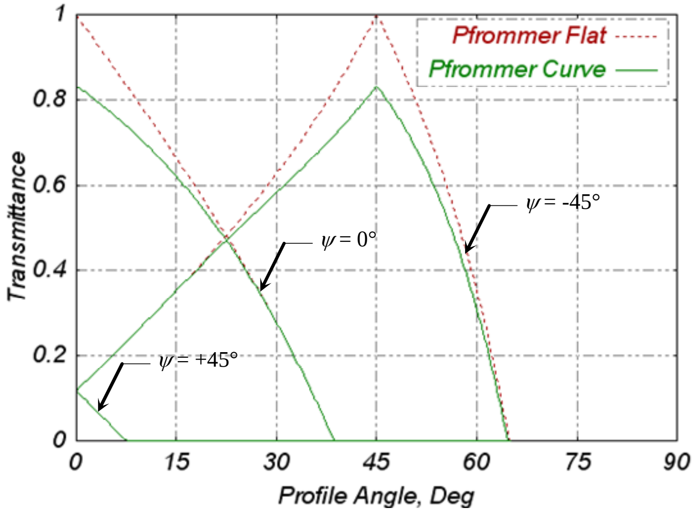

(b) Direct-to-Diffuse Transmittance

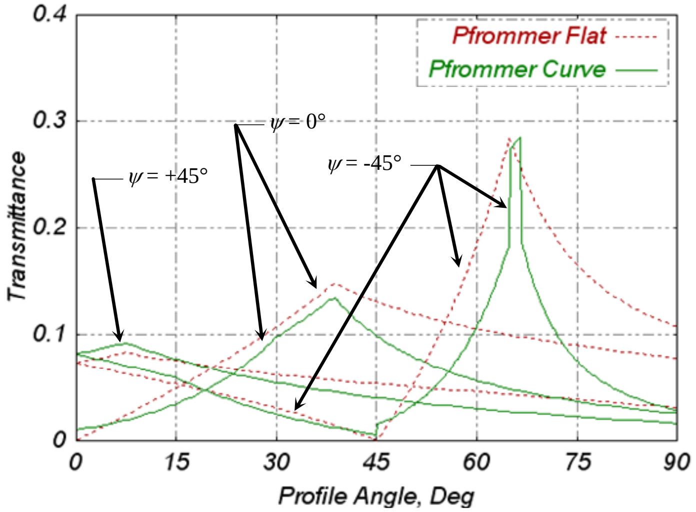

Figure 3-7 Effect of Slat Curvature (for Curved Slat with R/W Ratio of 1.0 and Slat Reflectance of 0.5): (a) Direct-to-Direct Transmittance, (b) Direct-to-Diffuse Transmittance

The figure shows results predicted by the Pfrommer flat and curved slat models. As shown, the slat curvature can have a significant effect on both the direct-to-direct and the direct-to-diffuse transmittances depending on the slat and profile angles. The slat curvature has no effect on the direct-to-direct transmittance for +45° slat angle case. However, the curvature correction reduces the peak direct-to-direct transmittance by more than 15% for both 0° and –45° slat angle cases.

3.4 Proposed New Optical Blind Model

In the previous section, three existing optical blind models – the Parmelee, Pfrommer, and EnergyPlus models [DOE 2002; Parmelee and Aubele 1952; Pfrommer et al. 1996] – are analytically and numerically compared. Various strengths and weaknesses in the models are identified. The study shown in the previous sections indicates the need for an improved optical blind model. Therefore, a new model for predicting optical properties of the slat-type blind is proposed. To be suitable for building simulation tools, the new model must predict optical properties for both direct and diffuse solar radiation. Also, the model should take into account slat thickness as well as slat curvature. In addition, the model should account for slat surfaces being non-perfect reflectors. Proposed technical aspects and capabilities of the new model are summarized below.

- The model is applicable to both blinds having non-zero-thickness flat slats and blinds having zero-thickness curved slats.
- The model is applicable to both blinds having horizontal slats (e.g. Venetian blinds, mini blinds, etc.) and blinds having vertical slats (commonly called vertical blinds).
- The model is applicable to blinds having purely diffuse-reflecting slats, blinds having purely specular-reflecting slats, as well as blinds having partially diffuse and partially specular-reflecting slats.

- The model is applicable to blinds having either opaque, translucent, or perforated slat surfaces.
- The model allows different radiative characteristics on different sides of the blind slats.
- The model treats direct and diffuse components of incident solar radiation separately.
- The model treats diffuse solar radiation from the sky and the ground separately.

The model is referred to in this thesis as the comprehensive blind model. A technical description of the comprehensive blind model is presented in Chapter 4 and detailed calculations of the model are presented in Appendices A to C. Table 3-1 compares the capabilities of the comprehensive blind model with other existing optical blind models. Yahoda's model [Yahoda and Wright 2005], which was not included in the inter-model comparison, is also included in Table 3-1.

Table 3-1 Comparison of Capabilities in Optical Blind Models

Capability	Comprehensive	Parmelee	Pfrommer	EnergyPlus	Yahoda
Flat-Slat Blind	Yes	Yes	Yes[1]	Yes	Yes[1]
Curved-Slat Blind	Yes	No	Yes[2]	No	No
Horizontal-Slat Blind	Yes	Yes	Yes	Yes	Yes
Vertical-Slat Blind	Yes	Yes	No	Yes	Yes
Purely-Diffuse-Slat Blind	Yes	Yes	Yes	Yes	Yes
Purely-Specular-Slat Blind	Yes	Yes	Yes	No	Yes
Partially-Diffuse/Specular-Slat Blind	Yes	No	Yes	No	Yes
Opaque-Slat Blind	Yes	Yes	Yes	Yes	Yes
Translucent-Slat Blind	Yes	No	No	Yes	No
Perforated-Slat Blind	Yes	No	No	No	No
Different Radiative Properties for Different Sides of Slats	Yes	No	No	Yes	Yes
Different Radiative Characteristics for Different Sides of Slats	Yes	No	No	No	Yes

[1] Applicable to zero-thickness flat-slat blind only

[2] Applicable for direct solar radiation but not for diffuse solar radiation, and applicable to a purely-diffuse-slat blind but not for a non-purely-diffuse-slat blind

3.5 Conclusions

This chapter theoretically and numerically compares three existing optical blind models suitable for building thermal load calculations. Overall, the three models predict similar results for horizontal-slat blinds having flat slats with zero thickness. However, the Pfrommer model tends to predict lower results than the other models when reflections between the slats become important (e.g. high slat reflectance) due to the two-reflection algorithms used in the model. Also, the Pfrommer model, which does not have a thickness correction, can significantly over-predict the results for flat-slat blinds when the slat thickness is non-trivial. Likewise, the EnergyPlus and Parmelee models, which do not account for slat curvature, can substantially over-predict the direct-to-direct transmittance for curved-slat blinds.

The chapter also investigates the influence of input parameters on solar blind transmittances predicted by the models. These parameters include slat angle, slat reflectance, slat thickness, and slat curvature. The optical characteristics of the blinds are primarily dependent on the slat angle, which not only affects the magnitude of the blind transmittance but also changes the shape of the transmittance curve. Other parameters have a secondary effect on the blind transmittance and do not affect the shape of the transmittance curve.

In summary, all three of the existing optical blind models studied have deficiencies that are significant enough to justify additional enhancements. The EnergyPlus and Parmelee models require a slat curvature calculation, and the Pfrommer model requires a thickness calculation. Consequently, a new comprehensive optical blind model, that not only includes advantage capabilities from each of the three models studied but also has enhanced features not available in any of the three models, is proposed. The new model is presented in detail in the next chapter.

CHAPTER 4

COMPREHENSIVE MODEL FOR PREDICTING BLIND SOLAR-OPTICAL PROPERTIES

4.1 Introduction

This chapter presents a new model for predicting optical properties of the slat-type blind. The new model is referred to here as the comprehensive blind model. The comprehensive blind model was developed specifically for building simulation tools. Therefore, the model predicts optical properties for both direct and diffuse solar radiation. Technical aspects and capabilities of the comprehensive blind model are previously summarized in Section 3.4.

In the next section, a technical description of the comprehensive blind model is presented. Then, details of the model for direct and diffuse solar radiation are described where detailed calculations are given in Appendices A to C. Finally, suggestions for implementation of the model in a building energy simulation tool are provided.

4.2 Technical Description

4.2.1 Model Overview

The comprehensive blind model consists of several sub-models used to handle various technical aspects as described above. The comprehensive blind model may be first divided into two models: one for direct solar radiation (direct blind model) and one for diffuse solar radiation (diffuse blind model). The direct blind model can be further subdivided into two sub-models: the flat-slat blind model and the curved-slat blind model as shown in Figure 4-1. The flat-slat blind model deals with a blind having non-zero-thickness flat slats, which is typical of a blind made of woods. On the other hand, the curved-slat blind model handles a blind having negligible-thickness curved slats, which is typical of a blind made of vinyl or aluminum. Both the flat-slat and curved-slat blind models can then be subdivided into two more sub-models: the net-radiation blind model for a blind having purely diffuse-reflecting slats and the ray-tracing blind model for a blind having non-purely diffuse-reflecting slats. Both net-radiation and ray-tracing models use analytically derived formulations to determine how much the sunlight passes directly through a blind assembly and how much the sunlight falls on the blind slats. To deal with reflected radiation, the net-radiation blind model utilizes the net-radiation (or radiosity) method while the ray-tracing blind model employs the so-called Monte-Carlo ray-tracing technique. Figure 4-1 illustrates the sub-models of the comprehensive blind model.

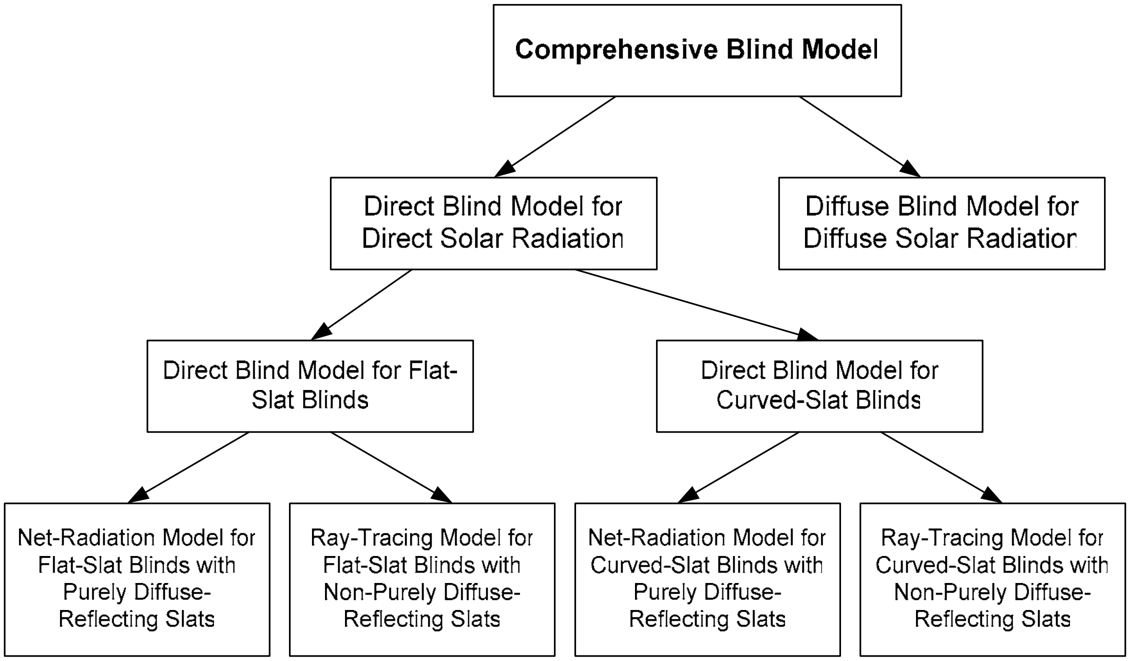

Figure 4-1 Sub-models of Comprehensive Blind Model

The diffuse blind model considers two different sources of diffuse solar radiation: the sky and the ground. The model treats diffuse solar radiation as direct solar radiation emitted from a large hemisphere in front of a blind assembly. Therefore, the diffuse blind model utilizes the direct blind model and a numerical integration technique to predict sky-diffuse and ground-diffuse optical blind properties.

4.2.2 Basic Assumptions

The comprehensive blind model considers a blind assembly as a series of equidistant slats. The slats are assumed to be of infinite length. In a theoretical analysis, the whole blind assembly is then represented by two consecutive slats. Therefore, the two adjacent slats along with fictitious surfaces at the outside and the inside openings form the enclosure of the problem domain.

In addition to the two basic assumptions mentioned above, several assumptions may also be required depending on sub-models used in the comprehensive blind model. For instance, the curved-slat blind model assumes that the slat thickness is negligible whereas the flat-slat blind model assumes that edges of the blind slats are rectangular. Additionally, the net-radiation blind model assumes that the slat surface is purely diffuse.

4.2.3 Blind Enclosure Geometries

As previously mentioned, the blind enclosure is formed by two consecutive slats along with fictitious surfaces at the outside and inside openings. Two blind enclosures are considered in the comprehensive blind model. Figure 4-2a shows the blind enclosure for the flat-slat blind model while Figure 4-2b shows the enclosure for the curved-slat blind model. Figure 4-2 also shows slat geometry, the profile angle, and the coordinate system used in the comprehensive blind model.

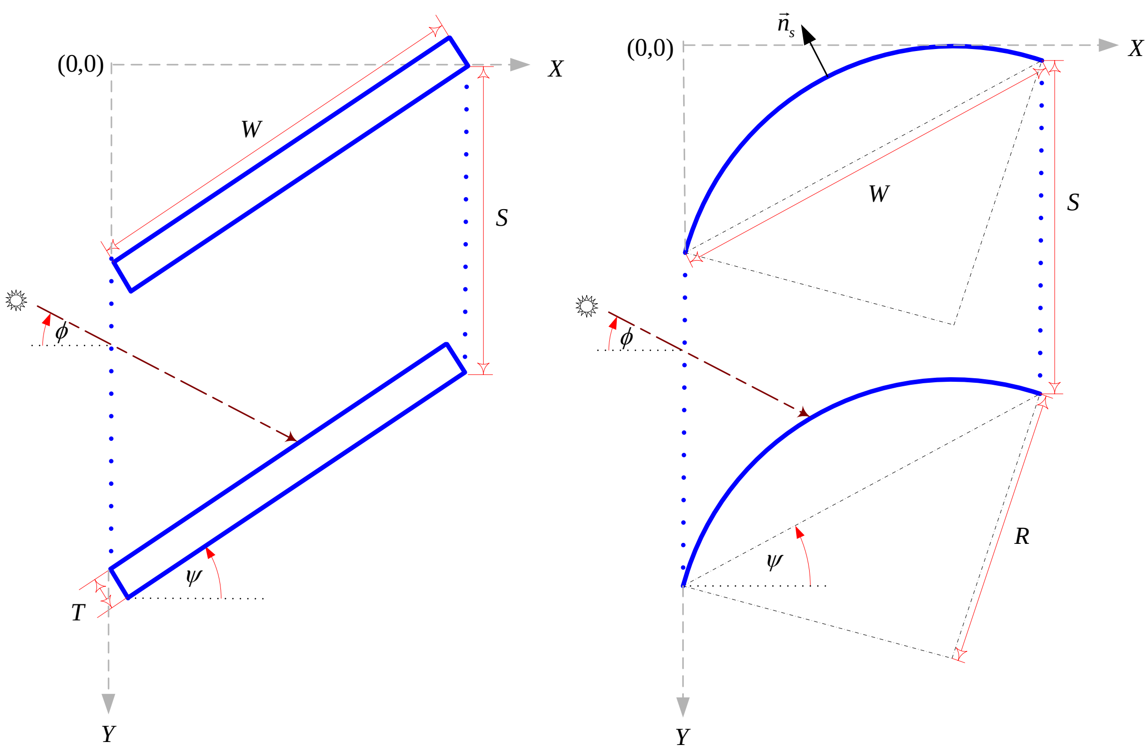

A) Enclosure Geometry for Flat Slat Blinds

B) Enclosure Geometry for Curved Slat Blinds

Figure 4-2 Blind Enclosure Geometries and Coordinate Systems

As shown in Figure 4-2, slat angle (ψ) is defined as the angle between the straight line connecting edges of the slat and the plane perpendicular to the blind assembly (i.e. the horizontal line shown in the figure). Figure 4-2 illustrates a downward facing blind (having horizontal slats) with a positive slat angle. Slat spacing (S) is defined as the distance between adjacent slats (measured vertically for blinds having horizontal slats). For a blind having non-zero-thickness flat slats, the slat spacing is the distance from the upper surface of the upper slat to the upper surface of the lower slat. Slat width (W) is defined as the distance of a straight line from one end of the slat to the other end. Slat thickness (T) is defined as the distance from the upper surface to the lower surface of each slat. Slat curvature radius (R) is defined as the distance from the center of curvature radius to the slat surface. These slat geometry parameters along with slat radiative parameters discussed in the next sections are required inputs for the comprehensive blind model.

4.2.4 Radiative Properties and Characteristics of Slat Surfaces

Due to a lack of detailed optical property data for each particular slat material, the implementation of the comprehensive blind model used in the current study only requires spectrally-averaged slat radiative parameters, but it can be easily extended to handle blinds having spectrally-selective slat materials. The model requires slat reflectance as well as slat transmittance for both sides of a slat so that the model can be used to handle blinds having either opaque, translucent, or perforated slat surfaces and blinds having different radiative properties on different sides of the slat. In addition to slat radiative properties, the model also requires reflective and transmissive specularity ratios for both sides of the slat because an actual slat surface is neither purely specular nor purely diffuse [Parmelee and Aubele 1952; Pfrommer et al. 1996]. The reflective specularity ratio[1] is defined as the ratio of the specular-reflected to the total-reflected components. Likewise, the transmissive specularity ratio is defined as the ratio of the specular-transmitted to the total-transmitted components. For a blind having opaque and perforated slats, for instance, although the reflective specularity ratios can be any values between zero and one, the transmissive specularity ratios are one for both sides since the incident radiation can only pass through the perforated area of the slats where the outgoing direction of the transmitted radiation is the same as the incoming direction of the incident radiation.

4.2.5 Profile Angle

The optical characteristics of a blind assembly depend on various parameters including slat geometry, slat radiative properties and characteristics, the orientation of the blind assembly as well as the sun position. The profile angle is typically used to relate the orientation of the blind

---

[1] The terminology used in a radiation heat transfer textbook [Mahan 2002] is adopted here. The reflective specularity ratio is equal to one minus the shining factor, which is the terminology used by Pfrommer et al. [1996] to describe slat reflective characteristics.

assembly to the sun position similar to the incident angle being commonly used to relate the orientation of the window to the sun position. According to Parmelee and Aubele [1952], the profile angle is defined as the angle between a plane perpendicular to the blind assembly (the normal plane) and a plane coincident with the line of sight to the sun (the line of sight plane). Figure 4-3 illustrates the definition of the profile angle. It should be noted that the normal plane must be parallel to the longitudinal dimension of the slats. The definition of the profile angle accounts for the orientation of the blind assembly (typically parallel to the plane of the window) and the orientation of slats (either horizontal or vertical). For a vertical blind assembly with horizontal slats, the normal plane will be horizontal; and for a vertical blind assembly with vertical slats, this plane will be vertical. The line of sight plane is obtained by rotating the normal plane around the common edge of the blind assembly plane and the normal plane as shown in Figure 4-3.

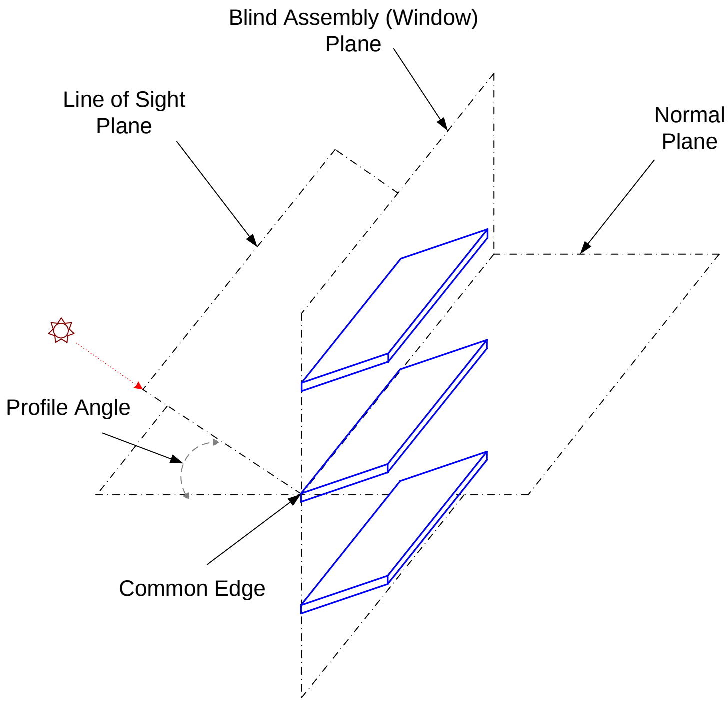

Figure 4-3 Definition of Profile Angle

The profile angle is dependent on the blind assembly orientation (typically window facing angle and window tilt angle), slat arrangement (i.e. horizontal or vertical), and sun position (i.e. solar altitude and azimuth). The profile angle can be determined from the following equations [Parmelee and Aubele 1952]:

$$\phi_{v,h} = \tan^{-1}\left(\frac{\tan(\beta)}{\cos(|\gamma - \xi|)}\right) \tag{4-1a}$$

$$\phi_{i,h} = \phi_{v,h} + \Sigma - 90^\circ \tag{4-1b}$$

$$\phi_{v,v} = \gamma - \xi \tag{4-1c}$$

$$\phi_{i,i} = \tan^{-1}\left(\frac{\cos(\phi_{v,h})\tan(\phi_{v,v})}{\cos(\phi_{i,h})}\right) \tag{4-1d}$$

where Σ = blind assembly tilt angle (0° to 180° from horizontal),
β = solar altitude angle (0° to 90°),
γ = solar azimuth angle (0° to 360° from north),
ξ = blind assembly facing (azimuth) angle (0° to 360° from north), and
ϕ = profile angle (-90° to 90°).

The first subscript on the profile angle specifies the plane of the blind assembly and the second subscript specifies the direction of the longitudinal dimension of the slat (slat arrangement) where *v*, *h* and *i* are vertical, horizontal, and inclined, respectively.

It should be noted that the profile angle is a required input for the direct blind model. In a building simulation tool implementation, however, the profile angle is essentially calculated for each time step in the simulation tool prior to the calculations of blind optical properties for direct solar radiation.

4.2.6 Blinds with Horizontal Slats versus Blinds with Vertical Slats

Although earlier explanations regarding the slat geometry parameters are specifically for a blind with horizontal slats, they are applicable to a blind with vertical slats as well, except the definition of slat angle. To clearly understand the difference between the blind with horizontal slats and the blind with vertical slats, we may imagine that Figure 4-2 shows a cross section of a wall as seen from the side view for the blind with horizontal slats whereas Figure 4-2 shows the cross section as seen from the top view for the blind with vertical slats. Figure 4-4 may better demonstrate the concept just mentioned.

A special caution is necessary regarding the slat angle and the profile angle for a curved-vertical-slat blind. The blind enclosure geometry used in the curved-slat blind model requires that the outward facing normal of the slat ($\vec{n}_s$ -- shown in Figures 4-2 and 4-4b) be defined as positive for an angle measured clockwise from the outward facing normal of the blind assembly ($\vec{n}_b$) and negative for an angle measured counter-clockwise from the outward facing normal of the blind assembly as illustrated in Figure 4-4b. For the positive outward facing normal of the slat, the profile angle and the slat angle shown in Figures 4-2 and 4-4 are both positive. For the negative outward facing normal of the slat, the profile angle and the slat angle shown in both figures are both negative. It should be noted that Equation (4-1c) is for the curved-vertical-slat blind with the positive outward facing normal of the slat. Therefore, for the curved-vertical-slat blind with the negative outward facing normal of the slat, the profile angle must be calculated as a negative value of Equation (4-1c) when the comprehensive blind model is implemented in a building simulation tool.

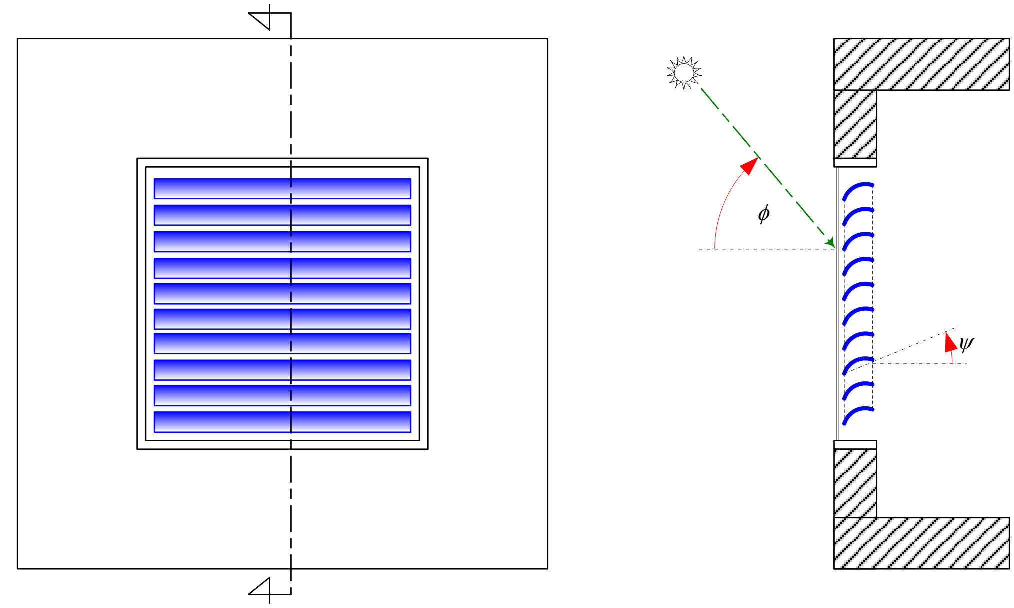

A) Blind with Horizontal Slats

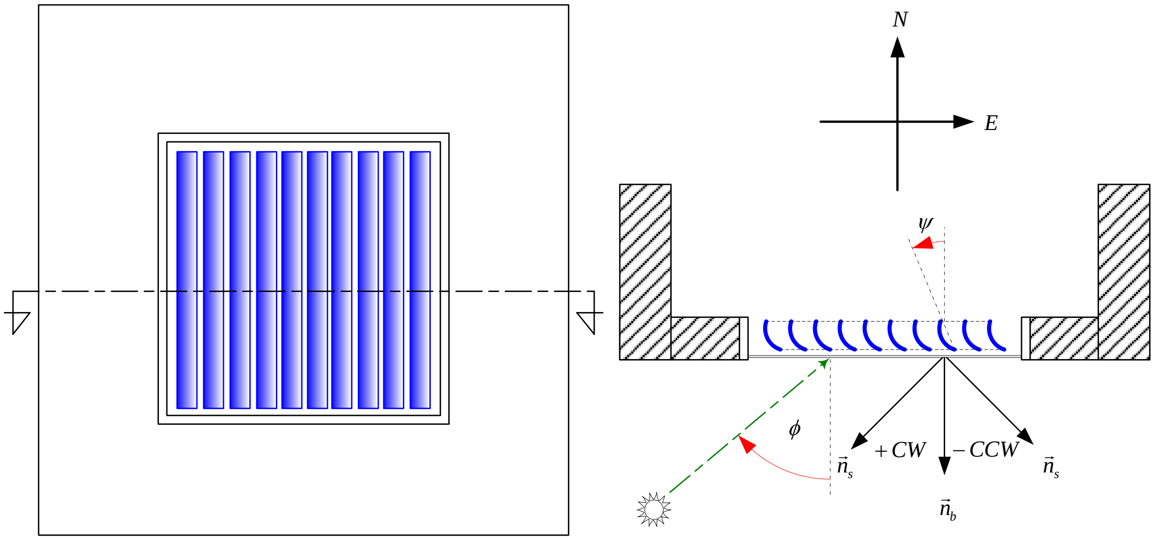

B) Blind with Vertical Slats

Figure 4-4 Illustrations of Positive Profile Angle and Positive Slat Angle

4.3 Direct Blind Model

The direct blind model employs various computational techniques in order to balance between the model functional capability and the model computational efficiency. To determine fractions of the sunlight incident on blind slats and of the sunlight passing through the blind assembly without any reflections, the direct blind model employs analytically derived formulations. Then, to deal with reflected/transmitted radiation initially incident on the blind slats, the direct blind model utilizes two different techniques: the net-radiation method for a blind with purely diffuse slats, and the Monte-Carlo ray-tracing technique for a blind with non-purely diffuse slats. Although the Monte-Carlo ray-tracing technique can also be used to handle a blind with purely diffuse slats, the net-radiation method is utilized to improve the computational efficiency of the direct blind model.

Figure 4-5 demonstrates calculation cases used by the direct blind model for a blind having curved slats. The calculations are subdivided into cases according to profile angle limits shown in Figure 4-6. The profile angle limits indicate how the sunlight falls on blind slats and how the sunlight passes through the blind assembly as a function of the profile angle. For example, the phenomena occurring for some calculation cases shown in Figure 4-5 can be explained as follows.

- For Case 1, there is no opening area, and lower slats are partially illuminated. For this case, the sunlight cannot pass directly through the blind assembly. The sunlight can only pass through the blind assembly by reflections mainly from the lower slats and by transmissions through blind slats if the slats are translucent or perforated.
- For Case 2, there is some opening area, and lower slats are entirely illuminated. For this case, the sunlight can pass directly through the blind assembly. The sunlight can also pass through the blind assembly by reflections mainly from the lower slats and by transmissions through blind slats if the slats are translucent or perforated.

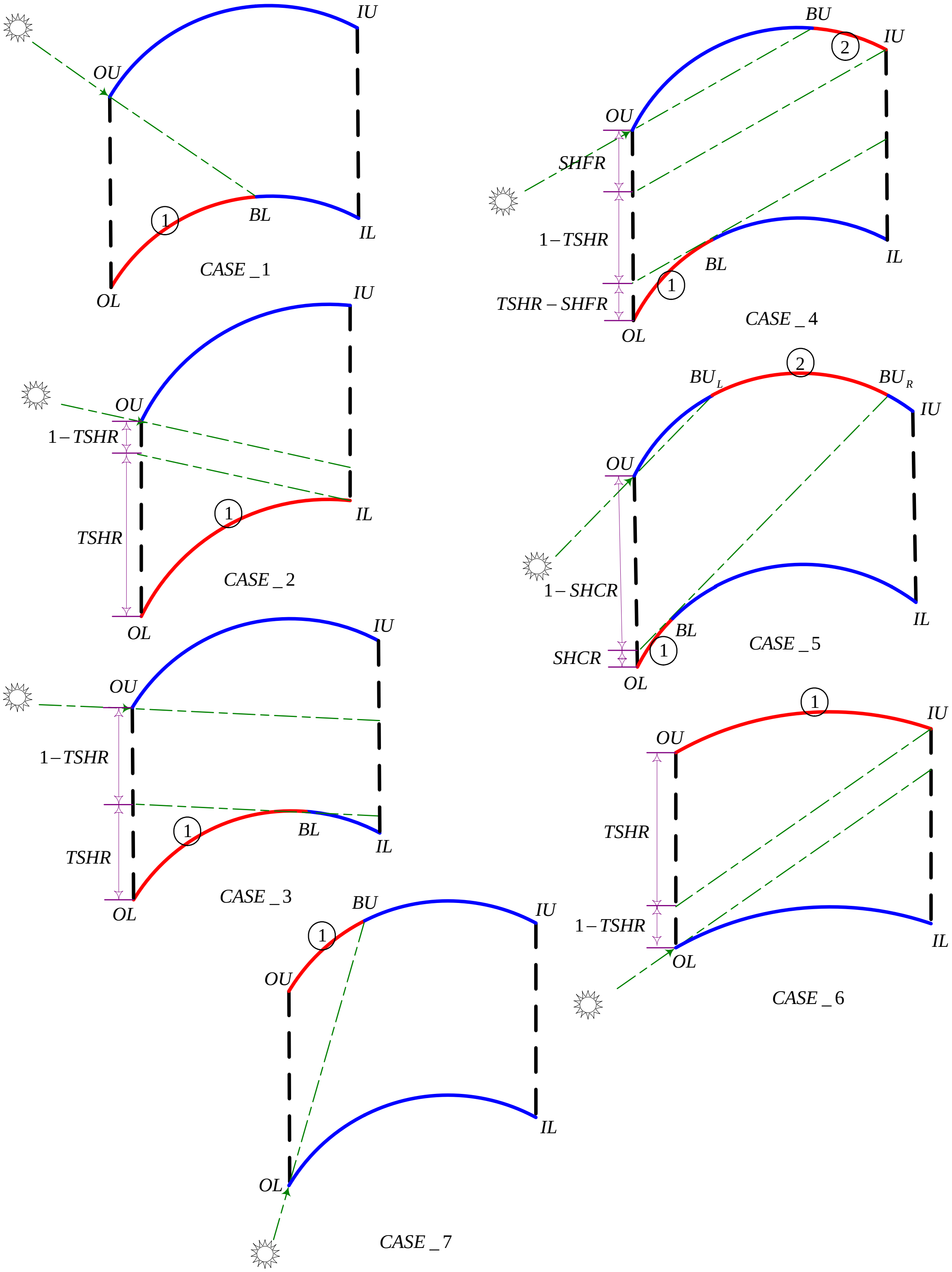

Figure 4-5 Calculation Cases for the Curved-Slat Blind Model

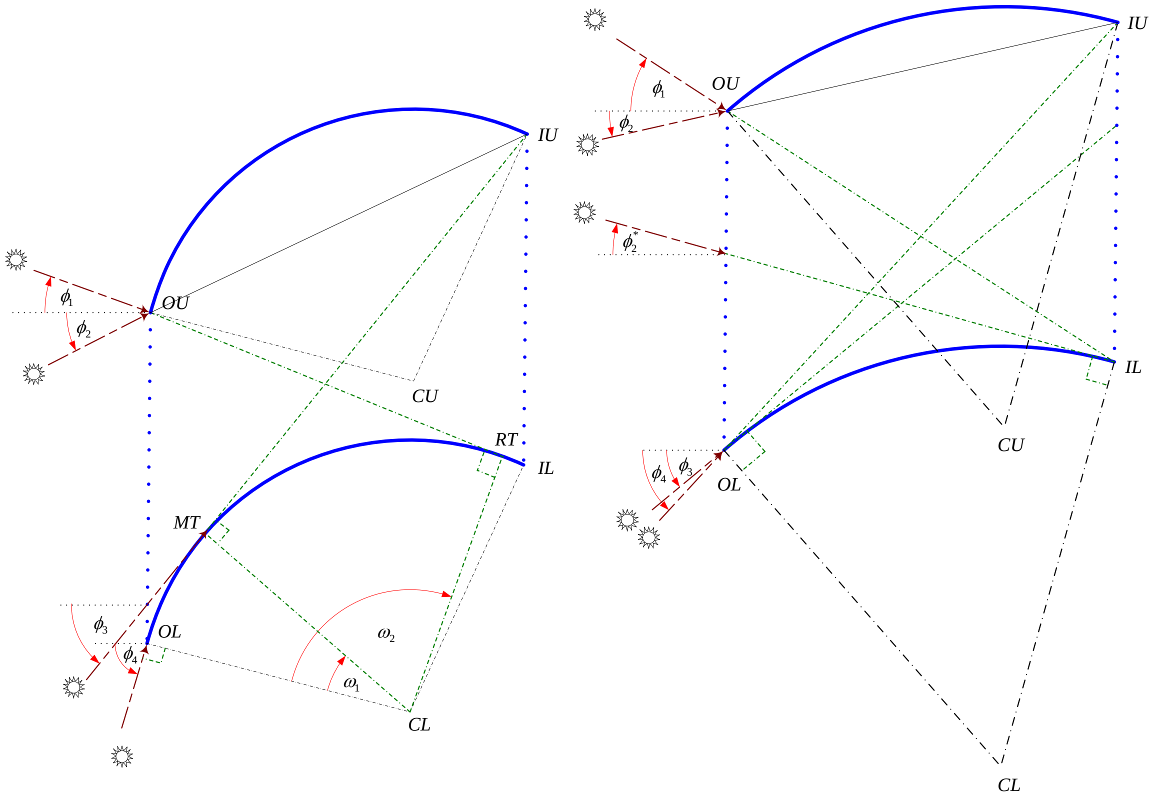

A) $0 < \omega_1 < 2\eta$ and $0 < \omega_2 < 2\eta$ B) $\omega_1 = 0$ and $\omega_2 = 2\eta$

Figure 4-6 Profile Angle Limits for the Curved-Slat Blind Model

- For Case 4, there is some opening area, and both upper and lower slats are partially illuminated. For this case, the sunlight can pass directly through the blind assembly. The sunlight can also pass through the blind assembly by reflections from both upper and lower slats and by transmissions through blind slats if the slats are translucent or perforated.

The calculation cases shown in Figure 4-5 are applicable for both the net-radiation and the ray-tracing blind sub-models. The direct blind model employs a similar analytical technique to derive calculation cases for a blind having flat slats. The analytically derived formulations for both the curved-slat and the flat-slat blinds are presented in detail in Appendix A.

4.3.1 Ray-Tracing Blind Model

The ray-tracing blind model is used to handle blinds having slat surfaces that are not purely-diffuse. To deal with transmitted and/or reflected portions of the direct sunlight incident on the blind slats, the model utilizes a computer graphic technique (i.e. the ray-tracing method) to trace rays transmitted through and/or reflected from illuminated slat surfaces. The model also employs a statistical technique (i.e. the Monte-Carlo method) to deal with rays transmitted through and/or reflected from slat surfaces that may be neither purely diffuse nor purely specular. The combined technique used by the ray-tracing blind model, referred to here as the Monte-Carlo ray-tracing (MCRT) algorithm, is illustrated in Figure 4-7. The figure shows the MCRT algorithm for tracing emitted rays from each illuminated surface.

As shown in Figure 7, the MCRT algorithm starts the ray tracing process by emitting a ray from a random location within the illuminated surface. The MCRT algorithm employs a random number to determine the location of an emitted ray. Shaded boxes shown in Figure 4-7 are where the statistical technique is utilized. In the ray-tracing blind model, the emitted ray is actually a ray incident from the outside opening that is then either transmitted through or reflected from the illuminated surface; hence, the MCRT algorithm must first check whether the incident ray is transmitted through or reflected from (but not absorbed by) the illuminated slat. If the ray is transmitted, it is necessary to determine the surface and the location where the transmitted ray emerges. The MCRT algorithm then determines whether the ray is transmitted (or reflected) diffusely or specularly before it determines the direction of the emitted ray.

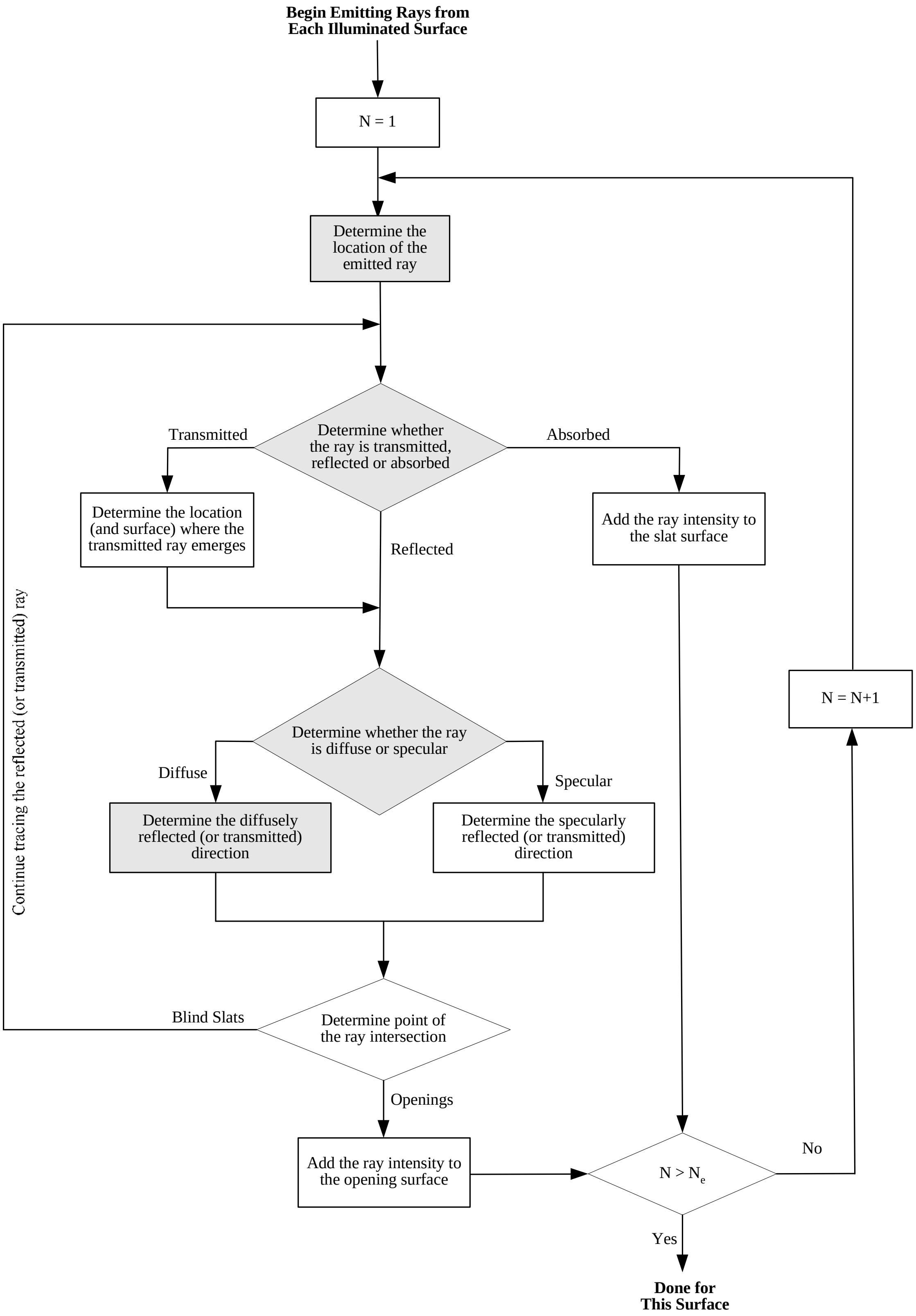

Figure 4-7 Flow Chart of the Monte-Carlo Ray-Tracing Algorithm

To determine how rays are transmitted and reflected, the ray-tracing blind model requires the transmissive and reflective specularity ratios discussed previously. The ray-tracing blind model utilizes the statistical technique by comparing the transmissive (or reflective) specularity ratio with a random number used to determine the type of the transmitted (or reflected) ray. If the random number is less than or equal to the transmissive (or reflective) specularity ratio, the ray is transmitted (or reflected) specularly. Otherwise, the ray is transmitted (or reflected) diffusely.

After the MCRT algorithm determines the direction of the transmitted (or reflected) ray, it then finds where the ray ends up (i.e. it determines the point of ray intersection). If the ray hits either the outside opening or the inside opening, the ray is assumed to be totally absorbed by the opening. Therefore, the ray tracing process for this ray is done. Otherwise, the MCRT algorithm continues tracing this ray by determining whether the ray is transmitted, reflected or absorbed. The algorithm continues the ray-tracing process until the ray is absorbed by either an opening or a slat surface as shown in Figure 4-7. The MCRT algorithm then starts emitting another ray. A similar ray tracing process previously described continues until all required rays for the illuminated surface (i.e. $N > N_e$) have been emitted. If there are more than one illuminated surfaces, the same MCRT algorithm is used to emit rays for another illuminated surface(s).

As shown in Figure 4-7, when a ray hits an opening or is absorbed by a slat surface, the ray intensity associated with the ray is added to the total intensity absorbed by each surface. The ray tracing blind model uses the accumulated intensity by surfaces of the blind enclosure to determine blind optical properties for direct solar radiation. Appendix A provides detailed calculations of the ray-tracing blind model.

4.3.2 Net-Radiation Model

The net-radiation blind model is used to handle blinds having slat surfaces that are purely-diffuse. To deal with transmitted and/or reflected portions of the direct sunlight incident on the blind slats, the model utilizes the net-radiation method, sometimes called the radiosity method. The model is fundamentally similar to the EnergyPlus and the WIS models [DOE 2006; Rosenfeld et al. 2000]. The main difference between the net-radiation blind model and the two existing models is that the net-radiation blind model can handle blinds having either flat slats or curved slats whereas both EnergyPlus and WIS models are only applicable to blinds having flat slats. In addition, the net-radiation blind model considers slat edges as parts of the problem to account for slat thickness, which may not be trivial for blinds having flat slats as discussed in Chapter 3. On the other hand, the EnergyPlus model applies a so-called slat edge correction to account for slat thickness and the WIS model has no correction for slat thickness.

Like the EnergyPlus model, blind slats are subdivided into several elements depending on how the slats are illuminated. For example, each blind slat is subdivided into two elements for Calculation Cases 1, 3 and 7 shown in Figure 4-5 for blinds having curved slats. However, each slat is subdivided into three and four elements for Calculation Cases 4 and 5, respectively. For Calculation Cases 2 and 6, there is no surface subdivision. Like the EnergyPlus model, view factors between surfaces are analytically derived using the Crossed-Strings method [Modest 2003]. Appendix B provides detailed calculations of the net-radiation blind model.

4.4 Diffuse Blind Model

The diffuse blind model adapts and extends a concept proposed by Parmelee and Aubele [1952] for estimating blind optical properties for diffuse solar radiation. In an analysis of the diffuse solar radiation, a hemisphere is placed in front of a plane parallel to a blind assembly (the blind assembly plane shown in Figure 4-8). The diffuse blind model assumes that there are only two sources of the diffuse solar radiation: the sky and the ground. As illustrated in Figure 4-8, a part of the hemisphere above the horizontal plane represents the sky while the other part below the horizontal plane represents the ground. Both the sky and the ground are subdivided into a number of small patches as shown in the figure. Then, the diffuse solar radiation leaving each patch is treated as direct solar radiation emitted from the center of the patch to the center of the hemisphere where the blind assembly is located. Consequently, the diffuse blind model utilizes the direct blind model along with a numerical integration method to predict optical blind properties for the diffuse solar radiation. Appendix C provides detailed calculations of the diffuse blind model.

It is worth mentioning that the diffuse blind model is applicable to slat-type blinds being installed on a vertical plane as well as on an inclined plane whereas the Parmelee diffuse model is applicable only for slat-type blinds being installed on a vertical plane. The vertical blind assembly is a special case where the upper half of the hemisphere represents the sky while the lower half of the hemisphere represents the ground. The diffuse blind model is also applicable for both isotropic and anisotropic diffuse radiance distributions. To deal with the anisotropic assumption, the diffuse blind model requires the knowledge of diffuse radiance distributions of the sky and the ground (i.e. sky/ground radiance distribution models). A literature search on the subject found several models available for predicting sky radiance distribution [Brunger and Hooper 1993; Igawa et al. 2004; Vida et al. 1999], but found no existing model for calculating ground radiance distribution. In this study, Igawa's sky radiance distribution model [Igawa et al.

2004] is used to investigate the anisotropic sky assumption. Since no ground radiance distribution model exists, the current study essentially assumes the isotropic ground.

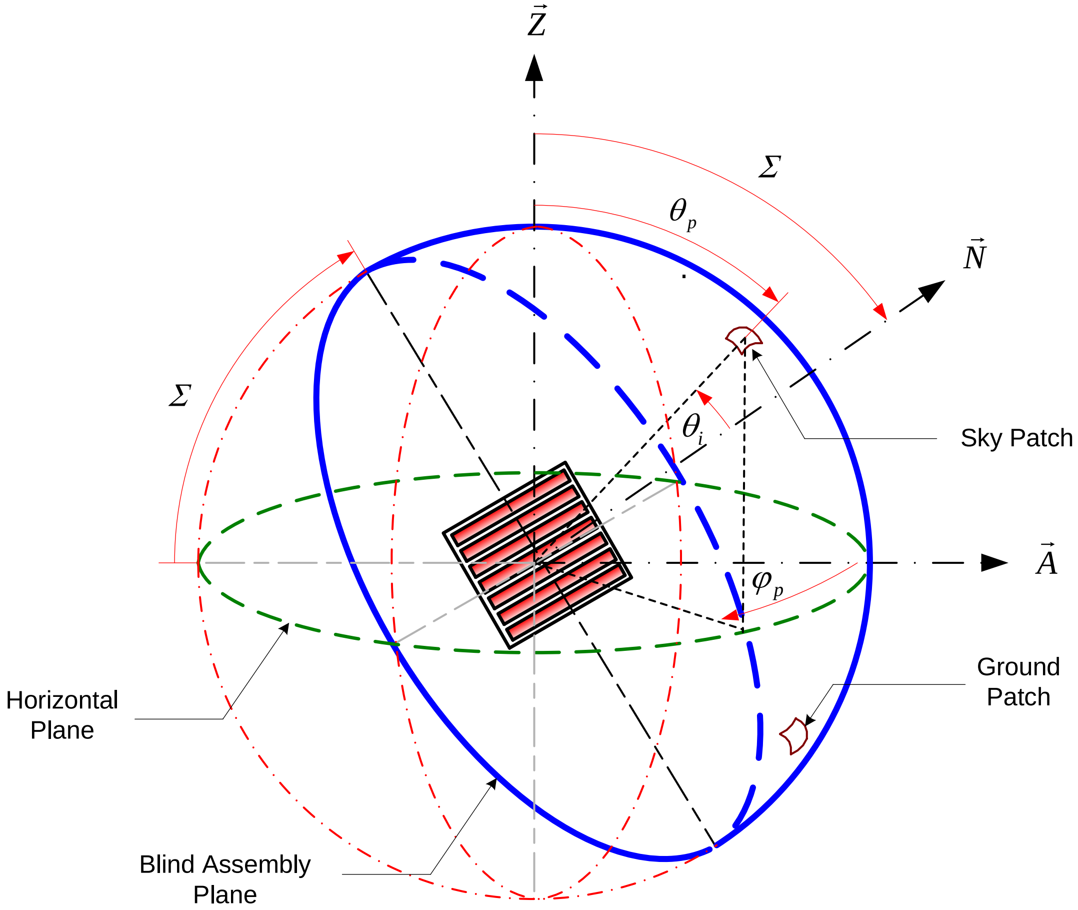

Figure 4-8 Half Sphere Representing Sky and Ground in Front of the Blind Assembly

4.5 Model Implementation

In order to deal with various types of slat-type blinds, the comprehensive blind model utilizes various techniques to extend model capabilities not available in existing blind models. The ray-tracing technique (combined with the statistical approach and referred to as the MCRT algorithm), in particular, is largely responsible for these enhanced capabilities. However, the use of the ray-tracing technique results in an increase in the computation time required by the comprehensive blind model as compared to that required by other existing models. To deal with the computational efficiency issue of the comprehensive blind model, this section provides suggestions for the model implementation.

The first suggestion, which is quite an obvious one, is to avoid unnecessary calculations in the ray-tracing loop (that try to find an appropriate surface where the ray is absorbed as shown in Figure 4-7) since the computation time used by the ray-tracing blind model is mostly spent in this loop. For example, the (fixed) surface normal of a flat slat surface can be pre-calculated outside the ray-tracing loop whereas the surface normal of a curved slat surface, which is varied depending on the location where the ray hits, must be calculated within the ray-tracing loop. On average, the computation time used for a flat-slat blind is about 70% of the computation time used for a curved-slat blind.

In addition, although ray-tracing calculations presented in Appendix A are essential, they are not inherent parts of the comprehensive blind model. This means that an algorithm used in the ray-tracing loop should be replaced by a more efficient algorithm if such an algorithm is available. For instance, O'Rourke [1994] discusses deficiencies in a segment intersection algorithm based on the slope/intercept approach, which is similar to the ray intersection on straight line presented in Appendix A, and then presents an alternative algorithm based on the signed-area approach. The implementation using the signed-area approach on average improves the computation time over the implementation using the slope/intercept approach by about 15%.

In Appendix A, the ray-tracing blind model uses a simple algorithm that requires the total number of emitted rays as an input which the model accuracy and model efficiency are mainly dependent on. The use of a high number theoretically would result in a more accurate result. However, it would also result in a longer computation time required by the model. The use of the total number of emitted rays does not provide a sense of a balance between the computational accuracy and efficiency since different sets of blind input parameters may require different values of the total number of emitted rays for the same accuracy. To provide a better balance between the computational accuracy and efficiency, an iterative algorithm shown in Figure 4-9 can be used. As shown, instead of performing the ray-tracing calculations for a large number of rays, the iterative algorithm performs the ray-tracing calculations for a small number of rays and then checks the convergence of the calculated optical properties by comparing predicted optical properties of the current iteration with those of the previous iteration. In stead of using the total number of rays, the iterative algorithm therefore uses an accuracy tolerance to terminate the iteration loop.

```
For Iterative Loop = 1 to Maximum Iteration

    For Ray Emission Loop = 1 to Number of Rays
        Perform Ray-Tracing Calculations
    Next

    Add Accumulated Radiative Fluxes

    Calculate Optical Properties

    If (All Optical Properties Converged) Then
        Exit Iterative Loop
    End If

Next
```

Figure 4-9 Iterative Algorithm for Ray-Tracing Calculations

To investigate the effect of the accuracy tolerance, Figure 4-10 shows differences between optical properties predicted by the iterative algorithm and results predicted by the simple algorithm using 10 million emitted rays for six different sets of blind input parameters. Figure 4-10 also illustrates the effect of using different number of rays for the ray-tracing loop. As shown, the ray-tracing loop using a smaller number of rays (i.e. results of the loop of 1000 shown in the left hand region) will requires a lower value of the accuracy tolerance to achieve relatively the same accuracy as the ray-tracing loop using a larger number of rays. In addition, Figure 4-11 shows computation time required by the iterative algorithm as a percentage of the computation time required by the simple algorithm using 10 million emitted rays. The results shown in Figures 4-10 and 4-11 indicates that using the ray-tracing loop of 10000 rays with the accuracy tolerance between 1.0E-04 and 1.0E-05 would yield reasonably accurate results with a dramatic reduction (more than 95%) in the computation time. Similarly, using the ray-tracing loop of 1000 rays with the accuracy tolerance between 1.0E-05 and 1.0E-06 would yield approximately the same results and the same computation time.

Until now, suggestions on the model implementation are all related to the ray-tracing blind sub-model(s). When the comprehensive blind model is implemented in a building simulation tool, several implementation techniques can be used to improve the simulation time. Since the direct optical blind properties are primarily dependent on the profile angle, they can be pre-calculated at the beginning of the simulation for a number of profiles (ranging from 90° to -90°). Then, for each time step, the interpolation technique can be used to determine the direct optical blind properties according to the profile angle of that particular time step. The interpolation technique can be computationally efficient, particularly for an annual simulation. However, the technique may be not as useful for a one-day simulation since the overhead can be more than the computation time required by a direct implementation.

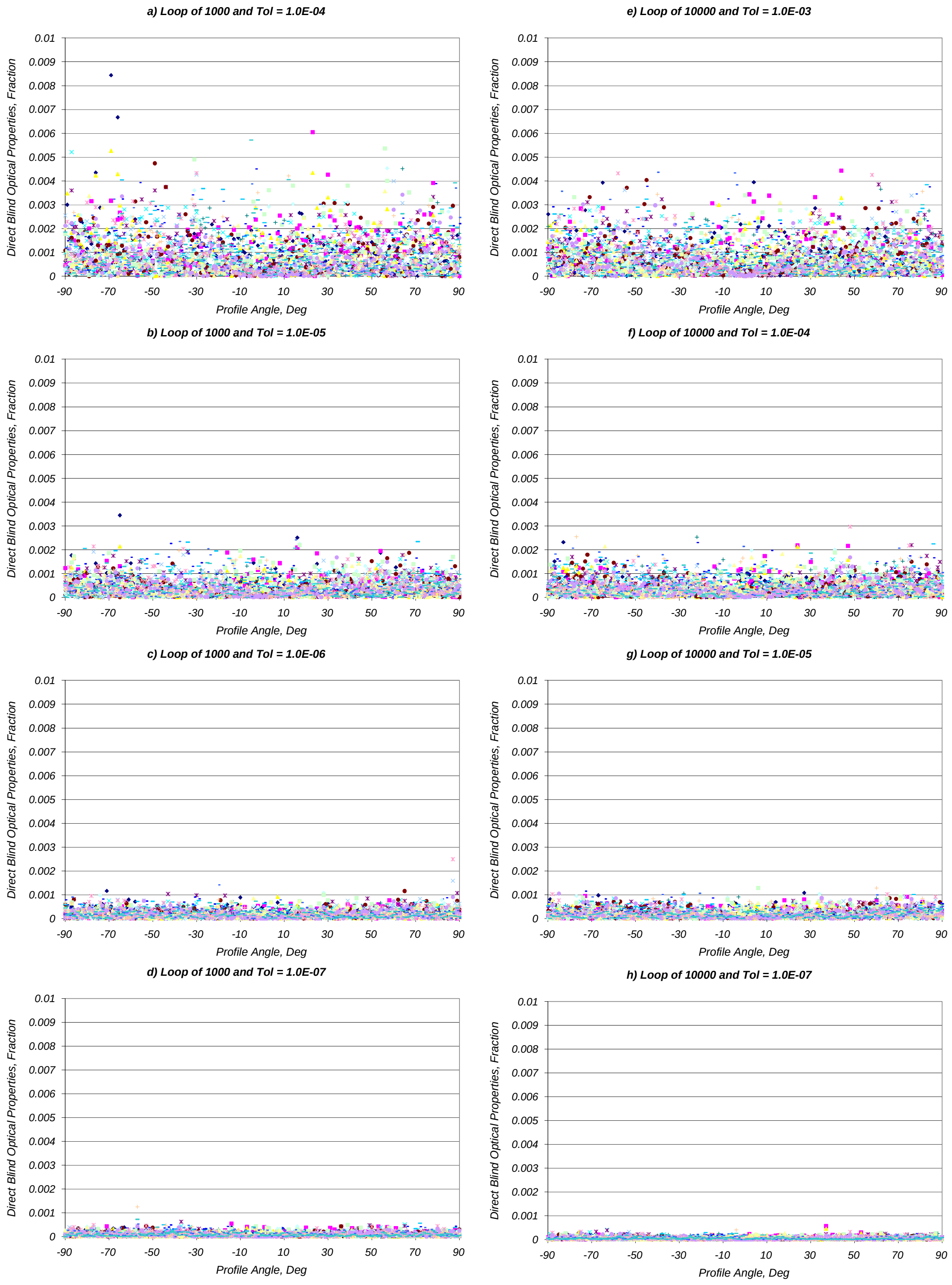

a) Loop of 1000 and Tol = 1.0E-04

b) Loop of 1000 and Tol = 1.0E-05

c) Loop of 1000 and Tol = 1.0E-06

d) Loop of 1000 and Tol = 1.0E-07

e) Loop of 10000 and Tol = 1.0E-03

f) Loop of 10000 and Tol = 1.0E-04

g) Loop of 10000 and Tol = 1.0E-05

h) Loop of 10000 and Tol = 1.0E-07

Figure 4-10 Effect of Accuracy Tolerance on Predicted Results

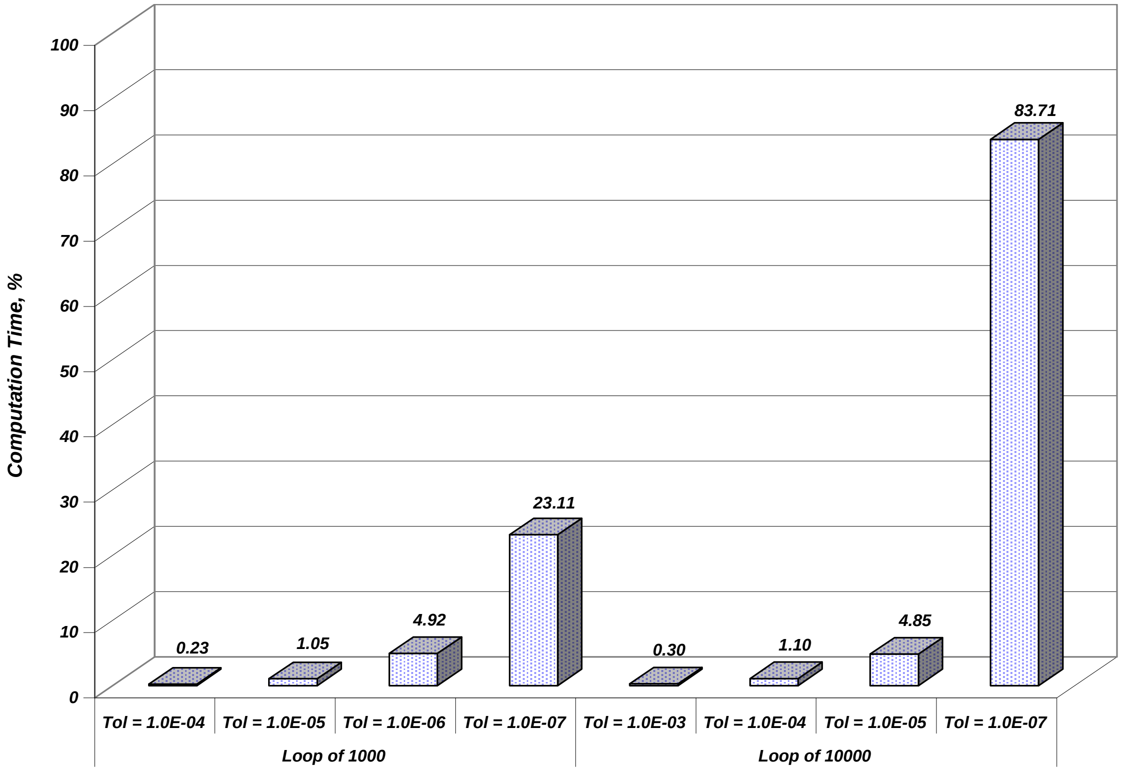

Figure 4-11 Computation Time Comparison

Although the anisotropic sky radiance distribution model agrees slightly better with measured data than the isotropic sky radiance distribution model does as illustrated in Chapter 5 (i.e., Figure 5-5), the computation time required by the anisotropic model is much higher than the time required by the isotropic model. Therefore, the isotropic model is more suitable for the building simulation tool. For the isotropic diffuse radiance assumption, the diffuse optical blind properties are independent on the time of the day. Therefore, they can be pre-calculated once at the beginning of the simulation and then can be used directly during the simulation. However, if the anisotropic sky radiance distribution model is implemented in the building simulation tool, the interpolation technique with pre-calculated direct optical blind properties is highly recommended to determine the direct blind properties required by the diffuse blind model (which utilizes the direct blind model along with a numerical integration method as previously discussed).

4.6 Conclusions

This chapter presents a newly developed model for predicting the solar-optical properties of a slat-type blind. The new model, referred to as the comprehensive blind model, is intentionally developed for implementing in a building simulation tool; hence, the model can be used to predict optical blind properties for both direct and diffuse solar radiation. The comprehensive blind model has various enhanced capabilities over existing optical blind models. For instance, the model is applicable to a blind having curved slats with partially-diffuse-reflecting and partially-specular-reflecting slat surfaces while other models are not. The comprehensive blind model utilizes various computational techniques to deal with various technical aspects. To predict optical properties for direct solar radiation, the model employs analytical formulations to predict fractions of the sunlight incident on blind slats and of the sunlight passing through the blind assembly without any reflections. Then, to deal with reflected/transmitted radiation initially incident on the blind slats, the comprehensive blind model utilizes two different techniques: the net-radiation method for a blind with purely diffuse slats, and the Monte-Carlo ray-tracing technique for a blind with non-purely diffuse slats. To predict optical properties for diffuse solar radiation, the comprehensive blind model uses a numerical integration method along with its sub-models for the direct solar radiation.

This chapter also provides suggestions for the model implementation in a building simulation tool. Various implementation techniques are suggested including (1) avoiding unnecessary calculations in the ray-tracing loop, (2) replacing an existing algorithm with a more efficient one if such a model is available, (3) using an iterative ray-tracing algorithm based on a balance between the computational accuracy and efficiency instead of a simple algorithm based on a total number of emitted rays, and (4) using an interpolation technique with pre-calculated optical properties.

In summary, this chapter presents the technical description of the comprehensive blind model and provides suggestions for the model implementation. The next chapter presents an in situ experimental method for measuring solar optical properties and compares the comprehensive blind model with measured data obtained by the in situ method.

CHAPTER 5

EXPERIMENTAL VALIDATION OF THE COMPREHENSIVE BLIND MODEL

5.1 Experimental Facility

In order to validate the comprehensive blind model, an experimental cooling load facility [Eldridge et al. 2003] was modified to accommodate slat-type blind experiments. The south facing glazing was covered and all opaque interior surfaces were painted a flat black. The west facing fenestration system, which was used in the experiments, consisted of single pane DSA glass[1] with various configurations of horizontal slat-type blinds. All instrumentation required for the experimental measurement of space cooling loads was left intact to facilitate investigation of the impact of fenestration parameters on the cooling load.

In this study, three types of commercial blinds were installed in the facility. Table 5-1 summarizes the blind parameters. The edges of the blinds were masked to prevent transmission of solar radiation between the blind and the window frame. To measure the total solar transmittance of the fenestration system with an interior blind, a single pyranometer was used to measure the incident solar radiation while a traversing dual pyranometer was used to measure the transmitted solar radiation. Two traversing pyranometers reduced the uncertainty due to non-uniformly spaced and oriented slats as discussed in the following section.

---

[1] Reference glazing for shading coefficient calculations; clear glass with nominal thickness of 3 mm (1/8 in.)

Table 5-1 Summary of Experimental Blind Parameters

Blind No.	Blind Description	Slat Width, mm	Slat Spacing, mm	Slat Color / Reflectance	Slat Curvature Radius, mm[a]	Slat Thickness, mm	Slat Angles, deg.
1	1 in. Vinyl White Blinds with Curved Slats	23.5	20.0	White / 0.82	20.6	0.5	+45, 0, -40
2	1 in. Vinyl Black Blinds with Curved Slats	23.5	20.0	Black / 0.10	20.6	0.5	+45, 0, -45
3	1 in. Vinyl Silver Blinds with Curved Slats	23.5	20.0	Silver / 0.59	20.6	0.5	+45, 0, -45
4	2 in. Vinyl White Blinds with Curved Slats	50.0	44.0	White / 0.81	53.8	1.0	+45, 0, -45
5	1 in. Wood Brown Blinds with Flat Slats	27.0	21.5	Brown / 0.45	-	3.0	+45, 0, -45

[a] The radius of slat curvature is calculated using the slat width (straight-line width) and the curvature width.

5.2 In Situ Experimental Method

5.2.1 Measurement of Total Solar Transmittance

The experimental procedure required a reasonably accurate measurement of the total solar transmittance through the fenestration system. Although laboratory measurements utilizing automated gonio-radiometer/photometers [Klems and Warner 1995] or gonio-spectrometers [Breitenbach et al. 2001] yield more detailed and accurate results, the traversing pyranometer method used by Pennington et al. [1964] is the most suitable procedure for the in situ measurement of total transmitted solar radiation in an experimental cooling load facility.

A traversing dual pyranometer was designed to operate continuously in the experimental cooling load facility at Oklahoma State University [Eldridge et al. 2003]. Two identical pyranometers, Kipp and Zonen Model CM11, were mounted 30 cm apart on a base plate as shown in Figure 5-1. A traversing mechanism moved the base plate along a 30 cm vertical path at a relatively constant rate of 12.5 cm/min. The mechanism was mounted inside the experimental enclosure directly behind and parallel to the fenestration system as shown in Figure 5-1. The constant rate pyranometer traverse through alternate shaded and sunlit bands produced by the slat-type blinds measured the total solar radiation transmitted through the fenestration system. A third pyranometer, Eppley Model 8-48, was mounted parallel to the plane of the fenestration system on the outside of the experimental cooling load facility. This pyranometer, which was exposed to the weather, measured the total incident solar radiation on the fenestration system.

All three pyranometers measure global solar irradiance within a spectral range of 0.3 to 2.8 μm. The calibration of the instruments was checked prior to installation by mounting all three on the same surface and recording measured incident solar radiation for one day. No additional correction of the output signal was necessary. The uncertainty associated with these measurements is estimated in the following section.

Although all data points were measured at 1-minute intervals, five minute averages were calculated to facilitate graphical representation of the data. The primary metric used to validate the optical blind model was the total solar transmittance defined as the ratio of total solar radiation transmitted through the fenestration system to total solar radiation incident on the outside of the fenestration system. Measured data from the traversing dual pyranometer were spatially averaged to calculate a total solar transmittance that represents an overall characteristic of the blind assembly rather than local characteristics of individual slats.

5.2.2 Estimation of Total Solar Transmittance Uncertainty

The measured total solar transmittance was the primary metric for model validation. The uncertainty in the derived solar transmittance due to uncertainties in the two measured independent variables (i.e. transmitted and incident solar radiation, T and I), may be estimated according to Beckwith et al. [1993] as:

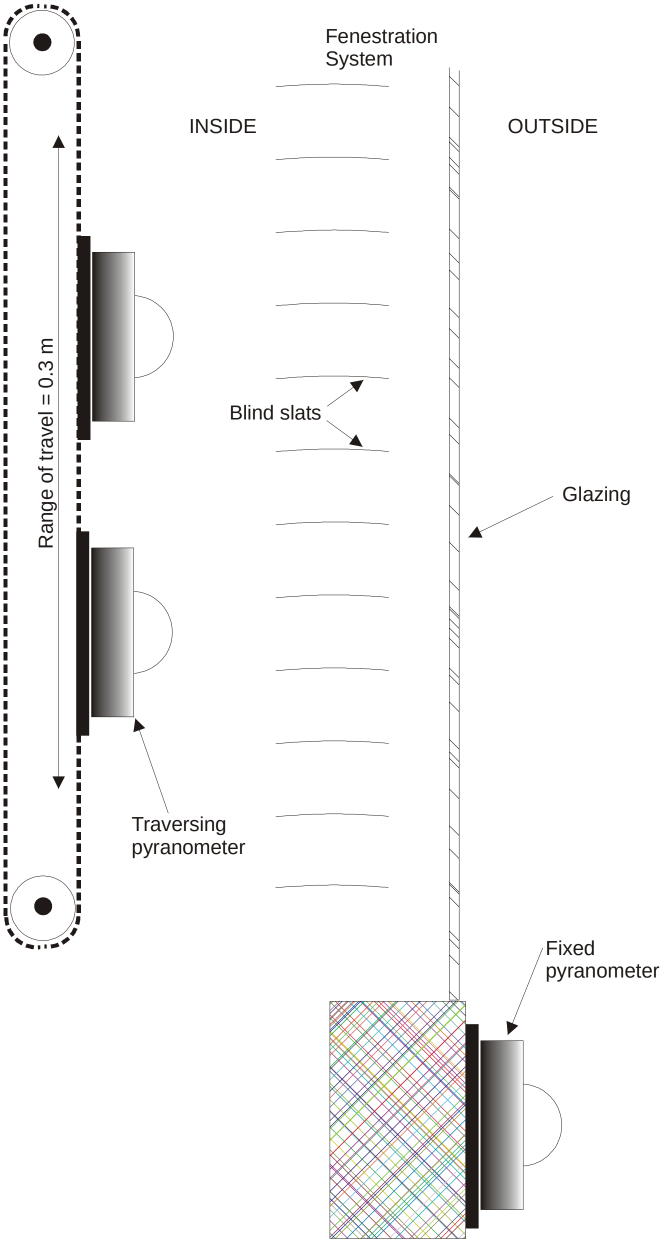

Figure 5-1 Measurements of Blind Total Solar Transmittance

$$u_\tau = \sqrt{\left(\frac{\partial \tau}{\partial I} u_I\right)^2 + \left(\frac{\partial \tau}{\partial T} u_T\right)^2} \tag{5-1a}$$

By substituting the solar transmittance ($\tau = \frac{T}{I}$) into Equation (5-1a), we can obtain the uncertainty as:

$$u_\tau = \sqrt{\left(\frac{T}{I^2} u_I\right)^2 + \left(\frac{1}{I} u_T\right)^2} \tag{5-1b}$$

This approach, which assumes that the measurements are independent, is commonly referred to as the method of Kline and McClintock [Beckwith et al. 1993; Kline and McClintock 1953]. For the incident solar radiation, the sources of uncertainty include setup of the pyranometer (its orientation relative to the fenestration system), and the accuracy of the sensor. For the transmitted solar radiation, the sources of uncertainty include setup of the pyranometers, the accuracy of the sensors, and the irregularity of the blind assemblies (both slat spacing and angle). The root mean square of all uncertainties associated with each measurement was used as an approximation of the total uncertainty associated with that measurement.

For the incident solar radiation, two sources of error were considered. First, the error in pyranometer orientation was expected to be less than 3° since the pyranometer was mounted directly on the outside wall parallel to the fenestration system. Thus, the uncertainty due to the setup of the pyranometer was estimated to be about 0.2% of measured incident solar radiation. Second, the uncertainty due to the accuracy of the sensor was estimated to be about 5.3% of measured incident solar radiation. The root mean square of sensor errors (i.e. temperature dependence, non-linearity, and directional response) as published by the manufacturer was used as an approximation of the uncertainty associated with the sensor.

For transmitted solar radiation, the two pyranometers were mounted on the same base plate. The orientation of the plate relative to the window plane could be accurately estimated. Over the entire traverse, the estimated error in both the facing and tilt angles of the sensors was less than 3°. This was equivalent to less than a 5° difference between the normal direction of the sensor plane and the normal direction of the window. Therefore, the uncertainty due to the setup of the pyranometers was estimated to be about 0.5% of measured transmitted solar radiation. Like the estimation of the uncertainty in incident solar radiation, the root mean square of sensor errors was used as an estimate of the uncertainty associated with the sensor accuracy. This uncertainty was estimated to be 3.2% of the averaged transmitted solar radiation. The error due to the irregularity of the blind assemblies was then estimated as the difference of the transmitted solar radiation values measured by the two pyranometers. Because all inside surfaces of the test cell were black, the uncertainty due to solar radiation reflected from the inside was neglected.

The maximum estimated uncertainty in the measured solar transmittance for all experimental tests was $u_\tau = \pm 0.05$. To provide a clear comparison between predicted and measured results, the uncertainty intervals are shown with the measured data for all reported results.

5.2.3 Measurement of Slat Reflectance

Although an accurate estimate of slat reflectance requires laboratory measurement using a spectrophotometer with an integrating sphere [ASTM 1996], a field method to obtain this input to blind models for load calculations may be useful. Since a net radiometer is generally available to estimate radiation exchanges between surfaces in cooling load experiments, a simple procedure was developed to estimate the slat reflectance of a blind assembly in the field using a net radiometer. The procedure proved to be sufficiently accurate for load calculation model validation and could be used where non-destructive testing of installed blind assemblies is the only option for obtaining the optical input parameters required by the blind model.

Ideally, the solar reflectance[1] of the individual slats of a blind assembly would be equal to the solar reflectance of the completely-closed blind assembly. For a diffusely reflecting blind, direct measurement of the incident and reflected solar radiation using a net radiometer will give a first order approximation of the surface reflectance in the solar spectrum. Two corrections significantly improve the approximation. First, the error introduced by reflected background radiation may be corrected by means of a calibration surface of known reflectance. Second, the error introduced by radiation transmitted through the closed blind assembly may be corrected by estimating the closed blind transmittance.

To correct for solar reflectance from the surroundings, the blind assembly is replaced with a blind-sized calibration surface of known reflectance[2] [Berdahl and Bretz 1997] in the solar spectrum. As shown in Figure 5-2, the incident and reflected solar radiation for the calibration surface and its surroundings are then measured using the net radiometer. The measured, reflected radiation ($R_{cal,meas}$) represented the combined effect of the calibration surface and the surroundings as follows:

$$R_{cal,meas} = \frac{\dot{q}_{cal} + \dot{q}_{surr}}{A_{pyr}} \tag{5-2a}$$

where $\dot{q}_x$ = rate at which the solar radiation leaves surface *x* and is intercepted by the pyranometer, and

A_y = surface area of surface *y*.

---

[1] In accordance with radiative heat transfer theory [Modest 2003], if the collimated light is used as a light source, then the measured reflectance is 'directional-hemispherical' reflectance. If the sun and sky are the light source, then the measured reflectance is 'total-hemispherical' reflectance.

[2] The calibrated surface was coated with Koolseal White Elastomeric, a roof coating with solar reflectance of 0.81 [Berdahl and Bretz 1997].

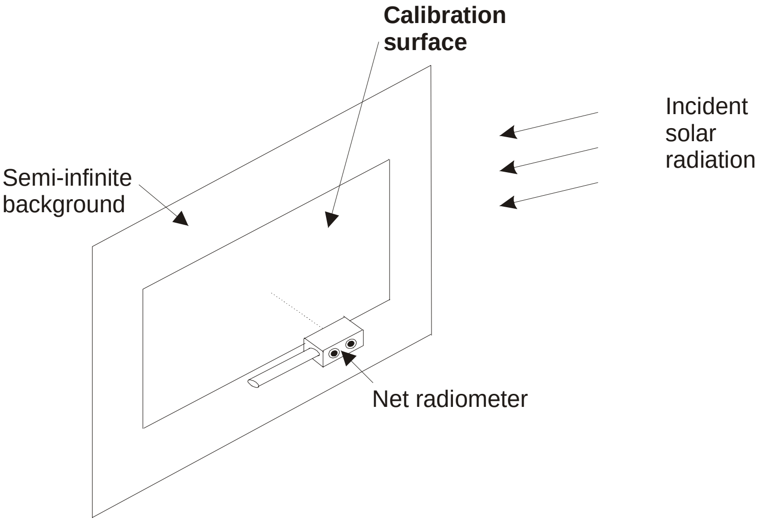

a). ESTIMATE RADIOMETER VIEW TO BACKGROUND

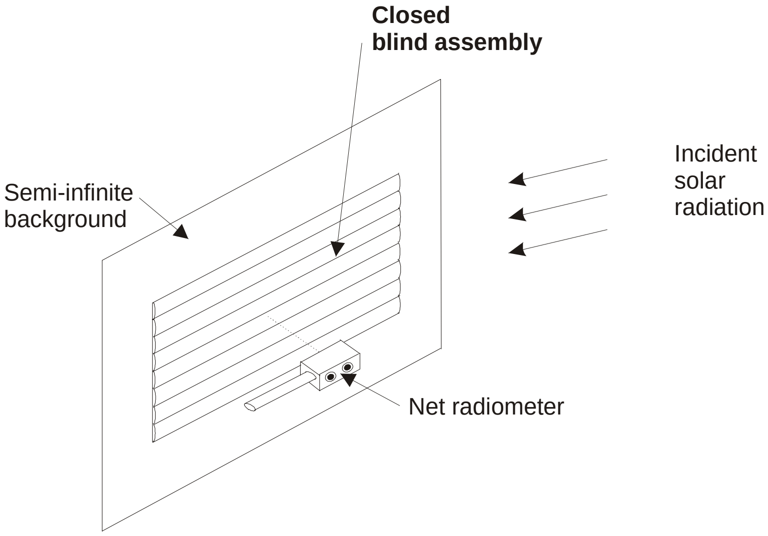

b). ESTIMATE BLIND REFLECTANCE

Figure 5-2 Measurements of Slat Solar Reflectance

The subscripts *cal*, *surr*, and *pyr* refer to the calibration surface, the semi-infinite background, and the pyranometer, respectively. Assuming that both the calibration surface and the semi-infinite background are diffuse, Equation (5-2a) may also be written as:

$$R_{cal,meas} = \frac{A_{cal} \cdot F_{cal \to pyr} \cdot J_{cal} + A_{surr} \cdot F_{surr \to pyr} \cdot J_{surr}}{A_{pyr}} \tag{5-2b}$$

where J_x = radiosity of surface *x*, and

$F_{x \to y}$ = view factor from surface *x* to surface *y*.

Using the reciprocity relation for view factors, Equation (5-2b) can then be expressed by:

$$R_{cal,meas} = F_{pyr \to cal} \cdot J_{cal} + F_{pyr \to surr} \cdot J_{surr} \tag{5-2c}$$

For shortwave radiation, the radiosity is equal to the reflected solar radiation. Therefore, Equation (5-2c) becomes:

$$R_{cal,meas} = F_{pyr \to cal} \cdot \rho_{cal,spec} \cdot I_{meas} + F_{pyr \to surr} \cdot \rho_{surr} \cdot I_{meas} \tag{5-2d}$$

where $\rho_{cal,spec}$ = specified reflectance of the calibration surface,

ρ_{surr} = solar reflectance from the surroundings, and

I_{meas} = incident solar radiation.

Since the summation of the view factors between the pyranometer and other surfaces is one, $F_{pyr \to surr}$ is equal to $1 - F_{pyr \to cal}$. In addition, $\rho_{cal,meas}$, which is defined as the in situ measured reflectance of the calibration surface including reflectance from surroundings, may be written as $\frac{R_{cal,meas}}{I_{meas}}$. We can then rearrange Equation (5-2d) to obtain the solar reflectance from the surroundings as:

$$\rho_{surr} = \frac{\rho_{cal,meas} - \rho_{cal,spec} \cdot F_{pyr \to cal}}{1 - F_{pyr \to cal}} \tag{5-3}$$

Since the calibration surface had the same dimensions as the blind assembly, a single view factor ($F_{pyr \to cal}$) designates the view from the net radiometer to both the calibration surface and the blind assembly. The view factor may be estimated using a view factor formula for a differential planar element and a finite parallel rectangle [Modest 2003].

To correct for transmission through the closed blind assembly, total solar transmittance through the fenestration system containing the closed blind, for each particular blind, is measured. Total solar transmittance through the fenestration system without the blind is also measured. Then, the transmission loss, τ_{loss}, may be approximated by

$$\tau_{loss} = \frac{\tau_{shaded}}{\tau_{unshaded}} \tag{5-4}$$

where τ_{shaded} = total solar transmittance of the fenestration system containing the closed blind,

$\tau_{unshaded}$ = total solar transmittance of the fenestration system without the blind.

The experimental procedure as described in Section 5.2.1 is also used for these measurements. It should be noted that Equation (5-4) neglects multiple reflections between the glazing and the blind.

It is then assumed that the solar reflectance of the closed blind assembly can be approximated as the difference between the slat reflectance (ρ_{slat}) and the transmission loss (τ_{loss}). Then, Equation (5-2d) may be employed along with the definition of $F_{pyr \to cal}$ to calculate the reflected solar radiation ($R_{bl,meas}$) for the closed blind assembly as:

$$R_{bl,meas} = F_{pyr \to cal} \cdot \left(\rho_{slat} - \tau_{loss} \right) \cdot I_{meas} + (1 - F_{pyr \to cal}) \cdot \rho_{surr} \cdot I_{meas} \tag{5-5}$$

By substituting $\rho_{bl,meas}$ (in situ measured reflectance of the closed blind assembly including reflectance from surroundings) for $\frac{R_{bl,meas}}{I_{meas}}$ and rearranging Equation (5-5), we obtain the slat reflectance (ρ_{slat}) as:

$$\rho_{slat} = \frac{\rho_{bl,meas} - \rho_{surr} \cdot \left(1 - F_{pyr \to cal} \right)}{F_{pyr \to cal}} + \tau_{loss} \tag{5-6}$$

In applying the transmission loss as shown in Equation (5-6), two main assumptions are made. First, all solar radiation is transmitted through the closed blind by reflections only. Second, the closed blind and its associated back wall behave like a small cavity or perfect absorber. To reduce the error associated with the second assumption, a black surface is placed behind the closed blind assembly during the measurement of the closed blind reflectance.

Figure 5-3 shows the results of estimating the slat reflectance using this procedure. As shown, the estimated slat reflectance for each blind is quite constant over long periods of time. The estimated slat reflectance varies by less than 0.10 for diffuse solar radiation (morning) and by less than 0.13 for total solar radiation (afternoon).

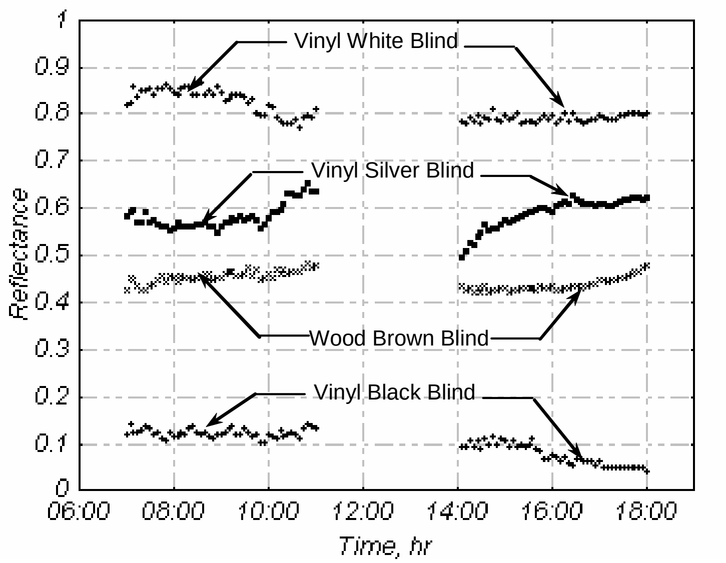

Figure 5-3 Calibrated Slat Reflectance

5.3 Comparison of the Comprehensive Blind Model with Measured Data

In this section, the comprehensive blind model is compared with five experimental data sets of solar transmittance obtained by the in situ experimental method described in the previous section. Table 5-1 summarizes the blind parameters, which are used as inputs to the model. The next section presents definitions of solar transmittances used in the current study. Since the comprehensive blind model consists of several sub-models, the following section then illustrates the effect of using different sub-models with baseline input parameters (i.e. the blind slats are assumed to be purely diffuse and the blind parameters presented in Table 5-1 are used). Following the effect of using different models, the effect of varying input parameters is then demonstrated. Finally, the experimental comparison using calibrated input parameters is presented to illustrate the validity of the comprehensive blind model.

5.3.1 Definitions

In this comparison, four effective transmittances are defined and used to calculate the total solar transmittance in the comprehensive blind model:

- ‘Direct-to-direct’ transmittance, τ_{bm-bm}, is defined as the fraction of beam solar radiation that directly passes through the fenestration system without striking the blind slats.
- ‘Direct-to-diffuse’ transmittance, τ_{bm-df}, is defined as the fraction of beam solar radiation that indirectly passes through the fenestration system by reflections between the slats and between layers of the fenestration system.
- ‘Sky-diffuse’ transmittance, τ_{sky}, is defined as the fraction of diffuse solar radiation from the sky that passes directly and indirectly through the fenestration system.
- ‘Ground-diffuse’ transmittance, τ_{gnd}, is defined as the fraction of diffuse solar radiation from the ground that passes directly and indirectly through the fenestration system.

The ‘effective’ modifier indicates that the predicted transmittances include interaction between the glazing and the blind. Using these terms, the total solar transmittance is calculated as follows:

$$\tau_t = \frac{I_{sky} \cdot \tau_{sky} + I_{gnd} \cdot \tau_{gnd} + I_{bm} \cdot \left(\tau_{bm-bm} + \tau_{bm-df}\right)}{I_{sky} + I_{gnd} + I_{bm}} \tag{5-7}$$

Because all experimental data were observed for a west-facing fenestration system, two additional effective transmittances are defined. Total solar transmittance measured (and/or predicted) during the morning hours (in the absence of beam solar radiation) is referred to as ‘diffuse’ solar transmittance. Total solar transmittance measured (and/or predicted) in the afternoon is referred to as ‘total’ solar transmittance.

5.3.2 Baseline Results

To illustrate the effect of using different sub-models of the comprehensive blind model, Figure 5-4 compares predicted results with measured data for the 1-in vinyl white blind with curved slats (Blind No. 1) oriented at three different angles. As shown in the figure, the plus symbols (labeled Measured) with error bars represent measured solar transmittance and its uncertainty range. The solid line (labeled NetRad - Flat) represents predicted results using the net-radiation sub-model for a flat-slat blind. The dash line (labeled NetRad – Curved) represents predicted results using the net-radiation sub-model for a curved-slat blind. The dotted line (labeled MCRT – Curved) represents predicted results using the ray-tracing sub-model for a curved-slat blind.

As shown in the left hand region of Figure 5-4, both the net-radiation and the ray-tracing models for a curved-slat blind predict lower diffuse solar transmittance than the net-radiation model for a flat-slat blind does for all three slat angles due to the effect of slat curvature accounted for in the curved-slat models. The predicted results by the curved-slat blind models appear to have slightly better agreements with measured diffuse solar transmittance for all three slat angles. It should be noted that both curved-slat blind models predict identical results since the model implementation assumes that blind slats behave like diffuse-reflecting surfaces for the diffuse solar radiation although they may behave otherwise for the direct solar radiation. This means that the net-radiation blind sub-model(s) is employed by the diffuse blind model for the model implementation used in the current investigation.

(a) 1 in Vinyl White - Downward Opened

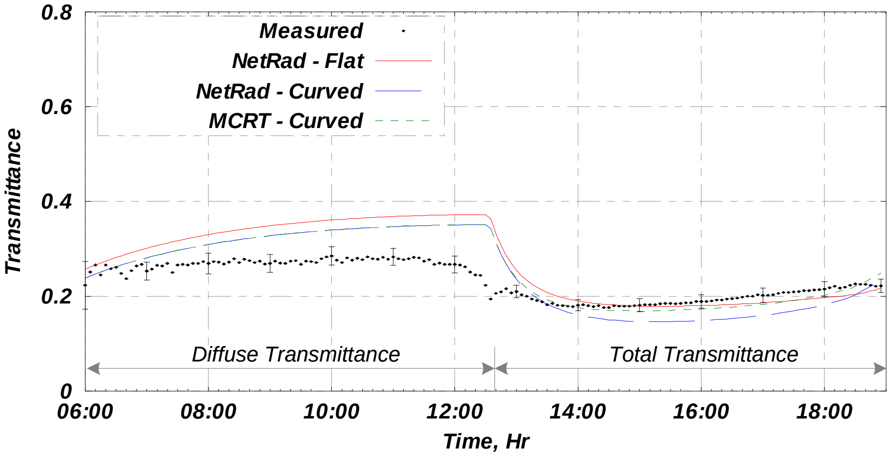

(b) 1 in Vinyl White - Horizontally Opened

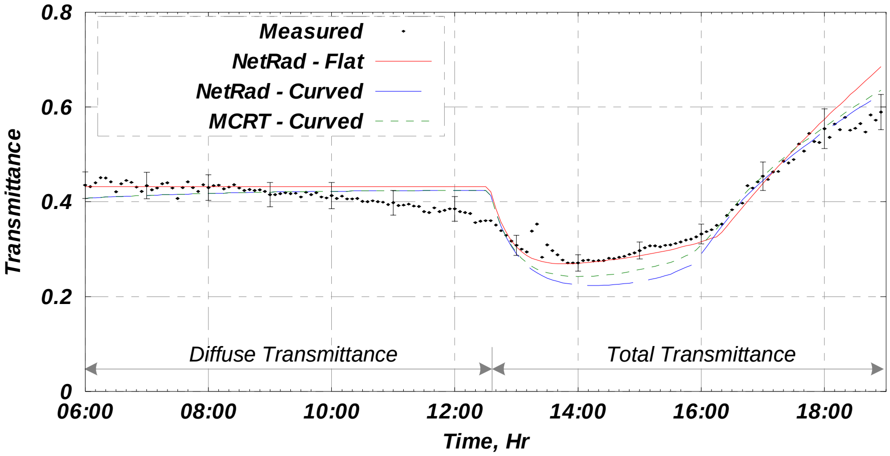

(c) 1 in Vinyl White - Upward Opened

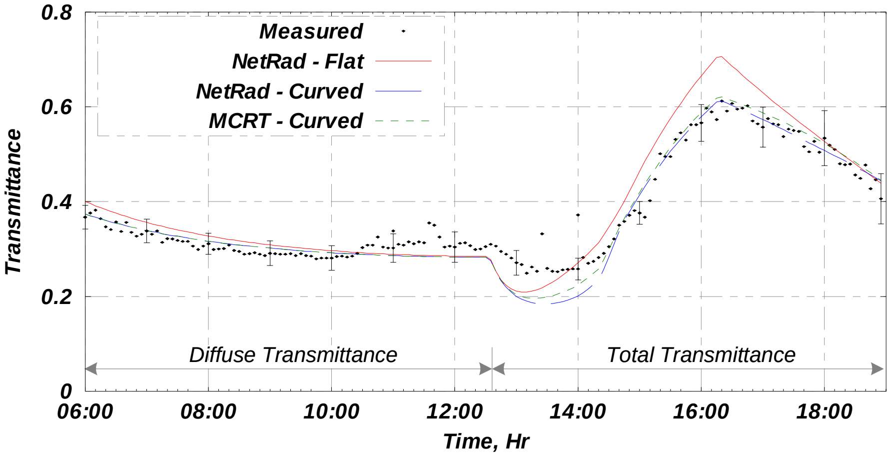

Figure 5-4 Effect of Different Direct Blind Sub-Models

For the total solar transmittance shown in the right hand region of Figure 5-4, both curved-slat blind models also mostly predict lower results than the flat-slat blind model does. The predicted results by the curved-slat blind models agree with measured data very well when a large amount of direct solar radiation is directly transmitted without any reflections (e.g. results during 3 to 6 p.m. shown in Figure 5-4c). The significant discrepancy between the flat-slat blind model results and measured data during this time period indicates the effect of neglecting the slat curvature. However, the predicted results by the flat-slat blind model show quite better agreements with measured data when a large amount of direct solar radiation is transmitted by reflections (e.g. results during 1 to 4 p.m. shown in Figure 5-4b) than results predicted by the other two models. This somewhat counterintuitive result may be due to the combined effect of model deficiencies and uncertainty in input parameters. As shown, results predicted by the ray-tracing model for a curved-slat blind have better agreements with measured total solar transmittance than results predicted by the net-radiation model for a curved-slat blind for all three slat angles. It is worth mentioning that, for a blind having purely-diffuse-reflecting slats, the net-radiation and the ray-tracing models typically predict different results of the direct-reflected blind transmittance. The differences are much smaller when the blind slats are completely illuminated (e.g. Case 2 shown in Figure 4-5) than when the blind slats are partially illuminated (e.g. Case 3 shown in Figure 4-5). The possible explanation is that the net-radiation model(s) uses inaccurate view factors, which may be due to the Crossed-Strings method and/or the insufficient surface subdivision. In the next section, a sensitivity to blind input parameters (i.e. the effect of uncertainty in input parameters) is investigated.

The predicted results shown in Figure 5-4 assume isotropic sky and ground radiance distributions. As previously discussed, however, the isotropic diffuse distribution is not an inherent assumption in the comprehensive blind model. To demonstrate the effect of an anisotropic assumption, Figure 5-5 compares predicted results using Igawa's anisotropic sky radiance distribution model [Igawa et al. 2004] with predicted results using isotropic sky assumption with the same direct blind sub-model (i.e. the ray-tracing model for a curved-slat blind). As shown, the effect of the anisotropic model on the total solar transmittance is very trivial as compared to its effect on the diffuse solar transmittance although the effect of the anisotropic model on the predicted sky diffuse irradiation is actually more significant in the afternoon than in the morning. This is due to the fact that the sky diffuse irradiation is a very small portion of the total insolation in the afternoon while it has a greater contribution in the morning. The model differences are noticeable for the diffuse solar transmittance, particularly for the horizontally opened blind shown in Figure 5-5b. As shown, the anisotropic model shows slightly better agreements with measured diffuse solar transmittance than the isotropic model does for the horizontally opened blind. It should be noted that although no anisotropic ground radiance distribution model exists, an attempt had been made to investigate the effect of an anisotropic ground assumption by calculating a simple ground radiance distribution based on a shadow in front of the test building. The investigation indicated that the effect of the shaded ground assumption on the diffuse solar transmittance might be trivial (the effect on the diffuse solar transmittance was trivial, and there was no effect on the total solar transmittance since there was no shadow in front of the west-facing test window in the afternoon).

(a) 1 in Vinyl White - Downward Opened

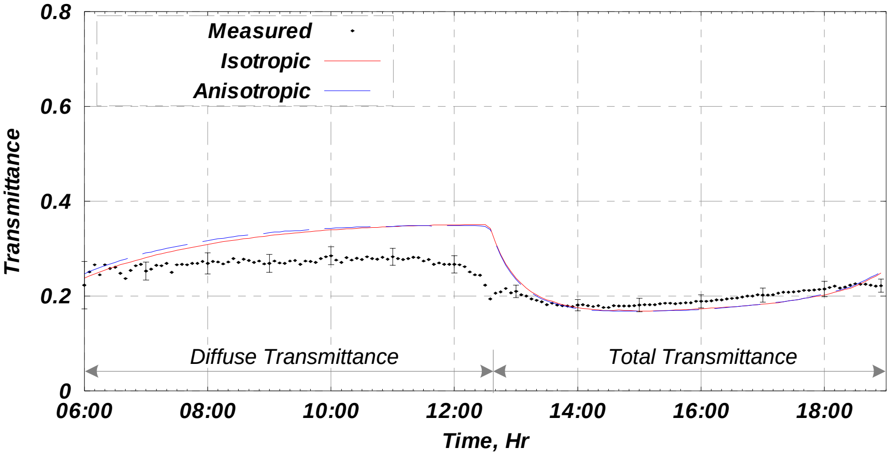

(b) 1 in Vinyl White - Horizontally Opened

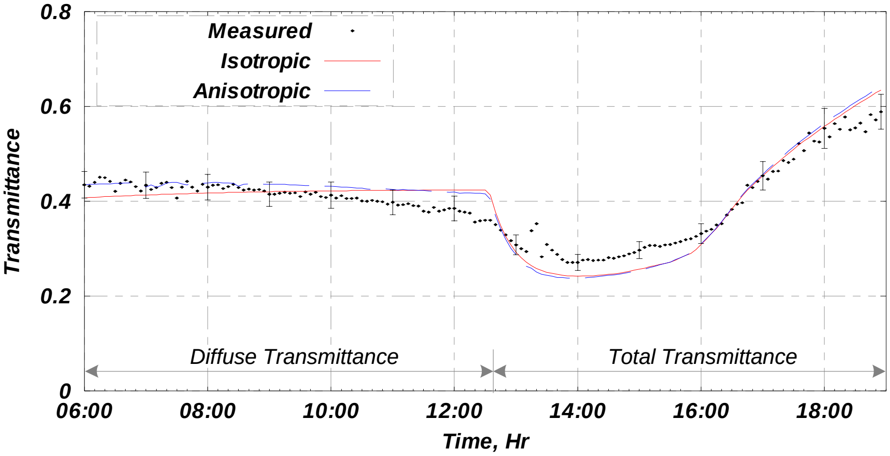

(c) 1 in Vinyl White - Upward Opened

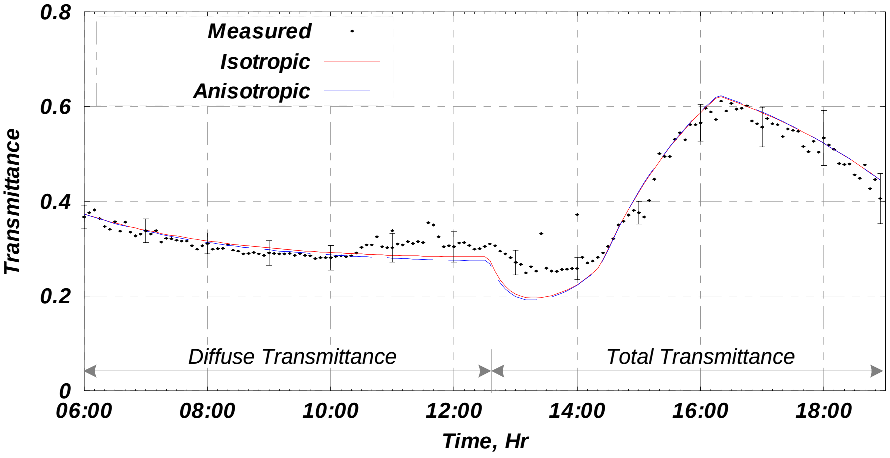

Figure 5-5 Effect of Different Diffuse Sky Radiance Distributions

5.3.3 Effect of Blind Input Parameters

As previously mentioned, uncertainty in input parameters can cause discrepancies between the predicted and measured results. Therefore, it is essential to investigate the sensitivity of predicted solar transmittance to the blind input parameters. The comprehensive blind model requires several blind input parameters including slat geometry parameters (slat angle, slat width, slat spacing, slat thickness for flat-slat blinds, and slat curvature for curved-slat blinds), and slat radiative parameters for both sides of blind slats (slat reflectance and slat reflective specularity ratio)[1]. In this investigation, the ray-tracing blind model and the anisotropic sky radiance distribution model (i.e. Igawa's sky radiance distribution model) are employed as baseline models for direct and diffuse optical blind properties, respectively.

Of all required input parameters, the slat angle is probably the most important parameter since changing the slat angle can change both the value and the profile of the solar transmittance curves as illustrated in Figures 5-4 and 5-5. Therefore, to investigate the sensitivity to a small change in the slat angle, predicted results with the slat angle varied by 5° are plotted against measured data in Figure 5-6. As shown in Figure 5-6c, increasing the slat angle for the upward opened blind not only results in an increase in the peak total solar transmittance but also a shift of the peak to a later time. For the upward opened blind, the time the peak occurs is useful information since matching the time of the predicted peak results to the time of the measured peak data indicates that the actual slat angle was about -40° although the slat angle was intentionally set at -45°. For the downward opened and horizontally opened blinds, increasing the slat angle results in only a decrease in the values of predicted total solar transmittance.

---

[1] Slat transmittance and transmissive specularity ratio are not necessary since all investigated blinds have opaque slats.

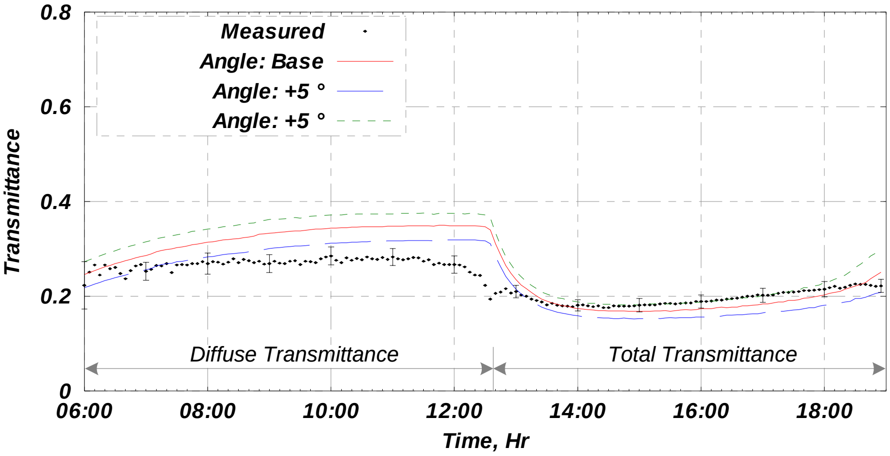

(a) 1 in Vinyl White - Downward Opened

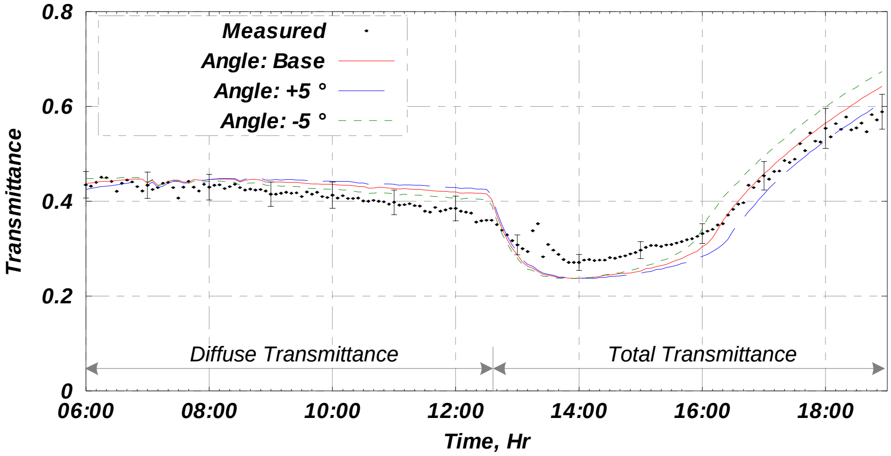

(b) 1 in Vinyl White - Horizontally Opened

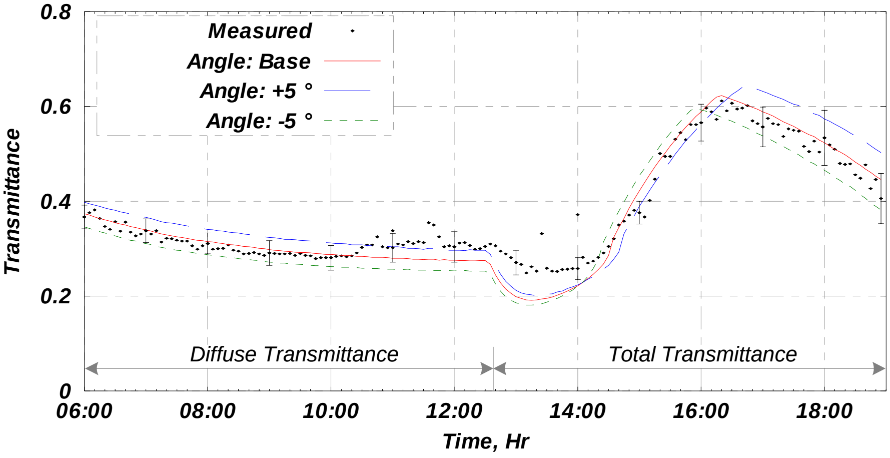

(c) 1 in Vinyl White - Upward Opened

Figure 5-6 Effect of Slat Angle

As shown in the left hand region of Figure 5-6, the effect of the slat angle on the diffuse solar transmittance is also dependent on the setting of the slat angle. Increasing the slat angle results in lower diffuse solar transmittance for the downward opened blind as shown in Figure 5-6a. On the other hand, as shown in Figure 5-6c, increasing the slat angle results in higher diffuse solar transmittance for the upward opened blind. For the horizontally opened blind shown in Figure 5-6b, changing the slat angle causes mixed results. Increasing the slat angle results in higher diffuse solar transmittance in the early morning but it results in lower diffuse solar transmittance later. The mixed results for the horizontally opened blind are due to the fact that changing the slat angle causes opposite changes in the sky and the ground diffuse blind transmittance for slat angle between +30° and -30° as illustrated in Figure 3-4 (for Parmelee and Pfrommer results). Therefore, for the horizontally opened blind, the diffuse solar transmittance is dependent not only on the sky and ground diffuse blind transmittance but also on the sky and ground diffuse components of the total insolation. For the test window, the sky diffuse component of the total insolation is larger than the ground diffuse component in the early morning and the reverse occurs in later morning.

Unlike the effect of the slat angle, changing the slat spacing only causes a change in the value of the predicted diffuse and total solar transmittance as illustrated in Figure 5-7. As shown for all three slat angles, increasing the slat spacing results in an increase in both the diffuse and the total solar transmittance. The effect of other parameters (including the slat thickness, the slat curvature, and the slat reflectance) is similar to the effect of the slat spacing such that changing these parameters only result in a value change but not a change in the shape or the time the peak occurs. The value change is certainly dependent on the change in those parameters.

(a) 1 in Vinyl White - Downward Opened

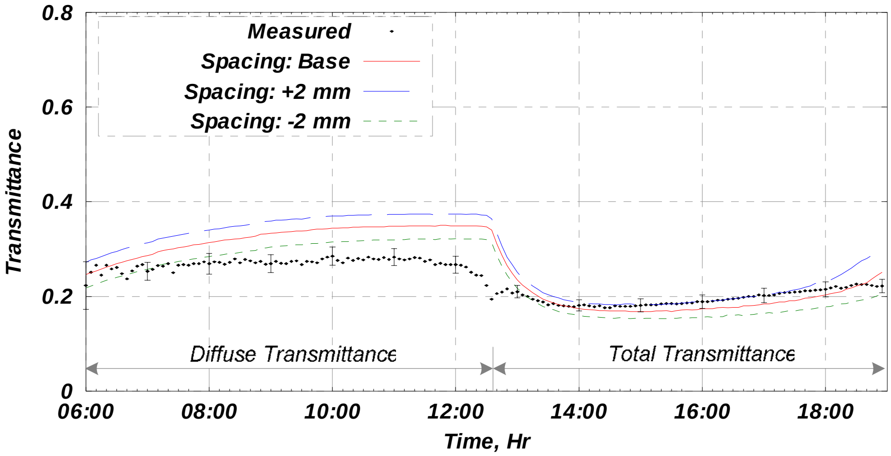

(b) 1 in Vinyl White - Horizontally Opened

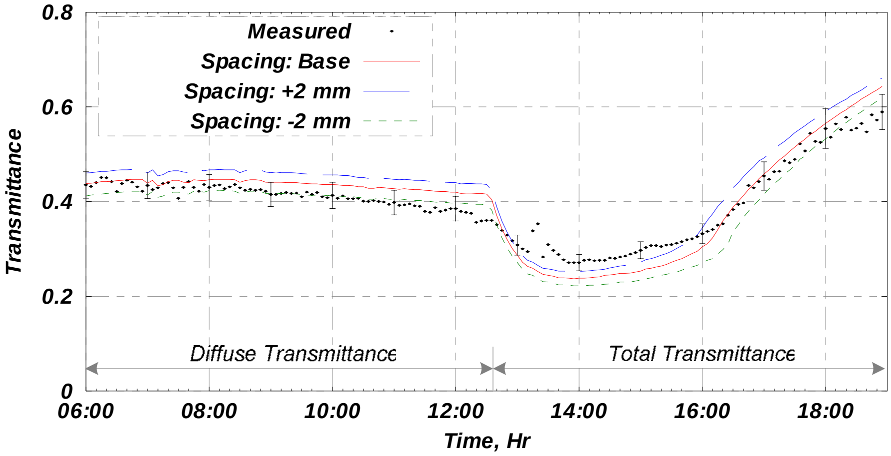

(c) 1 in Vinyl White - Upward Opened

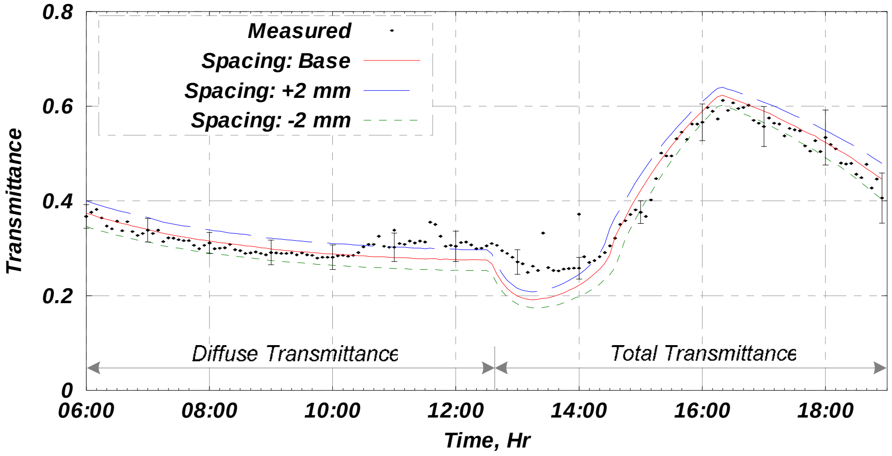

Figure 5-7 Effect of Slat Spacing

As previously discussed, the comprehensive blind model uses the reflective specularity ratio to deal with a blind having partially-specular- and partially-diffuse-reflecting slats. To illustrate the effect of the reflective specularity ratio, Figure 5-8 compares predicted results representing three different slat radiative characteristic types with measured data. It should be noted that the results labeled "Partial" use the specularity ratio(s) of 0.5 (i.e. 50% specular and 50% diffuse). As shown on the left hand region of the figure, the predicted diffuse solar transmittance are identical since the model implementation assumes that blind slats behave like diffuse-reflecting surfaces for the diffuse solar radiation although they may behave otherwise for the direct solar radiation as previously discussed. On the other hand, as shown on the right hand region of Figure 5-8, the predicted total solar transmittance are significantly different from one another. The good agreements between the measured data and the "Diffuse" predicted results indicate that the blind slats for the 1-in white vinyl blind with curved slats (Blind No. 1) behave more like the purely-diffuse-reflecting surfaces than like the purely-specular-reflecting surfaces. It should be noted that an investigation of the effects of different radiative properties and characteristics on different sides of the blind slats shows results that are not significantly different from those reported here.

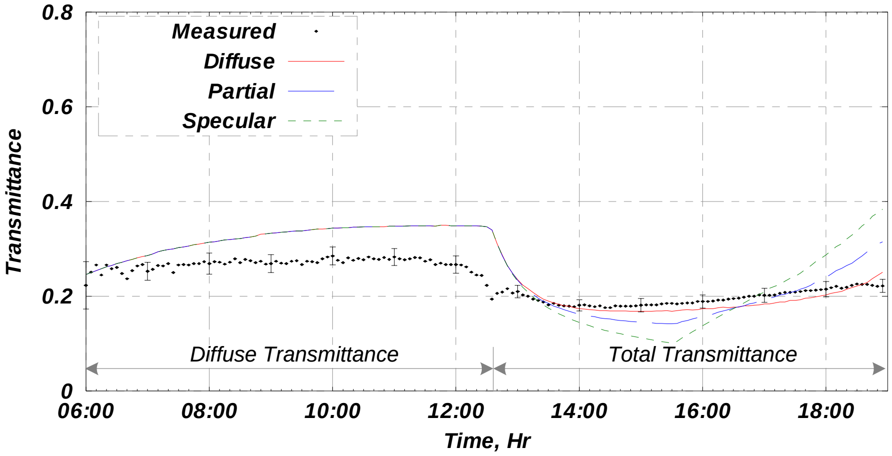
(a) 1 in Vinyl White - Downward Opened

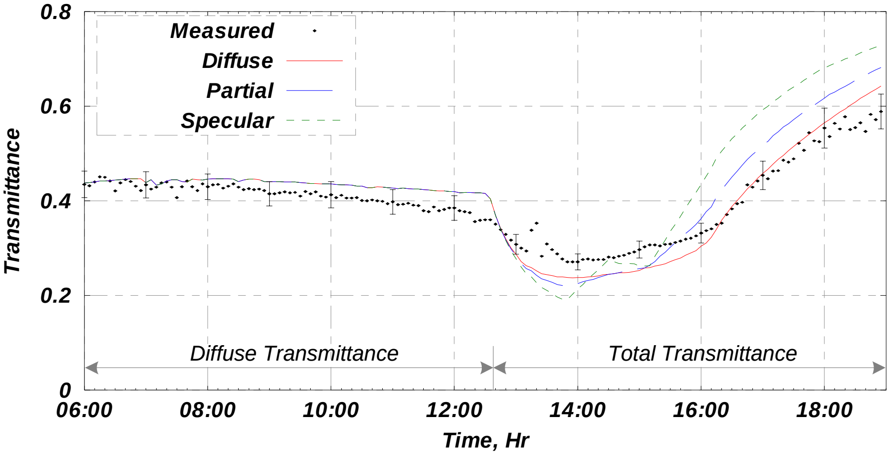
(b) 1 in Vinyl White - Horizontally Opened

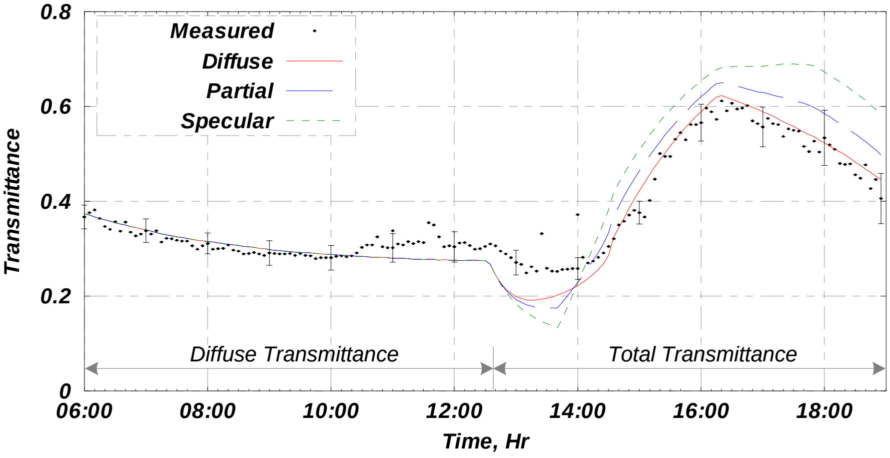
(c) 1 in Vinyl White - Upward Opened

Figure 5-8 Effect of Slat Reflective Specularity Ratio (Same Ratio on Both Sides)

5.3.4 Calibrated Results

In comparing experimental measurement with the comprehensive blind model, two types of uncertainty must be recognized. First, the experimental uncertainty associated with the measurements must be quantified. Then, the uncertainty in the blind model output due to uncertainty in specifying the model input parameters must be quantified. This uncertainty can be reduced by calibrating the input parameters using measured data. When this is not possible, it is useful to estimate the overall uncertainty in the predicted total solar transmittance due to an error in various input parameters. To estimate the uncertainty due to the error in each input parameter, the dimensional type 1 influence coefficient [Spitler et al. 1989] is used. The uncertainty in the total solar transmittance due to the error in each input parameter can be calculated by:

$$u_{p,i} = IC_i \cdot \Delta i \tag{5-8}$$

where $u_{p,i}$ = uncertainty due to the error in input parameter *i*,

IC_i = dimensional type 1 influence coefficient of input parameter *i*, and

Δi = estimated error of input parameter *i*.

Then, the overall uncertainty in the predicted total solar transmittance can be estimated as the root sum of the square of the uncertainties due to individual sources of error as follows:

$$u_p = \sqrt{u_{p,1}^2 + u_{p,2}^2 + ... + u_{p,n}^2} \tag{5-9}$$

where u_p = overall uncertainty in the predicted total solar transmittance, and

n = number of input parameters.

Based on the investigations illustrated in previous sections, the ray-tracing blind model and the anisotropic sky radiance model are used along with calibrated input parameters shown in Table 5-2 to support the validity of the comprehensive blind model. Table 5-2 shows calibrated input parameters and their estimated error used in this investigation. The calibrated input parameters are the same as those shown in Table 5-1, except the slat angle for the upward opened blind. As previously discussed, the slat angle for the upward opened blind can be calibrated by matching the time of the peaks of the predicted and measured results. For all the blinds, except the 1-in vinyl silver blind, the slat reflective specularity ratios (both front and back sides) are assumed to be about 0.05 (i.e. 95% diffuse). For the 1-in vinyl silver blind, which has slats coated with metallic and reflective paint, it is assumed that the slat reflective specularity ratios are 0.5. It should be noted that although the slat reflective specularity ratios seem somewhat arbitrary, they are considered educated guesses. An accurate instrument that can be used to measure bi-directional reflection distribution functions required for the estimation of the slat reflective specularity ratios, such as gonio-radiometer/photometers [Klems and Warner 1995] or gonio-spectrometers [Breitenbach et al. 2001], was not available for the current investigation.

Figure 5-9 illustrates the calibrated results (solid line) for the 1-in vinyl white blind. The figure also shows predicted results by the Parmelee model (dash line) and Pfrommer model (dotted line) to present the inter-model comparison. As shown, the comprehensive blind model has slightly better agreements with both measured diffuse and total solar transmittance than the Pfrommer model does. The comprehensive blind model also shows better agreements with measured diffuse solar transmittance than the Parmelee model does for all three slat angles. For the total solar transmittance, however, the comprehensive blind model only has better agreements with measured data when a large amount of direct solar radiation is directly transmitted without any reflections. These results are similar to the comparison between the flat-slat blind sub-model and the curved-slat blind sub-model previously discussed in Section 5.3.2 since the Parmelee model is equivalent to the flat-slat blind sub-model of the comprehensive blind model.

Table 5-2 Summary of Calibrated Input Parameters

Input Parameter	1 in. Vinyl White Blinds with Curved Slats	1 in. Vinyl Black Blinds with Curved Slats	1 in. Vinyl Silver Blinds with Curved Slats	2 in. Vinyl White Blinds with Curved Slats	1 in. Wood Brown Blinds with Flat Slats
Slat Width, mm	23.5±1.0	23.5±1.0	23.5±1.0	50.0±1.0	27.0±1.0
Slat Spacing, mm	20.0±1.0	20.0±1.0	20.0±1.0	44.0±1.0	21.5±1.0
Slat Radius, mm	20.6±2.0	20.6±2.0	20.6±2.0	53.8±2.0	-
Slat Thickness, mm	-	-	-	-	3.0±1.0
Slat Angle, deg	+45±5, 0±5, -40±2	+45±5, 0±5, -50±2	+45±5, 0±5, -45±2	+45±5, 0±5, -43±2	+45±5, 0±5, -45±2
Slat Reflectance (both front and back)	0.82±0.05	0.10±0.05	0.59±0.05	0.81±0.05	0.45±0.05
Slat Specularity Ratio (both front and back)	0.05±0.05	0.05±0.05	0.5±0.5	0.05±0.05	0.05±0.05

(a) 1 in Vinyl White - Downward Opened

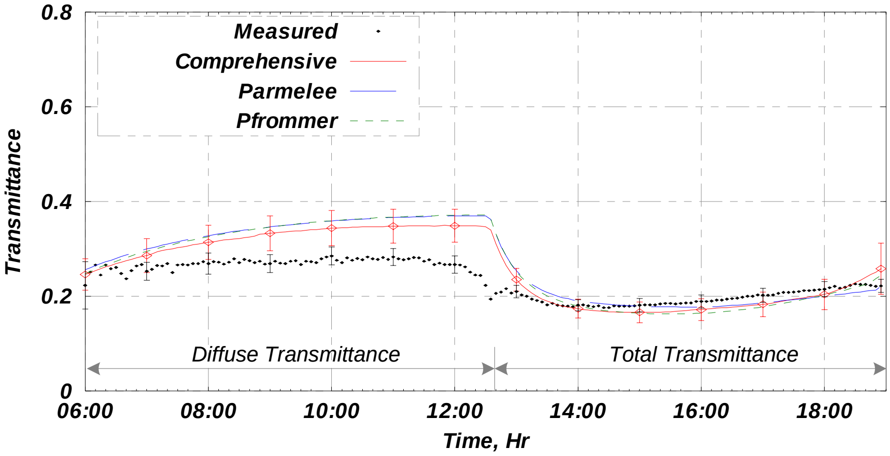

(b) 1 in Vinyl White - Horizontally Opened

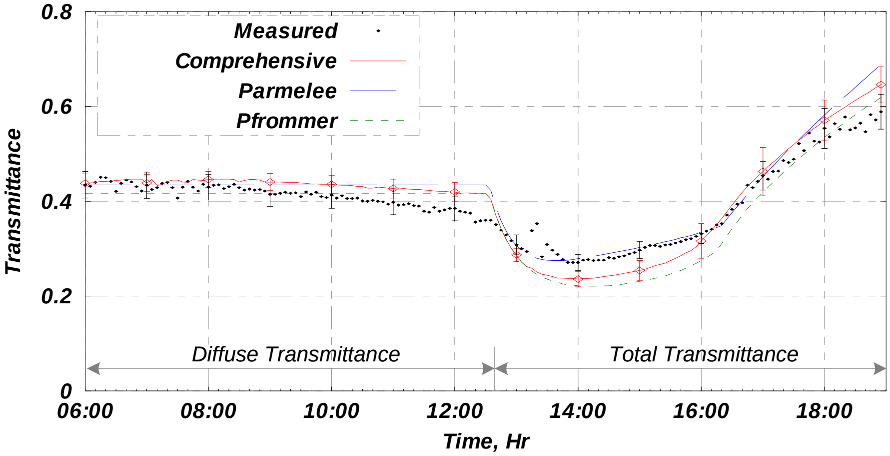

(c) 1 in Vinyl White - Upward Opened

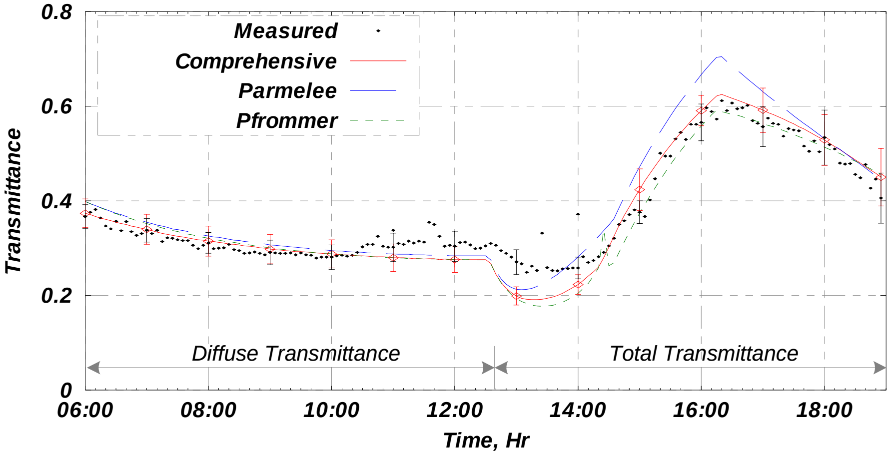

Figure 5-9 Calibrated Results for 1-in Vinyl White Blind

As shown in Figure 5-9, the comprehensive blind model agrees quite well with measured data for most cases. Although the comprehensive blind model shows improvements over the other two models for the diffuse solar transmittance, the discrepancy between the predicted and measured diffuse solar transmittance for the downward opened blind as shown in Figure 5-9a is still quite large and well outside either the experimental uncertainty range or the model uncertainty range. A possible explanation is that the isotropic ground assumption used in the diffuse blind sub-model of the comprehensive blind model does not reflect the change in the shadow cast by the test building. At present, no ground radiance distribution model is available as discussed in Chapter 4. It is worth noting that, however, the comparisons for all other blinds show good agreements for the downward opened blind as illustrated as follows.

Figure 5-10 compares predicted calibrated results with measured data for the 1-in vinyl black blind with curved slats (Blind No. 2). As shown in Figure 5-10a, the comprehensive blind model agrees well with both measured diffuse and total solar transmittance for the downward opened blind. Like the comparison for the 1-in vinyl white blind, the comprehensive blind model has slightly better agreements with measured diffuse solar transmittance than the Parmelee and the Pfrommer models do for all three slat angles. Similarly, the comprehensive blind model and the Pfrommer model, which account for the slat curvature, follows the measured total solar transmittance quite well when a large amount of direct solar radiation is directly transmitted without any reflections (3 to 5 p.m.) as shown on the right hand side region of Figure 5-10c. On the other hand, the Parmelee model over-predicts the total solar transmittance due to neglecting the slat curvature. When a large amount of direct solar radiation is transmitted by reflections (e.g. 1 to 4 p.m. for Figure 5-10b), all three models agree fairly well with measured total solar transmittance. Unlike the comparison for the 1-in vinyl white blind, the differences between predicted results during this period are trivial due to the fact that the 1-in vinyl black blind has low slat reflectance.

(a) 1 in Vinyl Black - Downward Opened

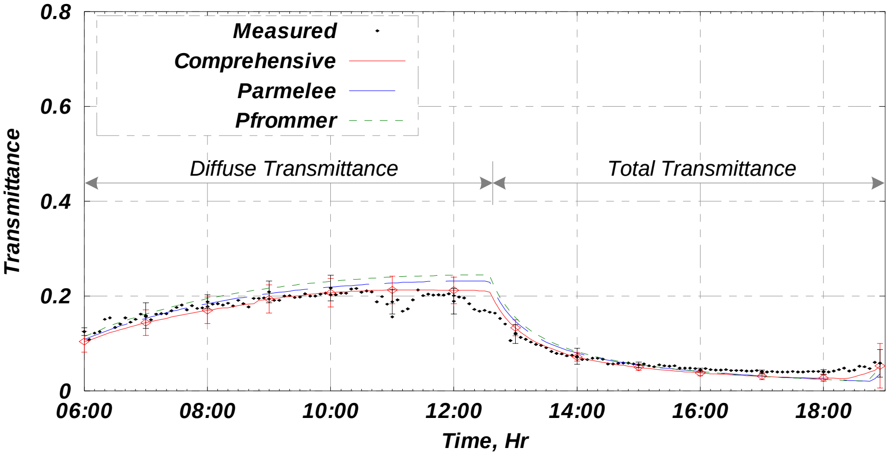

(b) 1 in Vinyl Black - Horizontally Opened

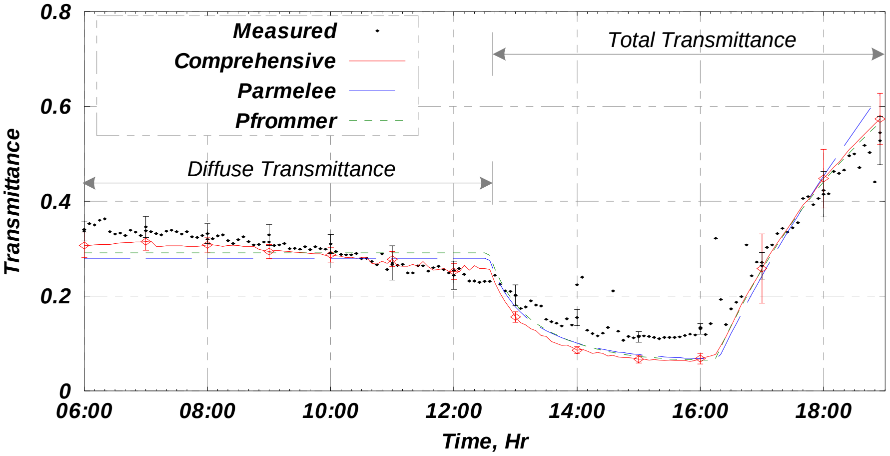

(c) 1 in Vinyl Black - Upward Opened

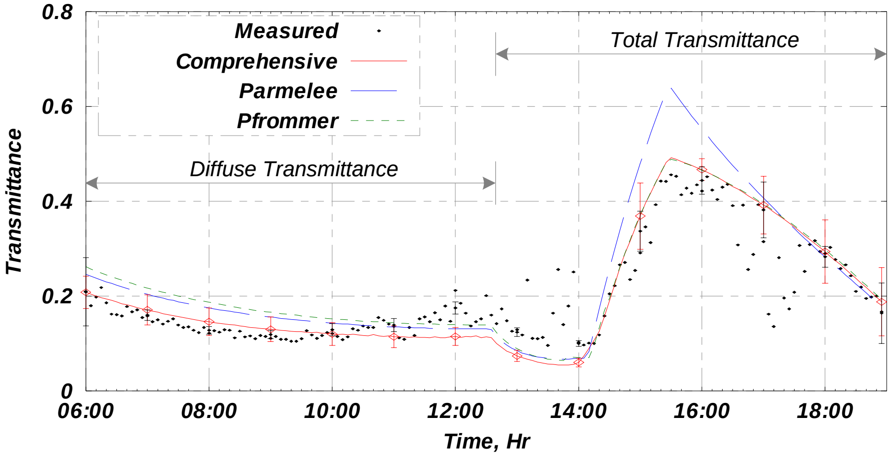

Figure 5-10 Calibrated Results for 1-in Vinyl Black Blind

As shown in Figures 5-9 and 5-10, the comprehensive blind model, which assumes 95% diffuse- and 5% specular-reflective slat surfaces, agrees quite well with measured data for both the 1-in vinyl white and 1-in vinyl black blinds. The good agreements suggest that slat surfaces of both blinds behave more like diffuse reflectors. To investigate a blind with slats likely behaving more like specular reflectors or quasi-specular reflectors, Figure 5-11 compares predicted calibrated results with measured data for the 1-in vinyl silver blind with curved slats (Blind No. 3). As previously discussed, it is assumed that the 1-in silver blind with metallic and reflective coated slats has 50% diffuse- and 50% specular-reflective slat surfaces. As shown in Figure 5-11, the comprehensive blind model agrees fairly well with measured data. However, as shown in Figure 5-11a, the discrepancies between the measured total solar transmittance and results predicted by the comprehensive blind model as well as the other two models for the downward opened blind (after 4 p.m.) are noticeable. This indicates that none of the models predicts the solar transmittance due to reflections well although both the comprehensive blind model and the Pfrommer model assume partially diffuse- and partially specular-reflecting slat surfaces (both models do slightly better than the Parmelee model, which assumes purely diffuse-reflecting slat surfaces). The possible explanation is that the blind slats were custom painted for the experiments. As a result, the radiative characteristics on opposite sides of the blind slats could be different.

To investigate the effect of different radiative characteristics on different sides, Figure 5-12 compares measured data with results predicted by the comprehensive blind model using the front- and back-side specularity ratios of 0.4 and 0.8, respectively. As shown in Figure 5-12a, the comprehensive blind model substantially improves its agreement with the measured total solar transmittance. However, as shown in Figure 5-12c, the comprehensive blind model using different radiative characteristics on different sides does not agree well with measured total solar transmittance (worse than the prediction using the same radiative characteristics on different sides). These contradictory results demonstrate the usefulness of the measured data obtained by the in situ experimental method since it is not easy to ‘consistently’ adjust input parameters to match the predicted results to the in situ measured data. This means that the predicted results can be easily matched to either measured diffuse or total solar transmittance for a particular slat angle, but it is difficult to match the predicted results to both measured diffuse and total solar transmittance for all three slat angles. Further investigations are essential to provide a good explanation of the contradictions of the 1-in silver blind results.

In addition to the 1-in vinyl curved-slat blinds, Figure 5-13 compares predicted results with measured data for the 2-in vinyl white blind with curved slats (Blind No. 4) to investigate how the comprehensive blind model performs for the curved-slat blinds with different slat geometry. As illustrated, the comprehensive blind model agrees reasonably well with measured data for all slat angles. Like the 1-in vinyl blinds, the comprehensive blind model has slightly better agreements with measured diffuse solar transmittance than the other two models do. Similarly, the Parmelee model over-predicts the peak total solar transmittance for the upward opened blind although the over-prediction is not as significant as for the 1-in vinyl blinds due to the ratio of the slat radius to the slat width for the 2-in blind higher than the ratio for the 1-in blinds (the higher the ratio, the more similar the curved slats to the flat slats).

In addition to the curved-slat blinds, Figure 5-14 compares predicted results with measured data for the 1-in wood brown blind with flat slats (Blind No. 5). As shown, both the comprehensive blind model and the Parmelee model, which account for the slat thickness, tend to under-predict measured data whereas the Pfrommer model, which does not take into account the slat thickness, tends to over-predict measured data. The discrepancy between results predicted by the comprehensive blind model and measured data is mostly within the uncertainty ranges. The under-prediction of the comprehensive blind model for the 1-in flat-slat blind is therefore not significant.

(a) 1 in Vinyl Silver - Downward Opened

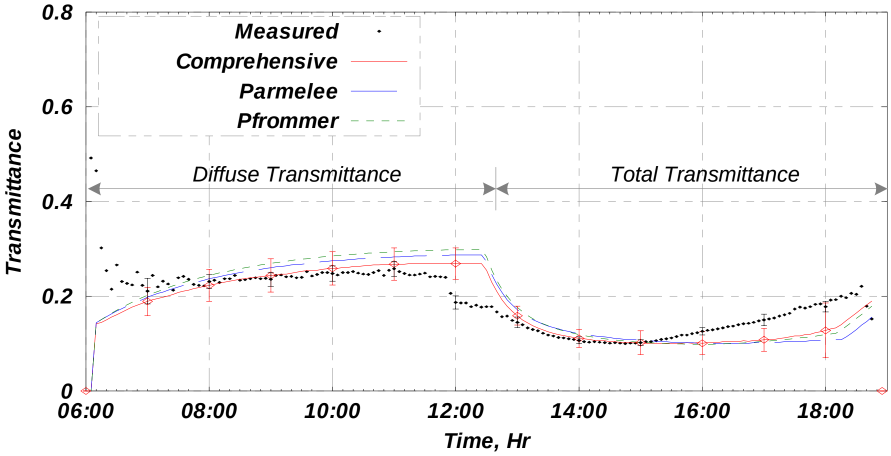

(b) 1 in Vinyl Silver - Horizontally Opened

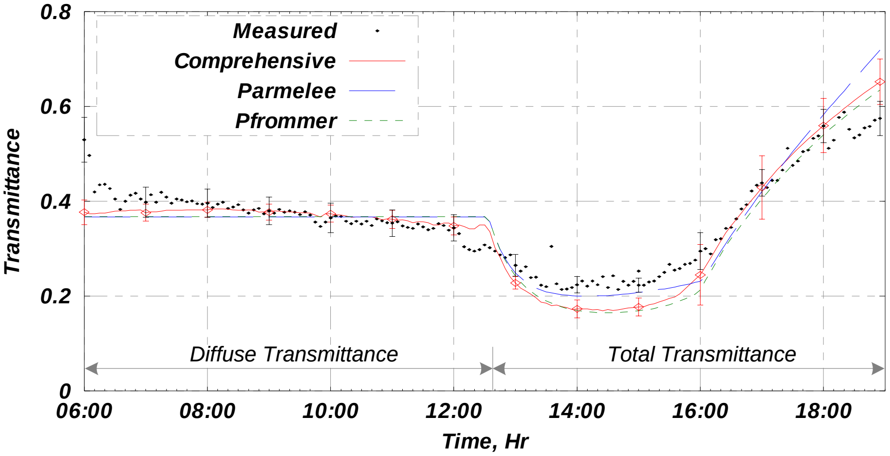

(c) 1 in Vinyl Silver - Upward Opened

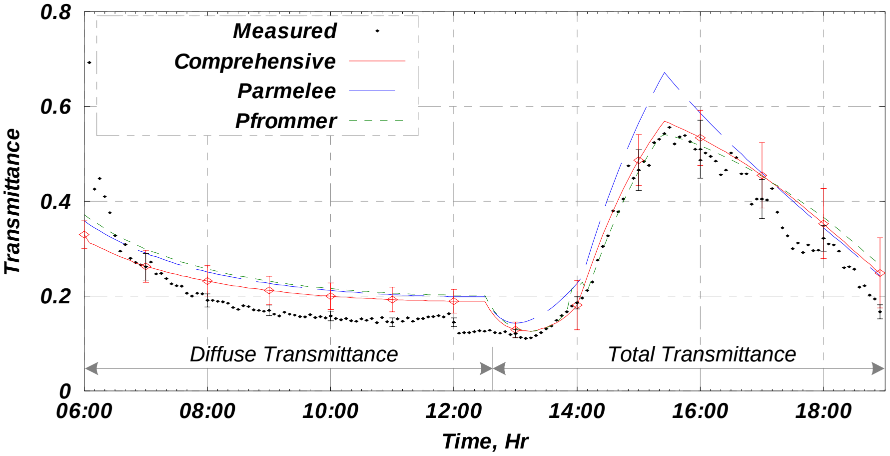

Figure 5-11 Calibrated Results for 1-in Vinyl Silver Blind

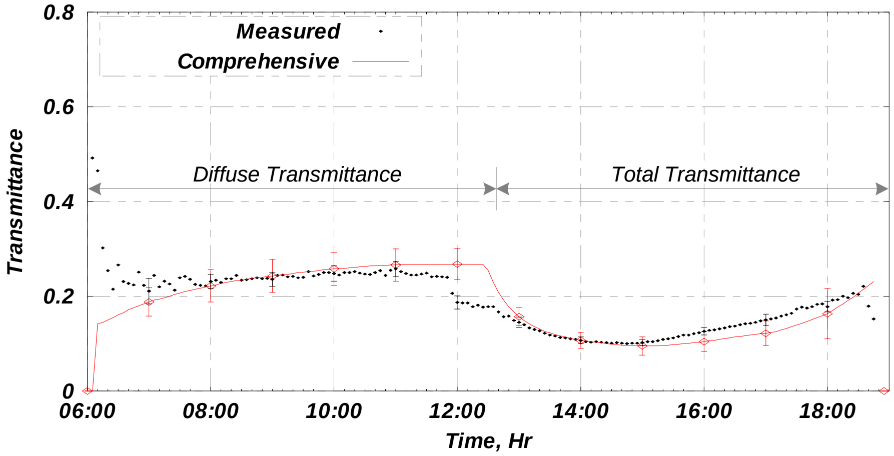

(a) 1 in Vinyl Silver - Downward Opened

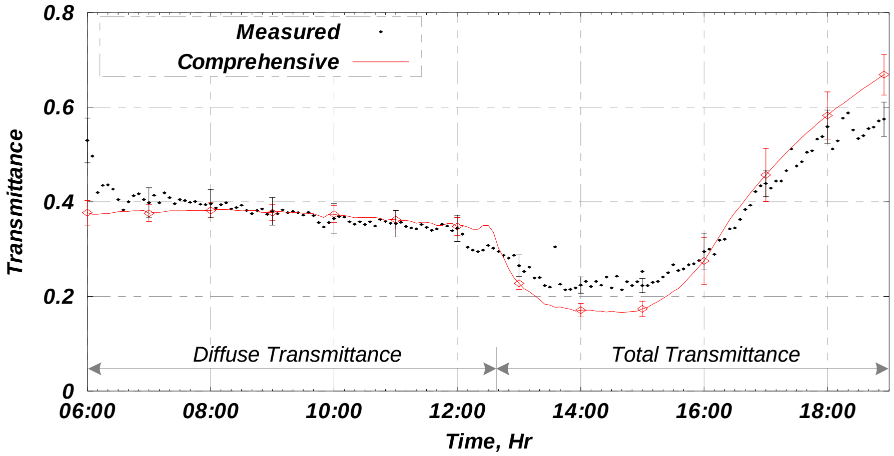

(b) 1 in Vinyl Silver - Horizontally Opened

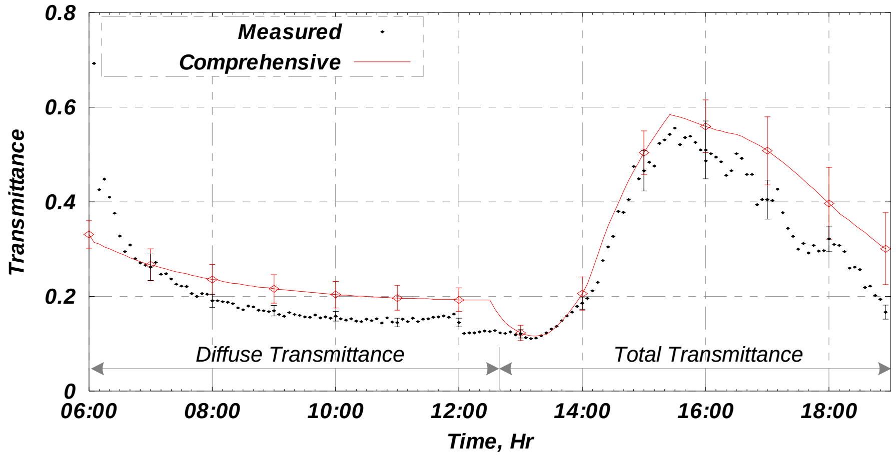

(c) 1 in Vinyl Silver - Upward Opened

Figure 5-12 Calibrated Results for 1-in Vinyl Silver Blind with Front- and Back-Side Slat Reflective Specularity Ratios of 0.40 and 0.80

(a) 2 in Vinyl White - Downward Opened

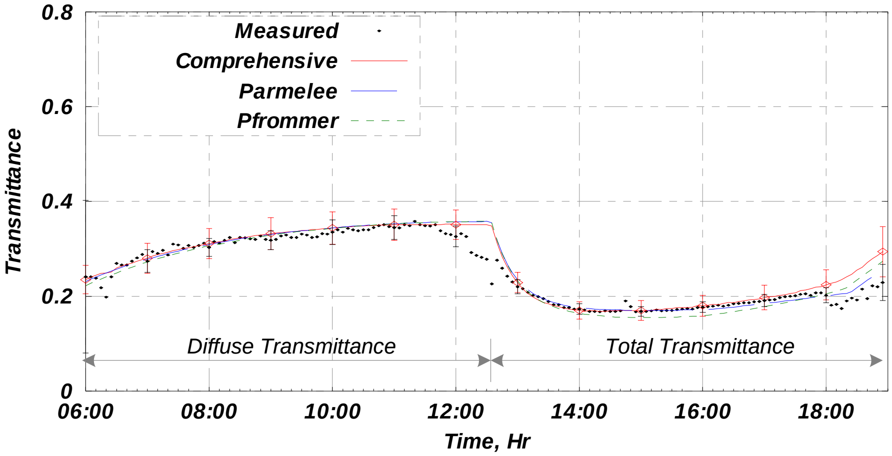

(b) 2 in Vinyl White - Horizontally Opened

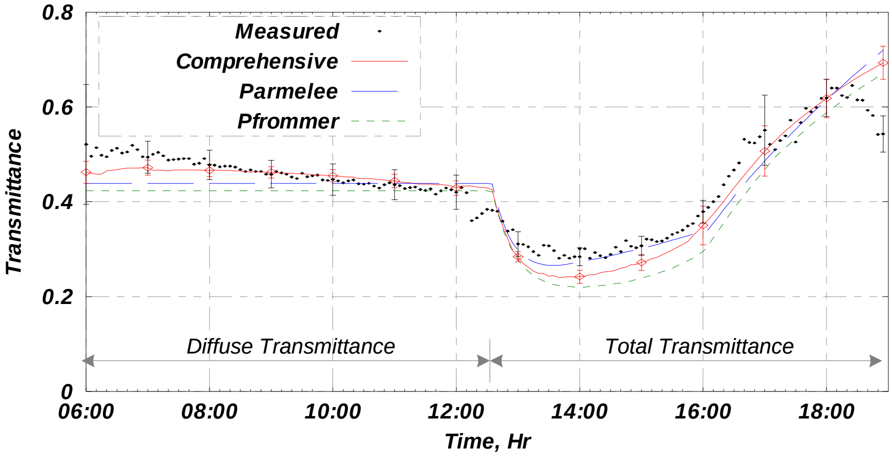

(c) 2 in Vinyl White - Upward Opened

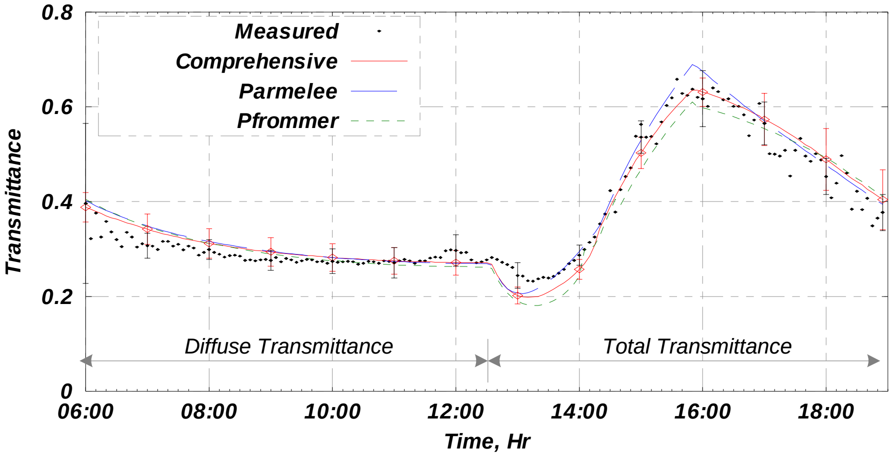

Figure 5-13 Calibrated Results for 2-in Vinyl White Blind

(a) 1 in Wood Brown - Downward Opened

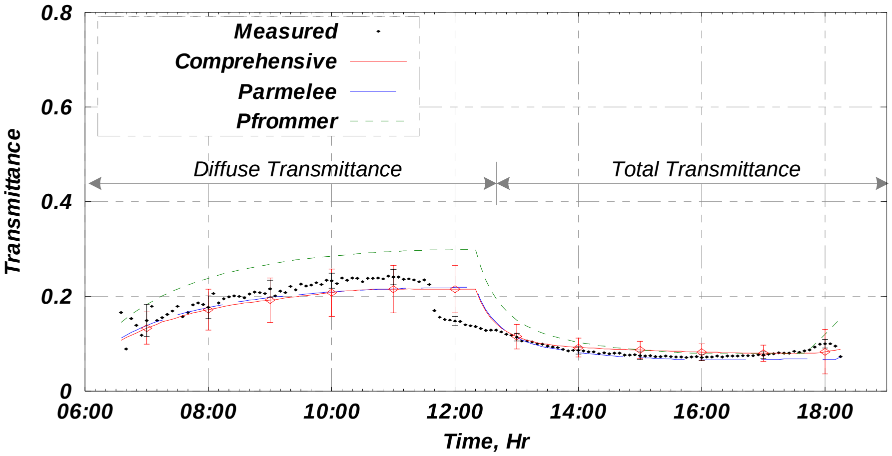

(b) 1 in Wood Brown - Horizontally Opened

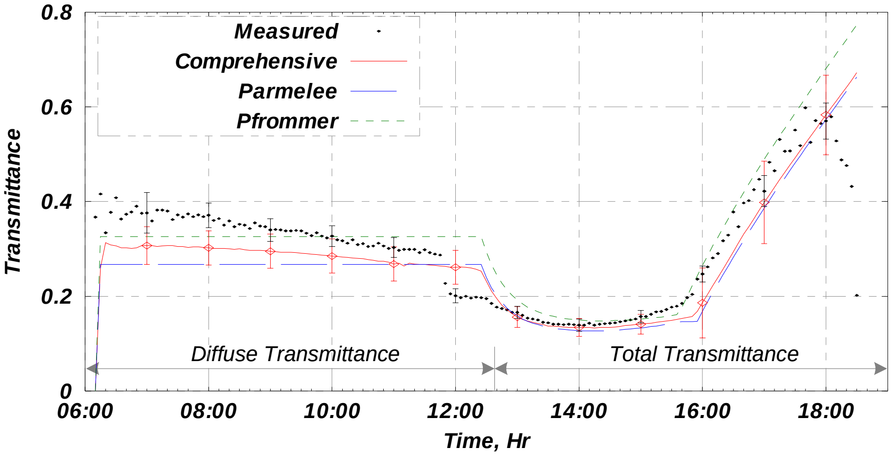

(c) 1 in Wood Brown - Upward Opened

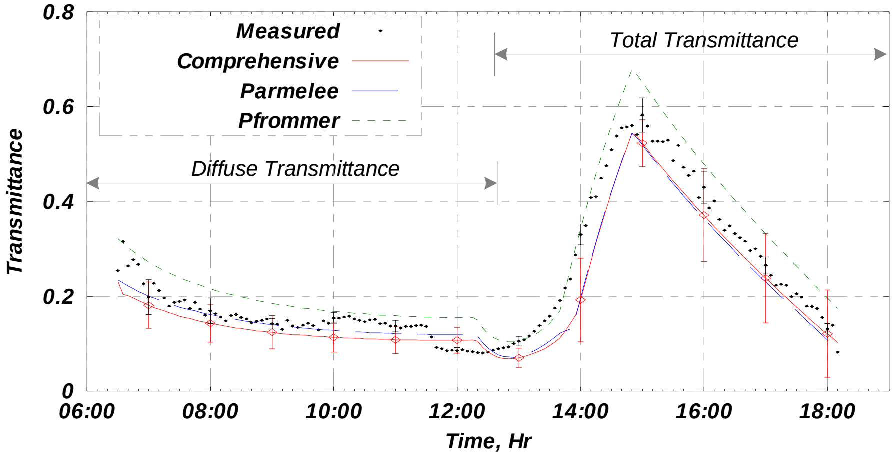

Figure 5-14 Calibrated Results for 1-in Wood Brown Blind

5.4 Conclusions

This chapter presents an in situ experimental method for measuring solar optical properties of the fenestration system containing a slat-type blind. In situ measurements of total solar transmittance were performed for various blind types and configurations. The total solar transmittance, defined as the ratio of total solar radiation incident on the fenestration system to total solar radiation transmitted through the fenestration system, is the primary metric commonly used to evaluate the optical blind model. The uncertainty associated with the in situ procedure is shown to be less than ±0.05 for all experimental tests. This chapter also demonstrates how to estimate slat solar reflectance of the blind assembly, an input required by the optical blind model, from field measurements.

In addition, the chapter illustrates the validity of the comprehensive blind model presented in the previous chapter by comparing the comprehensive blind model along with other existing models with measured data obtained by the in situ experimental method. Overall, the comprehensive blind model consistently agrees quite well with measured data for most tested blinds. The comprehensive blind model has slightly better agreements with measured diffuse solar transmittance than both the Parmelee and Pfrommer models do. For total solar transmittance, the comprehensive blind model shows better agreements with measured data than the Pfrommer model do. The comprehensive blind model agrees significantly better with measured total solar transmittance than the Parmelee model does when a large amount of direct solar radiation is directly transmitted without any reflections. However, the Parmelee model tends to do slightly better when a large amount of direct solar radiation is transmitted by reflections. For the 1-in vinyl silver blind with curved slats, the comprehensive blind model cannot consistently predict the measured data well. For instance, the model using the front- and back-side slat specular reflective ratios of 0.4 and 0.8 as inputs shows good agreements with measured total solar transmittance for the downward opened blind while it does not have good agreements for the upward opened blind. When the model uses the slat specular reflective ratios of 0.5 (both sides) as inputs, the model would then predict the measured data well for the upward opened blind but not for the downward opened blind. A further investigation is needed to explain these contradictory results for the 1-in vinyl silver blind with curved slats where its blind slats likely behave more like quasi-specular reflectors. Both the Parmelee and Pfrommer models do not have good agreements with measured total solar transmittance for the downward opened silver blind.

In summary, this chapter presents an in situ experimental method suitable for the validation and development of optical models for building simulation tools. The chapter then compares the newly developed optical blind model with measured data. The good agreements between predicted and measured results support the validity of the comprehensive blind model.

CHAPTER 6

DEVELOPMENT OF THERMAL MODELS AND A SUPPORTING EXPERIMENTAL METHOD FOR A FENESTRATION SYSTEM CONTAINING AN INTERIOR BLIND

6.1 Introduction

As discussed in Chapter 2, the thermal fenestration model implemented in the EnergyPlus building simulation program [DOE 2006] is currently the most fundamental model suitable for load calculations. The EnergyPlus thermal fenestration model is applicable for the HBM, but not for the RTSM. The model is basically based on two thermal models: one for glazing layers [Arasteh et al. 1989] and one for shading layers [ISO 2000; van Dijk and Goulding 1996]. According to van Dijk and Oversloot [2003], the thermal model for shading layers has not yet been validated. The model is quite complicated and requires various parameters including convection coefficients in the air gap between the glazing layers and the shading layer, a convection coefficient for convection from the (inside) shading layer to the room air, the air permeability between the air gap and the room (i.e., bulk convection), etc. At present, an experimental method that completely supports the model has not been developed. An acceptable experimental method would need to cover a range of realistic room airflow configurations and room surface temperatures in order to account for interactions between the fenestration system and the room. Consequently, the EnergyPlus thermal fenestration model is not supported by experimentally based convection correlations for the interior shading devices.

To enhance the thermal fenestration simulation, two new thermal fenestration models, applicable to a fenestration system containing an interior blind, have therefore been developed in this study: one for the HBM and one for the RTSM. Similar to the EnergyPlus fenestration model, the new model for the HBM is based on a one-dimensional multi-layer heat balance approach. However, the new model simplifies thermal calculations related to the shading device by combining the innermost glazing layer and the interior blind layer into a single layer. The new model requires two additional thermal parameters including the equivalent inside convection coefficient, which is defined at the inside surface of the combined layer, and the equivalent thermal conductance of the combined layers. These two parameters must be determined experimentally. Consequently, an experimental method has also been developed to support the new model for the HBM.

The model for the RTSM is not completely new but has not been clearly described in the literature in the context of building load and energy calculations. The model is based on the solar-thermal separation concept proposed by Klems et al. [Klems et al. 1995; Klems and Kelly 1996; Klems et al. 1996; Klems and Warner 1997]. The model for the RTSM includes both the fenestration heat gain calculation and the heat gain-to-cooling load conversion calculation. The model requires various input parameters including total solar transmittances, layer-specific solar absorptances, layer-specific inward flowing fractions, total thermal resistance, and radiative/convective splits. Optical models can be used to obtain the solar transmittances and absorptances whereas the thermal model for the HBM can be used to obtain the inward flowing fractions and the thermal resistance. The experimental method developed to support the thermal fenestration model for the HBM can be used to obtain the radiative/convective splits of the absorbed solar heat gain and the conduction heat gain. It is worth noting that the total electrical power applied to the window and the blind for the proposed experimental method simulates the total fenestration heat gain excluding the transmitted solar heat gain (i.e., only the sum of the absorbed solar heat gain and the conduction heat gain). Therefore, the radiative/convective splits of the absorbed solar heat gain and the conduction heat gain are essentially assumed to be the same.

In the current study, a limited number of experiments were performed to illustrate the feasibility of supporting the thermal models with experimental data and to investigate the sensitivity of the thermal parameters required by the thermal models. A comprehensive study covering full range of room boundary conditions is essential to the development of the empirical correlations, but is beyond the scope of this investigation. This means that the newly developed thermal models presented here are not yet ready to be used since the development of empirical correlations for thermal parameters required by the thermal model for the HBM is needed so that the ‘complete’ thermal model for the HBM can then be used to generate various thermal parameters required by the thermal model for the RTSM.

In the following section, the thermal model for the HBM is presented. Then, the thermal model for the RTSM is provided. Next, a calculation procedure (used in the thermal model for the HBM) is given to determine thermal parameters (i.e., the inward flowing fractions and the thermal resistance) required by the model for the RTSM. Then, the experimental method is presented. Finally, suggestions for future thermal model studies are provided.

6.2 Thermal Fenestration Model for HBM

6.2.1 Model Overview

The thermal fenestration model suitable for the HBM, referred to here as the HB thermal fenestration model, is based on the one-dimensional multi-layer heat balance approach. The HB thermal fenestration model directly performs an energy balance at each surface of the individual layers of the fenestration system. The HB thermal fenestration model simultaneously considers all three modes of heat transfer. The model assumes that overall energy flow through the fenestration system is perpendicular to the plane of the system and is one-dimensional. The model also assumes that the glazing layer is opaque to longwave radiation.[1] The model treats the glazing layers, except the innermost glazing layer, fundamentally the same as the EnergyPlus thermal fenestration model for a fenestration system without shading devices [DOE 2006; Winkelmann 2001]. However, for a fenestration system containing an interior blind, the model treats the innermost glazing layer and the blind layer as a single layer. Figure 6-1 conceptually illustrates the HB thermal fenestration model for the fenestration system with the interior blind. The left hand side figure shows an actual fenestration system consisting of *L* glazing layers and an interior blind layer while the right hand side figure shows a modeled fenestration system consisting of *L-1* glazing layers and a combined glazing and blind layer.

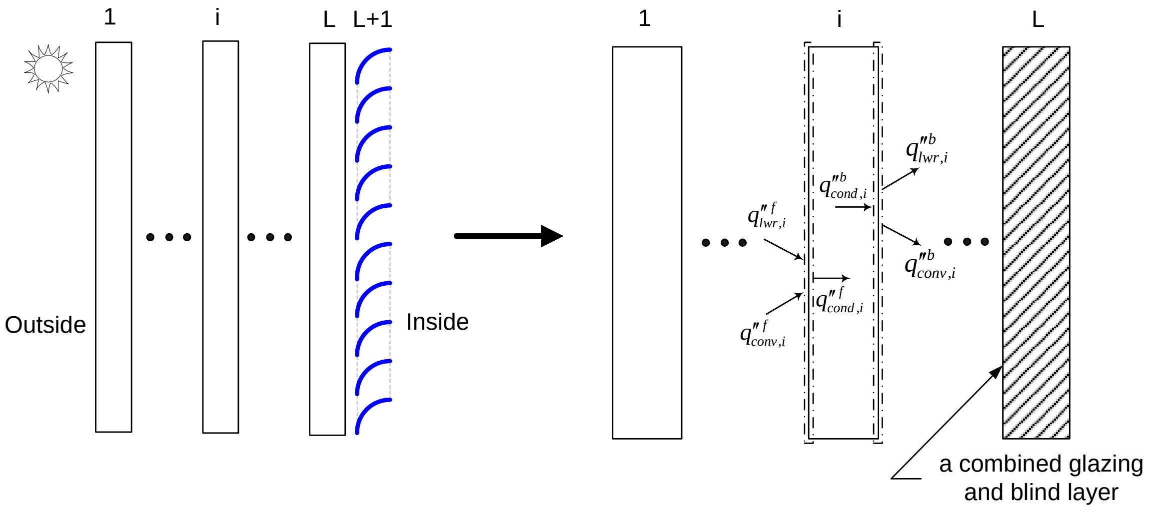

(a) actual fenestration system

(b) modeled fenestration system

Figure 6-1 Illustration of the HB thermal fenestration model for a Fenestration System Containing an Interior Blind

---

[1] According to Winkelmann [2001], this assumption is valid for most glass products but may not be good for thin plastic suspended films. Therefore, the heat balance equations should be modified for suspended films.

As shown in Figure 6-1b, the heat balances on the front and back surfaces of each individual layer (i.e., layer *i*) can simply be given as follows:

$$q''^{f}_{cond,i} = q''^{f}_{lwr,i} + q''^{f}_{conv,i} \tag{6-1}$$

$$q''^{b}_{cond,i} = q''^{b}_{lwr,i} + q''^{b}_{conv,i} \tag{6-2}$$

where q''_{cond} = net (conduction) heat flux to/from the surface (Btu/h·ft², W/m²),

q''_{conv} = convection heat exchange with adjacent air or surface (Btu/h·ft², W/m²), and

q''_{lwr} = net longwave radiation exchange with adjacent surface(s) or surroundings (Btu/h·ft², W/m²).

The superscript '*f*' refers to the (front) surface of each particular layer closest to the outside while the superscript '*b*' refers to the (back) surface of the layer closest to the inside. The subscript '*i*' refers to the i^{th} layer of the fenestration system. The conduction, convection, and longwave radiation terms can be expressed as a function of surface temperatures as discussed in the following sections. It should be noted that the absorbed solar radiation is included in the conduction terms.

It is worth mentioning that the HB thermal fenestration model presented in this chapter is only applied to the glazing area of the fenestration system through which solar radiation can be transmitted. The window frame, which is typically considered as a part of the fenestration system, can be handled by existing thermal models, such as the EnergyPlus thermal calculations for the window frame and divider [DOE 2006].

To estimate building thermal loads in the HBM, surface temperatures must be solved first. The HB thermal fenestration model described in this section must be used in conjunction with heat balance calculations for opaque surfaces to find the surface temperatures of each layer of the fenestration system as well as the surface temperatures of other opaque surfaces. The HBM and its treatment of opaque surfaces are described elsewhere [Liesen and Pedersen 1997; McClellan and Pedersen 1997; Pedersen et al. 1997; Pedersen et al. 1998]. Suggestions for the model implementation in the HBM are discussed in Section 6.6.2. In the following sections, calculations for the conduction, convection, and longwave radiation terms shown in Equations (6-1) and (6-2) for each particular layer of the fenestration system containing an interior blind are described in detail.

6.2.2 Calculations for Outermost Layer (Layer *1*)

Calculations identical to those used for the outside heat balance of an opaque surface can be employed to determine the longwave radiation and convection terms for the front surface of the outermost fenestration layer. These equations are given by McClellan and Pedersen [1997] as follows:

$$q''^{f}_{lwr,1} \quad = \quad \varepsilon_1^f \cdot \sigma \cdot \left(T^4_{a,out} - T^{f\,4}_{s,1} \right) + \varepsilon_1^f \cdot \sigma \cdot \left[F_{sky} (T^4_{sky} - T^4_{a,out}) \; + \; F_g (T^4_g - T^4_{a,out}) \right] \tag{6-3}$$

$$q''^{f}_{conv,1} \quad = \quad h_{c,out} \cdot \left(T_{a,out} - T^f_{s,1} \right) \tag{6-4}$$

where ε = longwave emittance,

σ = Stefan-Boltzmann constant (0.1714×10^{-8} Btu/h·ft²·°R^4, 5.669×10^{-8} W/m²·K^4),

$T_{a,out}$ = outdoor air (dry bulb) temperature (°R, K),

T_s = surface temperature (°R, K),

F_{sky} = view factor of surface to sky,

T_{sky} = sky temperature (°R, K),

F_g = view factor of surface to ground,

T_g = ground surface temperature (°R, K), and

$h_{c,out}$ = convective heat transfer coefficient at an outside surface (Btu/h·ft²·°F, W/m²·K).

McClellan and Pedersen [1997] discuss detailed calculations of Equations (6-3) and (6-4) including several models for estimating the sky temperature as well as the outside convective heat transfer coefficient. It is worth noting that all convective heat transfer coefficients used in the HB thermal fenestration model are 'average' heat transfer coefficients, not 'local' heat transfer coefficients.

For the back surface of the outermost fenestration layer, the longwave radiation term can simply be calculated using a net-radiation equation for infinite parallel plates [Incropera and Dewitt 2002] as:

$$q''^{b}_{lwr,1} = \frac{\varepsilon_1^b \cdot \varepsilon_2^f}{1-\left(1-\varepsilon_1^b\right)\left(1-\varepsilon_2^f\right)} \cdot \sigma \cdot \left({T_{s,1}^{b}}^4 - {T_{s,2}^{f}}^4\right) \tag{6-5}$$

The convection term can be determined based on the surface-to-surface convective heat transfer coefficient as:

$$q''^{b}_{conv,1} = h_{c,1-2} \cdot \left(T_{s,1}^b - T_{s,2}^f\right) \tag{6-6}$$

where $h_{c,1-2}$ = surface-to-surface convective heat transfer coefficient between surface 1 and surface 2 (Btu/h·ft²·°F, W/m²·K).

Existing natural convection correlations for the cavity between glazing layers [ISO 2000] can be utilized to estimate the surface-to-surface convective heat transfer coefficient.

Assuming that (1) shortwave radiation (including solar and shortwave from lights) is absorbed uniformly through the thickness of the glazing layer, and (2) thermal storage of the glazing layer is negligible, the conduction terms can be calculated as:

$$q''^{f}_{cond,1} = c_1 \cdot \left(T^{f}_{s,1} - T^{b}_{s,1}\right) - \frac{q''_{swr,1}}{2} \tag{6-7}$$

$$q''^{b}_{cond,1} = c_1 \cdot \left(T^{f}_{s,1} - T^{b}_{s,1}\right) + \frac{q''_{swr,1}}{2} \tag{6-8}$$

where c = thermal conductance of the fenestration layer (Btu/h·ft²·°F, W/m²·K), and

q''_{swr} = shortwave radiation absorbed by the fenestration layer (Btu/h·ft², W/m²).

The thermal conductance of the glazing layer can be calculated as the ratio of the glazing thermal conductivity to the glazing layer thickness. The absorbed shortwave radiation can be determined by Equation (6-23) given in a following section. Wright [1998] illustrates the derivation of the conduction terms (i.e., Equations (6-7) and (6-8)) and also shows an equation to calculate the temperature distribution (along the thickness) within the glazing layer. The derivation of the conduction terms is also given in Appendix E. It is worth mentioning that the shortwave radiation term includes solar radiation incident from the outside, reflected radiation (of the transmitted solar radiation) from the inside as well as shortwave radiation from lights.

6.2.3 Calculations for Between-Pane Layer (Layer *i*)

For the i^{th} glazing layer ($i = 2$ to L-1), which is neither the outermost nor the innermost glazing layer, calculations similar to those used for the back surface of the outermost fenestration layer can be utilized. The following equations summarize the required calculation terms.

$$q''^{f}_{lwr,i} = \frac{\varepsilon^{b}_{i-1} \cdot \varepsilon^{f}_{i}}{1 - \left(1 - \varepsilon^{b}_{i-1}\right)\left(1 - \varepsilon^{f}_{i}\right)} \cdot \sigma \cdot \left({T^{b}_{s,i-1}}^{4} - {T^{f}_{s,i}}^{4}\right) \tag{6-9}$$

$$q''^{f}_{conv,i} = h_{c,(i-1)-i} \cdot \left(T^{b}_{s,i-1} - T^{f}_{s,i}\right) \tag{6-10}$$

$$q''^{f}_{cond,i} = c_i \cdot \left(T^{f}_{s,i} - T^{b}_{s,i}\right) - \frac{q''_{swr,i}}{2} \tag{6-11}$$

$$q''^{b}_{lwr,i} = \frac{\varepsilon_i^b \cdot \varepsilon_{i+1}^f}{1-\left(1-\varepsilon_i^b\right)\left(1-\varepsilon_{i+1}^f\right)} \cdot \sigma \cdot \left({T_{s,i}^b}^4 - {T_{s,i+1}^f}^4\right) \qquad (6\text{-}12)$$

$$q''^{b}_{conv,i} = h_{c,i-(i+1)} \cdot \left(T_{s,i}^b - T_{s,i+1}^f\right) \qquad (6\text{-}13)$$

$$q''^{b}_{cond,i} = c_i \cdot \left(T_{s,i}^f - T_{s,i}^b\right) + \frac{q''_{swr,i}}{2} \qquad (6\text{-}14)$$

6.2.4 Calculations for Combined Glazing and Blind Layer (Layer *L*)

As previously mentioned, the HB thermal fenestration model treats the innermost glazing layer and the blind layer as a single layer. The (real) front surface of the innermost glazing layer represents the front surface of the combined glazing and blind layer whereas a fictitious surface at a plane parallel to the interior blind represents the back surface of the combined layer.

For the front surface of the combined layer, calculations similar to those used for the i^{th} glazing layer can be employed to estimate the longwave and convection terms as follows:

$$q''^{f}_{lwr,L} = \frac{\varepsilon_{L-1}^b \cdot \varepsilon_L^f}{1-\left(1-\varepsilon_{L-1}^b\right)\left(1-\varepsilon_L^f\right)} \cdot \sigma \cdot \left({T_{s,L-1}^b}^4 - {T_{s,L}^f}^4\right) \qquad (6\text{-}15)$$

$$q''^{f}_{conv,L} = h_{c,(L-1)-L} \cdot \left(T_{s,L-1}^b - T_{s,L}^f\right) \qquad (6\text{-}16)$$

For the (fictitious) back surface of the combined layer, the longwave radiation term includes the net radiation exchange between the fenestration system and other room surfaces, and the total longwave radiation from internal heat sources. Therefore, the longwave radiation term can be determined as:

$$q''^{b}_{lwr,L} = \frac{\sigma}{A_L} \sum_{j=1}^{M} \overline{S_L S_j} \cdot \left({T_{s,L}^b}^4 - {T_{s,j}}^4\right) - q''_{lwr,is} \qquad (6\text{-}17)$$

where M = total number of room surfaces,

A_L = (fictitious) inside surface area of the fenestration system (ft², m²),

$\overline{S_L S_j}$ = Hottel's total exchange area (ft², m²),

$T_{s,L}^{b}$ = equivalent temperature of the (fictitious) back surface of the combined layer (°R, K),

$T_{s,j}$ = temperature of room surface j (°R, K), and

$q''_{lwr,is}$ = total longwave radiation from internal heat sources (Btu/h·ft², W/m²).

Based on the experimentally determined convective transport from the combined layer, the convection term for the back surface of the combined layer can be formulated as:

$$q''^{b}_{conv,L} = h_{c,eqv,in} \cdot \left(T_{s,L}^{b} - T_{a,ref}\right) \tag{6-18}$$

where $h_{c,eqv,in}$ = equivalent convection coefficient of the (fictitious) back surface of the combined layer (Btu/h·ft²·°F, W/m²·K), and

$T_{a,ref}$ = reference air temperature (°R, K).

An experimental method presented in Section 6.5 is used to determine the equivalent convection coefficient of the back surface of the combined layer (i.e., $h_{c,eqv,in}$) for mixed and/or forced flow regimes. The reference air temperature is a subject of the experimental investigation.

By combining the innermost glazing layer and the interior blind into a single layer, the total heat transfer from the back (real) surface of the innermost glazing layer to the (imaginary) plane parallel to the interior blind can be modeled as the equivalent conduction heat transfer. All thermal interactions between the window and the blind (including convection and radiation) would be treated as the equivalent conduction heat transfer across the combined glazing and blind layer. The equivalent conduction model includes two homogeneous sub-layers having perfect thermal contact where the first sub-layer represents the innermost glazing layer and the second sub-layer represents the blind and the air gap between the glazing layer and the blind layer. The thermal conductance of the first sub-layer is calculated using thermo-physical properties of the glass (i.e., thermal conductivity and thickness) whereas the equivalent thermal conductance of the second sub-layer is experimentally determined using the proposed experimental method presented in Section 6.5.

The conduction terms of the combined layer can be calculated as:

$$q''^{f}_{cond,L} = \frac{c_L \cdot (c_L + c_{L+1} - 1)}{c_L + c_{L+1}} T^{f}_{s,L} - \frac{c_L \cdot c_{L+1}}{c_L + c_{L+1}} T^{b}_{s,L} - \frac{(c_L + c_{L+1} + 1)}{c_L + c_{L+1}} \frac{q''_{swr,L}}{2} \quad (6\text{-}19)$$

$$q''^{b}_{cond,L} = \frac{c_L \cdot c_{L+1}}{c_L + c_{L+1}} T^{f}_{s,L} - \frac{c_{L+1} \cdot (1 - c_L - c_{L+1})}{c_L + c_{L+1}} T^{b}_{s,L} + \frac{c_L}{c_L + c_{L+1}} \frac{q''_{swr,L}}{2} + q''_{swr,L+1} \quad (6\text{-}20)$$

where c_L = thermal conductance of the first sub-layer representing the glazing layer *L* (Btu/h·ft²·°F, W/m²·K),

c_{L+1} = equivalent thermal conductance of the second sub-layer representing the blind layer and the air gap between the glazing and blind layers (Btu/h·ft²·°F, W/m²·K),

$q''_{swr,L}$ = shortwave radiation absorbed by the glazing layer *L* (Btu/h·ft², W/m²), and

$q''_{swr,L+1}$ = shortwave radiation absorbed by the blind layer *L+1* (Btu/h·ft², W/m²).

The thermal conductance of the first sub-layer can simply be determined as the ratio of the glazing thermal conductivity to the glazing layer thickness. As previously mentioned, the experimental method presented in Section 6.5 is used to determine the equivalent thermal conductance of the second sub-layer (i.e., c_{L+1}). The derivation of the conduction terms (i.e., Equations (6-19) and (6-20)) and the conduction modeling assumptions are given in Appendix E.

By modeling the innermost glazing layer and the interior blind layer as a single layer, the HB thermal fenestration model relies on the proposed experimental method to provide the equivalent convection coefficient of the back surface of the combined layer and the equivalent thermal conductance within the combined layer (i.e., that of the second sub-layer representing the blind layer and the air gap between the glazing and blind layers). The modeling of the combined layer gives the HB thermal fenestration model two important advantages over the EnergyPlus thermal fenestration model. First, experimental measurements of the two thermal parameters required by the HB thermal fenestration model are feasible. As previously mentioned, no experimental method exists to measure thermal parameters required by the EnergyPlus thermal fenestration model (e.g., convection coefficients in the air gap between the glazing layers and the blind layer, the convection coefficient for convection from the interior blind to the room air, the bulk air convection (or the air permeability) between the air gap and the room, etc.). Second, the overall calculations are simplified (i.e., the calculations of the HB thermal fenestration model are simpler than the calculations of the EnergyPlus thermal fenestration model). The two experimentally determined thermal parameters required by the HB thermal fenestration model account for thermal interactions (including convection and radiation) between the window and the blind, thermal interactions between the window/air gap and the room, and thermal interactions between the blind and the room. Most of these thermal interactions are determined separately in the EnergyPlus thermal fenestration model.

6.2.5 Transmitted Solar Radiation

In this section, the calculation of transmitted solar radiation through the fenestration system is presented. Although the transmitted solar radiation is not directly involved in the heat balance calculations of the fenestration system, Fisher et al. [2002] showed that transmission of solar (and shortwave) radiation from inside to outside should be taken into account. Thus, the heat balance calculations for the fenestration system (i.e., a thermal fenestration model) should account for the reflections of transmitted solar radiation from other inside surfaces of the space.

The solar flux on the inside surface of the fenestration system may be determined by an internal solar distribution model in the HBM.

For modeling consistency with a typical internal solar distribution model, transmitted beam and diffuse solar radiation are treated separately. The beam solar radiation transmitted through the fenestration system ($q''_{tran-bm,sol}$) can be calculated by:

$$q''_{tran-bm,sol} = \left(\frac{A_{sunlit}}{A_{total}} \right) \cdot I_{bm} \cdot \tau^{sys}_{bm-bm} \tag{6-21}$$

where A_{sunlit} = sunlit area of the fenestration system,

A_{total} = total area of the fenestration system (not including frames and dividers),

I_{bm} = beam insolation on the outside surface of the fenestration system, and

τ^{sys}_{bm-bm} = system (overall) beam-to-beam transmittance of the fenestration system.

As shown, Equation (6-21) accounts for the effect of external shading devices, such as overhangs. The external shading device models are presented in the *ASHRAE Handbook - Fundamentals* [ASHRAE 2005] and discussed by McQuiston et al. [2005].

The diffuse solar radiation transmitted through the fenestration system ($q''_{tran-df,sol}$) can be calculated by:

$$q''_{tran-df,sol} = \left(\frac{A_{sunlit}}{A_{total}} \right) \cdot I_{bm} \cdot \tau^{sys}_{bm-df} + I_{sky-df} \cdot \tau^{sys}_{sky-df} + I_{gnd-df} \cdot \tau^{sys}_{gnd-df} \tag{6-22}$$

where I_{sky-df} = sky-diffuse insolation on the outside surface of the fenestration system,

I_{gnd-df} = ground-diffuse insolation on the outside surface of the fenestration system,

τ^{sys}_{bm-df} = system (overall) beam-to-diffuse transmittance of the fenestration system,

τ^{sys}_{sky-df} = system (overall) sky-diffuse transmittance of the fenestration system, and

τ^{sys}_{gnd-df} = system (overall) ground-diffuse transmittance of the fenestration system.

The above formulations explicitly indicate that direct solar radiation incident on the fenestration system can result in both transmitted beam and diffuse solar radiation. The two equations are applicable to fenestration systems with and without shading devices. For the fenestration system without shading devices, the system (overall) beam-to-diffuse transmittance becomes zero. Equation (6-22) also explicitly distinguishes the sky and the ground as different sources of diffuse solar radiation so that their effects can be taken into account more accurately. Specifically, the optical blind and fenestration models described in Chapter 4 and Appendices A to D can be used to estimate the system transmittances of the fenestration system containing a slat-type blind.

6.2.6 Absorbed Solar Radiation

As previously discussed, the HB thermal fenestration model accounts for both the solar radiation incident from the outside and the shortwave radiation incident from the inside (including transmitted solar radiation from other fenestration systems, reflected solar radiation and shortwave radiation from lights). In this section, the calculations of the shortwave radiation absorbed by fenestration layers are presented. Using layer-specific system absorptances predicted by the optical fenestration model described in Appendix D, the shortwave radiation term for a fenestration layer *i* (*i* = 1 to *L+1*) can be calculated by:

$$q''_{swr,i} = \left(\frac{A_{sunlit,f}}{A_{total}}\right) \cdot I_{bm} \cdot \alpha^{sys,f}_{bm-df,i} + \left(\frac{A_{sunlit,b}}{A_{total}}\right) \cdot q''_{bm,swr,is} \cdot \alpha^{sys,b}_{bm-df,i}$$

$$+ I_{sky-df} \cdot \alpha^{sys,f}_{sky-df,i} + I_{gnd-df} \cdot \alpha^{sys,f}_{gnd-df,i} + q''_{df,swr,is} \cdot \alpha^{sys,b}_{df,i} \qquad (6\text{-}23)$$

where $q''_{bm,swr,is}$ = net shortwave radiation from inside the room that behaves like beam solar radiation (i.e., transmitted beam solar radiation from other windows),

$q''_{df,swr,is}$ = net shortwave radiation from inside the room that behaves like diffuse solar radiation (i.e., shortwave radiation from lights, reflected solar radiation from other surfaces, and transmitted diffuse solar radiation from other windows),

$\alpha^{sys,f}_{bm-df,i}$ = system (overall) absorptance due to beam solar radiation from the outside ('front') for fenestration layer *i*,

$\alpha^{sys,b}_{bm-df,i}$ = system (overall) absorptance due to (beam) shortwave radiation from the inside ('back') for fenestration layer *i*,

$\alpha^{sys,f}_{sky-df,i}$ = system (overall) absorptance due to sky-diffuse solar radiation from the outside for fenestration layer *i*,

$\alpha^{sys,f}_{gnd-df,i}$ = system (overall) absorptance due to ground-diffuse solar radiation from the outside for fenestration layer *i*, and

$\alpha^{sys,b}_{df,i}$ = system (overall) absorptance due to (hemispherical diffuse) shortwave radiation from the inside for fenestration layer *i*.

Equation (6-23) can be used to determine the shortwave radiation term for either the glazing layer or the blind layer with appropriate system (overall) absorptances for that particular layer.

6.3 Thermal Fenestration Model for RTSM

6.3.1 Model Overview

The thermal fenestration model suitable for the RTSM, referred to here as the RTS thermal fenestration model, is based on the solar-thermal separation concept proposed by Klems et al. [1995] such that the inward flowing fractions of solar radiation absorbed by the fenestration layers are purely thermal properties (i.e., independent of solar-optical properties). The RTS thermal fenestration model requires various input parameters including solar transmittances of the fenestration system, solar absorptances of fenestration layers, inward flowing fractions of fenestration layers, total thermal resistance of the fenestration system, and the radiative/convective split of the absorbed solar heat gain of the fenestration system.

According to Pedersen et al. [Pedersen et al. 1998; Spitler et al. 1997], the computational procedure of the RTSM can be divided into two steps. In the first step, various instantaneous heat gains are calculated and then divided into radiative and convective portions according their radiative/convective split. In the second step, the convective portion of the heat gains is summed to give a cooling load due to convective heat gains. The radiative part of the heat gains is converted into a cooling load using radiant time factors. The total cooling load is the summation of the cooling loads due to both convective and radiative heat gains. The full description of the RTSM and its treatment of various heat gains are discussed in the literature [Pedersen et al. 1998; Spitler et al. 1997].

The RTS thermal fenestration model is utilized in the first step by the RTSM to predict fenestration heat gains and their convective and radiative portions. In the next section, fenestration heat gains are described. Then, the radiative/convective split of each particular heat gain is discussed. Finally, the conversion of the radiative portion of fenestration heat gains into cooling loads is also discussed.

6.3.2 Fenestration Heat Gains

Fenestration heat gains include both solar and conduction heat gains. For the correct application of the radiant time factors, beam and diffuse components of solar radiation are treated separately. For the correct application of the radiative/convective split, transmitted and absorbed components of solar radiation are treated separately. Consequently, fenestration heat gains are divided into four components: 1) transmitted beam solar heat gain, 2) transmitted diffuse solar heat gain, 3) absorbed solar heat gain, and 4) conduction heat gain.

The transmitted beam solar heat gain is defined as the transmitted solar heat transfer rate where the transmitted radiation behaves like beam solar radiation. Therefore, the transmitted beam solar heat gain is the beam portion of the transmitted solar gain due to beam insolation. The transmitted beam solar heat gain can thus be calculated by multiplying the total fenestration area (A_{total}) by the transmitted beam solar flux ($q''_{tran-bm,sol}$) determined according to Equation (6-21).

The transmitted diffuse solar heat gain is defined as the transmitted solar heat transfer rate where the transmitted radiation behaves like diffuse solar radiation. Therefore, the transmitted diffuse solar heat gain includes the diffuse portion of the transmitted solar gain due to beam insolation and the transmitted solar gain due to diffuse insolation. The transmitted diffuse solar heat gain can thus be calculated by multiplying the fenestration area by the transmitted diffuse solar flux ($q''_{tran-df,sol}$) determined according to Equation (6-22).

The absorbed solar heat gain is defined as the inward flowing heat transfer rate of total insolation absorbed by the fenestration system's layers. The absorbed solar heat gain ($\dot{q}_{abs,sol}$) can be calculated by:

$$\dot{q}_{abs,sol} = \sum_{i=1}^{n} Ni_i \cdot \left[\left(I_{bm} \cdot \alpha^{sys,f}_{bm-df,i} \cdot A_{sunlit} \right) + \left(I_{sky-df} \cdot \alpha^{sys,f}_{sky-df,i} + I_{gnd-df} \cdot \alpha^{sys,f}_{gnd-df,i} \right) \cdot A_{total} \right] \quad (6\text{-}24)$$

where n = number of layers of the fenestration system,

Ni_i = inward flowing fraction for layer *i*,

$\alpha^{sys,f}_{bm-df,i}$ = system (overall) absorptance due to beam insolation for layer *i*,

$\alpha^{sys,f}_{sky-df,i}$ = system (overall) absorptance due to sky-diffuse insolation for layer *i*, and

$\alpha^{sys,f}_{gnd-df,i}$ = system (overall) absorptance due to ground-diffuse insolation for layer *i*.

Unlike the HB thermal fenestration model, the RTS thermal fenestration model neglects shortwave radiation incident on the fenestration system from the inside due to an inherent assumption in the RTSM (i.e., the adiabatic zone assumption used to generate the radiant time factors).

The conduction heat gain is defined as the conduction heat transfer rate due to the outdoor and indoor temperature difference. Because the fenestration system usually consists of very thin layers of materials, the thermal storage effect can typically be neglected and the heat conduction through the fenestration system can commonly be assumed to be steady state. Therefore, the conduction heat gain ($\dot{q}_{cond}$) can be calculated by:

$$\dot{q}_{cond} = \frac{(T_{a,o} - T_{a,i})}{R_{fs,tot}} \cdot A_{total} \tag{6-25}$$

where $T_{a,o}$ = outside (ambient) air temperature,

$T_{a,i}$ = inside (room) air temperature, and

$R_{fs,tot}$ = total thermal resistance of the fenestration system.

In order to calculate the fenestration heat gains, both optical properties (i.e., transmittances and absorptances) and thermal properties (i.e., inward flowing fractions and thermal resistance) are needed. Optical models described in Chapter 4 and Appendices A to D can be used to obtain the optical properties. The HB thermal fenestration model can be utilized to generate the thermal properties. Section 6.4 describes a calculation procedure that utilizes the HB thermal fenestration model to obtain the inward flowing fractions and the total thermal resistance required by the RTS thermal fenestration model.

6.3.3 Radiative/Convective Split

The radiative/convective split of fenestration heat gains is required by the RTSM. A 100% radiative/0% convective split is used for both transmitted beam and diffuse solar heat gains since both are totally radiative heat gains. The experimental method presented in Section 6.5 can be used to measure the radiative/convective split of both absorbed solar and conduction heat gains. As discussed in Section 6.5.2.2, the total electrical power applied to the window and the blind simulates the fenestration heat gain representing the sum of the absorbed solar heat gain and the conduction heat gain. Consequently, it is assumed that the radiative/convective splits of the absorbed solar heat gain and the conduction heat gain are the same. In other words, the measured radiative/convective split is applied to both the absorbed solar heat gain and the conduction heat gain.

6.3.4 Conversion of Radiant Fenestration Heat Gains into Cooling Loads

In the RTSM, two types of periodic room response factors, commonly referred to as the radiant time factors (RTF), are used to convert radiant heat gains into cooling loads. The Solar RTF is applied to the transmitted beam solar heat gain while the non-Solar RTF is applied to all other heat gains [Pedersen et al. 1998; Spitler et al. 1997]. The different applications of these two radiant time factors are due to internal radiative distribution assumptions used to generate them. For the Solar RTF, it is assumed that the radiative heat gain entering the space is all apportioned onto the floor. On the other hand, it is assumed that the radiative heat gain entering the zone is uniformly distributed (e.g. area-averaged distribution) over all internal zone surfaces. However, according to the ASHRAE Load Toolkit implementation [Pedersen et al. 2001], only a portion of the transmitted beam solar heat gain absorbed by the floor should be converted into cooling load by the Solar RTF . Like other heat gains, a portion of the transmitted beam solar heat gain reflected from the floor should be converted into cooling load by the non-Solar RTF. As recommended by McQuiston et al. [2005], the calculations in the RTSM can be greatly simplified by using a single set of the radiant time factors (i.e., using the non-Solar RTF). This simplification would results in a minimal inaccuracy for cases where the amount of the transmitted beam solar gain absorbed by the floor is insignificant or where the thermal response of the floor is similar to the thermal responses of other room surfaces.

6.4 Generating RTS Thermal Model Input Parameters

As previously discussed, the HB thermal fenestration model can be utilized to generate the inward flowing fractions and the total thermal resistance required by the RTS thermal fenestration model. The following sections describe calculations used to determine the inward flowing fractions and the total thermal resistance.

6.4.1 Total Thermal Resistance

The total thermal resistance of the fenestration system required by the RTS thermal fenestration model can be given by:

$$R_{fs,tot} = R_{out} + \sum_{i=1}^{L-1} R_{gap,i} + \sum_{i=1}^{L} R_{g,i} + R_{gb,L+1} + R_{in} \tag{6-26}$$

where R_{out} = outside air film thermal resistance (h·ft²·°F/ Btu, m²·K/ W),

R_{gap} = thermal resistance of a cavity between glazing layers (h·ft²·°F/ Btu, m²·K/ W),

R_g = thermal resistance of a glazing layer (h·ft²·°F/ Btu, m²·K/ W),

$R_{gb,L+1}$ = thermal resistance within the combined glazing and blind layer (h·ft²·°F/ Btu, m²·K/ W), and

R_{in} = inside air film thermal resistance (h·ft²·°F/ Btu, m²·K/ W).

Utilizing the HB thermal fenestration model, the thermal resistance of the cavity between glazing layers can be calculated by:

$$R_{gap,i} = \frac{T_{s,i}^{b} - T_{s,i+1}^{f}}{q''^{b}_{cond,i}} \tag{6-27}$$

The thermal resistance of the glazing layer can simply be determined as a reciprocal of the glazing thermal conductance (i.e., the ratio of the glazing layer thickness to the glazing thermal conductivity) as follows:

$$R_{g,i} = \frac{1}{c_i} = \frac{t_{g,i}}{k_{g,i}} \tag{6-28}$$

Likewise, the thermal resistance within the combined glazing and blind layer can be expressed as a reciprocal of the thermal conductance of the combined layer as follows:

$$R_{gb,L+1} = \frac{1}{c_{L+1}} \tag{6-29}$$

As previously mentioned, the experimental method described in this chapter is used to determine the thermal conductance within the combined layer (i.e., c_{L+1}).

The outside air film thermal resistance can be given by:

$$R_{out} = \frac{1}{h_{r,o} + h_{c,o}} \tag{6-30}$$

where $h_{r,o}$, $h_{c,o}$ = radiative and convective heat transfer coefficients at the outside surface (Btu/h·ft²·°F, W/m²·K).

The outside convective heat transfer coefficient can be determined by an existing convection correlation employed in the HB thermal fenestration model. Using the HB thermal fenestration model, the outside radiative heat transfer coefficient can be calculated by:

$$h_{r,o} = \frac{q''^{f}_{lwr,1}}{T_{a,o} - T^{f}_{s,1}} \tag{6-31}$$

Similarly, the inside air film thermal resistance can be given by:

$$R_{in} = \frac{1}{h_{r,i} + h_{c,i}} \tag{6-32}$$

where $h_{r,i}$, $h_{c,i}$ = radiative and convective heat transfer coefficients at the inside (fictitious) surface (Btu/h·ft²·°F, W/m²·K), respectively.

Utilizing the HB thermal fenestration model, the heat transfer coefficients at the inside surface can be calculated by:

$$h_{r,i} = \frac{q''^{b}_{lwr,L}}{T^{b}_{s,L} - T_{a,i}} \tag{6-33}$$

$$h_{c,i} = \frac{q''^{b}_{conv,L}}{T^{b}_{s,L} - T_{a,i}} \tag{6-34}$$

where $T_{a,i}$ = room air temperature (°R, K).

It is worth noting that the inside convective heat transfer coefficient described in this section (i.e., $h_{c,i}$) can be different from the equivalent inside convective heat transfer coefficient described in Section 6.2 (i.e., $h_{c,eff,in}$) if the reference air temperature used for $h_{c,eff,in}$ is not the room air temperature.

6.4.2 Inward Flowing Fractions

According to Wright [1998], the inward flowing fraction can be calculated as the ratio of the thermal resistance from the location of the absorbed solar radiation to the outdoor (air) side and the total (indoor/outdoor air) thermal resistance. Therefore, the inward flowing fractions can be given by:

$$Ni_1 = \frac{R_{out} + \frac{1}{2} R_{g,1}}{R_{fs,tot}} \quad \text{for outermost glazing layer} \qquad (6\text{-}35)$$

$$Ni_i = \frac{R_{out} + \sum_{j=1}^{i-1}\left(R_{gap,j} + R_{g,j}\right) + \frac{1}{2} R_{g,i}}{R_{fs,tot}} \quad \text{for glazing layer } i = 2 \text{ to } L \qquad (6\text{-}36)$$

$$Ni_{L+1} = \frac{R_{fs,tot} - R_{in}}{R_{fs,tot}} \quad \text{for interior blind layer} \qquad (6\text{-}37)$$

6.5 Experimental Method for Thermal Fenestration Model Parameters

This section describes an experimental method developed to support the thermal fenestration models discussed in previous sections. The experimental method is used to measure various thermal parameters required by the thermal fenestration models. These parameters include the equivalent inside convection coefficient of the inside (fictitious) surface of the combined innermost glazing and blind layer (i.e., $h_{c,eqv,in}$ in Equation (6-18)) and the equivalent thermal conductance within the combined glazing and blind layer (i.e., c_{L+1} in Equations (6-19) and (6-20)) for the HBM thermal fenestration model, and the radiative/convective splits of the absorbed solar heat gain and the conduction heat gain for the RTSM thermal fenestration model.

In the following section, an overview of the experimental method is given. Following the overview, the experimental calculation procedure is presented. Then, the demonstration of the proposed experimental method is discussed. The experimental facility and instrumentation as well as the uncertainty analysis are described in detail by Wilson [2007].

6.5.1 Technical Overview of Experimental Method

The experimental method for determining the thermal parameters required by the proposed thermal fenestration models is based on the measurement of the radiative heat gain from a fenestration test unit representing the fenestration system containing an interior blind at steady state. For load calculation purposes, it is desirable that experimental tests are performed in a full-scale room with a typical flow regime (e.g. air supplied through radial or slot ceiling diffusers). The fenestration test unit required by the proposed experimental method consists of a heated slat-type blind, an insulated heated flat plate representing the window, and a heated guard plate as shown in Figure 6-2. For the current study, all heated layers of the fenestration test unit were electrically heated. The guard plate is used to prevent heat loss from the back of the fenestration test unit to the outside so that the total electrical heat applied to the window and the blind simulates the total heat gain from the fenestration system to the room. For the HB fenestration model, the ratio of the total electrical power consumed by the window and the blind to the window surface area is equal to the surface heat flux at the inside (fictitious) surface of the fenestration system (i.e., $q''^{b}_{cond,L}$ in Equation (6-20)). For the RTS fenestration model, the total electrical power consumed by the window and the blind is equivalent to the sum of the absorbed solar heat gain and the conduction heat gain. Essentially, the guard plate is controlled according to the temperature of the window. Figure 6-2 illustrates an experimental configuration where the fenestration test unit is installed in a full-scale, well-instrumented, and well-controlled test room.

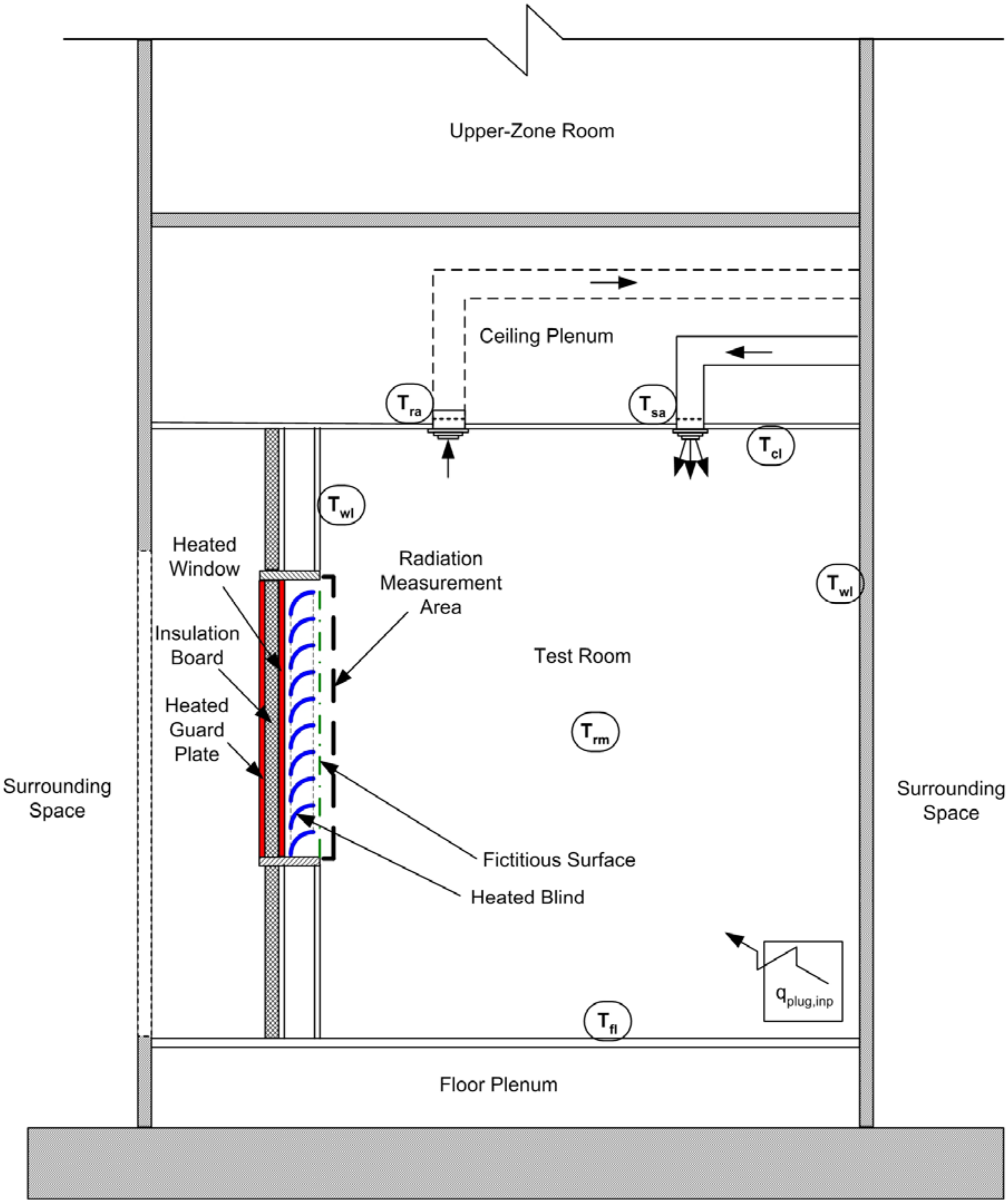

Figure 6-2 Experimental Configuration

Using the test room heat balance calculation, the steady-state error along with surface and air temperatures in the test room are used to determine if the test room has reached steady-state. Based on the energy conservation principle, the steady-state error is equal to the total heat gain in the room minus the sum of the room heat extraction rate and conduction heat losses through the test room surfaces. The total heat gain in the test room is equal to the sum of the ‘plug’ load and the total electrical power input used to heat the window and the blind layers of the fenestration test unit. The plug load is necessary to achieve ‘typical’ room operating conditions. It is worth noting that the test room heat balance calculation is not actually necessary for the proposed experimental method. However, according to previous research by the author [Chantrasrisalai and Fisher 2007], using the steady-state error along with temperatures in the test room is better than using only room temperatures to indicate the steady-state condition.

Once the test room has reached steady-state, the radiant heat gain from the fenestration test unit is measured using the scanning radiometer measurement technique developed by Hosni and Jones [Hosni et al. 1998; Jones et al. 1998]. Jones et al. [1998] show that the radiant heat gain from electrical equipment can be measured by scanning the entire hemisphere over the equipment with a net-radiometer. After scanning the hemisphere, the total radiant heat gain can then be determined by summing the product of the radiant fluxes and their associated area over the hemisphere. Ideally, due to the geometry of the fenestration system, a rectangular box covering the fenestration test unit is considered to be a more suitable scanning area than the hemisphere. The use of the rectangular box in place of the hemisphere is analogous to the use of the hemi-cube method [Cohen and Greenberg 1985; Rogers 1998] instead of the unit-sphere (or Nusselt Analog) method [Modest 2003] for calculating view factors between surfaces. However, due to physical and technical limitations, a parallel plane covering the fenestration test unit (about 1 inch (25 mm) from the fictitious plane representing the inside surface of the fenestration test unit) was used for the current study. Theoretically, the parallel plane measurement would result in about 5% lower measured radiant heat gain than the rectangular box measurement would. Due to a non-uniform radiant heat gain distribution (higher in the middle of the surface), the error due to using the parallel plane was expected to be lower than 5%. For calculation purposes, the uncertainty in the measured radiant heat gain due to using the parallel plane was estimated to be 5% of measured value.

Under steady-state conditions, the radiative/convective split required by the RTS thermal fenestration model can accurately be determined by measuring the total power input to the heated fenestration test unit (only the window and the blind) and the radiant heat gain from the fenestration test unit. The fraction that is transferred as thermal radiation can simply be calculated as the ratio of the radiant heat gain to the total power input. The convective fraction can then be calculated as one minus the radiative fraction. As previously mentioned, for the RTS thermal fenestration model, the total electrical heat applied to the window and the blind simulates the sum of the absorbed solar heat gain and the conduction heat gain (or the total fenestration heat gain excluding the transmitted solar heat gains). Consequently, it is assumed that the radiative/convective splits of the absorbed solar heat gain and the conduction heat gain are the same, meaning that the measured radiative/convective split is applied to both the absorbed solar heat gain and the conduction heat gain.

The determination of the equivalent inside convection coefficient (i.e., $h_{c,eqv,in}$ in Equation (6-18)) required by the HB thermal fenestration model is more complicated than the determination of the radiative/convective split. For the proposed experimental method, the measured equivalent inside convection coefficient represents a thermal parameter for the combined glazing and blind layer due to the fact that the measured convective heat gain include convective heat gains from both the window and the blind. This means that the equivalent convection coefficient measured by the proposed experimental method is only applicable to the HB thermal fenestration model presented in Section 6.2, but is not applicable to other multi-layer thermal fenestration models, such as the EnergyPlus thermal fenestration model [DOE 2006]. As discussed in Section 6.2, the HB thermal fenestration model treats the innermost glazing layer and the interior blind layer as a single layer. Therefore, an equivalent temperature representing the inside (fictitious) surface temperature of the combined glazing and blind layer is needed in order to determine the equivalent convection coefficient. To estimate the equivalent surface temperature, the technical approach utilizes Hottel's total exchange area method [Hottel and Sarofim 1967] with known net-radiation exchange between the fenestration test unit and other room surfaces, and known surface temperatures of other room surfaces. Therefore, the proposed experimental method requires that temperatures of all room inside surfaces besides the fenestration test unit are measured along with the measured radiant heat gain. After the equivalent surface temperature is determined, the equivalent convection coefficient can simply be determined using Newton's law of cooling with the measured convective heat gain and measured reference air temperature. The reference temperature is a subject of the investigation. For the current study, the (spatially averaged) room air temperature and the supply air temperature were investigated.

The determination of the equivalent thermal conductance within the combined glazing and blind layer (i.e., c_{L+1} in Equations (6-19) and (6-20)) required by the HB thermal fenestration model also needs the known equivalent surface temperature of the combined glazing and blind layer as well as the electrical power input to the heated window and the surface temperature of the heated window. As discussed in Section 6.2 and Appendix E, for conduction modeling purposes, the combined glazing and blind layer is modeled as two homogeneous sub-layers having perfect thermal contact where the first sub-layer represents the innermost glazing layer and the second sub-layer represents the blind and the air in the gap between the glazing and the blind layers. The electrical power applied to the window of the fenestration test unit simulates the heat transfer rate at the interface between the two sub-layers (i.e., the product of the conduction heat flux at the interface, $q''^{f}_{cond,ab}$ in Equation (E-7), and the window surface area). Since the electrical power input to the heated window is needed, separate watt transducers are necessary to measure the electrical power dissipated by the heated window and the heated blind. In addition to room surface temperatures, the surface temperature of the heated window must also be measured.

6.5.2 Experimental Calculation Procedure

6.5.2.1 Steady-State Space Heat Balance Calculations

The proposed experimental method requires that each experimental test be performed at steady-state. The application of the steady-state heat balance of the test room is utilized to monitor the steady-state condition along with air and surface temperatures in the test room. The steady-state test room heat balance error ($\dot{q}_{error}$) can be calculated by:

$$\dot{q}_{error} = \dot{q}_{plug} + \dot{q}_{fen,tot} - \dot{q}_{space} - \sum \dot{q}_{cond,loss} \approx 0 \qquad (6\text{-}38)$$

where $\dot{q}_{plug}$ = power input to the plug load,

$\dot{q}_{fen,tot}$ = fenestration heat gain representing the sum of the absorbed solar heat gain and the conduction heat gain of the fenestration system,

$\dot{q}_{space}$ = space heat extraction rate, and

$\dot{q}_{cond,loss}$ = conduction heat loss through a surface.

For each experimental test, the steady-state error and test room temperatures are monitored until the temperatures are stable and the steady-state error is below a specified threshold value (typically 10% of the total room heat gain). Once steady state conditions have been achieved, the radiant heat gain is measured.

The fenestration heat gain representing the sum of the absorbed solar heat gain and the conduction heat gain can simply be calculated by:

$$\dot{q}_{fen,tot} = \dot{q}_{wd,inp} + \dot{q}_{bl,inp} \tag{6-39}$$

where $\dot{q}_{wd,inp}$ = measured power input to the vertical plate representing the window, and

$\dot{q}_{bl,inp}$ = measured power input to the heated blind.

The power inputs to the window and the blind are directly and separately measured.

Assuming no air leakage, the space heat extraction rate of the test room for steady-state, steady flow conditions can be calculated by:

$$\dot{q}_{space} = \dot{m}_{sa} \cdot C_p \cdot \left(T_{ra} - T_{sa}\right) \tag{6-40}$$

where C_p = air specific heat,

$\dot{m}_{sa}$ = mass flow rate measured in a flow measurement chamber,

T_{ra} = air temperature measured at the return air grille, and

T_{sa} = air temperature measured at the supply air diffuser.

The steady-state heat conduction formulation is utilized to estimate conduction heat transfer between the test room and surrounding areas. For each surface, the conduction heat loss can be calculated by:

$$\dot{q}_{cond,loss} = U \cdot A \cdot \left(T_{si} - T_{ao}\right) \tag{6-41}$$

where U = overall heat transfer coefficient of a test room surface,

A = surface area,

T_{si} = temperature measured at the inside surface, and

T_{ao} = measured air temperature of the guarded space of that particular surface.

The overall heat transfer coefficients can be estimated using literature data [ASHRAE 2005].

6.5.2.2 Radiative/Convective Split Calculations

This section describes the calculation procedure used to obtain the radiative/convective split required by the RTS thermal fenestration model. As previously mentioned, the total electrical heat applied to the window and the blind simulates the fenestration heat gain representing the sum of the absorbed solar heat gain and the conduction heat gain. Consequently, it is assumed that the radiative/convective splits of the absorbed solar heat gain and the conduction heat gain are the same, meaning that the measured radiative/convective split is applied to both the absorbed solar heat gain and the conduction heat gain.

Once the test room has reached steady state, scanning radiometer measurements are used directly to calculate the total radiant heat gain from the fenestration test unit ($\dot{q}_{fen,rad}$) as follows:

$$\dot{q}_{fen,rad} = \sum_{i=1}^{m} q''_{rad,i} \cdot A_i \tag{6-42}$$

where $q''_{rad,i}$ = net radiant heat flux measured at measurement location *i*,

A_i = area associated with measurement location *i*, and

m = total number of measurement locations.

For the current study, the measured net radiant heat flux was the sum of the net shortwave radiant flux and the net longwave radiant flux although the amount of the net shortwave radiant flux was not significant. The scanning radiometer measurements are discussed in detail by Wilson [2007].

The radiative/convective split of the fenestration heat gain can be calculated by:

$$F_{fen,rad} = \frac{\dot{q}_{fen,rad}}{\dot{q}_{fen,tot}} \tag{6-43}$$

$$F_{fen,conv} = 1 - F_{fen,rad} \tag{6-44}$$

where $F_{fen,rad}$ = fraction of the fenestration heat gain that is transferred as thermal radiation, and

$F_{fen,conv}$ = fraction of the fenestration heat gain that is transferred as convection.

6.5.2.3 Equivalent Convection Coefficient Calculations

This section describes the calculation procedure used to obtain the equivalent inside convection coefficient (i.e., $h_{c,eqv,in}$ in Equation (6-18)) required by the HB thermal fenestration model. As discussed in Section 6.2, the HB thermal fenestration model combines the innermost glazing layer and the interior blind layer into a single layer[1]. Therefore, to determine the equivalent inside convection coefficient based on the proposed experimental method, the equivalent inside (fictitious) surface temperature of the combined innermost glazing and blind layer is first needed. To estimate the equivalent surface temperature, Hottel's total exchange area method [Hottel and Sarofim 1967] is utilized along with the measured radiant heat gain and measured inside surface temperatures of the test room (excluding the fenestration test unit). Although surface temperatures of the window and the blind of the fenestration test unit are measured, they are not required in the equivalent convection coefficient calculations.

---

[1] The HB thermal fenestration model treats the innermost glazing layer and the interior blind layer as a single layer for heat balance calculations. For the conduction modeling purposes, however, the combined layer along with the air gap between the glazing layer and the blind layer is modeled as two homogeneous sub-layers having perfect thermal contact as discussed in Section 6.2 and Appendix E.

Let the inside (fictitious) surface of the fenestration test unit be surface *1* of the test room. According to Hottel and Sarofim [1967], the net-radiation exchange between the fictitious surface and other room surfaces can be expressed by:

$$\dot{q}_{fen,rad} = \sigma \sum_{j=1}^{n} \overline{S_1 S_j} \cdot \left(T_1^4 - T_j^4 \right) \tag{6-45}$$

where $\dot{q}_{fen,rad}$ = radiant heat gain measured by the net radiometer,

σ = Stefan-Boltzmann constant,

$\overline{S_1 S_j}$ = Hottel's total exchange area between the fictitious surface and the inside surface *j*,

T_j = measured temperature of the inside room surface *j*, and

n = total number of inside surfaces of the test room including the fictitious surface.

The total exchange areas are calculated based on room surface areas, view factors between inside surfaces and room surface emissivities [Hottel and Sarofim 1967]. Due to the simple geometry of the test room, the view factors between inside surfaces were analytically calculated using equations for parallel planes and perpendicular planes [Modest 2003]. Data from the literature and paint manufactures were used to estimate emissivities of all inside surfaces for the current research. An average of the window and the blind layer emissivities was used to represent the emissivity of the fictitious surface.

Equations (6-45) can be rearranged to obtain the equivalent (fictitious) surface temperature as follows:

$$T_1 = \left(\frac{\dot{q}_{fen,rad} + \sigma \sum_{j=2}^{n} \overline{S_1 S_j} \cdot T_j^4}{\sigma \sum_{j=2}^{n} \overline{S_1 S_j}} \right)^{\frac{1}{4}} \tag{6-46}$$

Once the equivalent inside surface temperature of the fenestration test unit has been determined, the equivalent inside convective heat transfer coefficient of the fenestration system can be estimated using Newton's law of cooling as follows:

$$h_{c,eff,in} = \frac{\dot{q}_{fen,conv}}{A_1 \cdot (T_1 - T_{ref})} \tag{6-47}$$

where $\dot{q}_{fen,conv}$ = total convective heat gain from the fenestration test unit, and

T_{ref} = reference air temperature.

The convective heat gain can simply be calculated as the difference between the measured fenestration heat gain and the measured radiant heat gain. The measured fenestration heat gain (total window and blind electrical power) is determined using Equation (6-39) while the measured radiant heat gain is determined using Equation (6-42). Typically, the room air temperature is used as a reference air temperature in a building simulation tool. However, Fisher and Pedersen [1997] found that the supply air temperature gave less experimental uncertainty than the room air temperature when it was used in the development of their convection correlations. For the current research, both reference temperatures were investigated.

6.5.2.4 Equivalent Thermal Conductance Calculations

This section describes the calculation used to obtain the equivalent thermal conductance within the combined glazing and blind layer (i.e., c_{L+1} in Equations (6-19) and (6-20)) required by the HB thermal fenestration model. As discussed in Section 6.2, by modeling the innermost glazing layer and the blind layer as a single layer, the total heat transfer from the back (real) surface of the innermost glazing layer to the (imaginary) plane parallel to the interior blind is treated as the equivalent conduction heat transfer across the combined glazing and blind layer. The combined layer is modeled as two homogeneous sub-layers having perfect thermal contact where the first sub-layer represents the innermost glazing layer and the second sub-layer represents the blind and the air gap between the glazing layer and the blind layer. The thermal conductance of the first sub-layer can be calculated using thermo-physical properties of the glass (i.e., thermal conductivity and thickness) while the equivalent thermal conductance of the second sub-layer must be experimentally determined.

By guarding the back of the fenestration test unit[1], the electrical power applied to the window alone simulates the total heat transfer rate from the back surface of the innermost glazing layer to the plane parallel to the interior blind for the proposed experimental method. The aforementioned total heat transfer rate is the same as the heat transfer rate at the interface between the first sub-layer and the second sub-layer of the conduction model as illustrated in Figure 6-3. The equivalent conduction heat transfer is assumed to be steady state. The detailed conduction model used by the HB thermal fenestration model is given in Appendix E.

To determine the equivalent thermal conductance within the combined glazing and blind layer, the measured power input to the heated window ($\dot{q}_{wd,inp}$) is used along with the measured surface temperature of the heated window (T_{wd}) and the estimated equivalent surface temperature

---

[1] For a 50 W electrical power input to the window and a 1 °F temperature difference across the insulation board between the window and the guard plate, the estimated conduction loss/gain through the back of the fenestration test unit is less than 2% of the electrical power input. For the current study, an estimated conduction loss/gain using measured temperature difference was used in the uncertainty estimation of measured thermal parameters.

of the fenestration system (T_1). The equivalent thermal conductance within the combined glazing and blind layer (c_{L+1}) can simply be determined as follows:

$$c_{L+1} = \frac{\dot{q}_{wd,inp}}{A_1 \cdot (T_{wd} - T_1)} \tag{6-48}$$

where A_1 = plane area of the fenestration test unit (i.e., the window area).

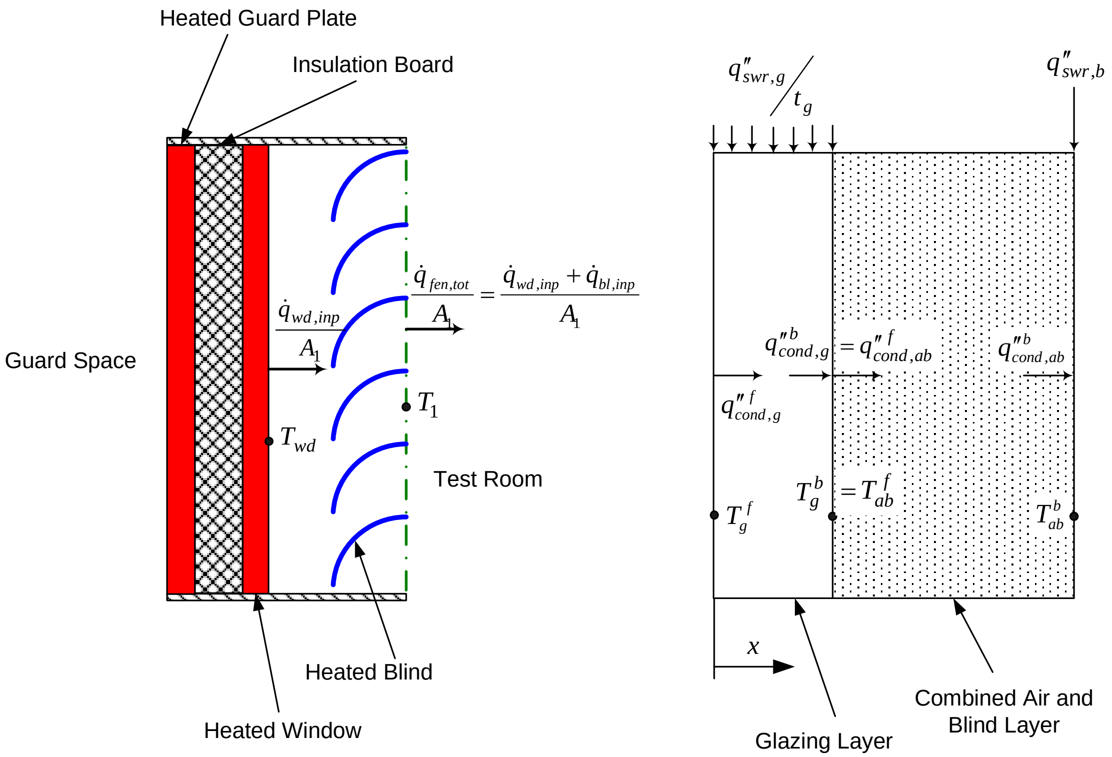

a) Fenestration Test Unit

b) Combined Glazing and Blind Layer for Conduction Modeling

Figure 6-3 Equivalent Conduction Heat Transfer within the Combined Glazing and Blind Layer

6.5.3 Demonstration of the Proposed Experimental Method

The primary objective of the heated window/blind experiments was to illustrate the feasibility of supporting the newly developed thermal fenestration models with measured data. As previously discussed, the development of empirical correlations is essential to support the proposed thermal models. Thus, the secondary objective of the current experimental investigation was to provide guidelines for the complete parametric set of experiments required to support the model.

6.5.3.1 Feasibility of Experimental Method

As mentioned in Section 6.1, the sub-model of the EnergyPlus thermal fenestration model for the shading layers has not yet been validated [van Dijk and Oversloot 2003] and no experimental method is available to measure various thermal parameters used in the shading layer model [ISO 2000]. For the current study, an experimental method has been developed along with the new thermal fenestration models. As previously discussed, the combined layer model makes measurements of the two thermal parameters required by the HB thermal fenestration model feasible.

Three approaches together are used to illustrate the feasibility of supporting the thermal models by the proposed experimental method. First, an uncertainty analysis is used to estimate the accuracy of both primary and derived experimental values. It is also used as a practical means of validating measured results. Second, a verification exercise is used to support the validity of primary experimental measurements as well as the estimation of the equivalent fenestration surface temperature. Both the equivalent thermal conductance within the combined layer and the equivalent convection coefficient of the combined layer inside surface, required by the HB thermal fenestration model, are derived based on the equivalent fenestration surface temperature. Third, in the absence of published experimental data, a comparison between measured results and published numerical data is used to illustrate that the proposed experimental method is sensitive enough to capture the effect of an experimental variable on the measured thermal parameters (i.e., changes in measured results due to a change in the test variable are demonstrably reasonable). These three approaches are discussed in detail in following sections.

6.5.3.2 Experimental Variables and Experimental Tests

There are a large number of variables that can have an effect on the thermal parameters required by the new thermal fenestration models. These variables may be categorized into four groups: outdoor environmental variables, indoor environmental variables, fenestration variables, and blind variables. The outdoor environmental variables include outdoor air temperature, wind direction, wind speed, amount of insolation, etc. The fenestration variables include number of glazing layers, type of glazing layers, (solar) optical properties of glazing and blind layers, the emissivity of the inside surface of the innermost glazing layer, etc. The blind variables include blind slat geometry (i.e. slat angle, slat width, and slat spacing), blind surface emissivity, distance between the window and the blind, type of blind assembly (horizontal-slat blind or vertical-slat blind), and type of blind installation (inside or outside mounting). The indoor environmental variables include room air temperature, supply air temperature, air circulation rate, air distribution configuration, other room surface temperatures, etc. By using the guard plate to prevent heat loss from the back of the fenestration test unit to the outside, the proposed experimental method essentially eliminates all of the outdoor environmental variables and most of the fenestration variables (except the emissivity of the inside surface of the innermost glazing layer). The window power input and the total power input (the sum of the window power input and the blind power input), which simulate the heat transfer rates at the inside surfaces of the innermost glazing layer and the fenestration system, account for these variables.

The current study investigates the influence of four experimental variables on the thermal parameters: the window power input, the blind power input, the blind slat angle, and the room airflow rate. The experimental tests for the current study were performed in the Building Airflow and Contaminant Transport Laboratory. The experimental configuration, which is described in detail by Wilson [2007] and conceptually illustrated in Figure 6-2, included:

- a guarded hot panel of dimension 3 ft. by 3 ft. (0.91 m by 0.91 m) used to represent a full scale fenestration system,
- a blind with 1-in horizontal and curved slats mounted inside the fenestration frame (i.e., inside mounting) with the distance of 2.25 inches (57.2 mm) between the window surface and the middle plane of the blind assembly,
- the window and the blind slats both painted white with an emissivity of approximately 0.9,
- The conditioned air supplied through the radial ceiling diffuser, and
- The return air configured for the ceiling plenum return (i.e., non-ducted return).

Figure 6-4 illustrates the location of the fenestration test unit, the supply air diffuser, and the return air grille. The test room conditions were controlled as follows:

- The average supply air temperature at the supply air diffuser was maintained between 60.6 °F and 61.1 °F (15.9 °C and 16.2 °C), and
- The average room air temperature was maintained between 71.1 °F and 72.7 °F (21.7 °C and 22.6 °C).

For the current study, two sets of tests were performed. The first set, which was performed using the fenestration test unit without the blind, was used in the verification exercise while the second set, which was performed using the fenestration test unit with the blind, was compared to published data and used to the evaluate the sensitivity of model parameters to the test variables. Essentially, only the window power input and the room airflow rate were investigated for the verification exercise.

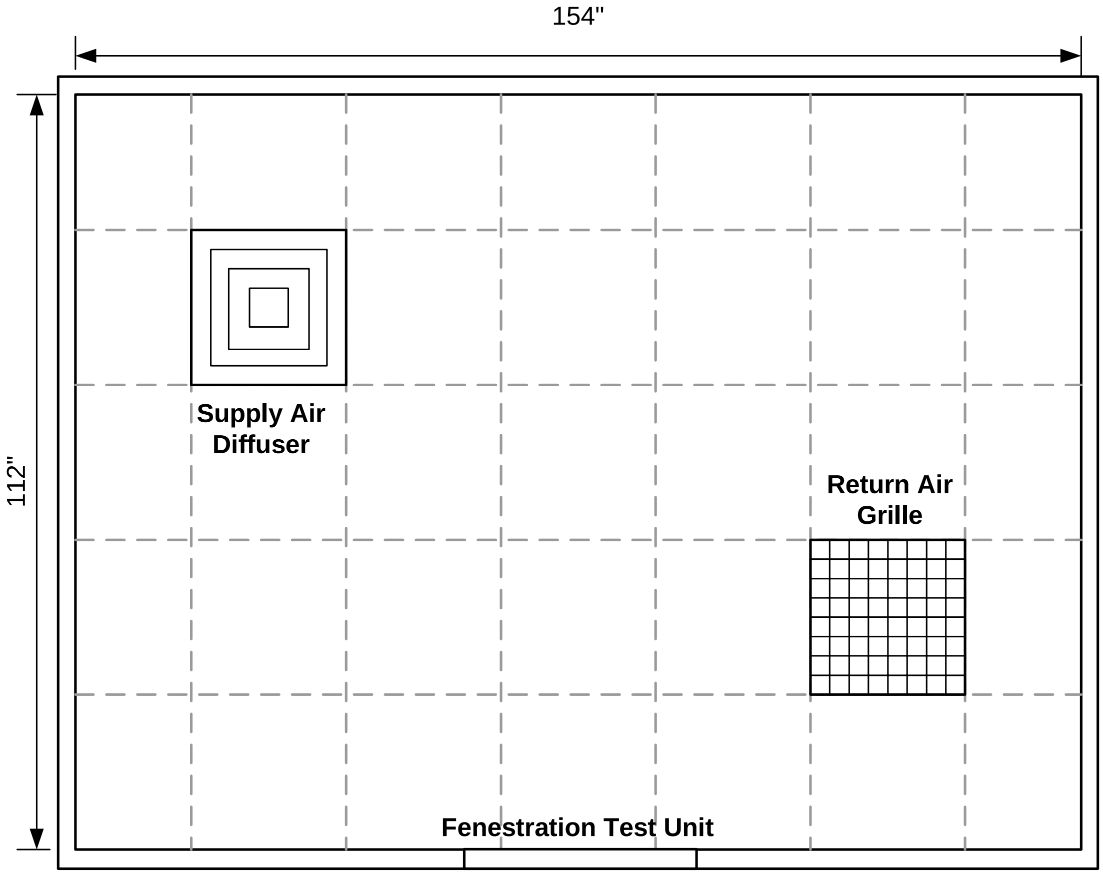

Figure 6-4 Ceiling Configuration

6.5.3.3 Estimation of Experimental Uncertainties

As previously discussed, an uncertainty analysis is used to estimate the accuracy of both primary and derived experimental results. The analysis is also used as a practical means of validating measured data. For the current study, the experimental uncertainty analysis based on the well-known method of Kline and McClintock [Kline and McClintock 1953] was performed to estimate the accuracy of the experimental results. A detailed analysis is presented by Wilson [2007]. In the following sections, the estimated experimental uncertainties are given along with the measured data.

6.5.3.4 Verification of Experimental Measurements

The proposed experimental method relies on the radiant heat gain measurement to determine the radiative/convective split of the total heat gain from the fenestration test unit. The method also relies on the radiant heat gain measurement and the surface temperature measurement to estimate the equivalent inside surface temperature of the fenestration test unit. The scanning radiometer measurement technique utilized in the current study has already been validated by Jones et al. [1998]. The technique has also been used successfully in previous work by the author to measure the radiative/convective split of the total room lighting heat gain [Chantrasrisalai and Fisher 2007]. To support the validity of the estimation of the equivalent (fictitious) surface temperature, however, several experimental tests were performed using the fenestration test unit without the blind.

For these experimental tests, the fenestration test unit consisting of only the insulated heated (window) panel and the heated guard plate was installed flush with the interior surface of the wall. For these tests, the temperature of the real inside surface of the fenestration system can be measured. Using the calculation procedure described in Section 6.5.2.3, the inside surface temperature of the fenestration system can also be estimated using measured radiant heat gain and measured temperatures of other room surfaces. To illustrate the validity of the experimental measurements used in the current study, Figure 6-5 shows the calculated surface temperature plotted against the measured surface temperature for the experimental tests with the fenestration test unit without the blind. The diagonal line represents the ideal temperature estimation. The estimated uncertainty of the calculated surface temperature is shown as a vertical error bar while the estimated uncertainty of the measured surface temperature is shown as a horizontal error bar on each data point. As shown in Figure 6-5, all data points lie close to the ideal line. The difference between the calculated and measured surface temperatures is mostly less than 0.40 °F (0.22 °C) and all less than 1.20 °F (0.67 °C). The excellent agreement between the calculated and measured surface temperatures demonstrably supports the validity of the measurements of the radiant heat gain and the surface temperatures as well as the estimation of the equivalent fenestration surface temperature.

As shown in Figure 6-5, the vertical error bar is not even due to the fact that the scanning area for the radiant heat gain measurement used for the current study was a parallel plane covering the fenestration test unit, which would theoretically result in lower measured radiant heat gain as discussed in Section 6.5.1. It should be noted that the measurement plane was about 2 inches (50 mm) far from the inside surface of the fenestration test unit for these tests. To reduce this uncertainty, the measurement plane was moved 1 inch (25 mm) closer to the fenestration test unit for experimental tests with the fenestration test unit with the blind.

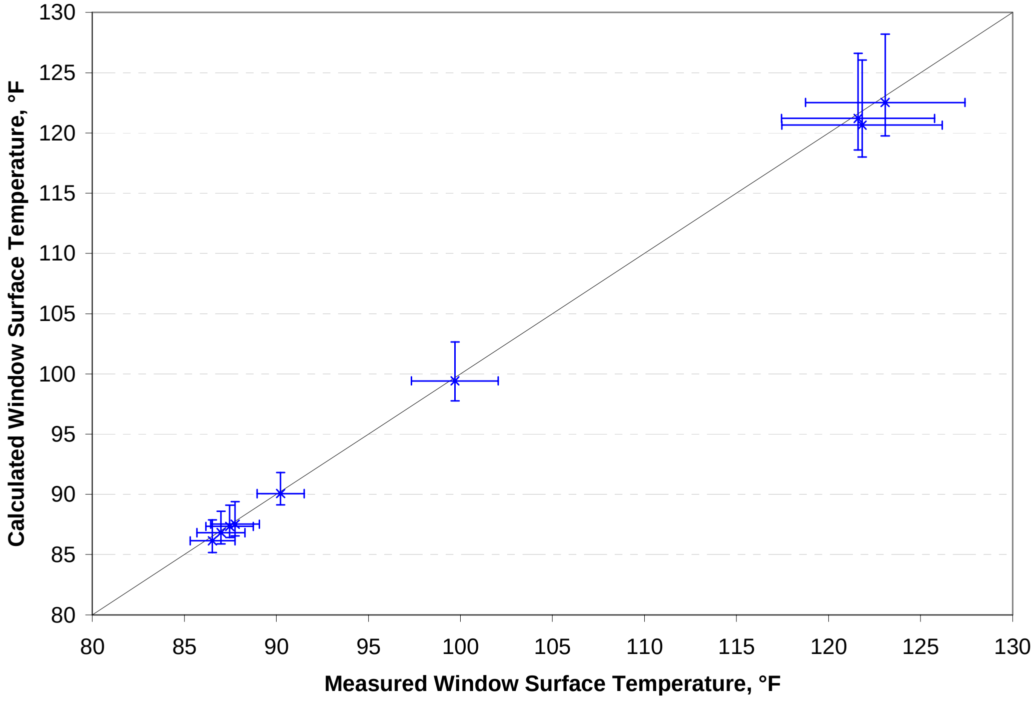

Figure 6-5 Comparison between Calculated and Measured Window Surface Temperatures

As also shown in Figure 6-5, the uncertainty in the measured surface temperature (the horizontal bar) is quite high for tests with high measured surface temperature. This was due to the fact that the surface temperature variation was higher when the vertical plate representing the window was operated using higher power input. The maximum temperature difference for a test with 200 W power input could be more than 10 °F (5.6 °C). Figure 6-6 illustrates the measured radiant heat flux distribution, which should be analogous to the surface temperature distribution. For the current study, the uncertainty in measured surface temperature due to spatial averaging was approximated as twice the standard deviation of the mean measured surface temperature. The uncertainty analysis as well as experimental instrumentation for the current study is discussed in detail by Wilson [2007].

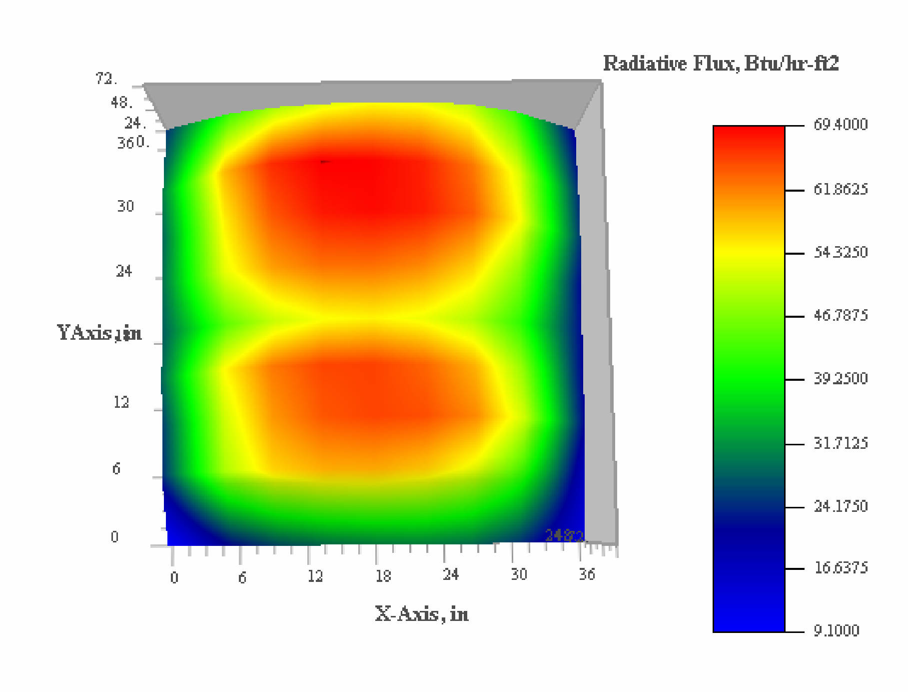

Figure 6-6 Measured Radiant Heat Flux Distribution of Heated Window Panel for a Test with 200 W Power Input

Since the real surface temperature of the fenestration test unit can be measured for tests using the fenestration unit without the blind, the net-radiation exchange rate between the fenestration test unit and other room surfaces (or the net radiant heat gain) can be calculated using measured temperatures of all room surfaces. Therefore, in addition to comparing fenestration surface temperatures, Figure 6-7 compares the calculated net radiant heat gain with the measured net radiant heat gain. In addition to a diagonal solid line representing an ideal estimation, diagonal dashed lines representing the ±10% estimation are also shown in Figure 6-7. As shown, all data points lie closely to the ideal line and well within the ±10% lines demonstrating the validity of the radiant heat gain measurement and the surface temperature measurements used in the current study.

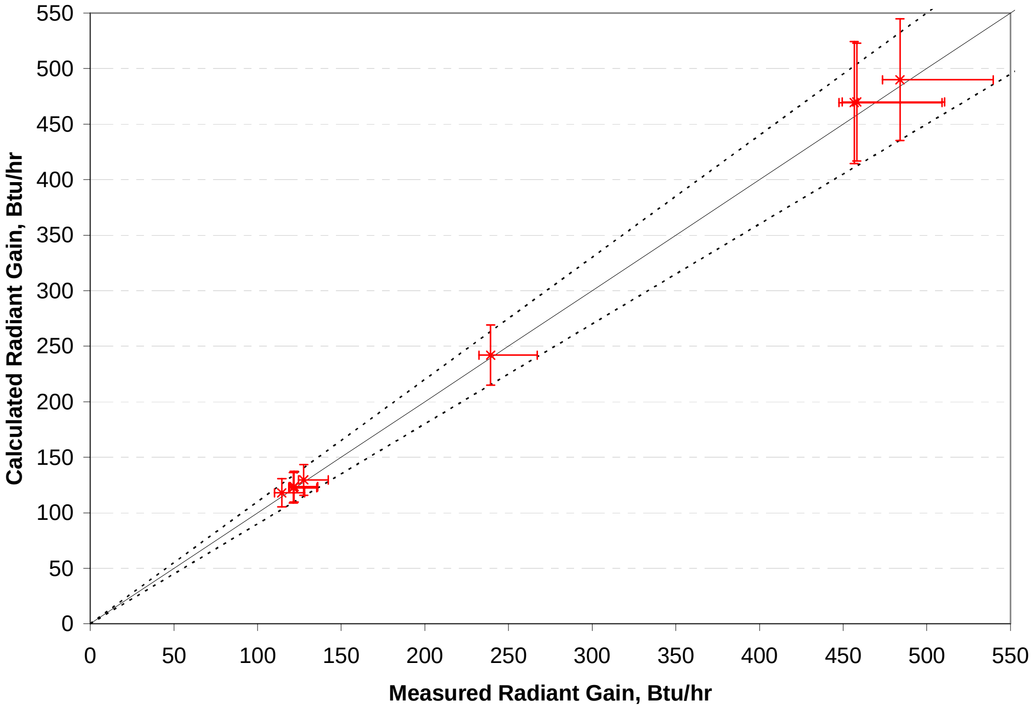

Figure 6-7 Comparison between Calculated and Measured Net Radiant Heat Gains

6.5.3.5 Experimental Evaluation of the Effect of Experimental Variables

Effect of Experimental Variables on Radiative Fraction

For the current study, a parametric set of fifteen experiments were performed to evaluate the effects of four experimental variables on the thermal parameters. As previously mentioned, the four experimental variables included the window power input, the blind power input, the blind slat angle, and the room airflow rate. Table 6-1 summarizes the measured radiative fraction for the experiments. General observations are summarized as follows:

- The thermal interactions between the fenestration system containing an interior blind and the room were substantially different from those between the fenestration system without an interior blind and the room. For experimental tests using the fenestration test unit without the blind (i.e., verification tests discussed in Section 6.5.3.4), the measured radiative fraction varied between 0.66 and 0.72. On the other hand, the measured radiative fraction, for tests using the fenestration test unit with the blind as shown in Table 6-1, varied between 0.28 and 0.38. These results indicated that the presence of the interior blind had a significant effect on the thermal interactions between the fenestration system and the room.
- A change in the measured radiative fraction due to a change in an experimental variable was normally noticeable and the trend in the change due to a change in a particular variable was mostly consistent (e.g., increasing an experimental variable caused a reduction in the measured radiative fraction or vice versa). However, the uncertainty in the measured radiative fraction was quite high, particularly for tests with the window power input of 50 W and the blind power input of 50 W. Therefore, the sensitivity of the measured radiative fraction appeared somewhat insignificant, particularly when the comparisons involved the tests with the window power input of 50 W and the blind power input of 50 W.

Table 6-1 Measured Radiative Fraction

Window Power, Watts		**150**	**150**	**50**
Blind Power, Watts		**150**	**50**	**50**
Slat Angle of 0°	**Airflow Rate of 14 ACH**	0.30±0.02	-	-
	Airflow Rate of 10 ACH	0.32±0.03	0.36±0.03	0.36±0.05
	Airflow Rate of 5 ACH	0.33±0.03	0.38±0.04	0.36±0.05
Slat Angle of +45°	**Airflow Rate of 10 ACH**	0.28±0.02	0.30±0.03	0.32±0.05
	Airflow Rate of 5 ACH	-	-	0.33±0.05
Slat Angle of -45°	**Airflow Rate of 10 ACH**	0.29±0.02	0.30±0.03	0.32±0.05
	Airflow Rate of 5 ACH	-	-	0.33±0.05

- For the comparisons not involving the tests with the window power input of 50 W and the blind power input of 50 W, the measured radiative fraction was more sensitive to changing the slat angle and changing the blind power input than changing the room airflow rate. A change in the measured radiative fraction due to changing the slat angle (from a fully-opened blind to a partially-opened blind) and changing the blind power input (for the slat angle of 0°) was higher than the experimental uncertainty in the measured radiative fraction. On the other hand, a change in the measured radiative fraction due to changing the room airflow rate was mostly lower than the uncertainty in the measured radiative fraction.
- Unlike changing the blind slat angle from a fully-opened blind to a partially-opened blind, changing the slat angle from a downward opened blind to an upward opened blind appeared to have a trivial effect on the measured radiative fraction. A change in the measured radiative fraction due to changing from a downward opened blind to an upward opened blind was lower than the uncertainty in the measured radiative fraction.

As previously discussed, the uncertainty in the measured radiative fraction was quite high. This was mainly due to the accuracy of the watt transducer used to measure the blind power input. According to its manufacturer, the accuracy of the watt transducer with 2500 W full scale used for the blind can be approximated as ±0.5% of full scale (the accuracy of the watt transducer with 500 W full scale used for the window can be approximated as ±0.04% of full scale). Therefore, the uncertainty in the measured radiative fraction was high, particularly for tests with the window power input of 50 W and the blind power input of 50 W since the total power input for these tests was lower than that for other tests. Consequently, the high experimental uncertainty for tests with the window power input of 50 W and the blind power input of 50 W caused the sensitivities of the measured radiative fraction to changing the total power input and to changing the window power input to appear somewhat trivial. To reduce the experimental uncertainty for future studies, a high accuracy watt transducer should be used.

As shown in Table 6-1, increasing the room airflow rate from 5 air changes per hour (ACH) to 10 ACH caused a reduction in the measured radiative fraction as expected. However, changes in the measured radiative fraction were unexpectedly small compared to the experimental uncertainties. This was likely due to the fact that the supply air diffuser was located quite far from the fenestration test unit as shown in Figure 6-4. As a result, the attached wall jet had fully dissipated and the air speeds in the vicinity of the fenestration test unit were somewhat low. Consequently, the overall convective heat transfer from the fenestration test unit was not dominated by an attached wall jet as might be expected for other diffuser configurations. Nevertheless, the effect of the room airflow rate was not negligible as illustrated in Figure 6-8. As shown, the reduction in the measured radiative fraction due to increasing the room airflow rate from 5 ACH to 14 ACH was slightly higher than the experimental uncertainties.

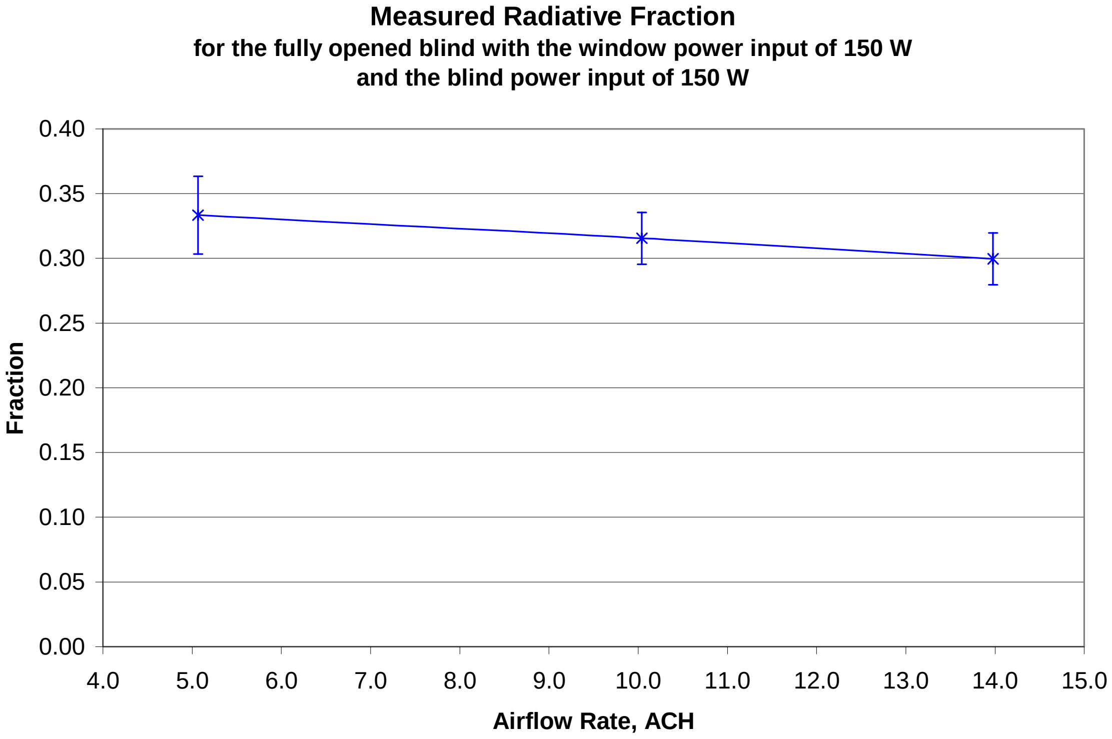

Figure 6-8 Effect of Room Airflow Rate on Radiative Fraction

Significance of HB Thermal Model Parameters

As previously discussed, the modeling of the combined innermost glazing and blind layer simplifies the calculations required for the HBM (i.e. the HB thermal fenestration model) and makes it possible to support the thermal model with experimental measurements. By combining the innermost glazing layer and the blind layer into a single layer, the equivalent thermal conductance within the combined layer and the equivalent convection coefficient of the equivalent (fictitious) inside fenestration surface are used to account for thermal interactions (both convection and radiation) between the window and the blind, thermal interactions between the window/air gap and the room, and thermal interactions between the blind and the room. The two thermal parameters are coupled by the equivalent surface fenestration temperature. This means that the equivalent thermal conductance accounts for all thermal interactions from the inside surface of the innermost glazing layer to the imaginary plane parallel to the blind assembly and the equivalent convection coefficient (along with a standard method for inside longwave exchange calculations) accounts for all thermal interactions from the imaginary plane to the room. Both thermal parameters are equally important to the HB thermal fenestration model.

For the proposed experimental method, the equivalent convection coefficient can be derived from the measured radiant heat gain, the measured power input to the window and to the blind, the measured reference air temperature, and the calculated equivalent surface fenestration temperature (derived from the measured radiant heat gain and the measured room surface temperatures). Table 6-2 summarizes the measured equivalent convection coefficient based on the measured room air temperature and Table 6-3 summarizes the measured equivalent convection coefficient based on the measured supply room air temperature. Essentially, the effect of an experimental variable on the measured equivalent convection coefficient(s) should be opposite to the effect of an experimental variable on the measured radiative fraction. A change in the experimental variable causes a reduction in the radiative fraction, and thus should result in an increase in the equivalent convection coefficient(s). An examination of the experimental results showed that the effects on the measured equivalent convection coefficient based on a spatially averaged room air reference temperature were all consistent with (i.e. opposite to) the effects on the measured radiative fraction. On the other hand, using a supply air reference temperature yielded inconsistent results for a few cases. The possible explanation is that the air temperature adjacent to the fenestration system was closer to the spatially averaged room air temperature than the supply air temperature since the attached wall jet had fully dissipated as previously discussed. Although using the spatially averaged room air reference temperature provided slightly more consistent results than using the supply air reference temperature, it resulted in higher experimental uncertainties due to lower temperature differences. Therefore, both room and supply air reference temperatures should be considered in a future study when developing the empirical correlation(s) of the equivalent convection coefficient.

Table 6-2 Measured Equivalent Convection Coefficient, Btu/hr-ft²-°F (W/m²-K), (Using Room Air Temperature as Reference Temperature)

Window Power, Watts		**150**	**150**	**50**
Blind Power, Watts		**150**	**50**	**50**
Slat Angle of 0°	**Airflow Rate of 14 ACH**	2.39±0.26 (13.6±1.5)	-	-
	Airflow Rate of 10 ACH	2.19±0.24 (12.5±1.4)	1.78±0.24 (10.1±1.4)	1.73±0.38 (9.8±2.1)
	Airflow Rate of 5 ACH	2.03±0.22 (11.5±1.3)	1.63±0.23 (9.2±1.3)	1.67±0.36 (9.5±2.0)
Slat Angle of +45°	**Airflow Rate of 10 ACH**	2.57±0.27 (14.6±1.5)	2.31±0.29 (13.1±1.7)	2.01±0.43 (11.4±2.4)
	Airflow Rate of 5 ACH	-	-	1.93±0.40 (10.9±2.3)
Slat Angle of -45°	**Airflow Rate of 10 ACH**	2.43±0.26 (13.8±1.5)	2.31±0.30 (13.1±1.7)	2.03±0.43 (11.5±2.4)
	Airflow Rate of 5 ACH	-	-	1.90±0.41 (10.8±2.3)

Table 6-3 Measured Equivalent Convection Coefficient, Btu/hr-ft²-°F (W/m²-K), (Using Supply Air Temperature as Reference Temperature)

Window Power, Watts		**150**	**150**	**50**
Blind Power, Watts		**150**	**50**	**50**
Slat Angle of 0°	**Airflow Rate of 14 ACH**	1.77±0.16 (10.0±0.9)	-	-
	Airflow Rate of 10 ACH	1.67±0.16 (9.5±0.8)	1.25±0.15 (7.1±0.8)	0.95±0.19 (5.4±1.1)
	Airflow Rate of 5 ACH	1.57±0.15 (8.9±0.9)	1.18±0.15 (6.7±0.8)	0.96±0.19 (5.4±1.1)
Slat Angle of +45°	**Airflow Rate of 10 ACH**	1.90±0.17 (10.8±1.0)	1.58±0.18 (9.0±1.0)	1.09±0.21 (6.2±1.2)
	Airflow Rate of 5 ACH	-	-	0.27±0.05 (1.54±0.30)
Slat Angle of -45°	**Airflow Rate of 10 ACH**	1.82±0.17 (10.4±0.9)	1.56±0.17 (8.8±1.0)	1.08±0.21 (6.1±1.2)
	Airflow Rate of 5 ACH	-	-	1.06±0.21 (6.0±1.2)

Similar to the equivalent convection coefficient, the equivalent thermal conductance is a derived experimental result using the measured window power input, the measured window surface temperature, and the calculated equivalent surface fenestration temperature. Table 6-4 summarizes the measured equivalent thermal conductance from the current experimental tests. Although a change in the measured equivalent thermal conductance due to a change in an experimental variable was comparatively higher than a change in the measured equivalent convection coefficient (both parameters have the same units), the change in the measured equivalent thermal conductance was relatively low compared to the uncertainty in the measured equivalent thermal conductance. Therefore, the sensitivity of the equivalent thermal conductance to most experimental variables appeared somewhat insignificant. As shown in Table 6-4, uncertainties in the thermal conductance were quite high (much higher than uncertainties in the convection coefficient shown in Tables 6-2 and 6-3).

Table 6-4 Measured Equivalent Thermal Conductance, Btu/hr-ft²-°F (W/m²-K)

Window Power, Watts		150	150	50
Blind Power, Watts		150	50	50
Slat Angle of 0°	Airflow Rate of 14 ACH	5.97±2.86 (33.9±16.2)	-	-
	Airflow Rate of 10 ACH	5.56±2.53 (31.6±14.4)	3.93±1.15 (22.3±6.5)	5.66±3.25 (32.1±18.4)
	Airflow Rate of 5 ACH	5.64±2.69 (32.0±15.3)	3.77±1.12 (21.4±6.4)	5.04±2.63 (28.6±14.9)
Slat Angle of +45°	Airflow Rate of 10 ACH	3.78±1.08 (21.4±6.1)	2.78±0.54 (15.8±3.1)	3.34±1.10 (18.9±6.2)
	Airflow Rate of 5 ACH	-	-	3.21±1.01 (18.2±5.7)
Slat Angle of -45°	Airflow Rate of 10 ACH	3.60±1.19 (20.4±6.8)	2.71±0.59 (15.4±3.3)	3.37±1.25 (19.1±7.1)
	Airflow Rate of 5 ACH	-	-	3.09±1.08 (17.5±6.1)

There are two primary reasons for the high uncertainties in the thermal conductance. First, as previously discussed in Section 6.5.3.4, the uncertainty in the measured surface temperature of the heated vertical plate used to represent the window was quite high due to non-uniformity in the surface temperature. Second, the differences between the measured window and the calculated equivalent fenestration surface temperatures used for the equivalent thermal conductance calculation were relatively low compared to the differences between the calculated equivalent fenestration and the measured reference air temperatures used for the equivalent convection coefficient calculation. The differences between the window and the equivalent fenestration surface temperatures ranged between 3.4 °F and 20.8 °F (1.9 °C and 11.6 °C). The differences between the equivalent fenestration and the reference air temperatures ranged between 12.6 °F and 37.2 °F (7.0 °C and 20.7 °C) for the spatially-averaged room air reference temperature. The difference between the window and the equivalent fenestration surface temperatures was primarily dependent on both power inputs to the window and to the blind. This means that the small temperature difference could not be avoided for some combinations of the power inputs.

For results presented in Table 6-4, the temperature differences were all positive meaning that the measured window surface temperatures were higher than the calculated equivalent fenestration surface temperatures for those experimental tests. However, the temperature difference can not only become very small, it can also become negative for certain power input combinations. To illustrate the situations when the temperature difference becomes very small or negative, Figure 6-9 shows the ideal equivalent thermal conductance as a function of the temperature difference and the heat transfer rate[1] at the window surface (i.e., the inside surface of the innermost glazing layer).

---

[1] More appropriately, the ideal equivalent thermal conductance would have been plotted as a function of the heat flux at the window surface. However, the heat transfer rate based on the size of the fenestration test unit employed in the current study was used to facilitate the comparison between the ideal thermal conductance and the measured one.

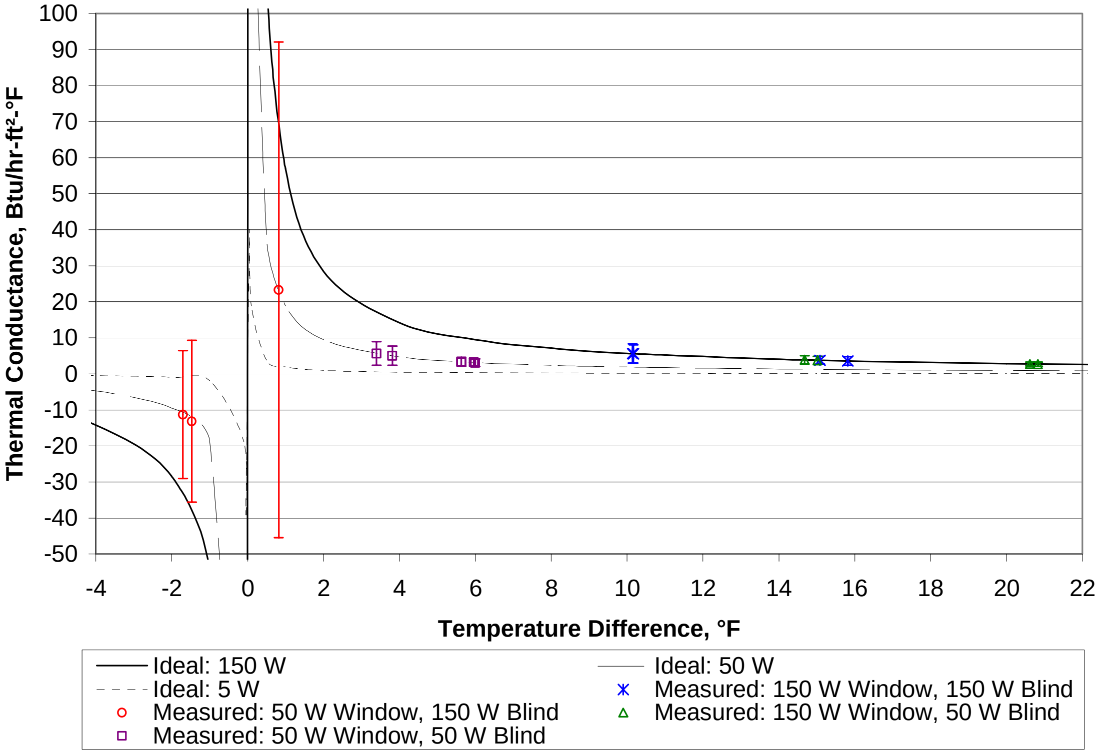

Figure 6-9 Equivalent Thermal Conductance as a Function of Surface Temperature Difference

Figure 6-9 also shows the measured equivalent thermal conductance plotted against the ideal equivalent thermal conductance where the measured data follows the ideal line(s) closely. As shown in Figure 6-9, measured temperature differences for tests with window power input of 50 W and blind power input of 150 W were either negative or lower than the temperature differences for other tests (i.e., tests with results presented in Table 6-4). For tests with the window power input of 50 W and the blind power input of 150 W, the uncertainty in the measured equivalent thermal conductance was very high compared to those for other tests since the measured temperature difference (either negative or positive) was much smaller. The tests with the window power input of 50 W and the blind power input of 150 W demonstrates the situations when the experimental uncertainty in the measured equivalent thermal conductance can become unacceptably large. Although this appears to be a serious limitation of the test procedure, the environmental conditions required to produce window power input of 50 W and the blind power input of 150 W would be difficult to replicate in an actual building. In laboratory tests, the heat transfer rate (or flux) at the window surface can be fixed by using a heated guard plate as being done for the current experiments. In real situations, however, the window surface heat flux likely decreases or becomes negative (i.e., heat conducted back to the outside) as the blind temperature increases (i.e., the temperature difference decreases). This means that, unlike the ‘laboratory’ equivalent thermal conductance, the ‘actual’ equivalent thermal conductance is unlikely to follow an ideal thermal conductance line based on a fixed heat transfer rate (or flux).

6.5.3.6 Comparison with Published Numerical Data

Although experimental data is not published in the literature, Collins et al. [2002] did some numerical studies with a program that was calibrated to their natural convection blind experiments. The measured data presented here cannot be directly compared with Collins numerical studies since the flowfield, fenestration geometry, and boundary conditions all differed. Nevertheless, the trends predicted by the numerical program for natural convection provide some insight into the measured results.

Figure 6-10 shows the comparison of the blind slat angle effect on the measured and numerical radiative fractions. As shown in Figure 6-10a, changing from a fully opened blind (slat angle of 0°) to a partially opened blind (either slat angle of +45° or slat angle of -45°) caused a reduction in the measured radiative fraction. This reduction was likely due to the fact that the blind slats at a partially opened position blocked the view of the window to the room surfaces and thus reduced the radiation exchange between the window and the room surfaces. The radiative fraction was decreased since the window was always at a higher temperature than the blind slat surfaces. Also, the convection from the partially-opened blind was likely higher than that from the fully-opened blind, leading to lower blind temperatures and thus a reduction in the radiative fraction. The measured results for the downward opened blind (slat angle of +45°) were nearly identical to those for the upward opened blind (slat angle of -45°). This is consistent with a relatively undisturbed buoyant plume from the blind for the natural convection case (Figure 6-10b) and for a minimally disturbed plume for the experimental case. This suggests that, for the ceiling diffuser, buoyant forces dominate the air flow in the window cavity even at 10 air changes per hour.

a) Measured Radiative Fraction

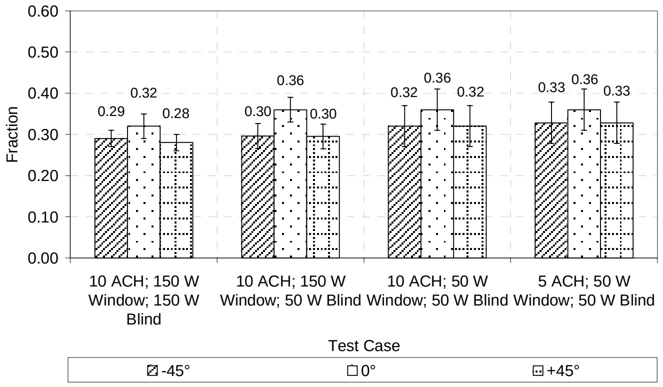

b) Numerical Radiative Fraction from Table 4 [Collins et al. 2002]

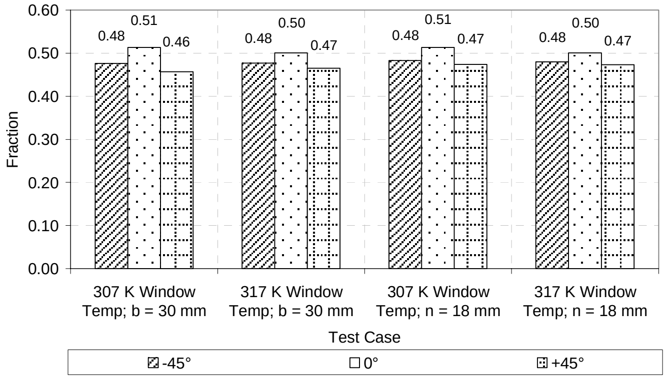

Figure 6-10 Comparison of Effect of Blind Slat Angle on Radiative Fraction

Figure 6-11a shows that increasing the blind power input caused a reduction in the measured radiative fraction. This indicates that the blind is more strongly dominated by convection than the window. This is a reasonable result since the blind interacts directly with the bulk airflow in the room and since the surface area of the blind is roughly twice that of the glazing. Figure 6-11b shows that increasing the blind absorbed solar radiation also caused a reduction in the numerical radiative fraction. Good agreements between measured and numerical results shown in both Figures 6-10 and 6-11 illustrate that the proposed experimental method can appropriately capture the effects of experimental variables on measured thermal parameters.

a) Measured Radiative Fraction

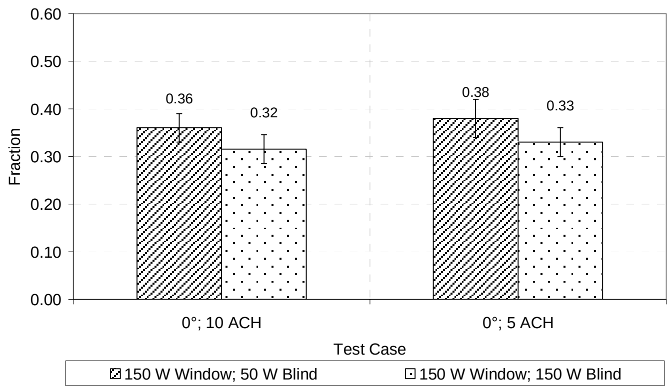

b) Numerical Radiative Fraction from Table 5 [Collins et al. 2002]
(Window Temperature of 307 K)

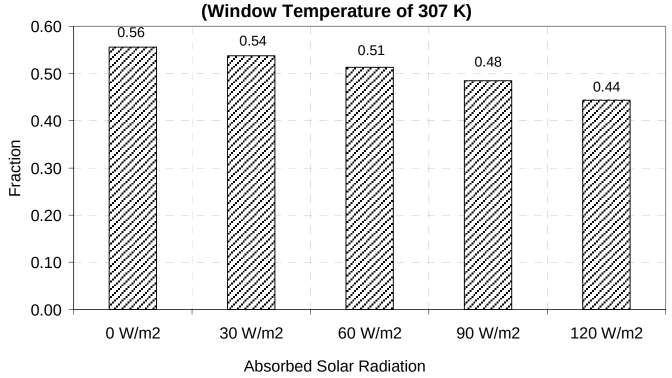

Figure 6-11 Comparison of Effect of Blind Input Power/Blind Absorbed Solar Radiation on Radiative Fraction

6.6 Future Development of the Thermal Fenestration Models

6.6.1 Development of Thermal Parameter Correlations

Empirical correlations of the equivalent convection coefficient and the equivalent thermal conductance are required by the HB thermal fenestration model. Therefore, a comprehensive study with a full parametric set of experiments is essential to the development of the empirical correlations. As discussed in Section 6.5.3.2, a large number of variables can have an influence on the thermal parameters. The use of the guard plate in the proposed experimental method eliminates all outdoor environmental variables and most fenestration variables, except the emissivity of the inside surface of the innermost glazing layer. The window power input and the total power input (the sum of the window power input and the blind power input), which simulate the heat transfer rates at the inside surfaces of the innermost glazing layer and the fenestration system, account for these variables. Indoor environmental variables (e.g., room airflow rates and diffuser configurations), blind variables (e.g., distance between the window and the blind and type of blind installation) as well as the inside surface emissivity of the innermost glazing layer should be investigated in order to develop the empirical correlations needed to fully support the HB thermal fenestration model. Collins' study [Collins et al. 2002; Collins and Harrison 2004] may be useful in the design of the full parametric experiments and in the selection of the forms of the empirical correlations.

The fenestration test unit used in the current study has an important limitation since it can only be used to simulate positive heat fluxes (i.e., all electrical heat applied to the window and the blind go into the room). In actual situations, negative heat fluxes can occur, particularly in the winter. To simulate the negative heat fluxes, a set of experiments should be run with a cooled instead of the heated window panel. For this configuration, the heated guard plate would also be replaced by a cooled guard plate to prevent conduction heat gain from the outside. For the heated blind, no change is needed since it can be expected that, for negative heat flux cases, the negative heat flux at the inside (fictitious) surface of the fenestration system would always be lower (in absolute value) than the negative heat flux at the inside surface of the innermost glazing layer. For the fenestration test unit using a cooled panel, the calculations presented Section 6.5.2 are still valid, except that the value of the power input to the window become negative instead of positive. The total heat transfer rate at the inside surface of the fenestration system can be either positive or negative depending on the power input to the blind and the heat removed from the cooled window. In conclusion, experimental tests should be performed for both positive and negative heat fluxes in order to provide correlations that are applicable to realistic situations.

According to Collins' study [2002], the total heat flux at the equivalent inside fenestration surface can vary between -132.6 W/m² and 119.8 W/m² for the natural air flowfield with the window surface temperature ranging from 277 K to 317 K, the blind absorbed solar radiation of 60 W/m², and the window and the blind emissivities of 0.6. Although the possible maximum positive and negative heat fluxes are likely higher than those found in Collins' study, the maximum (positive) heat flux of about 360 W/m² used in the current study is expected to be high enough to cover the positive realistic range.

6.6.2 Implementation of the HB Thermal Fenestration Model

In section 6.2, equations used in the HB thermal fenestration model are presented in terms of conductive, convective, and radiative heat fluxes in order to provide a clearer understanding of the surface heat balances of the fenestration layers. To implement the model in the HB load calculation scheme, equations for the conduction, convection, and radiation terms presented in Sections 6.2.2 to 6.2.4 must first be substituted into Equations (6-1) and (6-2) for each fenestration layer. Then, the heat balance equations for all fenestration layers must be solved simultaneously with the heat balance equations for room opaque surfaces to obtain the surface temperatures of each layer of the fenestration system as well as the surface temperatures of other opaque surfaces.

The calculation procedure will depend on the form(s) of the empirical correlations of the thermal parameters required by the HB thermal fenestration model. Assuming that the thermal parameters are correlated as a function of heat fluxes (neither heat transfer rates nor surface temperatures) at the inside surface of the innermost glazing layer and at the inside (fictitious) surface of the fenestration system, a suggested calculation procedure is illustrated in Figure 6-12. The suggested calculation procedure is an iterative procedure where all surface temperatures and the thermal parameters (i.e., HB Thermal Model Parameter) required by the HB thermal fenestration model are solved iteratively until the convergence criteria is met. Any solution technique (e.g., successive substitution method, matrix formulation with linearized radiative heat transfer coefficients, Newton-Raphson method, etc.) normally used in the HBM can be used in the calculation step used to solve all surface temperatures simultaneously.

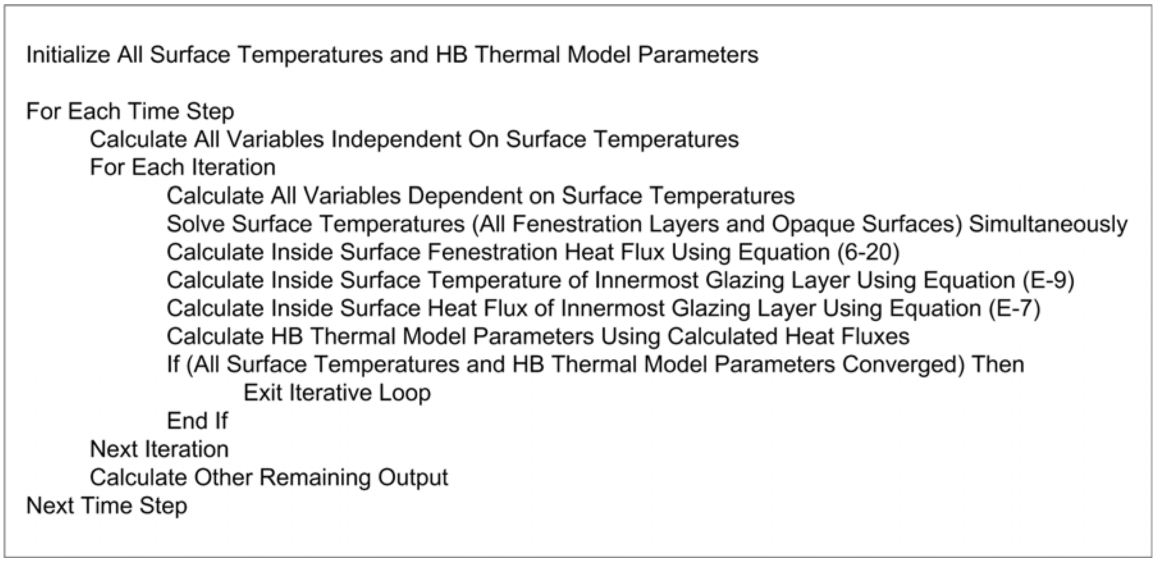

```
Initialize All Surface Temperatures and HB Thermal Model Parameters

For Each Time Step
    Calculate All Variables Independent On Surface Temperatures
    For Each Iteration
        Calculate All Variables Dependent on Surface Temperatures
        Solve Surface Temperatures (All Fenestration Layers and Opaque Surfaces) Simultaneously
        Calculate Inside Surface Fenestration Heat Flux Using Equation (6-20)
        Calculate Inside Surface Temperature of Innermost Glazing Layer Using Equation (E-9)
        Calculate Inside Surface Heat Flux of Innermost Glazing Layer Using Equation (E-7)
        Calculate HB Thermal Model Parameters Using Calculated Heat Fluxes
        If (All Surface Temperatures and HB Thermal Model Parameters Converged) Then
            Exit Iterative Loop
        End If
    Next Iteration
    Calculate Other Remaining Output
Next Time Step
```

Figure 6-12 Suggested Calculation Procedure for HB Load calculations Using HB Thermal Fenestration Model

As shown in Figure 6-12, Equations (E-7) and (E-9) are required in addition to the equations presented in Section 6.2 and those required for the opaque surfaces. Equations (E-7) and (E-9) are used to calculate the heat flux and the temperature of the inside surface of the innermost glazing layer, respectively. Since the innermost glazing layer and the blind are treated as a single layer in the HB thermal fenestration model, the inside surface temperature of the innermost glazing layer need not be solved simultaneously along with all other surface temperatures. As shown, it can be calculated explicitly using Equation (E-9) along with the known outside surface temperature of the innermost glazing layer and the known equivalent inside fenestration surface temperature.

6.6.3 Generation of RTS Thermal Model Input Parameters

In conventional window calculations (i.e. for product-rating method), the U-factor (a reciprocal of the total thermal resistance) is typically calculated based on specified winter and nighttime boundary conditions while the SHGC (the sum of the total solar transmittance and the total inward flowing solar absorption) is normally calculated based on specified summer and daytime boundary conditions [ISO 2000; LBL 2001]. For these specified boundary conditions, outdoor and indoor temperatures as well as outside and inside convection coefficients are commonly fixed. This means that these thermal parameters calculated using the product-rating method may not be suitable for load calculations where environmental conditions are variable.

Therefore, the total thermal resistance and the inward flow fractions should be generated by using the ‘complete’ HB thermal fenestration model implemented in the HBM based on design day calculations. Then, it is essential to correlate the generated output to the environmental conditions so that the results can be usable. For the RTSM, it is desirable that the generated data sets are presented in simple formats (e.g., tables, graphs and correlations). The data presentation is a subject of the future investigation.

Although the radiative/convective split of the conduction and absorbed solar heat gains can be measured directly using the proposed experimental method, it may be difficult to use the measured radiative/convective split directly since the power input to the window, one of the experimental variables, does not explicitly simulate any variable in the RTSM. Instead of correlating the measured radiative/convective split directly, it is therefore recommended that the HB thermal fenestration model also be used and the generated radiative/convective split then be correlated to the environmental conditions. In the HB thermal fenestration model, the required radiative fraction can be calculated as the ratio of the radiation term shown in Equation (6-17) to the conduction term shown in Equation (6-20). The comparison of the generated radiative fraction and the measured radiative fraction is essential to support the validity of the generated radiative fraction. Good agreements between the generated and measured radiative fractions will also support the validity of the HB thermal fenestration model.

In parallel with the current study, Spitler and Nigusse [2007] are proposing a thermal fenestration model for the RTSM for an ASHRAE research project. The model is simpler than the RTS thermal fenestration model proposed in the current study since the model combines the transmitted and absorbed solar heat gains. The model utilizes the solar heat gain coefficients (*SHGCs*) for the window and the interior solar attenuation coefficient (*IAC*) to handle the fenestration system containing an interior shading device. The optical and thermal models presented in the current study can be employed to provide information required by Spitler's model. The *IAC* for the fenestration system containing an interior blind can be approximated using the inward flowing fractions generated by the HB thermal fenestration model and the solar transmittances determined by the optical models as follows:

$$q''_{trn,sol} = I_{bm} \cdot \left(\tau^{sys}_{bm-bm} + \tau^{sys}_{bm-df}\right) + I_{sky-df} \cdot \tau^{sys}_{sky-df} + I_{gnd-df} \cdot \tau^{sys}_{gnd-df} \tag{6-49a}$$

$$q''_{abs,sol} = \sum_{i=1}^{n} Ni_i \cdot \left[\left(I_{bm} \cdot \alpha^{sys,f}_{bm-df,i}\right) + \left(I_{sky-df} \cdot \alpha^{sys,f}_{sky-df,i} + I_{gnd-df} \cdot \alpha^{sys,f}_{gnd-df,i}\right)\right] \tag{6-49b}$$

$$IAC = \frac{q''_{trn,sol} + q''_{abs,sol}}{I_{bm} \cdot SHGC_{bm} + (I_{sky-df} + I_{gnd-df}) \cdot SHGC_{df}} \tag{6-49c}$$

where $q''_{trn,sol}$ = transmitted solar heat flux of the fenestration system containing the interior blind,

$q''_{abs,sol}$ = absorbed solar heat flux of the fenestration system containing the interior blind,

$SHGC_{bm}$ = beam solar heat gain coefficient of the fenestration system without a shading device,

$SHGC_{df}$ = diffuse solar heat gain coefficient of the fenestration system without a shading device.

Like the inward flowing fractions and total thermal resistance, the *IAC* should be generated by using the HB thermal fenestration model implemented in the HBM based on design day calculations. Essentially, Equation (6-49) is implemented as a part of the HB thermal fenestration model.

6.7 Conclusions

This chapter presents two newly developed thermal fenestration models suitable for load calculation methods: one for the HBM, called The HB thermal fenestration model, and one for the RTSM, called the RTSM thermal fenestration model. The two models were developed specifically for the fenestration system containing an interior blind. The HB thermal fenestration model is based on the one-dimensional multi-layer heat balance approach. The model directly performs an energy balance at each surface of the individual layers of the fenestration system. The model treats the glazing layers, except the innermost glazing layer, fundamentally the same as existing thermal models (for a fenestration system without shading devices) that are suitable for the HBM. However, for a fenestration system containing an interior blind, the model treats the innermost glazing layer and the blind layer as a single layer. By modeling the innermost glazing layer and the blind layer as a single layer, the HB thermal fenestration model relies on an experimental method to provide two additional required parameters including the equivalent inside convection coefficient of the inside surface of the combined layer and the equivalent thermal conductance within the combined layer. Therefore, an experimental method has also been developed along with the thermal fenestration models.

The RTSM thermal fenestration model is based on the solar-thermal separation concept. The RTSM thermal fenestration model includes both the fenestration heat gain calculation and the heat gain-to-cooling load conversion calculation. The model requires various input parameters including total solar transmittances, layer-specific solar absorptances, layer-specific inward flowing fractions, total thermal resistance, and radiative/convective splits. Optical models can be used to obtain the solar transmittances and absorptances while the HB thermal fenestration model can be used to obtain the inward flowing fractions, the thermal resistance as well as the radiative/convective splits. Consequently, the chapter also presents a calculation procedure used in the HB thermal fenestration model to generate thermal parameters required by the RTSM thermal fenestration model.

Moreover, the chapter also presents the experimental method used to support the new thermal fenestration models. In addition to measuring the two HB thermal model parameters, the experimental method can also be used to obtain the radiative/convective splits of the absorbed solar heat gain and the conduction heat gain required by the RTSM thermal fenestration model. The experimental method is based on the measurement of the radiative heat gain from a fenestration test unit representing the fenestration system containing an interior blind at steady state. In addition to the radiant heat gain measurement, the measurements of the electrical power input used to heat the fenestration layers and various temperatures are all essential. For the current study, a limited set of experiments were performed to illustrate the feasibility of supporting the thermal models with measured data and to evaluate the effects of experimental variables on the thermal model parameters. Based on the experimental findings, various suggestions for future studies are also provided.

CHAPTER 7

CONCLUSIONS AND RECOMMENDATIONS

7.1 Conclusions

The objective of this study was to enhance the modeling of fenestration systems containing shading devices for building thermal load and energy calculations. The models considered for the current study were those compatible with the Heat Balance Method (HBM) and the Radiant Time Series Method (RTSM), which are currently the recommended ASHRAE cooling load calculation procedures. The focus of the current study was on the simulation of the fenestration system containing a slat-type blind.

To enhance the fenestration simulation, a new comprehensive blind model, a new optical fenestration model and new thermal fenestration models were developed. The optical models were based on the multi-layer optical calculation approach where overall optical properties of the fenestration system containing a slat-type blind can be determined as a function of the optical properties of glazing and blind layers. The current study emphasized only the optical models for predicting blind and overall optical properties. The thermal model developed for the HBM was based on the one-dimensional multi-layer heat balance approach while the thermal model developed for the RTSM was based on the solar-thermal separation concept. The new thermal models (the model for the HBM, in particular) are applicable to the fenestration system containing an interior blind only. The thermal model for the RTSM relies on the thermal model for the HBM as well as optical models to generate its required input parameters. The thermal model for the HBM relies on an experimental method (as well as existing correlations for glazing layers) to provide its required thermal parameters. In the following sections, the significant contributions of the current study are summarized.

7.1.1 Optical Models

The contributions of the optical study may be summarized as follows:

- A comprehensive model for predicting optical properties of a slat-type blind has been developed. Capabilities of the comprehensive blind model surpass those of existing models in various aspects. The comprehensive blind model takes into account slat thickness as well as slat curvature. The model also accounts for slat surfaces being non-perfect reflectors (i.e. partially diffuse and partially specular-reflecting surfaces). The model can handle both blinds having horizontal slats (e.g. Venetian blinds, mini blinds, etc.) and blinds having vertical slats (commonly called vertical blinds). In addition, the model can be used for blinds having either opaque, translucent, or perforated slat surfaces. Moreover, the model allows different radiative characteristics on different sides of the blind slats. To handle these various aspects, the comprehensive blind model utilizes several computation techniques including (1) analytical formulations to predict fractions of the sunlight incident on blind slats and of the sunlight passing through the blind assembly without any reflections, (2) the net radiation method to deal with reflected radiation for a blind with purely diffuse slats, (3) the Monte-Carlo ray-tracing technique to deal with reflected radiation for a blind with non-purely diffuse slats, (4) numerical integration to deal with diffuse solar radiation.
- An optical fenestration model for predicting overall optical properties of the fenestration system has been developed. Unlike existing models, the new optical fenestration model is consistent with the comprehensive blind model and suitable for load calculations. The model treats beam and diffuse components of solar radiation separately, and the model

distinguishes between diffuse solar radiation from the sky and from the ground. The model is applicable to the fenestration system containing an exterior blind, a between-pane blind, or an interior blind. The model is presented in analytical formulations that require optical properties of the glazing layers and the blind layer as inputs.

- An in situ experimental method has been developed for measuring the total solar transmittance of the fenestration system and the slat solar reflectance of the blind assembly from field measurements. The total solar transmittance of the fenestration system is a primary metric commonly used to evaluate optical models, and the slat solar reflectance is a required input of the optical blind model. Measured data obtained by the in situ experimental method were used to illustrate the validity of the comprehensive blind model. Overall, the comprehensive blind model consistently agreed quite well with measured total solar transmittance for the blinds that were tested. However, further investigation is needed for quasi-specular reflectors. Overall good agreements between measured and predicted results supported the validity of the comprehensive blind model.

7.1.2 Thermal Models

The contributions of the thermal study may be summarized as follows:

- A thermal model suitable for the HBM, called the HB thermal fenestration model, has been developed. Like existing models suitable for the HBM, the HB thermal fenestration model utilizes a thermal glazing model (i.e. a thermal model for a fenestration system without shading devices) to handle the thermal interactions of the glazing layers. However, the HB thermal fenestration model simplifies the thermal interactions between the innermost glazing layer and the blind, the thermal interactions between the innermost glazing layer/air gap and the room, and the thermal interactions between the blind and the room. These interactions are simplified by modeling the innermost glazing layer and the interior blind layer as a single layer. Consequently, the model requires two additional thermal parameters, the so-called equivalent convection coefficient and the so-called equivalent thermal conductance, which together account for all the aforementioned thermal interactions. Unlike thermal parameters required by existing thermal models, these two thermal parameters can be feasibly measured in a relatively simple laboratory procedure.

- To support the HB thermal fenestration model, an experimental method has been developed along with the new model. The experimental method is based on the measurement of the radiative heat gain from a simulated fenestration test unit at steady state. In addition to the radiant heat gain measurement, the measurement of the electrical power input used to heat the fenestration layers and the measurement of various temperatures are required. To illustrate the feasibility of supporting the thermal models with measured data, a limited set of experiments were performed in the current study. As discussed in detail in Chapter 6, the feasibility of the experimental method was supported by the experimental uncertainty analysis, the verification of experimental measurements, and a comparison between measured data and published numerical results. In addition, the experimental investigation evaluated the effects of experimental variables on thermal parameters in order to provide useful information for the design of the full parametric experiments required for the development of empirical correlations for the HB thermal fenestration model.
- In addition to the HB thermal fenestration model, a thermal model suitable for the RTSM, called the RTS thermal fenestration model, has been developed. The RTS thermal fenestration model is based on the solar-thermal separation concept and thus requires various (solar) optical and thermal parameters as input data. The newly developed optical models discussed in the previous section can be used to provide the required optical input parameters. The HB thermal fenestration model can be used to provide the required thermal input parameters. As a result, the calculation procedure for the required

thermal parameters, which is considered as a part of the HB thermal fenestration model, has also been developed.

7.2 Recommendations for Future Work

Although the current study has enhanced the fenestration simulation by developing several new models as well as their supporting experimental methods used to handle both optical and thermal phenomena, much work still remains. Some recommendations for future work are provided as follows:

- To fully utilize the new thermal fenestration models, several additional studies are needed as discussed in Chapter 6. These studies include (1) the development of the empirical correlations of thermal parameters required by the HB thermal fenestration model, (2) the implementation of the HB thermal fenestration model in the load calculation procedure (i.e., in the HBM), and (3) the generation of the thermal parameters required by the RTS thermal fenestration model.
- When the development of the thermal models is complete (i.e., they are ready to be used), it is then essential to validate these new models. Various validation techniques may be used. For instance, as discussed in Chapter 6, the comparison of the radiative fraction generated by the HB thermal fenestration model and that measured by the proposed experimental method can be used to illustrate the validity of the generated radiative fraction as well as the validity of the HB thermal fenestration model. Also, an experimental validation (similar to the ASHRAE RP-1117 study [Fisher et al. 2002]) of the load calculation methods using the new thermal models should be conducted. For this validation, it is essential to perform experimental tests for both the fenestration system without the blind and the fenestration with the blind so that the effect of the thermal fenestration model(s) on thermal loads can be quantified. It will also be useful to

test various types of the fenestration system (various combinations of the glazing layers and the interior blind) to illustrate the general applicability of the thermal models.

- The current study only emphasized the simulation of the fenestration system containing a slat-type blind. However, a vast number of shading devices exist including drapes, roller shades, shade screens, etc. Therefore, future studies of these shading devices (both optical and thermal) are also recommended to further enhance the simulation of fenestration systems with these shading devices.

REFERENCES

Arasteh, D. K., M. S. Reilly, and M. D. Rubin. 1989. A Versatile Procedure for Calculating Heat Transfer through Windows. *ASHRAE Transactions*. 95 (2): 755-765.

ASHRAE. 2001. *2001 ASHRAE Handbook - Fundamentals*. Atlanta, GA: American Society of Heating, Refrigerating and Air-Conditioning Engineers, Inc (ASHRAE).

ASHRAE. 2005. *2005 ASHRAE Handbook - Fundamentals*. Atlanta, GA: ASHRAE.

ASTM. 1996. *ASTM Standard E 903-96, Standard Test Method for Solar Absorptance, Reflectance, and Transmittance of Materials Using Integrating Spheres*. West Conshohocken, PA: ASTM International.

Beckwith, T. G., R. D. Marangoni, and J. H. Lienhard V. 1993. *Mechanical Measurements, Fifth Edition*. Reading, MA: Addison-Wesley.

Berdahl, P. and S. E. Bretz. 1997. Preliminary Survey of the Solar Reflectance of Cool Roofing Materials. *Energy and Buildings*. 25 (2): 149-158.

Breitenbach, J. S., Lart I. Längle, and J. L. J. Rosenfeld. 2001. Optical and Thermal Performance of Glazing with Integral Venetian Blinds. *Energy and Buildings*. 33 (5): 433-442.

Brunger, A. P. and F. C. Hooper. 1993. Anisotropic Sky Radiance Model Based on Narrow Field of View Measurements of Shortwave Radiance. *Solar Energy*. 51 (1): 53-64.

Chantrasrisalai, C. and D. E. Fisher. 2004. Comparative Analysis of One-Dimensional Slat-Type Blind Models. Proceedings of SimBuild 2004, First National Conference of IBPSA-USA, August 2004, Boulder, CO. International Building Performance Simulation Association - USA Affiliate (IBPSA-USA).

Chantrasrisalai, C. and D. E. Fisher. 2006. An In Situ Experimental Method for the Development and Validation of Slat-Type Blind Models in Cooling Load Calculations. *Journal of Solar Energy Engineering*. 128 (2): 189-198.

Chantrasrisalai, C. and D. E. Fisher. 2007. Lighting Heat Gain Parameters: Experimental Method. *HVAC&R Research*. 13 (2): 283-303.

Clarke, J. A. 2001. *Energy Simulation in Building Design, Second Edition*. Woburn, MA: Butterworth-Heinemann.

Cohen, M. F. and D.P. Greenberg. 1985. The Hemi-Cube: a Radiosity Solution for Complex Environments. *Computer Graphics*. 19: 31-40.

Collins, M. R. and S. J. Harrison. 1999. Calorimetric Measurement of the Inward-Flowing Fraction of Absorbed Solar Radiation in Venetian Blinds. *ASHRAE Transactions*. 105 (2): 1022-1030.

Collins, M. R., S. J. Harrison, P. H. Oosthuizen, and D. Naylor. 2002. Sensitivity Analysis of Heat Transfer from an Irradiated Window and Horizontal Louvered Blind Assembly. *ASHRAE Transactions*. 108 (1): 503-511.

Collins, M. R. 2004. Convective Heat Transfer Coefficients from an Internal Window Surface and Adjacent Sunlit Venetian Blind. *Energy and Buildings*. 36 (3): 309-318.

Collins, M. R. and S. J. Harrison. 2004. Estimating the Solar Heat and Thermal Gain from a Window with an Interior Venetian Blind. *ASHRAE Transactions*. 110 (1): 486-500.

Collins, M. R. and J. L. Wright. 2006. Calculating Center-Glass Performance Indices of Windows with a Diathermanous Layer. *ASHRAE Transactions*. 112 (2): 22-29.

DOE. 2002. EnergyPlus Engineering Document: the Reference to EnergyPlus Calculations. Reference Manual, U.S. Department of Energy.

DOE. 2006. EnergyPlus Engineering Document: the Reference to EnergyPlus Calculations. Reference Manual, U.S. Department of Energy.

Duarte, N., D. Naylor, P. H. Oosthuizen, and S. J. Harrison. 2001. An Interferometric Study of Free Convection at a Window Glazing with a Heated Venetian Blind. *HVAC&R Research*. 7 (2): 169-184.

EIA. 1998. A Look at Commercial Buildings in 1995: Characteristics, Energy Consumption, and Energy Expenditures. DOE/EIA-0625 (95) Report, Energy Information Administration, US Department of Energy, Washington, DC.

EIA. 1999. A Look at Residential Energy Consumption in 1997. DOE/EIA-0632 (97) Report, Energy Information Administration, US Department of Energy, Washington, DC.

EIA. 2000. Annual Energy Review 1999. DOE/EIA-0384 (99) Report, Energy Information Administration, US Department of Energy, Washington, DC.

Eldridge, D., D. E. Fisher, I. S. Iu, and C. Chantrasrisalai. 2003. Experimental Validation of Design Cooling Load Procedures: Facility Design. *ASHRAE Transactions*. 109 (2): 151-159.

Farber, E. A., W. A. Smith, C. W. Pennington, and J. C. Reed. 1963. Theoretical Analysis of Solar Heat Gains through Insulating Glass with Inside Shading. *ASHRAE Transactions*. 69: 392-405.

Finlayson, E. U., D. K. Arasteh, C. Huizenga, M. D. Rubin, and M. S. Reilly. 1993. Window 4.0: Documentation of Calculation Procedures. Reference Manual, LBL-33943 Report, Lawrence Berkeley National Laboratory, Berkeley, CA.

Fisher, D. E. and C. O. Pedersen. 1997. Convective Heat Transfer in Building Energy and Thermal Load Calculations. *ASHRAE Transactions*. 103 (2): 137-148.

Fisher, D. E., J. D. Spitler, D. Eldridge, C. Chantrasrisalai, and I. S. Iu. 2002. Experimental Validation of Heat Balance/RTS Cooling Load Procedures. ASHRAE RP-1117 Final Report, ASHRAE, Atlanta, GA.

Gueymard, C. 1987. An Anisotropic Solar Irradiance Model for Tilted Surfaces and Its Comparison with Selected Engineering Algorithms. *Solar Energy*. 38 (5): 367-386.

Hosni, M. H., B. W. Jones, J. M. Sipes, and Y. Xu. 1998. Total Heat Gain and the Split Between Radiant and Convective Heat Gain from Office and Laboratory Equipment in Buildings. *ASHRAE Transactions*. 104 (1A): 356-365.

Hottel, S. C. and A.F. Sarofim. 1967. *Radiative Transfer*. New York City, New York: McGraw-Hill.

Huang, N. Y. T., J. L. Wright, and M. R. Collins. 2006. Thermal Resistance of a Window with an Enclosed Venetian Blind: Guarded Heater Plate Measurements. *ASHRAE Transactions*. 112 (2): 13-21.

Igawa, N., Y. Koga, T. Matsuzawa, and H. Nakamura. 2004. Models of Sky Radiance Distribution and Sky Luminance Distribution. *Solar Energy*. 77 (2): 137-157.

Incropera, F. P. and D. P. Dewitt. 2002. *Fundamentals of Heat and Mass Transfer, Fifth Edition*. New York, NY: John Wiley & Son Inc.

ISO. 2000. *ISO 15099, Thermal Performance of Windows, Doors, and Shading Devices -- Detailed Calculations (Draft)*. Geneva, Switzerland: International Organization for Standardization.

Jones, B. W., M. H. Hosni, and J. M. Sipes. 1998. Measurement of Radiant Heat Gain from Office Equipment Using a Scanning Radiometer. *ASHRAE Transactions*. 104 (1B): 1775-1783.

Jordan, R. C. and J. L. Threlkeld. 1959. Determination of the Effectiveness of Window Shading Materials on the Reduction of Solar Radiation Heat Gain. *ASHRAE Transactions*. 65: 683-696.

Kerrisk, J. F., N. M. Schnurr, J. E. Moore, and B. D. Hunn. 1981. The Custom Weighting-Factor Method for Thermal Load Calculations in the DOE-2 Computer Program. *ASHRAE Transactions*. 87 (2): 569-584.

Keyes, M. W. 1967. Analysis and Rating of Drapery Materials Used for Indoor Shading. *ASHRAE Transactions*. 73 (1): 8.4.1-8.4.15.

Klems, J. H. 1994a. A New Method for Predicting the Solar Heat Gain of Complex Fenestration Systems - 1. Overview and Derivation of the Matrix Layer Calculation. *ASHRAE Transactions*. 100 (1): 1065-1072.

Klems, J. H. 1994b. A New Method for Predicting the Solar Heat Gain of Complex Fenestration Systems - 2. Detailed Description of the Matrix Layer Calculation. *ASHRAE Transactions*. 100 (1): 1073-1086.

Klems, J. H. and J. L. Warner. 1995. Measurement of Bidirectional Optical Properties of Complex Shading Devices. *ASHRAE Transactions*. 101 (1): 791-801.

Klems, J. H., J. L. Warner, and G. O. Kelly. 1995. A New Method for Predicting the Solar Heat Gain of Complex Fenestration Systems. LBL-36995 Report, Lawrence Berkeley National Laboratory, Berkeley, CA.

Klems, J. H. and G. O. Kelly. 1996. Calorimetric Measurements of Inward Flowing Fraction for Complex Glazing and Shading Systems. *ASHRAE Transactions*. 102 (1): 947-954.

Klems, J. H., J. L. Warner, and G. O. Kelly. 1996. A Comparison between Calculated and Measured SHGC for Complex Fenestration Systems. *ASHRAE Transactions*. 102 (1): 931-939.

Klems, J. H. and J. L. Warner. 1997. Solar Heat Gain Coefficient of Complex Fenestrations with a Venetian Blind for Differing Slat Tilt Angles. *ASHRAE Transactions*. 103 (1): 1026-1034.

Klems, J. H. 2002. Solar Heat Gain through Fenestration Systems Containing Shading: Summary of Procedures for Estimating Performance from Minimal Data. *ASHRAE Transactions*. 108 (1): 512-524.

Kline, S. J. and F. A. McClintock. 1953. Describing Uncertainties in Single-Sample Experiments. *Mechanical Engineering*. 75: 3-8.

LBL. 1994. Window 4.1: Program Description. User Manual, LBL-35298 Report, Lawrence Berkeley National Laboratory, Berkeley, CA.

LBL. 2001. Window 5.0 User Manual: Program Description. User Manual, LBNL-44789 Report, Lawrence Berkeley National Laboratory, Berkeley, CA.

Liesen, R. J. and C. O. Pedersen. 1997. An Evaluation of Inside Surface Heat Balance Models for Cooling Load Calculations. *ASHRAE Transactions*. 103 (2): 485-502.

Littlefair, P. J. 1992. Daylight Coefficients for Practical Computation of Internal Illuminances. *Lighting Research & Technology*. 24 (3): 127-135.

Machin, A. D., D. Naylor, S. J. Harrison, and P. H. Oosthuizen. 1998. Experimental Study of Free Convection at an Indoor Glazing Surface with a Venetian Blind. *HVAC&R Research*. 4 (2): 153-166.

Mahan, J. R. 2002. *Radiation Heat Transfer: a Statistical Approach*. New York, NY: John Wiley & Sons.

McClellan, T. M. and C. O. Pedersen. 1997. Investigation of Outside Heat Balance Models for Use in a Heat Balance Cooling Load Calculation Procedure. *ASHRAE Transactions*. 103 (2): 469-484.

McCluney, R. and L. Mills. 1993. Effect of Interior Shade on Window Solar Gain. *ASHRAE Transactions*. 99 (2): 565-570.

McCluney, R. 2002. Suggested Methodologies for Determining the SHGC of Complex Fenestration Systems for NFRC Ratings. FSEC-PF-422-02 Report, Florida Solar Energy Center, University of Central Florida.

McQuiston, F. C., J. D. Parker, and J. D. Spitler. 2005. *Heating, Ventilating, and Air Conditioning: Analysis and Design, Sixth Edition*. Hoboken, NJ: John Wiley & Sons.

Modest, M. F. 2003. *Radiative Heat Transfer, Second Edition*. Boston, MA: Academic Press.

Moore, G. L. and C. W. Pennington. 1967. Measurement and Application of Solar Properties of Drapery Shading Materials. *ASHRAE Transactions*. 73 (1): 8.3.1-8.3.15.

O'Rourke, J. 1994. *Computational Geometry in C*. New York, N.Y.: Cambridge University Press.

Oosthuizen, P. H., L. Sun, S. J. Harrison, D. Naylor, and M. Collins. 2005. The Effect of Coverings on Heat Transfer from a Window to a Room. *Heat Transfer Engineering*. 26 (5): 47-65.

Ozisik, N. and L. F. Schutrum. 1959. Heat Flow through Glass with Roller-Shades. *ASHRAE Transactions*. 65: 697-716.

Ozisik, N. and L. F. Schutrum. 1960a. Solar Heat Gain Factors for Windows with Drapes. *ASHRAE Transactions*. 66: 228-239.

Ozisik, N. and L. F. Schutrum. 1960b. Solar Heat Gains through Slat-Type Between-Glass Shading Devices. *ASHRAE Transactions*. 66: 359-373.

Parmelee, G. V. and W. W. Aubele. 1952. The Shading of Sunlit Glass: an Analysis of the Effect of Uniformly Spaced Flat Opaque Slats. *ASHVE Transactions*. 58: 377-398.

Parmelee, G. V., W. W. Aubele, and D. J. Vild. 1953. The Shading of Sunlit Glass: an Experimental Study of Slat-Type Sun Shades. *ASHVE Transactions*. 59: 221-240.

Parmelee, G. V. and D. J. Vild. 1953. Design Data for Slat-Type Sun Shades for Use in Load Estimating. *ASHVE Transactions*. 59: 403-434.

Pedersen, C. O., D. E. Fisher, and R. J. Liesen. 1997. Development of a Heat Balance Procedure for Calculating Cooling Loads. *ASHRAE Transactions*. 103 (2): 459-468.

Pedersen, C. O., D. E. Fisher, J. D. Spitler, and R. J. Liesen. 1998. *Cooling and Heating Load Calculation Principles*. Atlanta, GA: ASHRAE.

Pedersen, C. O., R. J. Liesen, R. K. Strand, D. E. Fisher, L. Dong, and P. G. Ellis. 2001. A Toolkit for Building Load Calculations. Computer Program, ASHRAE, Atlanta, GA.

Pennington, C. W., W. A. Smith, E. A. Farber, and J. C. Reed. 1964. Experimental Analysis of Solar Heat Gains through Insulating Glass with Indoor Shading. *ASHRAE Transactions*. 70: 54-68.

Perez, R., P. Ineichen, R. Seals, J. Michalsky, and R. Stewart. 1990. Modeling Daylight Availability and Irradiance Components from Direct and Global Irradiance. *Solar Energy*. 44 (5): 271-289.

Pfrommer, P. 1995. Thermal Modelling of Highly Glazed Spaces. Ph.D. Thesis, De Montfort University, Leicester, UK.

Pfrommer, P., K. J. Lomas, and Chr. Kupke. 1996. Solar Radiation Transport through Slat-Type Blinds: a New Model and Its Application for Thermal Simulation of Buildings. *Solar Energy*. 57 (2): 77-91.

Phillips, J., D. Naylor, S. J. Harrison, and P. H. Oosthuizen. 1999. Free Convection from a Window Glazing with a Venetian Blind: Numerical Model Development. *Transactions of the CSME*. 23 (1B): 159-172.

Phillips, J., D. Naylor, P. H. Oosthuizen, and S. J. Harrison. 2001. Numerical Study of Convective and Radiative Heat Transfer from a Window Glazing with a Venetian Blind. *HVAC&R Research*. 7 (4): 383-402.

Rheault, S. and E. Bilgen. 1989. Heat Transfer Analysis in an Automated Venetian Blind Window System. *Journal of Solar Energy Engineering*. 111: 89-95.

Rheault, S. and E. Bilgen. 1990. Experimental Study of Full-Size Automated Venetian Blind Windows. *Solar Energy*. 44 (3): 157-160.

Rogers, D. F. 1998. *Procedural Elements for Computer Graphics*. Boston, MA: WCB/McGraw-Hill.

Rosenfeld, J. L. J., W. J. Platzer, H. van Dijk, and A. Maccari. 2000. Modelling the Optical and Thermal Properties of Complex Glazing: Overview of Recent Development. *Solar Energy*. 69 (Supplement) (1-6): 1-13.

Rousseau, P. G. and E. H. Mathews. 1993. Needs and Trends in Integrated Building and HVAC Thermal Design Tools. *Building and Environment*. 28 (4): 439-452.

Rubin, M., K. von Rottkay, and R. Powles. 1998. Window Optics. *Solar Energy*. 62 (3): 149-161.

Simmler, H., U. Fischer, and F. C. Winkelmann. 1996. Solar-Thermal Window Blind Model for DOE-2. Simulation Research Group Internal Report, Lawrence Berkeley National Laboratory, Berkeley, CA.

Spitler, J. D., D. E. Fisher, and D. C. Zietlow. 1989. A Primer on the Use of Influence Coefficients in Building Simulation. *Proceedings of Building Simulation '89, June 1989, Vancouver, British Columbia, Canada*. IBPSA.

Spitler, J. D., D. E. Fisher, and C. O. Pedersen. 1997. The Radiant Time Series Cooling Load Calculation Procedure. *ASHRAE Transactions*. 103 (2): 503-515.

Spitler, J. D. and B. Nigusse. 2007. Personal Communication.

Todesco, G. 1996. Super-Efficient Buildings: How Low Can You Go? *ASHRAE Journal*. 38 (12): 35-40.

van Dijk, D. and J. Goulding. 1996. WIS -- Advanced Windows Information System. WIS Reference Manual, TNO Building and Construction Research, Delft, Netherlands.

van Dijk, D. and H. Oversloot. 2003. WIS, the European Tool to Calculate Thermal and Solar Properties of Windows and Window Components. *Proceedings of Building Simulation '03, August 2003, Eindhoven, Netherlands*. IBPSA.

Van Dyck, R. L. and T. P. Konen. 1982. Energy Conservation through Interior Shading of Windows: An Analysis, Test and Evaluation of Reflective Venetian Blinds. LBL-14369 Report, Lawrence Berkeley National Laboratory, Berkeley, CA.

Vartiainen, E. 2000. A New Approach to Estimating the Diffuse Irradiance on Inclined Surfaces. *Renewable Energy*. 20 (1): 45-64.

Vida, J., I. Foyo-Moreno, and L. Alados-Arboledas. 1999. Performance Validation of MURAC, a Cloudless Sky Radiance Model Proposal. *Energy*. 24 (8): 705-721.

Wilson, B. A. 2007. Experimental Measurement of Radiation Heat Transfer from Complex Fenestration Systems. Master Thesis, Oklahoma State University, Stillwater, Oklahoma, USA.

Winkelmann, F. C., B. E. Birdsall, W. F. Buhl, K. L. Ellington, A. E. Erdem, J. J. Hirsch, and S. Gates. 1993. DOE-2 Supplement, Version 2.1E. LBL-34947 Report, Lawrence Berkeley National Laboratory, Berkeley, CA.

Winkelmann, F.C. 2001. Modeling Windows in EnergyPlus. *Proceedings of Building Simulation '01, August 2001, Rio de Janeiro, Brazil*. IBPSA.

Wright, J. F. and H. F. Sullivan. 1995. VISION 4 Glazing System Thermal Analysis. Reference Manual, Department of Mechanical Engineering, University of Waterloo, Ontario, Canada.

Wright, J. L. 1998. Calculating Center-Glass Performance Indices of Windows. *ASHRAE Transactions*. 104 (1B): 1230-1241.

Wright, J. L. and N. A. Kotey. 2006. Solar Absorption by Each Element in a Glazing/Shading Layer Array. *ASHRAE Transactions*. 112 (2): 3-12.

Yahoda, D. S. and J. L. Wright. 2004a. Methods for Calculating the Effective Longwave Radiative Properties of a Venetian Blind Layer. *ASHRAE Transactions*. 110 (1): 463-473.

Yahoda, D. S. and J. L. Wright. 2004b. Heat Transfer Analysis of a Between-Panes Venetian Blind Using Effective Longwave Radiative Properties. *ASHRAE Transactions*. 110 (1): 455-462.

Yahoda, D. S. and J. L. Wright. 2005. Methods for Calculating the Effective Solar-Optical Properties of a Venetian Blind Layer. *ASHRAE Transactions*. 111 (1): 572-586.

Ye, P., S. J. Harrison, and P. H. Oosthuizen. 1999. Convective Heat Transfer from a Window with a Venetian Blind: Detailed Modeling. *ASHRAE Transactions*. 105 (2): 1031-2037.

Yellott, J. I. 1965. Drapery Fabrics and Their Effectiveness in Solar Heat Control. *ASHRAE Transactions*. 71 (1): 260-272.

BIBLIOGRAPHIES

Dewey, B. R. 1988. *Computer Graphics for Engineers*. New York, NY: Harper & Row.

Edwards, D. K. 1981. *Radiation Heat Transfer Notes*. Washington, D.C.: Hemisphere Publishing Corporation.

Farin, G. E. and D. Hansford. 1998. *The Geometry Toolbox for Graphics and Modeling*. Natick, MA: A.K. Peters.

Ferguson, R. S. 2001. *Practical Algorithms for 3D Computer Graphics*. Natick, MA: A K Peters.

Foley, J. D., A. van Dam, S. K. Feiner, J. F. Hughes, and R. L. Phillips. 1994. *Introduction to Computer Graphics*. Reading, MA: Addison-Wesley.

Hammersley, J. M. and D. C. Handscomb. 1965. *Monte Carlo Methods*. New York, NY: Chapman and Hall.

Harrington, S. 1983. *Computer Graphics: a Programming Approach*. New York, NY: McGraw-Hill.

Love, T. J. 1968. *Radiative Heat Transfer*. Columbus, OH: Charles E. Merrill Publishing.

Mäntylä, M. 1988. *An Introduction to Solid Modeling*. Rockville, MD: Computer Science Press.

Newman, W. M. and R. F. Sproull. 1979. *Principles of Interactive Computer Graphics*. New York, NY: McGraw-Hill.

Sedgewick, R. 1988. *Algorithms, Second Edition*. Reading, MA: Addison-Wesley.

Wiebelt, J. A. 1966. *Engineering Radiation Heat Transfer*. New York City, NY: Holt, Rinehart and Winston.

Williams, C. S. and O. A. Becklund. 1972. *Optics: a Short Course for Engineers and Scientists*. New York, NY: Wiley-Interscience.

Wilt, N. 1994. *Object-Oriented Ray Tracing in C++*. New York, NY: John Wiley & Sons.

APPENDIX A

RAY-TRACING OPTICAL BLIND MODEL FOR DIRECT SOLAR RADIATION

A.1 Overview

The ray-tracing optical blind model consists of two sub-models: the flat-slat blind sub-model and the curved-slat blind sub-model. The flat-slat blind sub-model is used to deal with slat-type blinds having non-zero-thickness flat slats, which are typical of blinds made of wood. On the other hand, the curved-slat blind sub-model is used to deal with slat-type blinds having negligible-thickness curved slats, which are typical of blinds made of vinyl and aluminum. Figure A-1 illustrates blind enclosure geometries used in the ray-tracing model for the flat-slat and the curved-slat blinds.

To determine optical blind properties, the ray-tracing model uses analytically derived formulations to determine how much the sunlight passes directly through the blind assembly, and how much the sunlight falls on blind slats. The model then utilizes the so-called Monte-Carlo ray tracing technique [Mahan 2002] to deal with the sunlight that reflects from the blind slats. Detailed calculations required by the ray-tracing model are described in the following sections.

The calculation procedure used in the ray-tracing blind model is summarized below.

- First, calculate essential information used to define the blind enclosure.
- Then, calculate limits of profile angle and determine calculation cases.
- Next, calculate ratios of sunlight passing directly through the blind and falling on slat surface(s).
- Then, determine illuminated slat surface(s).
- Next, perform ray-tracing calculations to trace rays emitted from the illuminated slat surface(s).
- Finally, calculate optical blind properties.

A.2 Blind Enclosure Geometries

In the ray-tracing model, the whole blind assembly is represented by two consecutive slats. The blind enclosure is formed by two adjacent slats along with fictitious surfaces at the outside and inside openings. Figure A-1 shows blind enclosures along with slat geometry, profile angle, and the coordinate systems used in the model. As illustrated in Figure A-1, the left hand side figure shows the enclosure for the flat-slat blind sub-model while the right hand side figure shows the enclosure for the curved-slat blind sub-model. As shown, the sunlight comes from the left side of the figure. Therefore, the outside opening is represented by the left hand side fictitious surface and the inside opening is represented by the right hand side fictitious surface.

A.2.1 Definitions of Slat Geometry

The following terms are used to define slat geometry as shown in Figure A-1.

- Slat angle (ψ) is defined as the angle between the straight line connecting edges of the slat and the plane perpendicular to the blind assembly (the horizontal line shown in Figure A-1). Figure A-1 shows a downward facing blind (having horizontal slats) with a positive slat angle.

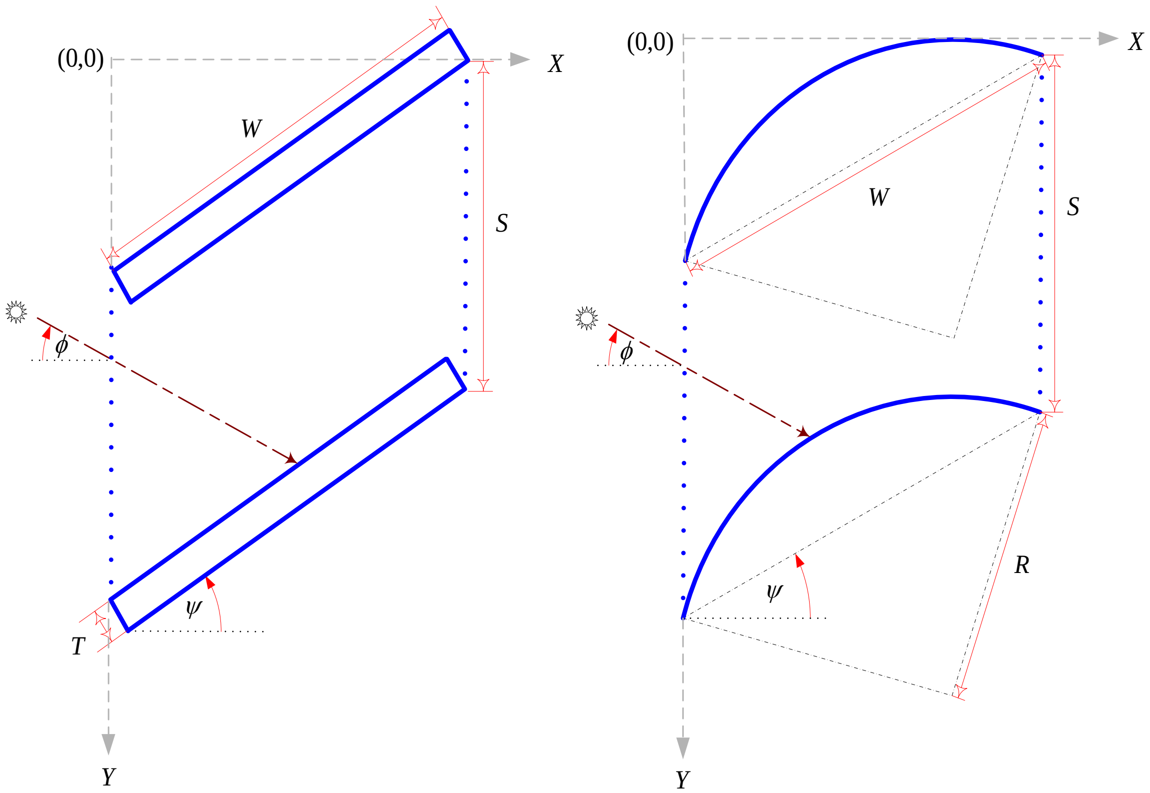

A) Enclosure Geometry for Flat Slat Blinds

B) Enclosure Geometry for Curved Slat Blinds

Figure A-1 Blind Enclosure Geometries and Coordinate Systems

- Slat spacing (*S*) is defined as the distance between adjacent slats (measured vertically for blinds having horizontal slats). For blinds having non-zero-thickness flat slats, the slat spacing is the distance from the upper surface of the upper slat to the upper surface of the lower slat.
- Slat width (*W*) is defined as the distance of a straight line from one end of the slat to the other end as shown in the figure.
- Slat thickness (*T*) is defined as the distance from the upper surface to the lower surface of each slat. The slat thickness is used only for the flat-slat blind sub-model.

- Slat curvature radius (*R*) is defined as the distance from the center of curvature radius to the slat surface. The slat curvature radius is used only for the curved-slat blind sub-model.

A.2.2 Calculations for Blinds with Flat Slats

Figure A-2 shows the blind enclosure for the flat-slat blind model. The figure also shows six essential points (*A* to *F*) used to define the blind enclosure, the x-y coordinate system used in the model, and the total width (*TW*) and total height (*TH*) of the blind enclosure. The flat-slat blind model assumes known slat geometry previously defined including slat angle, slat spacing, slat width, and slat thickness (i.e. these parameters are required inputs).

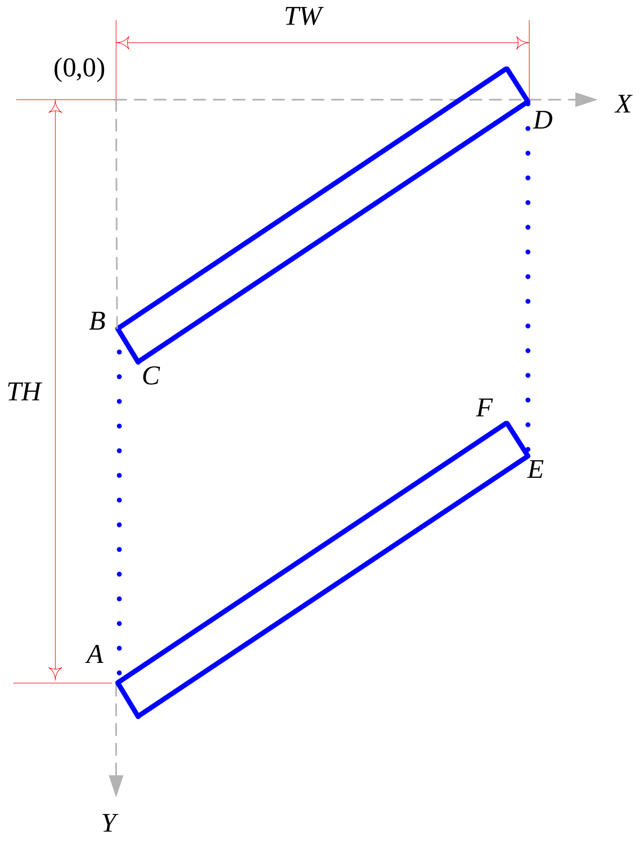

Figure A-2 Blind Enclosure for the Flat-Slat Blind Model

Knowing slat geometry, the total width and total height can then be given by:

$$TW = W\cos(\psi) + T\sin(\psi) \tag{A-1}$$

$$TH = S + W\sin(\psi) - T\cos(\psi) \tag{A-2}$$

Next, the six points defining the blind enclosure can be determined by:

$$A = (0, TH) \tag{A-3}$$

$$B = (0, TH - S) \tag{A-4}$$

$$C = (T\sin(\psi), W\sin(\psi)) \tag{A-5}$$

$$D = (TW, 0) \tag{A-6}$$

$$E = (TW, S) \tag{A-7}$$

$$F = (W\cos(\psi), S - T\cos(\psi)) \tag{A-8}$$

Finally, surfaces forming the blind enclosure are determined as straight lines connecting two points. As shown in Figure A-2, the outside opening is the line from points *A* to *B*, the upper slat edge the line from points *B* to *C*, the upper slat the line from points *C* to *D*, the inside opening the line from points *D* to *E*, the lower slat edge the line from points *E* to *F*, and the lower slat the line from points *F* to *A*.

A.2.3 Calculations for Blinds with Curved Slats

Figure A-3 shows the blind enclosure for the curved-slat blind model. The figure also shows essential parameters used to define the blind enclosure, the x-y coordinate system used in the model, and the total width (*TW*) and total height (*TH*) of the blind enclosure. The curved-slat blind model assumes known slat geometry previously defined including slat angle, slat spacing, slat width, and slat curvature radius.

As shown in Figure A-3, the angle η that relates slat width to slat radius is defined as a half of an angle between a straight line from the right slat edge to the curvature center and a straight line from the left slat edge to the curvature center. The angle η can be determined by:

$$\eta = \sin^{-1}(W/2R) \tag{A-9}$$

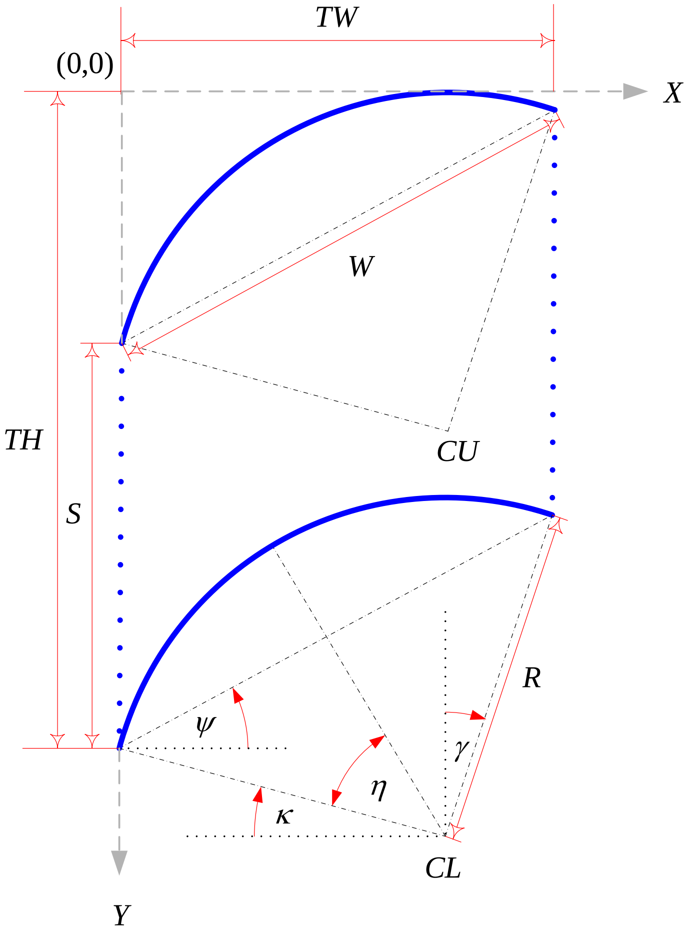

Figure A-3 Blind Enclosure for the Curved-Slat Blind Model

Also, two additional angles, κ and γ, are required prior to the calculations of the curved-slat blind enclosure geometry. The angle κ is defined as an angle between a straight line from a slat edge to the curvature center and the horizontal line. For a positive slat angle, the straight line is from the left edge to the curvature center as shown in Figure A-3. However, the straight line is from the right edge to the curvature center for a negative slat angle. The angle κ can be calculated by:

$$\kappa = \pi / 2 - (\eta + |\psi|) \tag{A-10}$$

The angle γ is defined as an angle between a straight line from a slat edge to the curvature center and the vertical line. For a positive slat angle, the straight line is from the right edge to the curvature center as shown in Figure A-3. On the other hand, the straight line is from the left edge to the curvature center for a negative slat angle. The angle γ can be determined by:

$$\gamma = \eta - |\psi| \tag{A-11}$$

Figure A-3 shows the curved-slat blind enclosure with a positive slat angle, a positive angle κ, and a positive angle γ.

Knowing the three angles and the specified slat geometry, the total width and total height of the curved-slat blind enclosure can then be calculated by:

$$TW = W\cos(\psi) \quad \text{for positive } \kappa \tag{A-12a}$$

$$TW = R[1 + \sin(\gamma)] \quad \text{for negative } \kappa \tag{A-12b}$$

$$TH = S + R[1 - \sin(\kappa)] \quad \text{for positive } \gamma \tag{A-13a}$$

$$TH = S + W\sin|\psi| \qquad \text{for negative } \gamma \tag{A-13b}$$

In the curved-slat blind model, curved slats are represented by their center of curvature and two angles defining the left and right edges of the slats. Similar to the flat-slat blind model, openings are described by straight lines connecting two points. The following data are essential for defining the blind enclosure used in the curved-slat blind model.

- *CL* and *CU* are centers of the lower and the upper slat curvatures, respectively.
- α_L and α_R are angles defining the left and the right edges of the curved slats, respectively.
- *OL* and *OU* are two end points of the straight line representing the outside opening.
- *IL* and *IU* are two end points of the straight line representing the inside opening.

Figure A-4 shows these essential data required by the curved-slat blind model. The left hand side figure shows the curved-slat blind with a positive slat angle and a positive angle κ while the right hand side figure shows the curved-slat blind with a positive slat angle and a negative angle κ. It should be noted that only the back side of the upper slat and the front side of the lower slat are parts of the blind enclosure for the positive angle κ. However, for the negative angle κ, the front side of the upper slat is also a part of the blind enclosure as illustrated in Figure A-4.

The center of upper slat curvature can be calculated by:

$$CU_x = R\cos(\kappa) \qquad \text{for positive } \psi \text{ and positive } \kappa \tag{A-14a}$$

$$CU_x = R \qquad \text{for positive } \psi \text{ and negative } \kappa \tag{A-14b}$$

$$CU_x = TW - R\cos(\kappa) \qquad \text{for negative } \psi \text{ and positive } \kappa \tag{A-14c}$$

$$CU_x = TW - R \qquad \text{for negative } \psi \text{ and negative } \kappa \tag{A-14d}$$

$$CU_y = R \qquad \text{for positive } \gamma \tag{A-15a}$$

$$CU_y = R\cos(\gamma) \qquad \text{for negative } \gamma \tag{A-15b}$$

Then, the center of the lower slat curvature can be calculated by:

$$CL = (CU_x, CU_y + S) \tag{A-16}$$

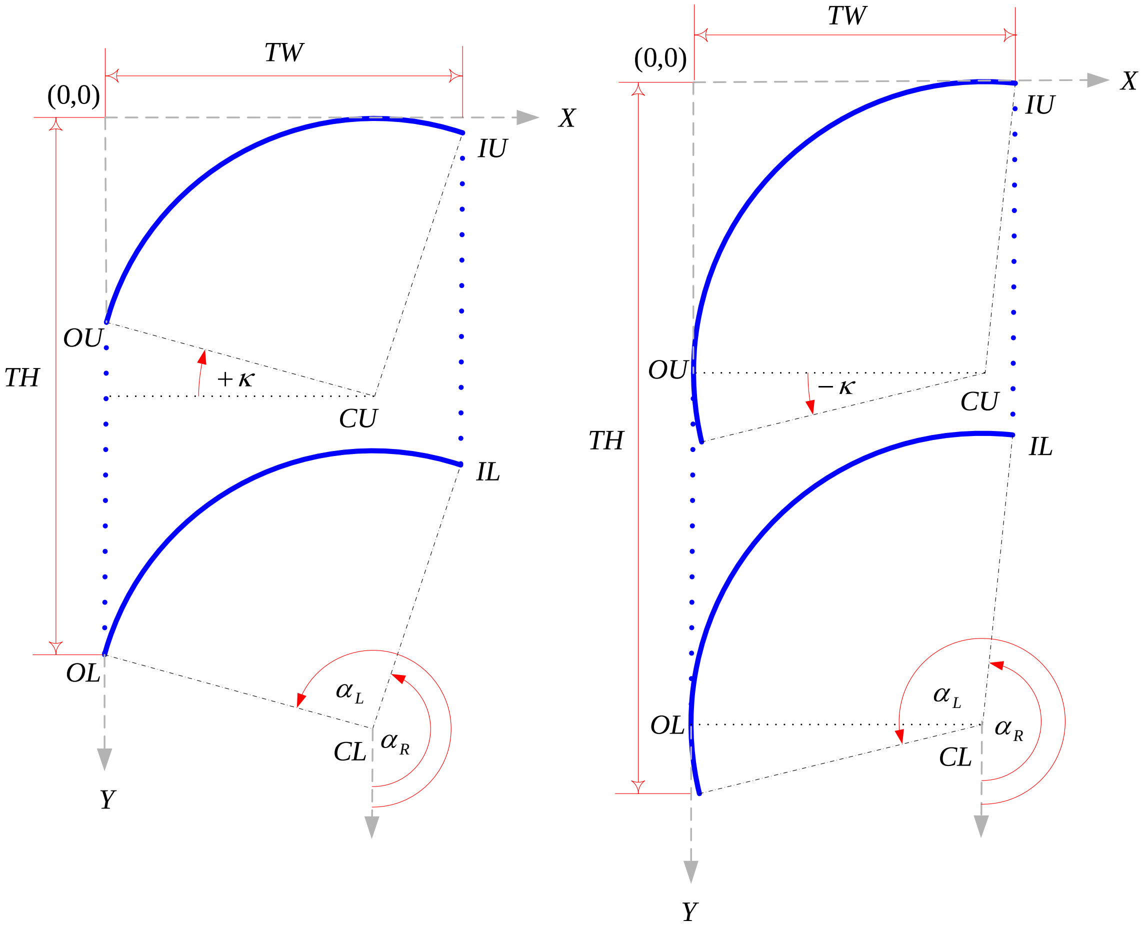

A) Positive Angle κ B) Negative Angle κ

Figure A-4 Essential Data for Defining Blind Enclosure in the Curved-Slat Blind Model

Let *LU* and *RU* be points representing the left and the right edges of the upper slat curvature, respectively. Then, for the positive slat angle, they can be determined by:

$$LU = (CU_x - R\cos(\kappa), CU_y - R\sin(\kappa)) \tag{A-17a}$$

$$RU = (CU_x + R\sin(\gamma), CU_y - R\cos(\gamma)) \tag{A-18a}$$

For the negative slat angle, they can be determined by:

$$LU = (CU_x - R\sin(\gamma), CU_y - R\cos(\gamma)) \tag{A-17b}$$

$$RU = (CU_x + R\cos(\kappa), CU_y - R\sin(\kappa)) \tag{A-18b}$$

Knowing the points *LU* and *CU*, the angle representing the left edge of curved slats (i.e. the angle α_L) can be determined as follows.

- Let $\vec{N}$ be a unit vector having the same direction as the y-axis. Thus,

$$\vec{N} = \begin{bmatrix} 0 \\ 1 \end{bmatrix} \tag{A-19}$$

- Let $\vec{V}$ be a vector from CU to LU. Thus,

$$\vec{V} = \begin{bmatrix} LU_x - CU_x \\ LU_y - CU_y \end{bmatrix} \tag{A-20}$$

- Then, if ($LU_x >= CU_x$),

$$\alpha_L = \cos^{-1}\left(\vec{V} \bullet \vec{N} \big/ \left|\vec{V}\right| \right) \tag{A-21}$$

- Otherwise,

$$\alpha_L = 2\pi - \cos^{-1}\left(\vec{V} \bullet \vec{N} \big/ \left|\vec{V}\right| \right) \tag{A-22}$$

In the above calculations, the angle α_L is measured in the counter-clockwise direction as shown in Figure A-4. Similarly, the angle representing the right edge of curved slats (i.e. the angle α_R) can be determined by substituting the point *LU* by the point *RU* in the above calculations.

Next, the two end points representing the outside opening can be calculated by:

$OU = (0, CU_y - R\sin(\kappa))$ for positive ψ and positive κ (A-23a)

$OU = (0, CU_y)$ for positive ψ and negative κ (A-23b)

$OU = (0, CU_y - R\cos(\gamma))$ for negative ψ and positive γ (A-23c)

$OU = (0,0)$ for negative ψ and negative γ (A-23d)

$$OL = (0, OU_y + S) \tag{A-24}$$

Finally, the two end points representing the inside opening can be calculated by:

$IU = (TW, CU_y - R\cos(\gamma))$ for positive ψ and positive γ (A-25a)

$IU = (TW, 0)$ for positive ψ and negative γ (A-25b)

$IU = (TW, CU_y - R\sin(\kappa))$ for negative ψ and positive κ (A-25c)

$IU = (TW, CU_y)$ for negative ψ and negative κ (A-25d)

$$IL = (TW, IU_y + S) \tag{A-26}$$

The slat radius, used to describe the curvature of the blind slats in the curved-slat blind model, is a required input. However, three other parameters may also be used to describe the slat curvature: the angle η, the curvature length (*CW*) defined as the distance from one end of the slat to the other end measured along the slat curvature, and the curvature height (*CH*) defined as the distance from the straight line connecting slat edges to the top of slat curvature. Figure A-5 shows these four parameters along with the slat width (*W*). The slat radius can be related to the other three parameters and the slat width as follows:

$$R = \frac{W}{2\sin(\eta)} \tag{A-27}$$

$$R = \frac{CW}{2\eta} \tag{A-28}$$

$$R = \frac{CH^2 + (W/2)^2}{2CH} \tag{A-29}$$

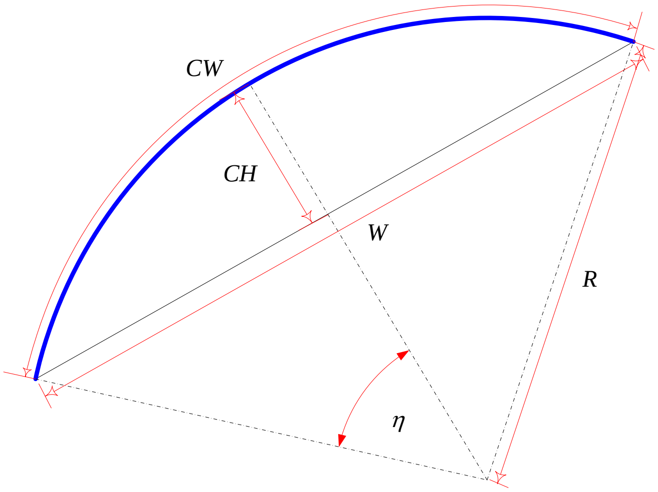

Figure A-5 Parameters for Describing Slat Curvature

If either the angle η or the curvature height is known, the slat radius can be solved directly from Equation (A-27) or (A-29), respectively. However, if only the curvature length is known, it is essential to use one of numerical methods for root finding (e.g. the secant method) with Equations (A-27) and (A-28) to determine the slat radius.

A.2.4 Physical Limitations

Figure A-6 shows completely closed blinds with a positive slat angle. The maximum slat angle for a flat-slat blind can be obtained from the following relationship:

$$\frac{S}{\sin(90°)} = \frac{T}{\sin(90° - \psi_{\max})} \tag{A-30}$$

The relationship in Equation (A-30) suggests that the slat angle specified for the flat-slat blind model must satisfy the following equation.

$$-\cos^{-1}\left(\frac{T}{S}\right) \le \psi \le \cos^{-1}\left(\frac{T}{S}\right) \tag{A-31}$$

Otherwise, the flat-slat blind is considered to be completely closed.

Utilizing Equations (A-9) to (A-18) for the curved-slat blind model, distances from the lower curvature center to the left and right edges of upper curvature can be calculated by:

$$\overline{CL - LU} = \sqrt{[S + R\cos(\eta + \psi)]^2 + [R\sin(\eta + \psi)]^2} \tag{A-32}$$

$$\overline{CL - RU} = \sqrt{[S + R\cos(\eta - \psi)]^2 + [R\sin(\eta - \psi)]^2} \tag{A-33}$$

Due to physical limitations, the distances $\overline{CL-LU}$ and $\overline{CL-RU}$ must always be greater than or equal to the slat radius for a blind with zero-thickness curved slats. This means that the slat angle specified for the curved-slat blind model must satisfy the following equation.

$$\eta - \cos^{-1}\left(-\frac{S}{2R}\right) \le \psi \le \cos^{-1}\left(-\frac{S}{2R}\right) - \eta \qquad \text{(A-34)}$$

Otherwise, the curved-slat blind is considered to be completely closed.

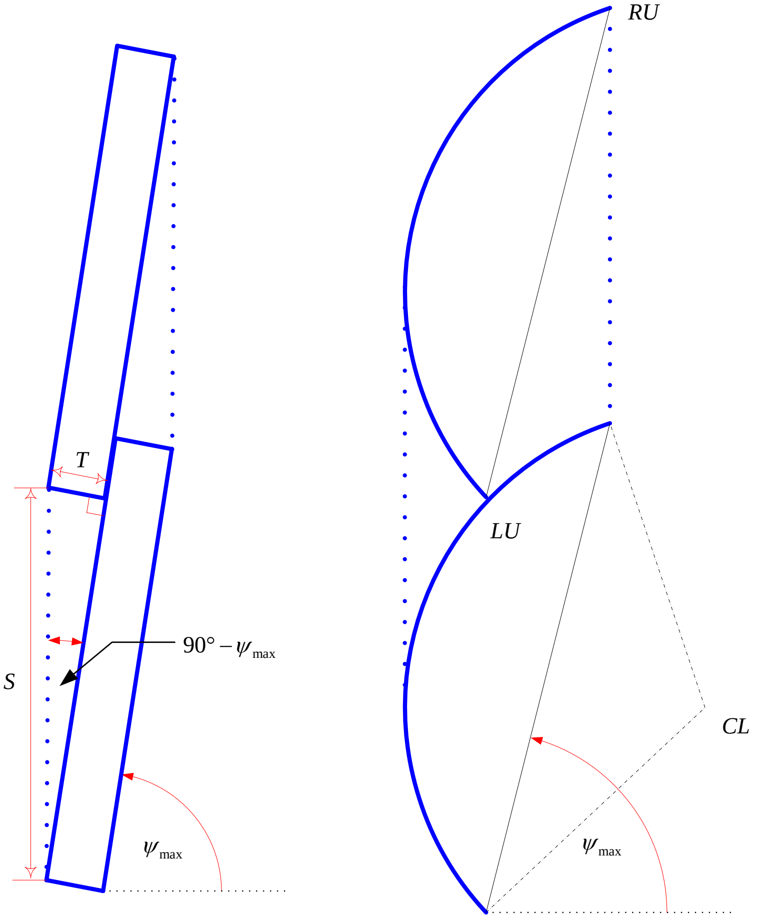

A) Closed Flat Slat Blinds

B) Closed Curved Slat Blinds

Figure A-6 Completely Closed Blinds with Positive Slat Angle

A.3 Limits of Profile Angle, Calculation Cases, and Radiative Ratios

To establish calculation cases in the ray-tracing blind model, the profile angle limits are utilized. Figure A-7 illustrates the limits of the profile angle for the flat-slat blind sub-model while Figures A-10, A-11, and A-12 illustrate the limits for the curved-slat blind sub-model. These limits indicate how the sunlight can pass through the blind assembly as a function of the profile angle. For instance, the phenomenon for a blind with flat-slats can be explained as follows.

- For $\phi_1 < \phi < +90°$, there is no opening area, and upper edges and lower slats are illuminated. This means that the sunlight can only pass through the blind assembly by reflections (mainly from the lower slats).
- For $\phi_2 < \phi < \phi_1$, there is some opening area, and upper edges and lower slats are illuminated. For this profile angle range, the sunlight can pass directly through the opening area and indirectly by reflections (mainly from the lower slats).
- For $\phi_3 < \phi < \phi_2$, there is some opening area, and upper edges and upper slats are illuminated. For this profile angle range, the sunlight can pass directly through the opening area and indirectly by reflections (mainly from the upper slats).
- For $\phi_4 < \phi < \phi_3$, there is no opening area, and upper edges and upper slats are illuminated. This means that the sunlight can only pass through the blind assembly by reflections (mainly from the upper slats).
- For $-90° < \phi < \phi_4$, there is no opening area, and only upper edges are illuminated. This means that the sunlight can only pass through the blind assembly by reflections. It should be noted that this case only occurs when the slat angle is not zero.

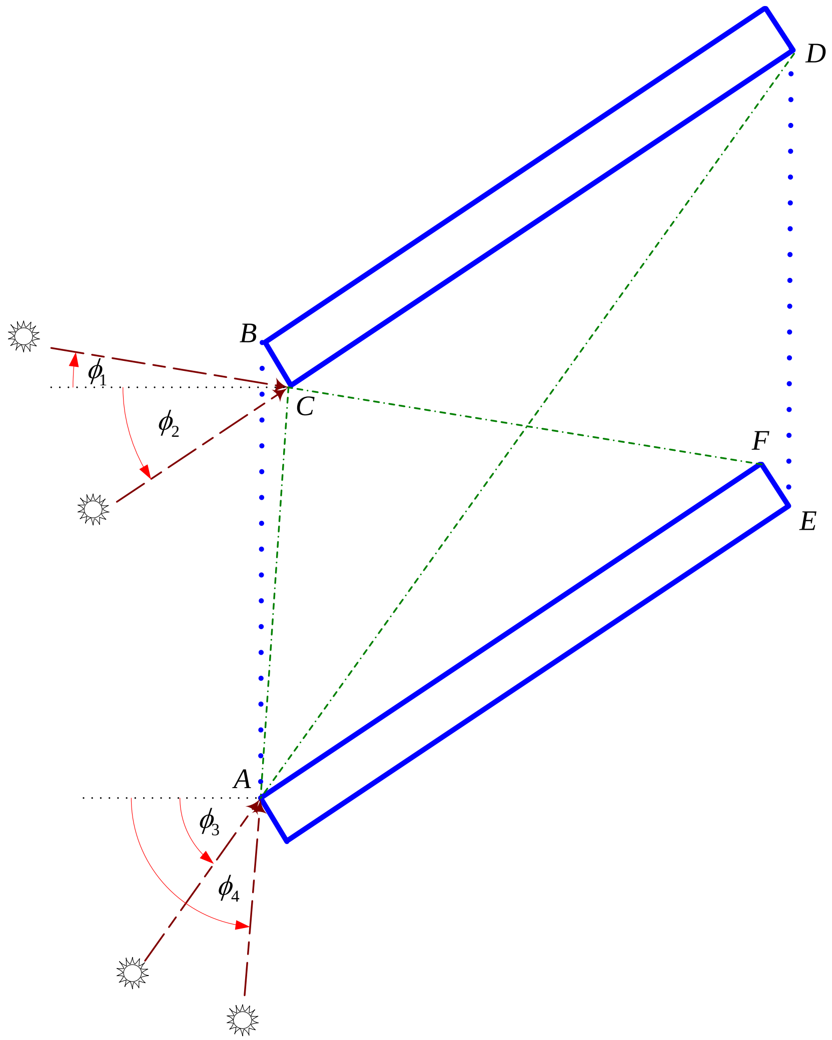

Figure A-7 Limits of Profile Angle for the Flat-Slat Blind Model

A.3.1 Calculations for Blinds with Flat Slats

The limits of profile angle for the flat-slat blind model can be calculated by:

$$\phi_1 = \tan^{-1}\left\{\frac{S - W \cdot \sin(\psi) - T \cdot \cos(\psi)}{W \cdot \cos(\psi) - T \cdot \sin(\psi)}\right\} \tag{A-35}$$

$$\phi_2 = -\psi \tag{A-36}$$

$$\phi_3 = -\tan^{-1}\left\{\frac{S + W \cdot \sin(\psi) - T \cdot \cos(\psi)}{W \cdot \cos(\psi) + T \cdot \sin(\psi)}\right\} \tag{A-37}$$

$$\phi_4 = -\pi / 2 \qquad \text{for } \psi = 0 \tag{A-38a}$$

$$\phi_4 = -\tan^{-1}\left\{\frac{S/T - \cos(\psi)}{|\sin(\psi)|}\right\} \qquad \text{for } \psi \neq 0 \tag{A-38b}$$

Utilizing the limits of profile angle, calculations for the flat-slat blind model may be divided into five cases as shown in Figure A-8. As shown, Figure A-8 illustrates how the sunlight can pass through the flat-slat blind for each case. The figure also shows fractions of the sunlight that passes directly through the blind, falls on the slat edge, and falls on the blind slat. As shown in Figure A-8, the opening ratio (*OR*) is defined as a fraction of sunlight that can pass directly through the blind assembly without any reflections. The edge ratio (*ER*) is defined as a fraction of sunlight that falls on the slat edge. The slat ratio defined as a fraction of sunlight that falls on the blind slat can thus be determined as the difference between one and the sum of the opening and edge ratios. The calculations of the opening and the edge ratios are summarized below.

Case 1 for $\varphi_1 < \varphi < +90°$:

$$ER = \max\left(0, \frac{T}{S} \cdot \frac{\cos(\psi + \phi)}{\cos(\phi)}\right) \tag{A-39a}$$

$$OR = 0 \tag{A-40a}$$

Case 2 for $\varphi_2 \leq \varphi \leq \varphi_1$:

$$ER = \frac{T}{S} \cdot \frac{\cos(\psi + \phi)}{\cos(\phi)} \tag{A-39b}$$

$$OR = 1 - ER - \frac{W}{S} \cdot \frac{\sin(\psi + \phi)}{\cos(\phi)} \tag{A-40b}$$

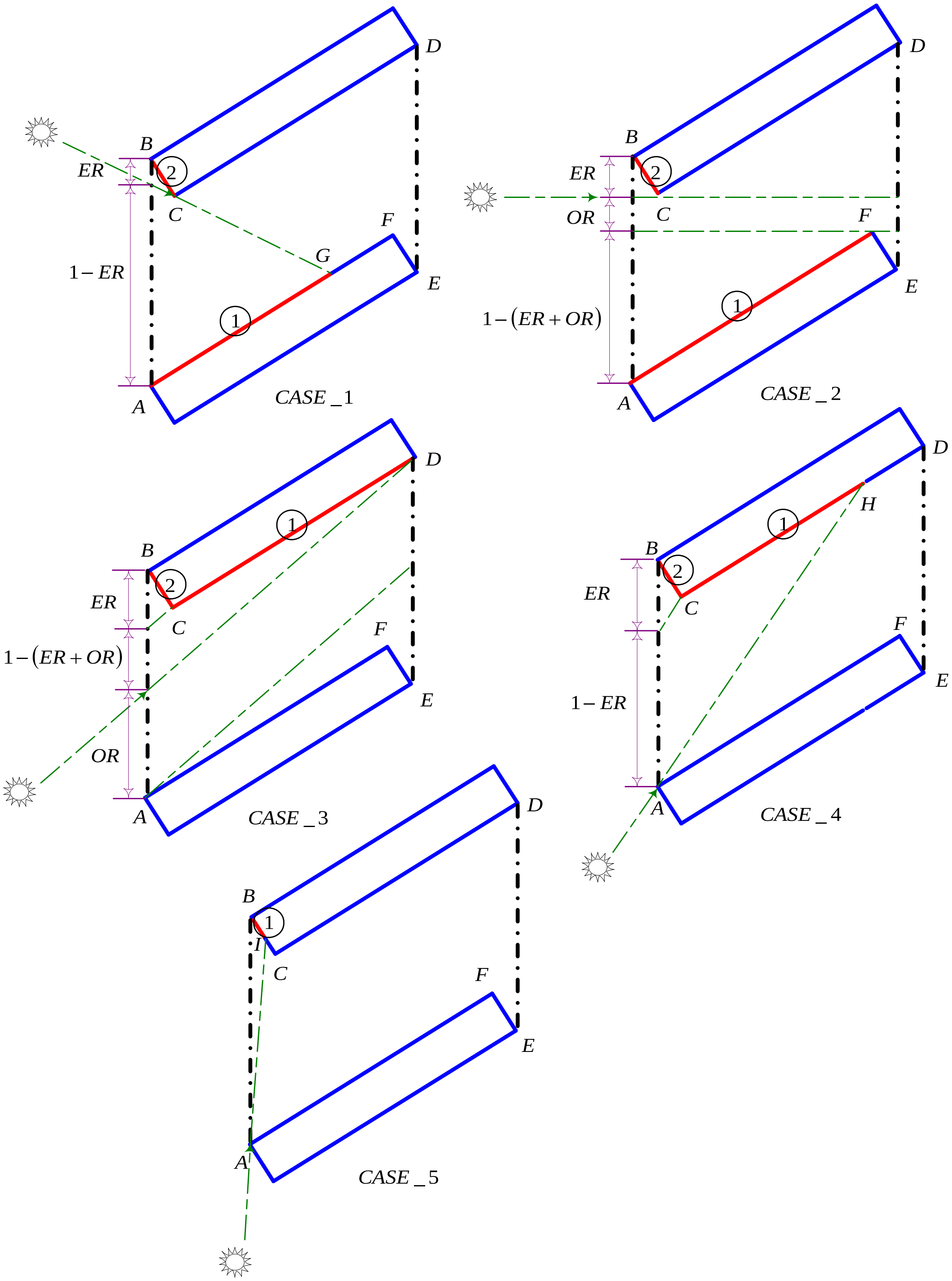

Figure A-8 Calculation Cases for the Flat-Slat Blind Model

Case 3 for $\varphi_3 \le \varphi < \varphi_2$:

$$ER = \frac{T}{S} \cdot \frac{\cos(\psi + \phi)}{\cos(\phi)} \tag{A-39c}$$

$$OR = 1 - \frac{T}{S \cdot \cos(\psi)} + \left[\frac{T \cdot \tan(\psi) + W}{S}\right] \cdot \left[\frac{\sin(\psi + \phi)}{\cos(\phi)}\right] \tag{A-40c}$$

Case 4 for $\varphi_4 < \varphi < \varphi_3$:

$$ER = \frac{T}{S} \cdot \frac{\cos(\psi + \phi)}{\cos(\phi)} \tag{A-39d}$$

$$OR = 0 \tag{A-40d}$$

Case 5 for $-90° < \varphi \le \varphi_4$ and $\psi \ne 0$:

$$ER = 1 \tag{A-39e}$$

$$OR = 0 \tag{A-40e}$$

A.3.2 Calculations for Blinds with Curved Slats

Prior to the calculations of the profile angle limits for the curved-slat blind models, three angles (ω_1 to ω_3) shown in Figure A-9 are needed. These angles are dependent on slat geometry but independent on the profile angle. To determine these angles, first let DT_1 and DT_2 be distances from the center of the lower curvature to the right and left edges of the upper curvature (i.e. the distances from *CL* to *IU* and *CL* to *LU* shown in Figure A-9), respectively. They can be determined by:

$$DT_1 = \sqrt{[S + R\cos(\eta - \psi)]^2 + [R\sin(\eta - \psi)]^2} \tag{A-41}$$

$$DT_2 = \sqrt{[S + R\cos(\eta + \psi)]^2 + [R\sin(\eta + \psi)]^2} \tag{A-42}$$

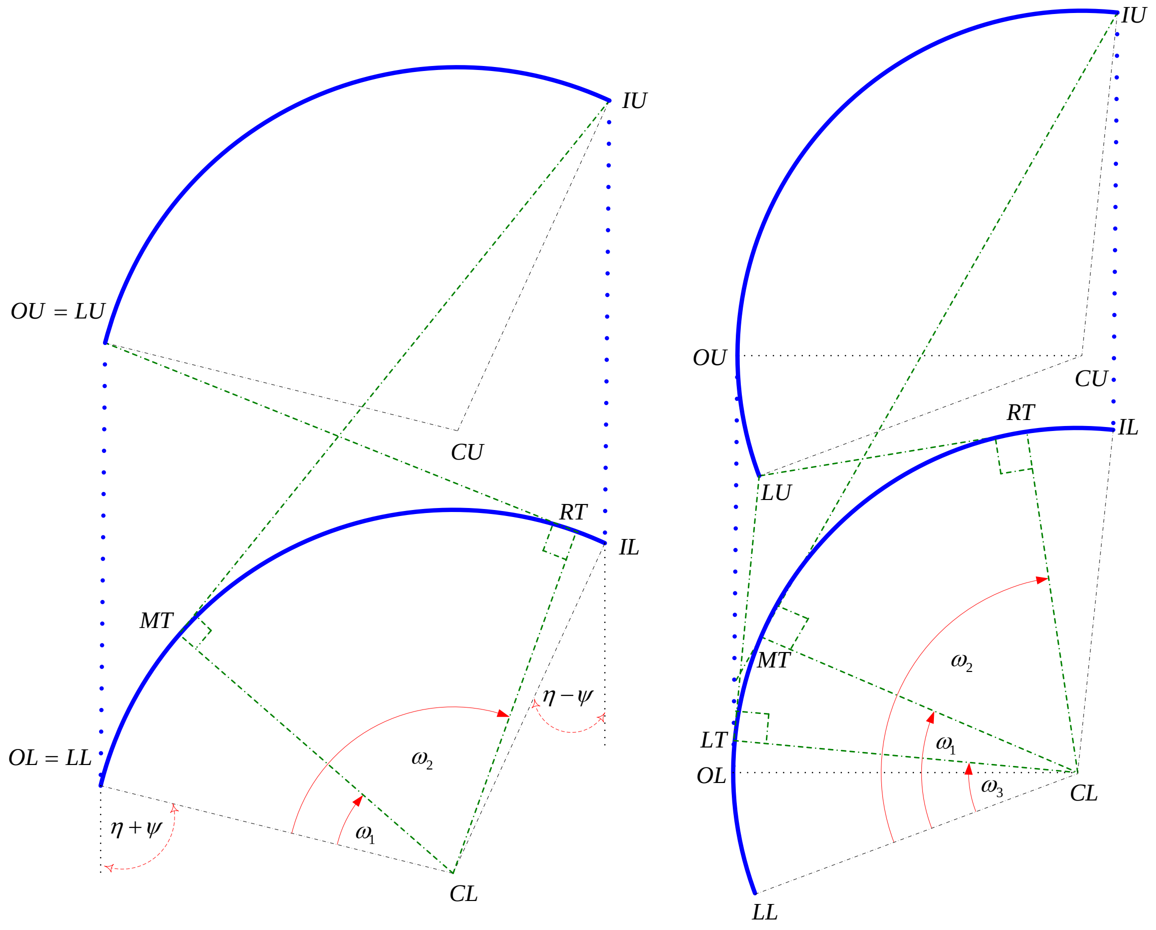

A) Positive Angle κ

B) Negative Angle κ

Figure A-9 Angles ω_1 to ω_3 Required by the Curved-Slat Blind Model

Then, let χ_1 be the angle *IL-CL-IU* and χ_2 be the angle *IU-CL-MT*. They can be determined by:

$$\chi_1 = \sin^{-1}\left[\frac{S\cdot\sin(180-(\eta-\psi))}{DT_1}\right] = \sin^{-1}\left[\frac{S\cdot\sin(\eta-\psi)}{DT_1}\right] \tag{A-43}$$

$$\chi_2 = \cos^{-1}\left[\frac{R}{DT_1}\right] \tag{A-44}$$

Also, let χ_3 be the angle *LL-CL-LU* and χ_4 be the angle *LU-CL-RT* (or the angle *LU-CL-LT).* They can be determined by:

$$\chi_3 = \sin^{-1}\left[\frac{S \cdot \sin(180 - (\eta + \psi))}{DT_2}\right] = \sin^{-1}\left[\frac{S \cdot \sin(\eta + \psi)}{DT_2}\right] \tag{A-45}$$

$$\chi_4 = \cos^{-1}\left[\frac{R}{DT_2}\right] \tag{A-46}$$

As shown in Figure A-9, the angles ω_1, ω_2, and ω_3 are the angles *LL-CL-MT, LL-CL-RT*, and *LL-CL-LT*, respectively. Therefore, they can be determined by

$$\omega_1 = 2\eta - (\chi_1 + \chi_2) \tag{A-47}$$

$$\omega_2 = \chi_3 + \chi_4 \tag{A-48}$$

$$\omega_3 = \chi_3 - \chi_4 \tag{A-49}$$

These angles are physically bounded between zero and 2η. The angles are measured in the clockwise direction as shown in Figure A-9. The angle ω_3 is zero when the angle κ is positive.

Figures A-10 and A-11 illustrates the limits of profile angle for the positive angle κ for the curved-slat blind model. Figure A-10 shows the limits of profile angle when both angles ω_1 and ω_2 are greater than zero and less than 2η while Figure A-11 shows the limits of profile angle when the angle ω_1 is equal to zero and the angle ω_2 is equal to 2η. For the negative angle κ, Figure A-12 illustrates the limits of profile angle when both angles ω_1 and ω_2 are greater than zero and less than 2η.

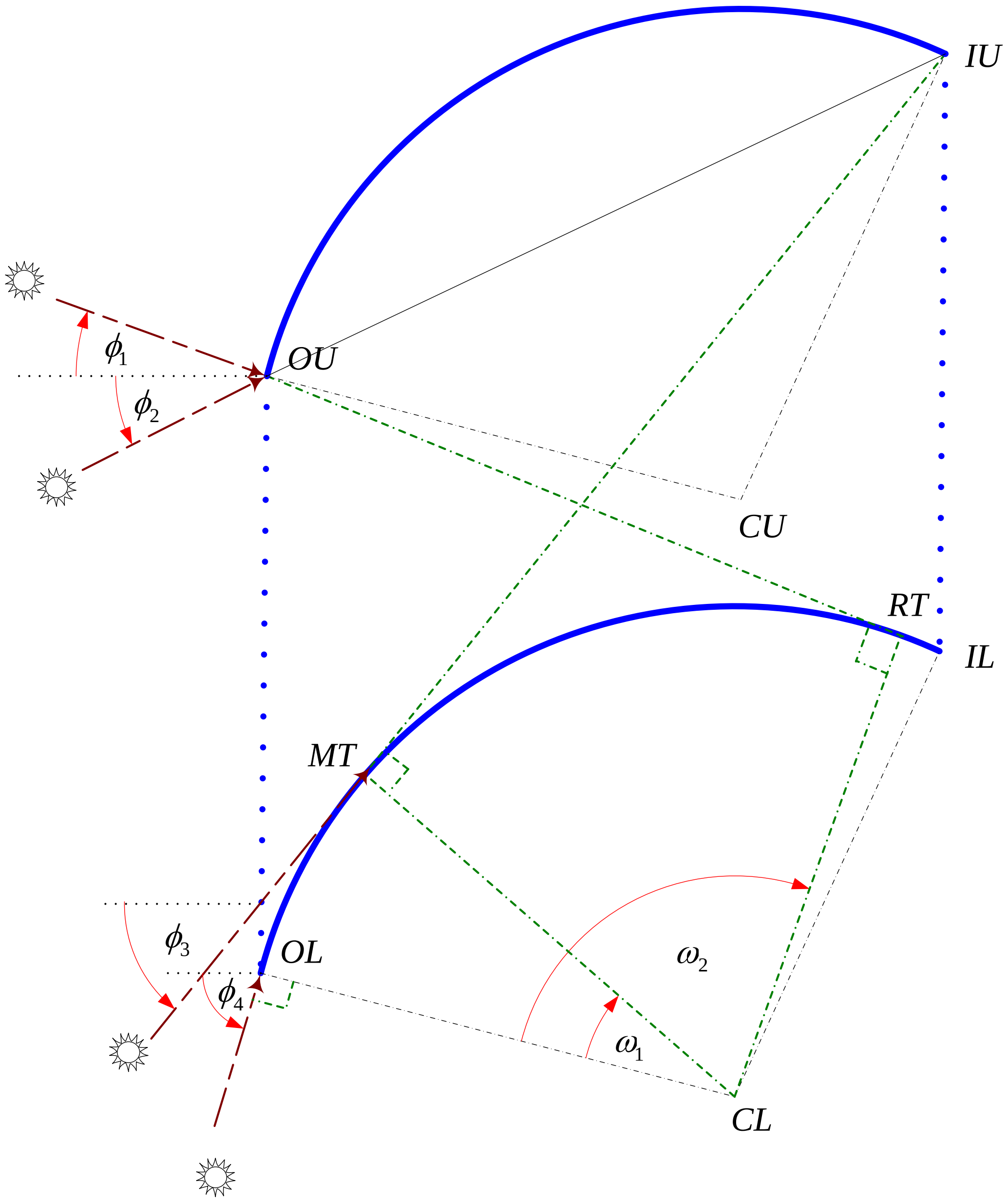

Figure A-10 Profile Angle Limits for Positive Angle κ for the Curved-Slat Blind Model When $0 < \omega_1 < 2\eta$ and $0 < \omega_2 < 2\eta$

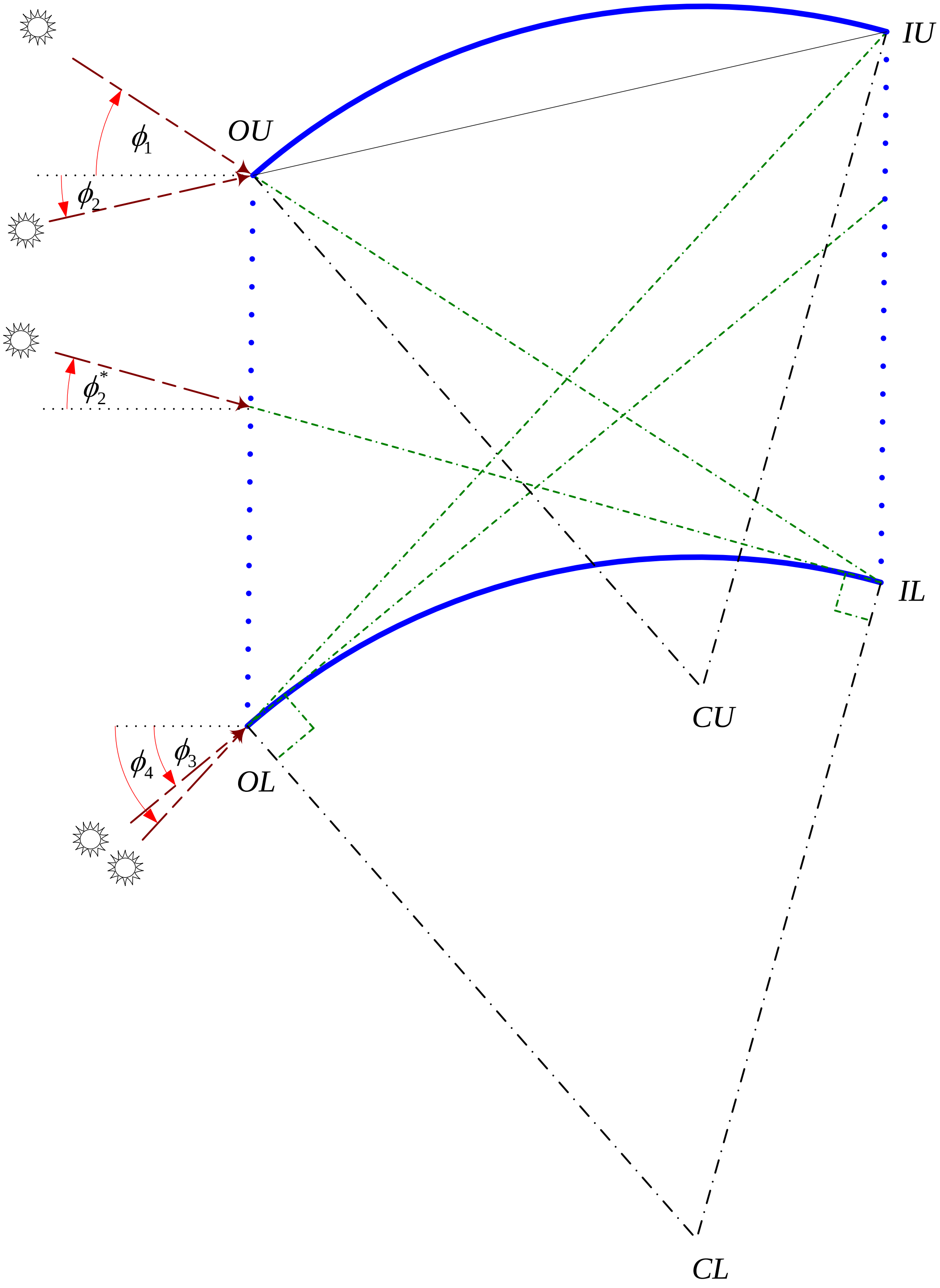

Figure A-11 Profile Angle Limits for Positive Angle κ for the Curved-Slat Blind Model When $\omega_1 = 0$ and $\omega_2 = 2\eta$

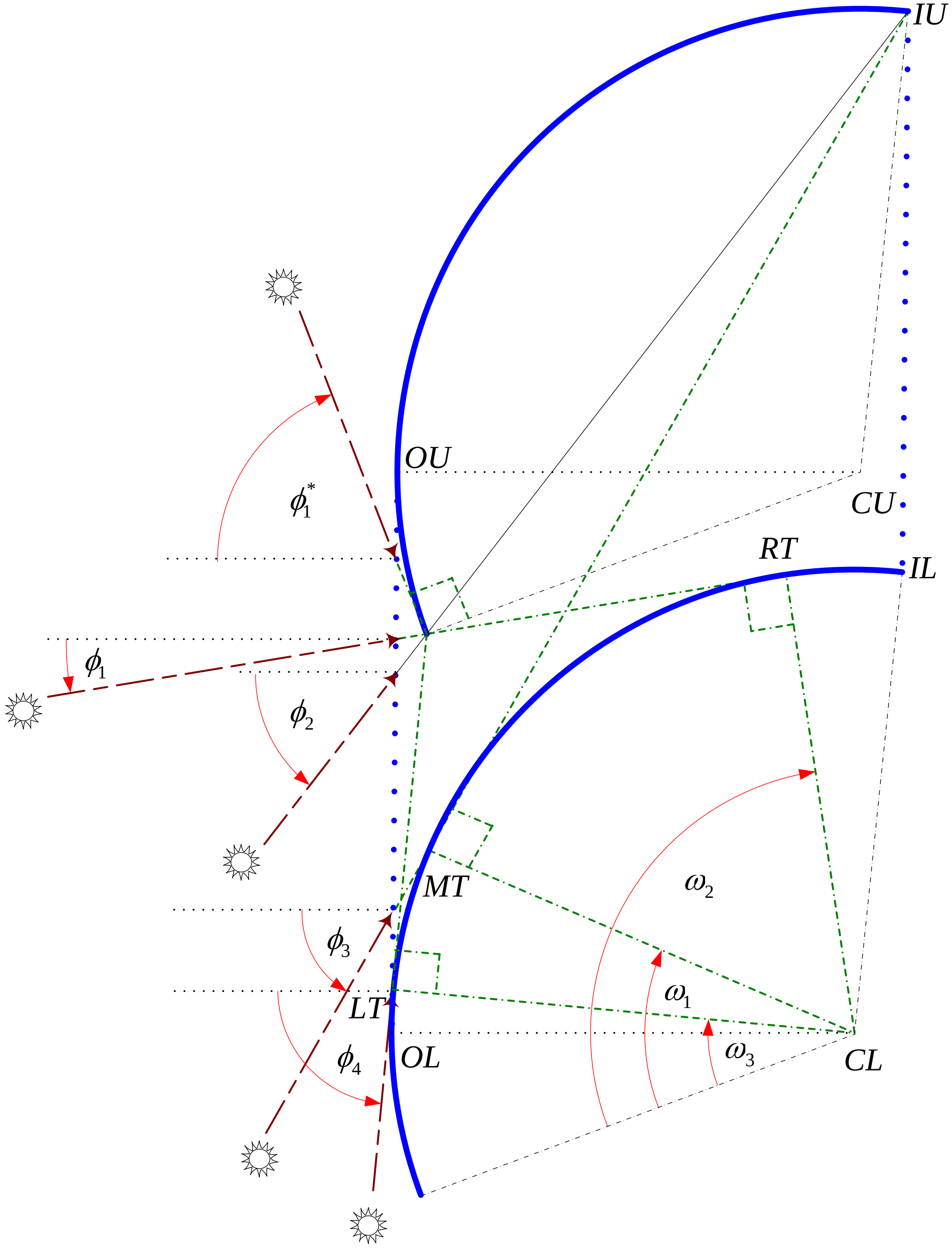

Figure A-12 Profile Angle Limits for Negative Angle κ for the Curved-Slat Blind Model When $0 < \omega_1 < 2\eta$ and $0 < \omega_2 < 2\eta$

Knowing the angles ω_1 to ω_3, the limits of profile angle for the curved-slat blind model can be determined using the following algorithm.

If ($\kappa < 0$) and ($\psi > 0$) Then

$$\phi_1^* = \pi - \left(\eta + \psi\right) \tag{A-50a}$$

Else

$$\phi_1^* = \pi/2 \tag{A-50b}$$

End If

If ($\omega_2 < 2\eta$) Then

$$\phi_1 = \omega_2 - (\eta + \psi) \tag{A-51a}$$

$$\phi_2^* = -\psi \tag{A-52a}$$

Else

$$\phi_1 = \cos^{-1}\left\{\frac{R\left[\sin(\eta+\psi) + \sin(\eta-\psi)\right]}{\sqrt{[S + R\cos(\eta+\psi) - R\cos(\eta-\psi)]^2 + [R\sin(\eta+\psi) + R\sin(\eta-\psi)]^2}}\right\} \tag{A-51b}$$

$$\phi_2^* = \eta - \psi \tag{A-52b}$$

End If

$$\phi_2 = -\psi \tag{A-53}$$

$$\phi_3 = \omega_1 - (\eta + \psi) \tag{A-54}$$

If ($\omega_1 > 0$) Then

$$\phi_4 = \omega_3 - (\eta + \psi) \tag{A-55a}$$

Else

$$\phi_4 = -\cos^{-1}\left\{\frac{R\left[\sin(\eta+\psi) + \sin(\eta-\psi)\right]}{\sqrt{[S - R\cos(\eta+\psi) + R\cos(\eta-\psi)]^2 + [R\sin(\eta+\psi) + R\sin(\eta-\psi)]^2}}\right\} \tag{A-55b}$$

End If

Utilizing the limits of profile angle, calculations for the curved-slat blind model may be divided into seven cases as shown in Figures A-13 and A-14 for the positive angle κ. Like the flat-slat blind model, the opening ratio (*OR*) is defined as a fraction of sunlight that can pass directly through the blind assembly without any reflections. The upper slat front ratio (*URF*) is defined as a fraction of sunlight that falls on the front side of the upper slat. The upper slat back ratio (*URB*) is defined as a fraction of sunlight that falls on the back side of the upper slat. The lower slat ratio (*LR*) is defined as a fraction of sunlight that falls on (the front side of) the lower slat. The sum of these ratios is equal to one. These ratios can be calculated as a function of intermediate variables including *USHR*, *TSHR*, *SHCR*, and *SHFR* (*TSHR*, *SHCR*, and *SHFR* are shown in Figures A-13 and A-14). It should be noted that the *URF* is required only for cases when the angle k is negative and the slat angle is positive. For these cases, the front side of the upper slat must also be considered as a part of the blind enclosure (see Figure A-12).

For the positive angle κ, the calculations of the opening ratio, the upper slat back ratio, and the lower slat ratio are summarized below. In the following calculations, values of *TSHR*, *SHCR*, and *SHFR* cannot be greater than one or less than zero. Therefore, if they exceed these limits, they must be set to their maximum (one) or minimum (zero) limit.

Case 1 for $\varphi_1 < \varphi < +90°$:

$$OR = 0 \tag{A-56a}$$

$$URB = 0 \tag{A-56b}$$

$$LR = 1 \tag{A-56c}$$

Case 2 for $\varphi_2^* \le \varphi \le \varphi_1$ and $\omega_2 = 2\eta$:

$$TSHR = \frac{W}{S}\left|\frac{\sin(\psi + \phi)}{\cos(\phi)}\right| \tag{A-57a}$$

$$OR = 1 - TSHR \tag{A-57b}$$

$$URB = 0 \tag{A-57c}$$

$$LR = TSHR \tag{A-57d}$$

Case 3 for a) $\varphi_2 \le \varphi \le \varphi_1$ and $\omega_2 < 2\eta$, or b) $\varphi_2 \le \varphi < \varphi_2^*$ and $\omega_2 = 2\eta$:

$$TSHR = \frac{R}{S}\left[\frac{1-\cos(\eta+\psi+\phi)}{\cos(\phi)}\right] \tag{A-58a}$$

$$OR = 1 - TSHR \tag{A-58b}$$

$$URB = 0 \tag{A-58c}$$

$$LR = TSHR \tag{A-58d}$$

Case 4 for a) $\varphi_3 < \varphi < \varphi_2$, or b) $\varphi = \varphi_3$ and $\omega_1 > 0$:

$$TSHR = \frac{R}{S}\left[\frac{1-\cos(\eta-\psi-\phi)}{\cos(\phi)}\right] \tag{A-59a}$$

$$SHFR = \frac{W}{S}\left|\frac{\sin(\psi+\phi)}{\cos(\phi)}\right| \tag{A-59b}$$

$$OR = 1 - TSHR \tag{A-59c}$$

$$URB = SHFR \tag{A-59d}$$

$$LR = TSHR - SHFR \tag{A-59e}$$

Case 5 for $\varphi_4 < \varphi < \varphi_3$ and $\omega_1 > 0$:

$$SHCR = \frac{R}{S}\left[\frac{1-\cos(\eta+\psi+\phi)}{\cos(\phi)}\right] \tag{A-60a}$$

$$OR = 0 \tag{A-60b}$$

$$URB = 1 - SHCR \tag{A-60c}$$

$$LR = SHCR \tag{A-60d}$$

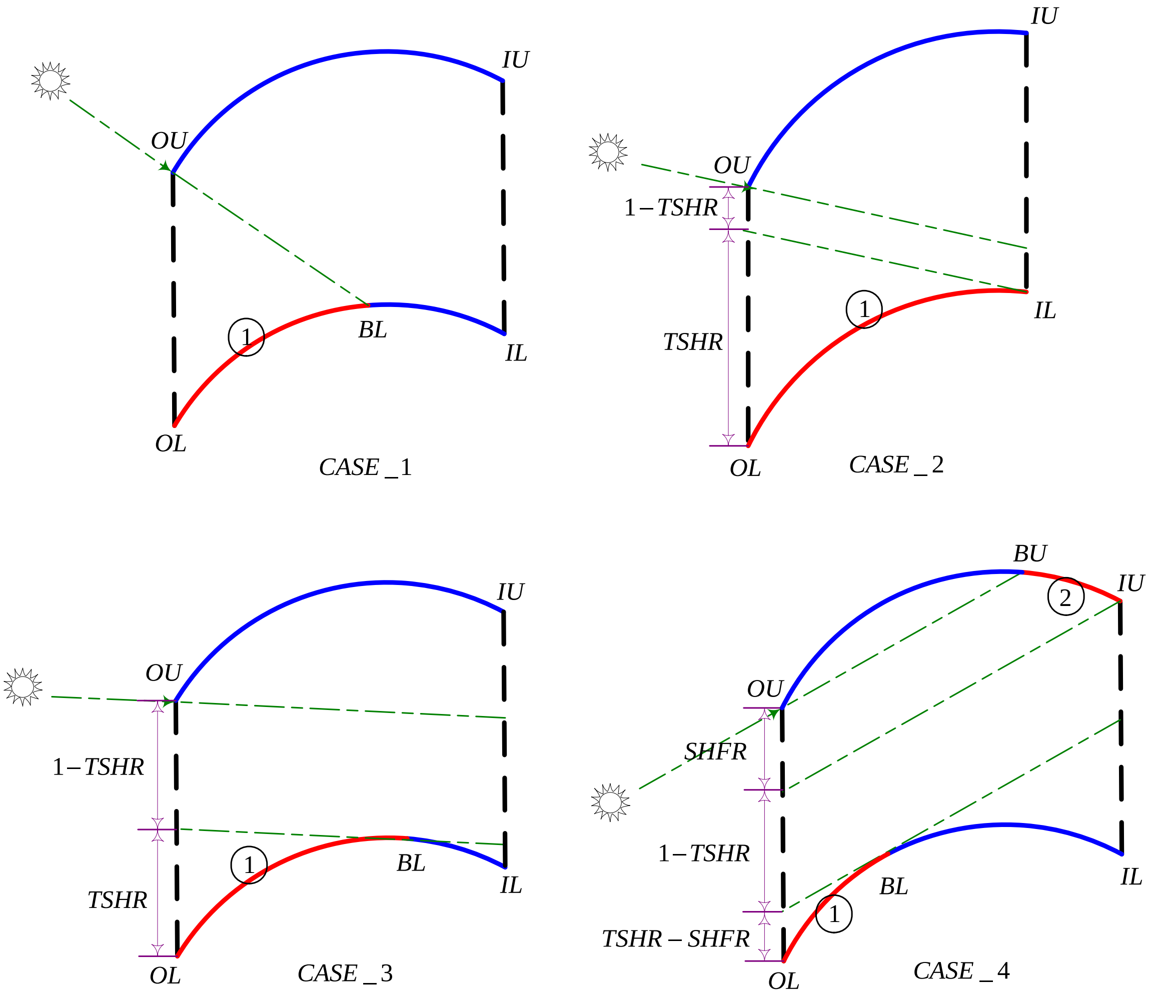

Figure A-13 Calculation Cases 1 to 4 for the Curved-Slat Blind Model for Positive Angle κ

Case 6 for $\varphi_4 \le \varphi \le \varphi_3$ and $\omega_1 = 0$:

$$TSHR = \frac{W}{S}\left|\frac{\sin(\psi + \phi)}{\cos(\phi)}\right| \tag{A-61a}$$

$$OR = 1 - TSHR \tag{A-61b}$$

$$URB = TSHR \tag{A-61c}$$

$$LR = 0 \tag{A-61d}$$

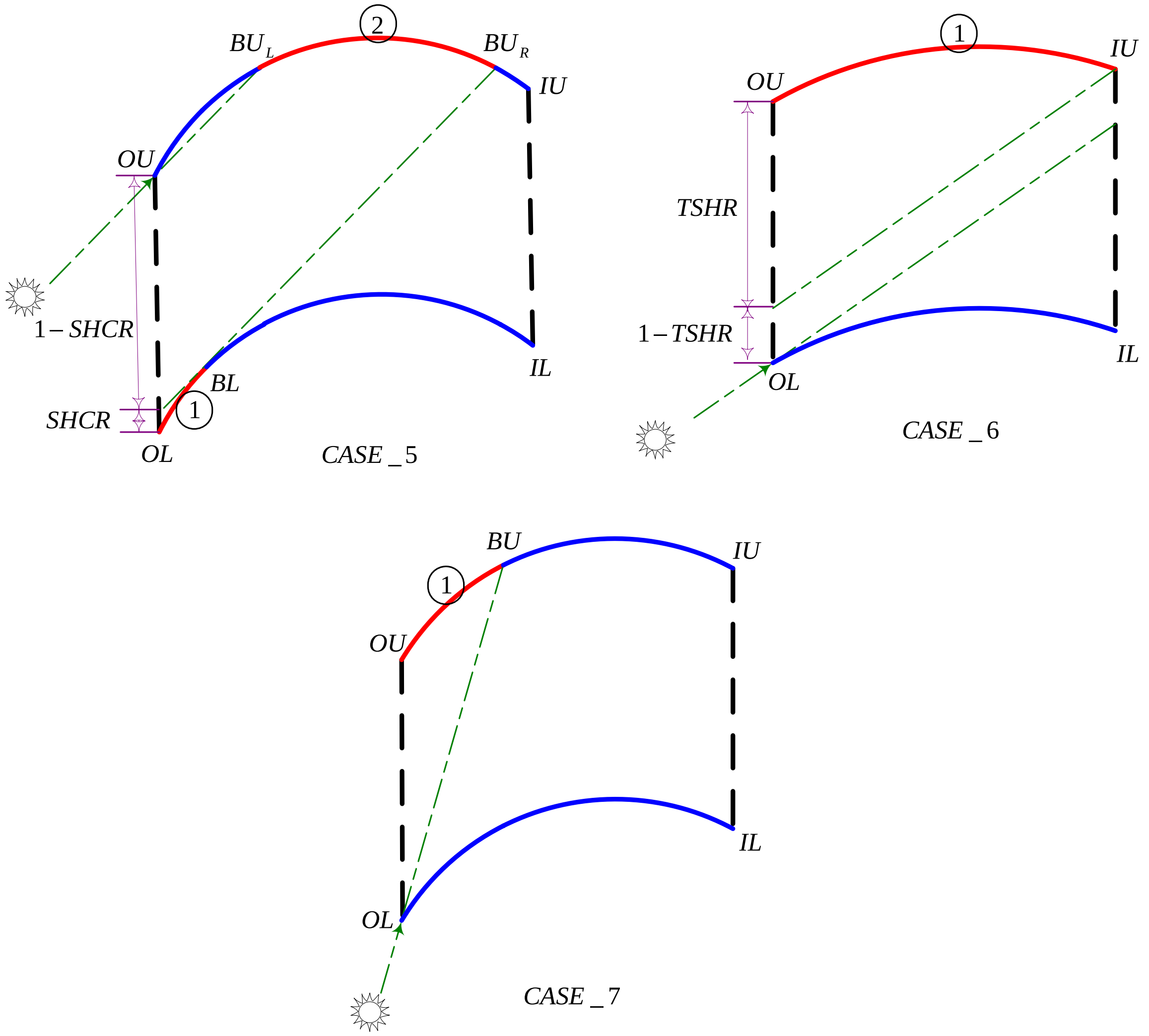

Figure A-14 Calculation Cases 5 to 7 for the Curved-Slat Blind Model for Positive Angle κ

Case 7 for a) $-90° < \varphi \le \varphi_4$ and $\omega_1 > 0$, or b) $-90° < \varphi < \varphi_4$ and $\omega_1 = 0$:

$$OR = 0 \qquad \text{(A-62a)}$$

$$URB = 1 \qquad \text{(A-62b)}$$

$$LR = 0 \qquad \text{(A-62c)}$$

Equations (A-56) to (A-62) can also be used for cases when both the slat angle and the angle κ are negative. For cases when the slat angle is positive and the angle κ is negative, the calculations of the opening ratio, the upper slat back ratio, and the lower slat ratio are summarized as follows. Similar to the variables *TSHR*, *SHCR*, and *SHFR*, the value of *USHR* cannot be greater than one or less than zero. Therefore, if it exceeds these limits, it must be set to its maximum (one) or minimum (zero) limit.

Case 1 for $\varphi_1^* < \varphi < +90°$:

$$USHR = \frac{R}{S}\left[\cos(\phi) - \tan(\phi)\cdot\{1-\sin(\phi)\}\right] \tag{A-63a}$$

$$OR = 0 \tag{A-63b}$$

$$URF = USHR \tag{A-63c}$$

$$URB = 0 \tag{A-63d}$$

$$LR = 1 - USHR \tag{A-63e}$$

Case 2 for $\varphi_1 < \varphi \le \varphi_1^*$:

$$USHR = \frac{R}{S}\left[\sin|\kappa| - \tan(\phi)\cdot\{1-\cos(\kappa)\}\right] \tag{A-64a}$$

$$OR = 0 \tag{A-64b}$$

$$URF = USHR \tag{A-64c}$$

$$URB = 0 \tag{A-64d}$$

$$LR = 1 - USHR \tag{A-64e}$$

Case 3 for $\varphi_2^* \le \varphi \le \varphi_1$ and $\omega_2 = 2\eta$:

$$USHR = \frac{R}{S}\left[\sin|\kappa| - \tan(\phi)\cdot\{1-\cos(\kappa)\}\right] \tag{A-65a}$$

$$TSHR = \frac{W}{S}\left|\frac{\sin(\psi+\phi)}{\cos(\phi)}\right| \tag{A-65b}$$

$$OR = 1 - TSHR \tag{A-65c}$$

$$URF = USHR \tag{A-65d}$$

$$URB = 0 \tag{A-65e}$$

$$LR = TSHR - USHR \tag{A-65f}$$

Case 4 for a) $\varphi_2 \le \varphi \le \varphi_1$ and $\omega_2 < 2\eta$, or b) $\varphi_2 \le \varphi < \varphi_2^*$ and $\omega_2 = 2\eta$:

$$USHR = \frac{R}{S}\left[\sin|\kappa| - \tan(\phi)\cdot\{1-\cos(\kappa)\}\right] \tag{A-66a}$$

$$TSHR = \frac{R}{S}\left[\frac{1-\cos(\eta+\psi+\phi)}{\cos(\phi)}\right] \tag{A-66b}$$

$$OR = 1 - TSHR \tag{A-66c}$$

$$URF = USHR \tag{A-66d}$$

$$URB = 0 \tag{A-66e}$$

$$LR = TSHR - USHR \tag{A-66f}$$

Case 5 for $\varphi_3 \le \varphi < \varphi_2$:

$$USHR = \frac{R}{S}\left[\sin|\kappa| - \tan(\phi)\cdot\{1-\cos(\kappa)\}\right] \tag{A-67a}$$

$$TSHR = \frac{R}{S}\left[\frac{1-\cos(\eta-\psi-\phi)}{\cos(\phi)}\right] \tag{A-67b}$$

$$SHFR = \frac{W}{S}\left|\frac{\sin(\psi+\phi)}{\cos(\phi)}\right| \tag{A-67c}$$

$$OR = 1 - TSHR \tag{A-67d}$$

$$URF = USHR \tag{A-67e}$$

$$URB = SHFR \tag{A-67f}$$

$$LR = TSHR - (USHR + SHFR) \tag{A-67g}$$

Case 6 for $\varphi_4 < \varphi < \varphi_3$:

$$USHR = \frac{R}{S}\left[\sin|\kappa| - \tan(\phi)\cdot\{1-\cos(\kappa)\}\right] \tag{A-68a}$$

$$SHCR = \frac{R}{S}\left[\frac{1-\cos(\eta+\psi+\phi)}{\cos(\phi)}\right] \tag{A-68b}$$

$$OR = 0 \tag{A-68c}$$

$$URF = USHR \tag{A-68d}$$

$$URB = 1 - SHCR \tag{A-68e}$$

$$LR = SHCR - USHR \tag{A-68f}$$

Case 7 for $-90° < \varphi \le \varphi_4$:

$$USHR = 1 - \frac{R}{S}\left[\cos(\phi) - \tan|\phi|\cdot\{1-\sin|\phi|\}\right] \tag{A-69a}$$

$$OR = 0 \tag{A-69b}$$

$$URF = USHR \tag{A-66c}$$

$$URB = 0 \tag{A-69d}$$

$$LR = 1 - USHR \tag{A-69e}$$

A.4 Boundaries between Illuminated and Shaded Areas

In the ray-tracing blind model, illuminated surfaces are used as sources for emitting rays. Figure A-8 shows these surfaces (identified by numbers) for calculation cases used by the flat-slat blind sub-model. Figures A-13 and A-14 illustrates the illuminated surfaces for calculation cases with the positive angle *k* used by the curved-slat blind sub-model. As shown, a blind slat (and/or a slat edge) is completely illuminated in several calculation cases. In other cases, the blind slat(s) is partially illuminated. For completely illuminated slat cases, calculations described in Section A.2 can adequately be employed to determine essential data used to represent the illuminated surface(s). For partially illuminated slat cases, a point used to represent a boundary between illuminated and shaded surfaces is required in addition to points used to define the blind enclosure geometry. In the following sections, calculations of the boundary point are presented.

A.4.1 Calculations for Blinds with Flat Slats

As shown in Figure A-8, a point representing a boundary between illuminated and shaded surfaces is not required for Calculation Cases 2 and 3. However, the boundary point is needed for the other cases. As shown, points *G*, *H* and *I* are needed for Calculation Cases 1, 4 and 5, respectively.

For Calculation Case 1, the point *G* can be determined by finding a ray intersection on the lower slat. For $\phi > 90° - \psi$, the point *B* is the origin of the ray. Otherwise, the point *C* is the origin of the ray. According to Figure A-1, the unit vector representing the direction of the ray can be given as a function of the profile angle by:

$$\vec{V}_e = \begin{bmatrix} \cos(\phi) \\ \sin(\phi) \end{bmatrix} \tag{A-70}$$

Then, a ray intersection algorithm described later in Section A.8.1 can be used to find the ray intersection on the slat (represented by a straight line).

Similarly, for Calculation Case 4, the point *H* can be determined by finding the ray intersection on the upper slat with the point *A* as the origin of the ray. For Calculation Case 5, the point *I* can be determined by finding the ray intersection on the upper slat edge with the point *A* as the origin of the ray.

A.4.2 Calculations for Blinds with Curved Slats

For the positive angle *k*, no boundary point is required for Calculation Cases 2 and 6 as shown in Figures A-13 and A-14. A boundary point on the lower slat (*BL*) is however required for Calculation Cases 1, 3, 4, and 5. A boundary point on the upper slat (*BU*) is also required for Calculation Cases 4, and 7. For Calculation Case 5, two boundary points on the upper slat (BU_L and BU_R) are required as shown in Figure A-14.

For Calculation Case 1, the point *BL* can be calculated by finding a ray intersection on the lower slat with the upper slat left edge (the point *OU*) as the origin of the ray. Similar to the flat-slat blind model, Equation (A-70) can be used to determine the direction of the ray in the curved-slat blind model. Ray intersection calculations described in Section A.8.2 can be used to find the ray intersection on the slat (represented by a curvature).

For Calculation Case 3, the point *BL* is calculated differently from that discussed for Calculation Case 1. As shown in Figure A-13, the ray direction is tangential to the lower slat curvature at the point *BL*. Therefore, the surface normal at the point *BL* is perpendicular to the ray direction. Because a dot product of perpendicular vectors is zero, a unit vector of the surface normal can be determined as (by using Equation (A-70) as the ray direction vector):

$$\vec{U}_n = \begin{bmatrix} \sin(\phi) \\ -\cos(\phi) \end{bmatrix} \tag{A-71}$$

Knowing the unit surface normal vector, point *BL* can then be determined as a function of the curvature center of the lower slat (CL) and the curvature radius (*R*) as follows:

$$BL = \left(CL_x + R \cdot \sin(\phi), CL_x - R \cdot \cos(\phi)\right) \tag{A-72}$$

For Calculation Case 4, Equation (A-72) can be used to determine the point *BL*. The point *BU* can be calculated by finding a ray intersection on the upper slat with the point *OU* as the origin of the ray. Equation (A-70) is used to determine the ray direction whereas ray intersection calculations described in Section A.8.2 is used to determine the ray intersection on the upper slat.

For Calculation Case 5, the points *BL* and BU_L are identically calculated as the points *BL* and *BU* for Calculation Case 4, respectively. The point BU_R is similarly calculated as the point BU_L except that the point *BL* is used as the origin of the ray instead of the point *OU*.

For Calculation Case 7, the point *BU* can similarly be calculated as the point *BU* for Calculation Case 4. However, the lower slat left edge (the point *OL*) is used as the origin of the ray instead of the point *OU*.

Similar to the calculations of the profile angle limits, the calculations of the boundary points just described for the positive angle *k* cases can also be used for cases when both the slat angle and the angle κ are negative. For cases when the slat angle is positive and the angle κ is negative, slightly different calculations are required since, for these cases, the front side of the upper slat becomes a part of the blind enclosure as shown in Figure A-12. It should be noted that Calculation Cases 2 to 6 when the slat angle is positive and the angle κ is negative are similar to Calculation Cases 1 to 5 when the angle *k* is positive except that there is one more illuminated surface in addition to illuminated areas shown in Figures A-13 and A-14. For these cases, the front side of the upper slat is completely illuminated. The calculations previously described for Calculation Cases 1 to 5 for the positive angle *k* can be used to determine the boundary point(s) for the partially illuminated slat(s).

For Calculation Case 1 when the slat angle is positive and the angle κ is negative, the front side of the upper slat is partially illuminated. Equation (A-72) can be used to determine the boundary point on the front side of the upper slat except that the curvature center of the upper slat is used in place of the curvature center of the lower slat (i.e. CU is used instead of CL). For this case, (the front side of) the lower slat is also partially illuminated. Similar calculations used for the point *BL* for Calculation Case 1 when the angle *k* is positive can be used to determine the lower slat boundary point. However, the boundary point on the front side of the upper slat is used as the origin of the ray instead of the upper slat left edge (i.e. the point *OU*).

For Calculation Case 7 when the slat angle is positive and the angle κ is negative, only the front side of the upper slat and the lower slat are partially illuminated. Equation (A-72) can be used to determine the boundary point on the lower slat. Then, the lower slat boundary point is used as the origin of the ray for the calculations of the boundary point on the front side of the upper slat. Similar calculations used for the point *BU* for Calculation Case 7 when the angle *k* is positive can be used to determine the boundary point on the front side of the upper slat.

A.5 Monte-Carlo Ray-Tracing Algorithm

Section A.3 presents analytically derived formulations used by the ray-tracing blind model to determine how much the sunlight passes directly through the blind assembly (i.e. the opening ratio -- *OR*), and how much the sunlight falls on blind slats (i.e. the slat ratios -- *URF*, *URB*, *LR*). This section describes a Monte-Carlo ray tracing algorithm used by the ray-tracing blind model to handle transmitted and/or reflected portions of the sunlight falling on the blind slats. The Monte-Carlo ray tracing (MCRT) algorithm utilizes a computer graphic technique (i.e. the ray-tracing technique) to trace rays transmitted through and/or reflected from illuminated surfaces. The MCRT algorithm also employs a statistical technique (i.e. the Monte-Carlo method) to deal with blinds having slat surfaces that may be neither purely-diffuse nor purely-specular.

In the ray-tracing blind model, a large number of rays are emitted from illuminated surfaces. Number of emitted rays from each illuminated surface can be determined according to Section A.6.1. Figure A-15 shows a flow chart of the MCRT algorithm used to trace emitted rays from each illuminated surface. As shown, the MCRT algorithm starts the ray tracing process by emitting a ray from a random location within the illuminated surface. The MCRT algorithm employs a random number to determine the location of an emitted ray as described in Section A.6.3. It should be noted that shaded boxes shown in Figure A-15 are where the statistical technique is utilized. In the ray-tracing blind model, the emitted ray is actually a ray incident from the outside opening that is then either transmitted through or reflected from the illuminated surface; hence, the MCRT algorithm must check whether the incident ray is transmitted through or reflected from the illuminated slat as discussed in Section A.7. If the ray is transmitted, it is necessary to determine the surface and the location where the transmitted ray emerges as discussed in Section A.8.1. Then, the MCRT algorithm will determine whether the ray is transmitted (or reflected) diffusely or specularly before it determines the direction of the emitted ray. Section A.8.2 discusses how to determine the type of the transmitted (and/or reflected) ray, and Sections A.8.4 and A.8.5 describe calculations used to determine the direction of the ray. Next, the MCRT algorithm uses calculations described in Section A.9 to determine where the emitted ray ends up (i.e. the point of ray intersection). If the emitted ray hits either the outside opening or the inside opening, the ray is assumed to be totally absorbed by the surface. Therefore, the ray tracing process for this ray is done. Otherwise, the MCRT algorithm continues tracing this ray until it is absorbed by either an opening or a slat surface as shown in Figure A-15. The MCRT algorithm then starts emitting another ray. A similar ray tracing process previously described continues until all required rays for the illuminated surface (i.e. $N > N_e$) have been emitted. If there are more than one illuminated surfaces, the same MCRT algorithm is used to emit rays for another illuminated surfaces.

As shown in Figure A-15, when a ray hits an opening or is absorbed by a slat surface, the ray intensity associated with the ray is added to the total intensity absorbed by each surface. Section A.6.2 describes the calculations of the emitted ray intensity. The ray-tracing blind model uses the accumulated intensity by surfaces of the blind enclosure to determine blind optical properties as discussed in Section A.10.

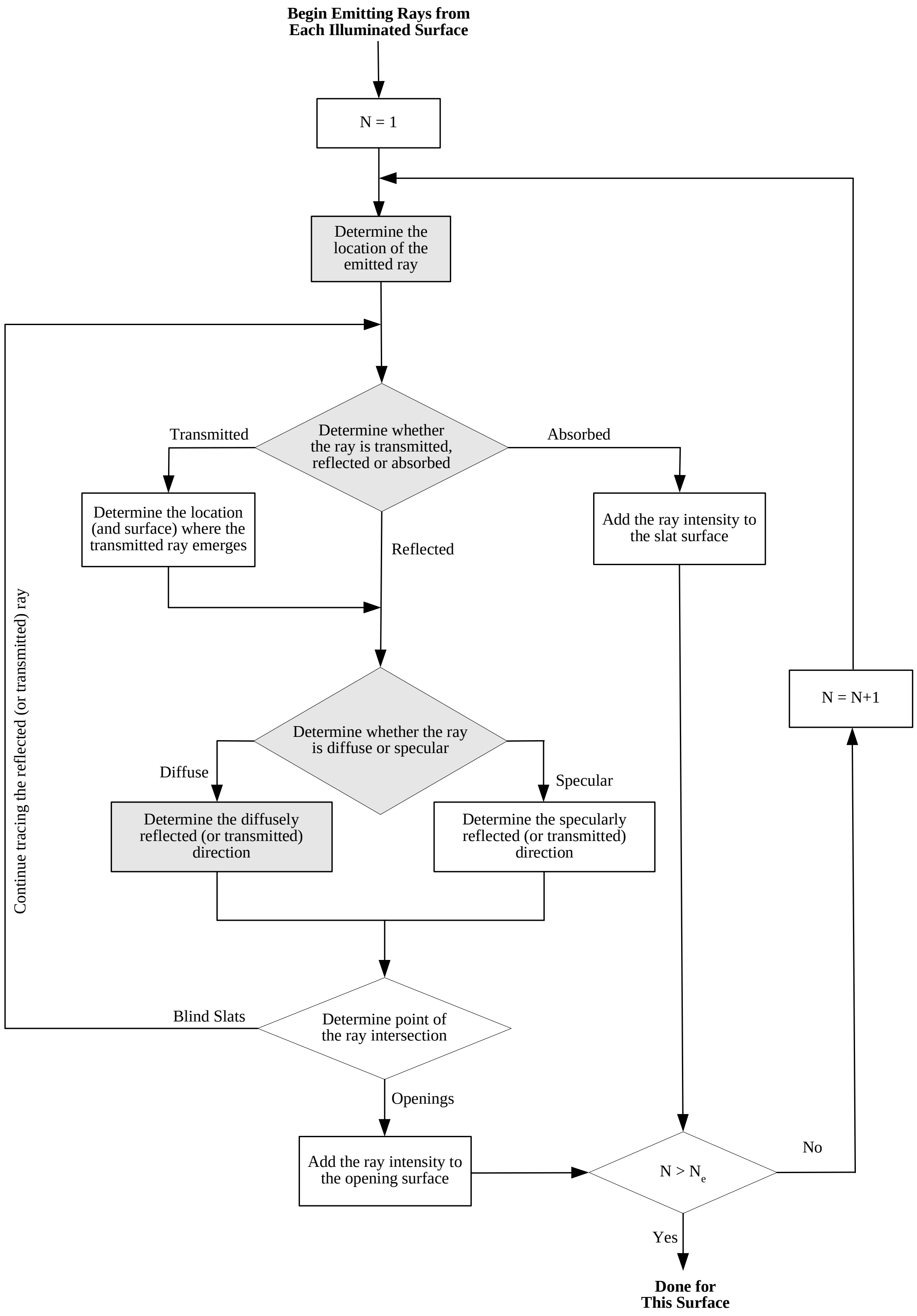

Figure A-15 Flow Chart of the Monte-Carlo Ray-Tracing Algorithm

A.6 Ray Emission

A.6.1 Number of Emitted Rays

The ray-tracing blind model requires the total number of emitted rays ($N_{e,tot}$) as an input. As shown in Figures A-8, A-13 and A-14, some calculation cases have only one illuminated surface while other cases have two illuminated surfaces. For the curved-slat blind model when the slat angle is positive and the angle k is negative, some cases may have three illuminated surfaces. For cases with one illuminated surface, the number of emitted rays from the illuminated surface is simply equal to the total number of emitted rays. For cases with two or more illuminated surfaces, the number of emitted rays from each illuminated surface can commonly be calculated by:

$$N_{e,i} = Int\left(\frac{IR_i}{1-OR}\right)\cdot N_{e,tot} \qquad \text{(A-73)}$$

where $N_{e,i}$ = number of emitted rays from the illuminated surface i,

IR_i = illuminated slat ratio of the illuminated surface i, and

Int = function used to convert a floating point number to an integer number.

Depending on the illuminated surface considered, the illuminated ratio is equal to either one of the slat ratios or the edge ratio. The slat ratios, the edge ratio, and the opening ratio can be calculated as discussed in Section A.3.

A.6.2 Emitted Ray Intensity

With a unit radiative flux of the incident solar radiation on the outside opening, the radiative fraction of each illuminated surface is simply equal to the illuminated ratio. The ray radiative intensity (i.e. the radiative fraction associated with an emitted ray) from an illuminated surface can generally be determined by:

$$I_{ray} = \frac{IR_i \cdot (\tau_i + \rho_i)}{N_{e,i}} \tag{A-74}$$

where I_{ray} = ray intensity from the illuminated surface *i*, and

τ_i = solar transmittance of the illuminated surface *i*.

ρ_i = solar reflectance of the illuminated surface *i*.

It should be noted that the ray-tracing blind model allows different solar optical properties of the front side and the back side of the blind slats. Therefore, the ray intensity from an illuminated front surface may be different from that from an illuminated back surface if the front slat optical properties are not the same as the back slat optical properties. Otherwise, the ray intensity would be the same for all illuminated surfaces assuming no numerical error. Since the flat-slat blind sub-model considers slat edges as parts of the blind enclosure, the sub-model assumes that the solar reflectance of the slat edges is equal to the average of the solar reflectance of the front side and the back side of the blind slats. The sub-model also assumes that the solar transmittance of the slat edges is equal to zero even though the slat surfaces are translucent or perforated.

A.6.3 Emitted Ray Location

Figure A-8 shows illuminated surfaces for calculation cases used by the flat-slat blind model whereas Figures A-13 and A-14 illustrates illuminated surfaces for calculation cases with the positive angle *k* used by the curved-slat blind model. Calculations described in Sections A.2 and A.4 can be employed to determine two end points used to define an illuminated surface.

To determine the location of an emitted ray for the flat-slat blind sub-model, let *PA* and *PB* be the end points of an illuminated flat surface. Also, let F_{loc} be a random number (number between zero and unity) used to determine the location of an emitted ray. Then, the emission point, *PE*, on the illuminated flat surface can be calculated by:

$$PE_x = PA_x + F_{loc} \cdot \left(PB_x - PA_x \right) \tag{A-75a}$$

$$PE_y = PA_y + F_{loc} \cdot \left(PB_y - PA_y \right) \tag{A-75b}$$

To determine the location of an emitted ray for the curved-slat blind sub-model, let *AA* and *AB* be angles representing the end points of an illuminated curved surface. Then, the emission angle (*AE*) that represents the emission point on the illuminated curved surface can be calculated by:

$$AE = AA + F_{loc} \cdot \left(AB - AA \right) \tag{A-76}$$

Next, the emission point, *PE*, can be calculated as a function of the curvature center (*C*) and the radius (*R*) of the illuminated curved surface by:

$$PE_y = C_y + R \cdot \cos\left(AE \right) \tag{A-77a}$$

$$PE_x = C_x + \sqrt{R^2 - \left(PE_y - C_y\right)^2} \quad \text{for } AE < \pi \qquad \text{(A-77b)}$$

$$PE_x = C_x - \sqrt{R^2 - \left(PE_y - C_y\right)^2} \quad \text{for } AE > \pi \qquad \text{(A-77c)}$$

It is worth mentioning that, with known end points of the illuminated curved surface, the angles *AA* and *AB* can be determined using the calculation procedure (i.e. Equations (A-19) to (A-22)) described in Section A.2.3.

A.7 Transmission/Reflection/Absorption Probability

To determine whether a ray incident on a slat surface is transmitted, reflected or absorbed, the ray-tracing blind model utilizes the statistical technique by comparing a random number with the solar optical properties of the slat surface. If the random number is less than or equal to the slat solar reflectance, the model treats this ray as a reflected ray from the surface at a point of the ray intersection. If the random number is less than or equal to the sum of the slat solar reflectance and the slat solar transmittance, the model treats this ray as a transmitted ray. Otherwise, the model considers this ray to be totally absorbed by the slat surface. As previously discussed in Section A.6.2, the ray-tracing blind model allows different solar optical properties of the front side and the back side of the blind slats. Therefore, different slat optical properties are used in the comparison for different sides of the slat surface.

It should be noted that the previous paragraph describes a comparison used for a ray after multiple transmissions and/or reflections. However, as discussed in Section A.5, an emitted ray is actually a ray from the outside opening that is initially incident on an illuminated surface and then either transmitted through or reflected from the surface (but not absorbed by the surface). Therefore, the multiplication of the random number and the sum of the slat solar reflectance and the slat solar transmittance is used in place of the random number in the initial comparison used for the emitted ray.

A.8 Tracing of Transmitted/Reflected Rays

A.8.1 Emerging Location of Transmitted Rays

If an incident ray is transmitted through a slat, it is necessary to determine the surface and the location where the transmitted ray emerges. For the flat-slat blind model, it is assumed that the solar transmittance of the slat edges is equal to zero even though the slat surfaces are translucent or perforated as previously mentioned. This means that the ray can only be transmitted through slat surfaces (used to represent the blind enclosure as discussed in Section A.2). If the ray is incident on the upper slat, the transmitted ray essentially emerges from the lower slat. Then, the location on the lower slat can be calculated by:

$$(x_e, y_e) = (x_i, y_i) + (T\sin(\psi), S - T\cos(\psi)) \tag{A-78}$$

where (x_e, y_e) and (x_i, y_i) are the emerging location and the incident location, respectively. If the incident ray is from the outside opening (i.e. the transmitted ray is considered to be the emitted ray), the emitted ray location described in Section A.6.3 is used as the incident location. Otherwise, the ray intersection calculations described in Section A.9 can be used to determine the incident location. Equation (A-78) can also be used when the ray is incident on the lower slat and the transmitted ray essentially emerges from the upper slat. However, the positive sign in front of the second term on the right hand side of the equation is replaced by a negative sign.

For the curved-slat blind model, if the ray is incident on the front side of the upper slat (when the angle κ is negative), the transmitted ray essentially emerges from the back side of the upper slat and the emerging location is the same as the incident location (the curved-slat blind model assumes that slat thickness is negligible). If the ray is incident on the lower slat (always on the front side), the transmitted ray also emerges from the back side of the upper slat. The *x*-value of the emerging location is the same as the *x*-value of the incident location whereas the y-value of the emerging location can be determined by subtracting the slat spacing from the *y*-value of the incident location. If the ray is incident on the back side of the upper slat and the angle κ is positive, the transmitted ray essentially emerges from the lower slat. The *x*-value of the emerging location is the same as the *x*-value of the incident location whereas the *y*-value of the emerging location can be determined by adding the slat spacing to the *y*-value of the incident location. However, if the ray is incident on the back side of the upper slat and the angle κ is negative, it is necessary to check whether the transmitted ray emerges from either the front side of the upper slat or from the lower slat. If the transmitted emerges from the front side of the upper slat, the emerging location is simply the same as the incident location. If the transmitted emerges from the lower slat, the emerging location can be determined as previously described for the case when the ray is incident on the back side of the upper slat and the angle κ is positive.

A.8.2 Type of Transmitted or Reflected Rays

The ray-tracing blind model requires an input, called the reflective specularity ratio, to handle blinds having partially diffuse-reflecting and partially specular-reflecting slats. The reflective specularity ratio is defined as the ratio of the specularly reflected rays to the total reflected rays. The ray-tracing blind model then utilizes a statistical approach by comparing the reflective specularity ratio with a random number used to determine the type of the reflected ray. If the random number is less than or equal to the reflective specularity ratio, the ray is reflected specularly. Otherwise, the ray is reflected diffusely.

Similarly, the ray-tracing blind model also requires an input, called the transmissive specularity ratio, to handle blinds having partially diffuse-transmitting and partially specular-transmitting slats (e.g. blinds with perforated and translucent slats). The transmissive specularity ratio is defined as the ratio of the specularly transmitted rays to the total transmitted rays. Likewise, the ray-tracing blind model then utilizes the statistical approach by comparing the transmissive specularity ratio with a random number used to determine the type of the transmitted ray. If the random number is less than or equal to the transmissive specularity ratio, the ray is transmitted specularly. Otherwise, the ray is transmitted diffusely.

Like the slat radiative properties, the ray-tracing blind model allows different specularity ratios for the front side and the back side of the blind slats. Therefore, different specularity ratios are used in the comparison for different sides of the slat surface.

A.8.3 Surface Normal

Prior to calculations of the transmitted/reflected ray direction, it is essential to know the surface normal first. The surface normal for a flat surface is fixed while the surface normal for a curved surface varies depending on the point of ray emission/intersection. This means that the surface normal of the flat surface can once be pre-calculated at the beginning while the surface normal of the curved surface must be calculated after calculations of the ray emission/intersection.

Referring to Figure A-1, unit normal vectors of surfaces used in the flat-slat blind model can be calculated as a function of the slat angle as follows:

$$\vec{U}_{UpperSlat} = \begin{bmatrix} \sin(\psi) \\ \cos(\psi) \end{bmatrix} \tag{A-79a}$$

$$\vec{U}_{LowerSlat} = -\vec{U}_{UpperSlat} \tag{A-79b}$$

$$\vec{U}_{UpperEdge} = \begin{bmatrix} -\cos(\psi) \\ \sin(\psi) \end{bmatrix} \tag{A-79c}$$

$$\vec{U}_{LowerEdge} = -\vec{U}_{UpperEdge} \tag{A-79d}$$

It should be noted that the unit normal vectors of openings are not needed since rays hitting the openings are considered to be absorbed only.

For the curved-slat blind model, a unit normal vector of a curved blind slat can be determined as a vector from the curvature center to a point of the ray emission/intersection or a vector from the ray emission/intersection to the curvature center depending on which side of the blind slat is under consideration. For the lower slat, only the front side is considered to be a part of the blind enclosure. Therefore, the unit normal vector of the lower slat is always determined as the unit vector from the curvature center to the ray emission/intersection. For the upper slat, however, there are two cases. If an angle κ is positive, only the back side of the upper slat is considered to be a part of the blind enclosure. If the angle κ is negative, the front side of the upper slat is also considered to be a part of the blind enclosure. The unit normal vector of the back side of the upper slat is determined as the unit vector from the ray emission/intersection to the curvature center. On the other hand, the unit normal vector of the front side of the upper slat is determined in the opposite direction. For the case when the angle κ is negative, if the ray hits the upper slat curvature, it is essential to check which side of the upper slat the ray actually hits. To determine which side of the upper slat the ray hits, let $\vec{V}$ and $\vec{U}$ be unit direction vectors of the incident ray and surface normal of the upper-slat back side, respectively. If the dot product of $\vec{V}$ and $\vec{U}$ is less than zero, the incident ray hits the back side of the upper slat. Otherwise, the incident ray hits the front side of the upper slat.

A.8.4 Direction of Specularly Transmitted or Reflected Rays

Essentially, the direction of a specularly transmitted ray is the same as its incident direction; hence, no additional calculation is needed. On the hand, the calculation of the direction of a specularly reflected ray is necessary. Figure A-16 shows a relationship between directions of incident and specularly reflected rays. As shown in the figure, $\vec{I}$ is a vector representing the direction of the incident ray, $\vec{U}$ a unit normal vector representing the normal direction of a specularly reflecting surface, and $\vec{S}$ a vector representing the direction of the specularly reflected ray. The vector $\vec{S}$ can be expressed by:

$$\vec{S} = \vec{I} + 2 \cdot \left|\vec{I}\right| \cdot \cos(\theta) \cdot \vec{U} \tag{A-80a}$$

where the cosine of the angle of incidence can be given by:

$$\cos(\theta) = \frac{\vec{I} \bullet \left(-\vec{U}\right)}{\left|\vec{I}\right|\left|-\vec{U}\right|} = -\frac{\vec{I} \bullet \vec{U}}{\left|\vec{I}\right|} \tag{A-80b}$$

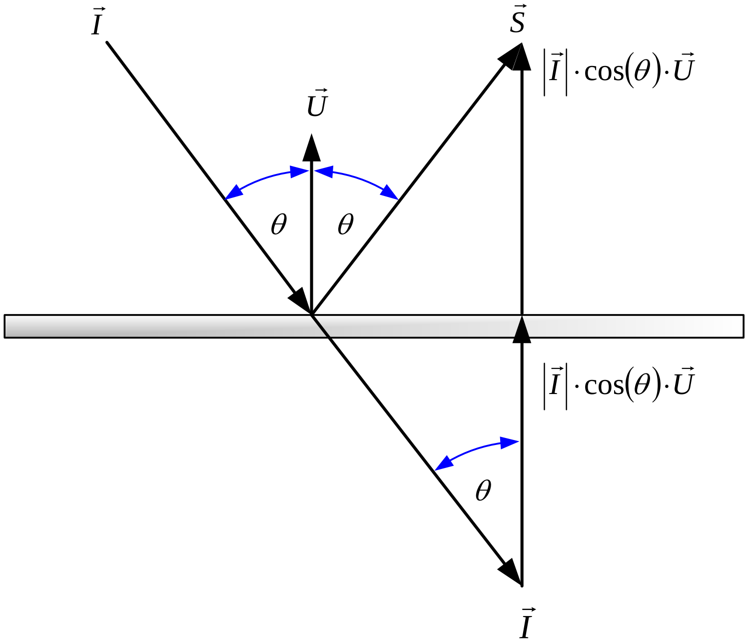

Figure A-16 Relationship between Directions of Incident and Specularly Reflected Rays

Combining the two equations above, the specularly reflected direction can be calculated in the vector form as follows:

$$\vec{S} = \vec{I} - 2\left(\vec{I} \bullet \vec{U}\right)\vec{U} \tag{A-80c}$$

A.8.5 Direction of Diffusely Transmitted or Reflected Rays

The same calculation can be used to determine the direction of a diffusely transmitted ray and the direction of a diffusely reflected ray. To determine the direction of a diffusely transmitted or reflected ray, the ray tracing blind model utilizes a random number (F_{dir}) to calculate an angle (β) between the diffusely-reflected (or transmitted)-ray direction and the surface normal as follows:

$$\beta = -\pi / 2 + \pi \cdot F_{dir} \tag{A-81}$$

Equation (A-81) implies that the angle β must be within –π/2 and π/2.

Figure A-17 illustrates a relationship between the direction of a diffusely reflected ray and the surface normal. As shown in the figure, $\vec{D}$ is a vector representing the direction of the diffusely reflected ray, and $\vec{U}$ a unit normal vector representing the normal direction of a diffusely reflecting surface. The vector $\vec{D}$ can be derived as follows:

$$\theta_1 = \tan^{-1}\left(U_x / U_y\right) \quad \text{for } U_y \neq 0 \tag{A-82a}$$

$$\theta_1 = \pi / 2 \quad \text{for } U_y = 0 \text{ and } U_x \geq 0 \tag{A-82b}$$

$$\theta_1 = -\pi / 2 \quad \text{for } U_y = 0 \text{ and } U_x < 0 \tag{A-82c}$$

$$\theta_2 = \theta_1 + \beta \tag{A-82d}$$

$$D_x = D_y \cdot \tan(\theta_2) \tag{A-82e}$$

$$\vec{U} \bullet \vec{D} = U_x D_x + U_y D_y = [U_x \tan(\theta_2) + U_y] \cdot D_y = \cos(\beta) \tag{A-82f}$$

Therefore, the direction of the diffusely reflected ray can be determined by:

$$D_y = \frac{\cos(\beta)}{[U_x \tan(\theta_2) + U_y]} \tag{A-83a}$$

$$D_x = D_y \tan(\theta_2) \tag{A-83b}$$

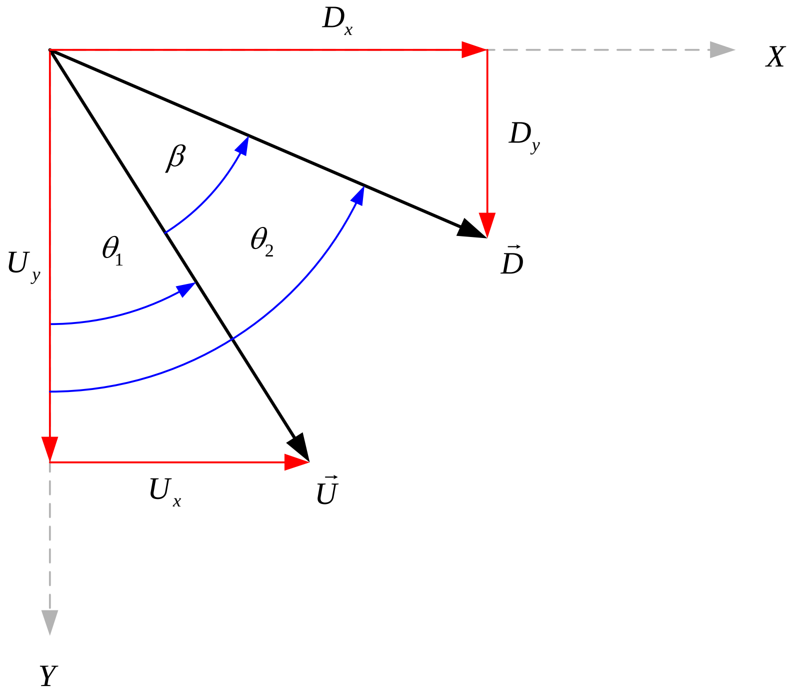

Figure A-17 Relationship between Directions of Diffusely Reflected Ray and Surface Normal

A.9 Ray Intersection Calculations

As shown in Section A.2, in the flat-slat blind model, the blind enclosure consists of six surfaces (two openings, two flat slats, and two slat edges) all represented by straight lines. There are two cases in the curved-slat blind model. For the positive angle κ, the blind enclosure consists of four surfaces where two openings are represented by straight lines and two curved slats (the back side of the upper slat and the front side of the lower slat) are represented by curved lines. For the negative angle κ, the blind enclosure consists of five surfaces with an addition of the front side of the upper slat represented by a curved line. Calculations of ray intersections on straight lines and curved lines are described in detail in the following sections.

A.9.1 Ray Intersection on Straight Line

Figure A-18 shows a ray intersection on a given surface represented by a straight line. As shown in the figure, the point (x_0,y_0) represents the origin of the incident ray, the unit vector (v_x,v_y) indicates the direction of the ray, the point (x_1,y_1) represents the ray intersection, and the points (x_L,y_L) and (x_R,y_R) represent a given surface.

Using an equation for a straight line from the ray origin to the ray intersection, the intersection can then be given by:

$$(x_1, y_1) = (x_0 + Tv_x, y_0 + Tv_y) \tag{A-84}$$

where T is the length of the ray path, the distance from the ray origin to the ray intersection.

The intersection can also be described using the following relationship (typically used for a straight line represented by two joining points):

$$y_1 = m_l x_1 + b_l \tag{A-85}$$

where $m_l = \frac{y_R - y_L}{x_R - x_L}$ is the slope of the line representing the given surface, and $b_l = \frac{x_R y_L - x_L y_R}{x_R - x_L}$ is the y-intercept of the line.

Substituting x_1 and y_1 from Equation (A-84) into Equation (A-85), the path length of the ray can then be determined by:

$$T = \frac{y_0 - m_l x_0 - b_l}{m_l v_x - v_y} \tag{A-86}$$

For a negative value of T, the intersection would be behind the ray origin meaning that the ray cannot hit the given surface. For a positive value of T, the calculated intersection using Equation (A-84) would represent a possible intersection on the given surface. Because the equations of a straight line (e.g. Equation (A-85)) typically describe an infinitely long line, it is essential to check if this possible intersection is actually on the given surface to avoid a fault ray intersection as illustrated in Figure A-19.

The above calculations illustrate the general case where a component of the ray direction vector is not zero and the slope of the given surface is finite (i.e. the surface is not a vertical line). To avoid computational errors due to infinite numbers (e.g. numbers divided by zero), however, the following algorithm shown in Figure A-20 is used in the ray-tracing blind model to determine the path length of the ray for the ray intersection on the straight line.

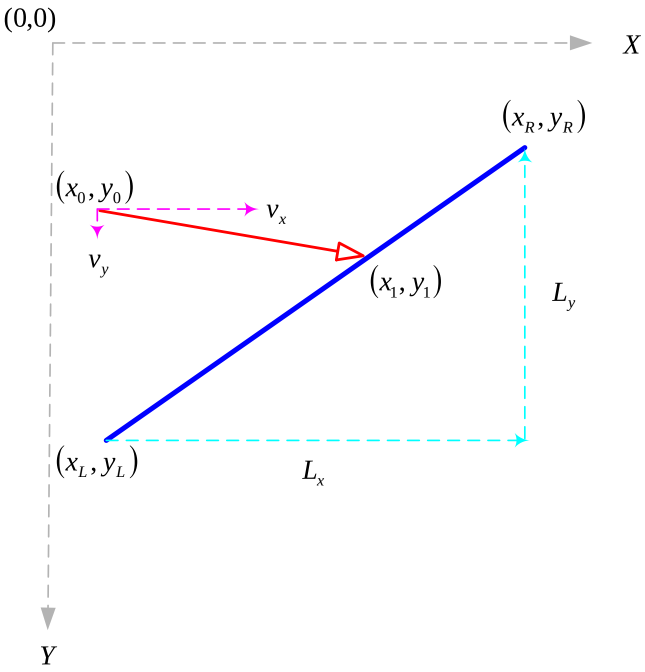

Figure A-18 Ray Intersection on Straight Line

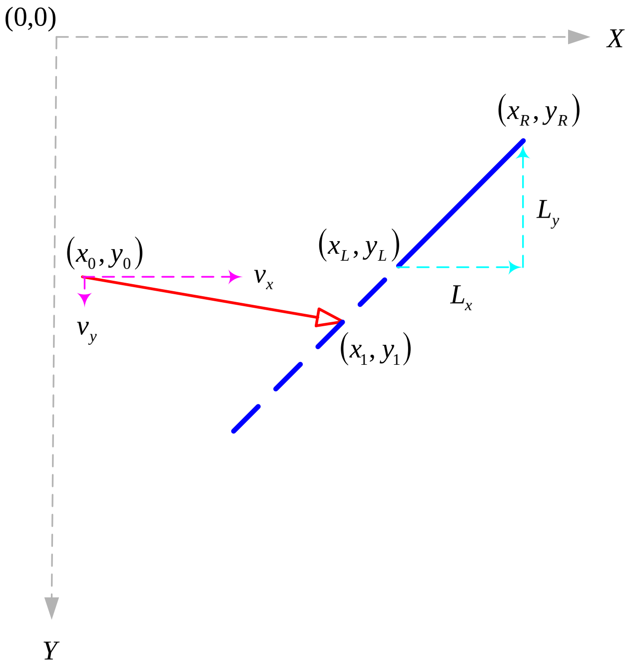

Figure A-19 Fault Ray Intersection on Straight Line

```
If ( $v_x = 0$ ) Then
      If ( $L_x = 0$ ) Then
            $T = -999$
      Else If ( $L_y = 0$ ) Then
            $T = (y_L - y_0)/v_y$
      Else
            $T = [(y_L - y_0) + m_l(x_0 - x_L)]/v_y$
      End If
Else If ( $v_y = 0$ ) Then
      If ( $L_x = 0$ ) Then
            $T = (x_L - x_0)/v_x$
      Else If ( $L_y = 0$ ) Then
            $T = -999$
      Else
            $T = [(x_L - x_0) + (y_0 - y_L)/m_l]/v_x$
      End If
Else
      If ( $L_x = 0$ ) Then
            $T = (x_L - x_0)/v_x$
      Else If ( $L_y = 0$ ) Then
            $T = (y_L - y_0)/v_y$
      Else
            If ( $(v_y / v_x) = m_l$ ) Then
                  $T = -999$
            Else
                  $T = \frac{y_0 - m_l x_0 - b_l}{m_l v_x - v_y}$
            End If
      End If
End If
```

Figure A-20 Algorithm to Calculate Ray Path Length for Ray Intersection on Straight Line

A.9.2 Ray Intersection on Curvature

Figure A-21 shows a ray intersection on a given surface represented by a curvature (a part of a circle). Similar to the ray intersection on the straight line, the point (x_0,y_0) represents the origin of the incident ray, the unit vector (v_x,v_y) indicates the direction of the ray, and the point (x_1,y_1) represents the ray intersection. However, the given surface is described by the curvature radius (R), the curvature center (x_c,y_c) and two angles (α_L and α_R) representing the left and right edges of the curvature.

Similar to the ray intersection on the straight line, the ray intersection can be determined using Equation (A-84). Using an equation for a circle, the relationship of the intersection and the center of the slat curvature can be given by

$$(x_1 - x_c)^2 + (y_1 - y_c)^2 - R^2 = 0 \tag{A-87}$$

Substituting x_1 and y_1 from Equation (A-84) into the circle equation, we get

$$\left(v_x^2 + v_y^2\right)T^2 + 2\left\{v_x(x_0 - x_c) + v_y(y_0 - y_c)\right\}T + \left\{(x_0 - x_c)^2 + (y_0 - y_c)^2 - R^2\right\} = 0 \tag{A-88}$$

Equation (A-88) is a quadratic equation in T where

$$A = v_x^2 + v_y^2 = 1 \tag{A-89a}$$

$$B = 2 \cdot \left\{v_x(x_0 - x_c) + v_y(y_0 - y_c)\right\} \tag{A-89b}$$

$$C = (x_0 - x_c)^2 + (y_0 - y_c)^2 - R^2 \tag{A-89c}$$

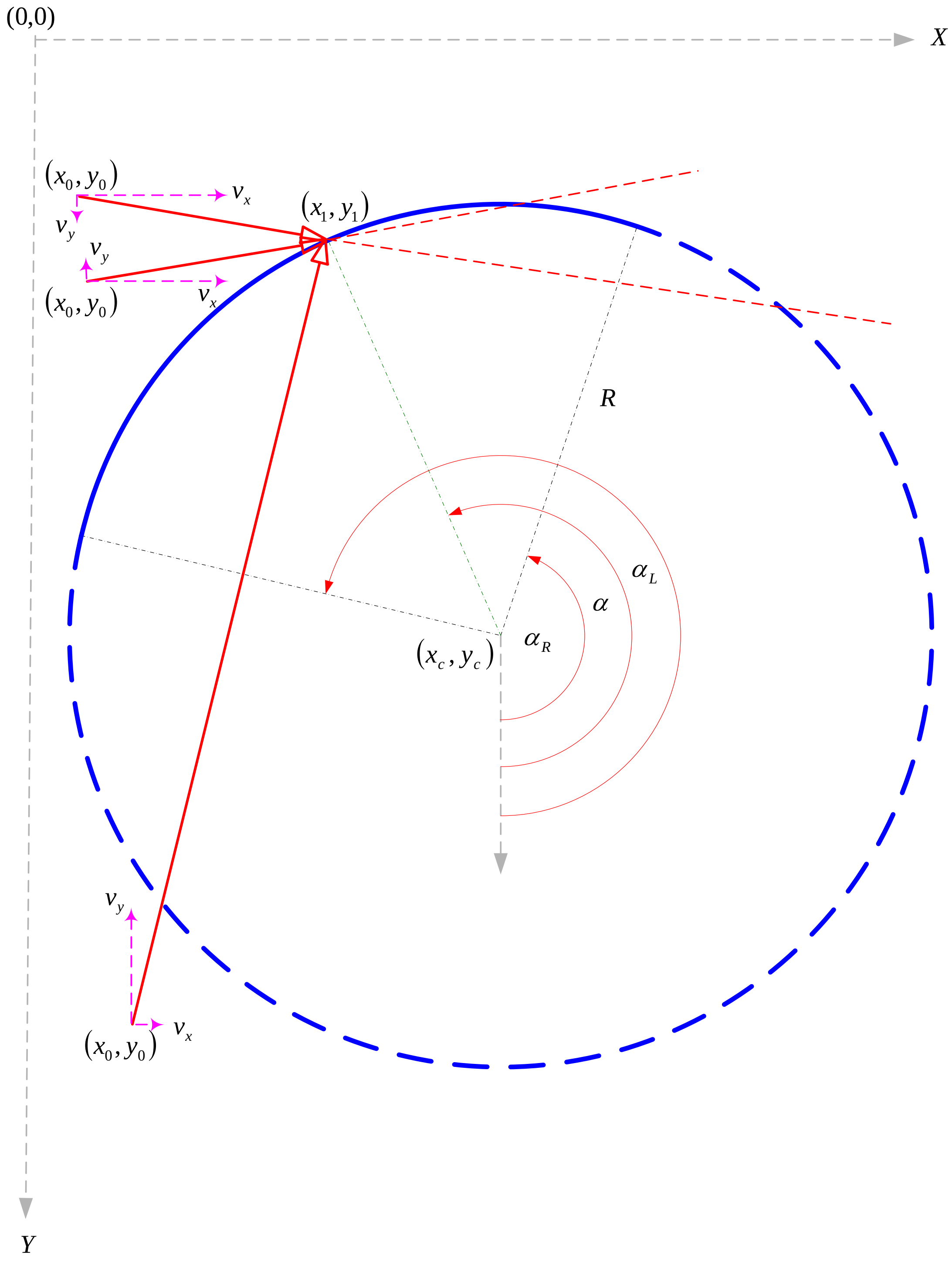

Figure A-21 Ray Intersection on Curved Line

Let $D = B^2 - 4AC$. Then, the solutions of the quadratic equation can be given by

$$T = \frac{-B \pm \sqrt{D}}{2A} \tag{A-90}$$

If $D < 0$, there are no real roots meaning that the ray does not intersect the circle.

If $D = 0$, there is one real root meaning that the ray is tangential to the circle.

If $D > 0$, there are two real roots representing two possible points of intersection with the circle.

For $D > 0$, if values of T are less than zero, the two roots represent points behind the ray origin implying that the ray does not actually hit the curvature. If both Ts are greater than zero, it is essential to check if the two possible points are on the curvature. The point is on the curvature if the angle α of that point is between angles α_L and α_R of the curvature as shown in Figure A-21. The angle α of each point can be determined using the same calculation procedure (Equations (A-19) to (A-22)) used to determine the angles α_L and α_R as previously discussed in Section A.2.3. If both points are on the curvature, the point closest to the ray origin (i.e. the point with lesser T) is the only possible intersection on the curvature.

A.9.3 Improving Ray Intersection Calculations

The previous two sections describe the calculations for a possible intersection on a given surface. To determine the actual ray intersection, the straightforward approach would first find all possible points of intersection between the ray path and the blind enclosure (e.g. points *1* to *5* shown in Figure A-22). Then, the approach would check the path length of each possible intersection to find the surface where the ray actually hits (surface with the least path length). In Figure A-22, point *1* is the actual ray intersection.

The straight forward approach is quite simple to implement. However, it requires ray intersection calculations for all surfaces of the blind enclosure. Thus, the approach usually performs unnecessary calculations. To improve the computational efficiency, the unnecessary calculations should be avoided. For example, for a flat-slat blind, a ray originated from the lower slat cannot hit the lower edge and the lower slat itself. Therefore, ray intersection calculations for both surfaces are not needed. Also, if the *x*-component of the ray-direction vector is positive, the ray cannot hit the outside opening; hence, the ray intersection calculation for the outside opening is not required as well. It is worth mentioning that a ray originated from a flat surface cannot hit its original surface whereas a ray originated from a curved surface may hit its original surface. Figure A-23 show a ray intersection algorithm used in the flat-slat blind model. Figures A-24 and A-25 show a ray intersection algorithm used in the curved-slat blind model for the positive and the negative angle κ, respectively.

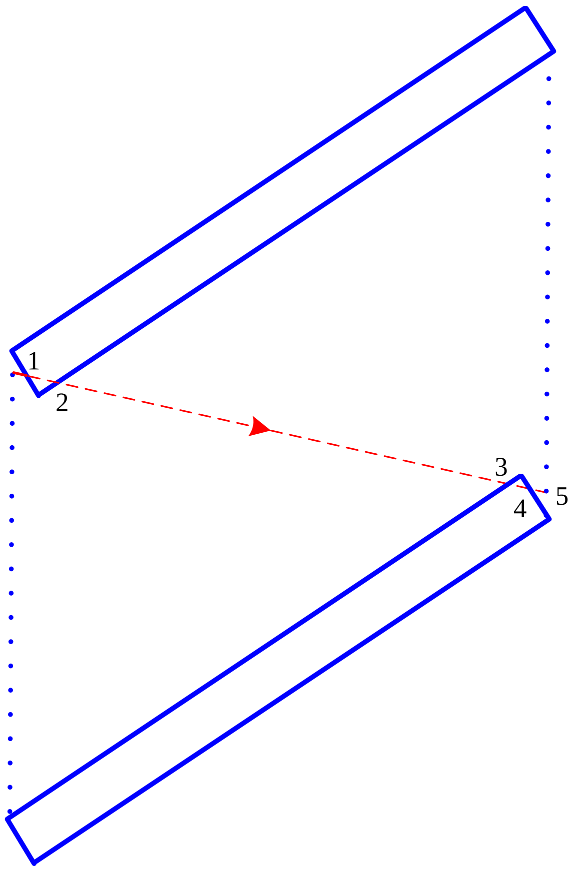

Figure A-22 Possible Ray Intersections in Flat-Slat Blind Model

```
If (Ray Origin = Upper Slat) Then
    Determine possible ray intersections on lower slat and lower edge
    If (an intersection found on both surfaces) Then
        Compare path lengths to find the actual intersection
    Else If (an intersection found on either one of surfaces) Then
        Done
    Else If (no intersection found on both surfaces) Then
        Check x-component of ray direction vector to find the actual
        intersection on an opening
    End If
Else If (Ray Origin = Lower Slat) Then
    Determine possible ray intersections on upper slat and upper edge
    If (an intersection found on both surfaces) Then
        Compare path lengths to find the actual intersection
    Else If (an intersection found on either one of surfaces) Then
        Done
    Else If (no intersection found on both surfaces) Then
        Check x-component of ray direction vector to find the actual
        intersection on an opening
    End If
If (Ray Origin = Upper Edge) Then
    Determine possible ray intersection on lower slat
    If (an intersection found on the surface) Then
        Done
    Else If (no intersection found on the surface) Then
        Find the actual intersection (on the outside opening)
    End If
Else If (Ray Origin = Lower Edge) Then
    Determine possible ray intersection on upper slat
    If (an intersection found on the surface) Then
        Done
    Else If (no intersection found on the surface) Then
        Find the actual intersection (on the inside opening)
    End If
End If
```

Figure A-23 Ray Intersection Algorithm for the Flat-Slat Blind Model

```
If (Ray Origin = Upper Slat) Then
    Determine possible ray intersections on upper slat and lower slat
    If (an intersection found on both surfaces) Then
        Compare path lengths to find the actual intersection
    Else If (an intersection found on either one of surfaces) Then
        Done
    Else If (no intersection found on both surfaces) Then
        Check x-component of ray direction vector to find the actual
        intersection on an opening
    End If
Else If (Ray Origin = Lower Slat) Then
    Determine possible ray intersection on upper slat
    If (an intersection found on the surface) Then
        Done
    Else If (no intersection found on the surface) Then
        Check x-component of ray direction vector to find the actual
        intersection on an opening
    End If
End If
```

Figure A-24 Ray Intersection Algorithm for the Curved-Slat Blind Model for Positive κ

```
If (Ray Origin = Front Side of Lower Slat) Then
    Determine possible ray intersection on lower slat
    If (an intersection found on the surface) Then
        Done
    Else If (no intersection found on the surface) Then
        Check x-component of ray direction vector to find the actual
        intersection on an opening
    End If
Else If (Ray Origin = Back Side of Upper Slat) Then
    Determine possible ray intersections on (back side of) upper slat and
    lower slat
    If (an intersection found on both surfaces) Then
        Compare path lengths to find the actual intersection
    Else If (an intersection found on either one of surfaces) Then
        Done
    Else If (no intersection found on both surfaces) Then
        Check x-component of ray direction vector to find the actual
        intersection on an opening
    End If
Else If (Ray Origin = Lower Slat) Then
    Determine possible ray intersection on upper slat
    If (an intersection found on the slat) Then
        Check which side of the slat where the ray actually hits
    Else If (no intersection found on the slat) Then
        Check x-component of ray direction vector to find the actual
        intersection on an opening
    End If
End If
```

Figure A-25 Ray Intersection Algorithm for the Curved-Slat Blind Model for Negative κ

A.10 Blind Solar-Optical Properties

The ray-tracing blind model determines four blind solar-optical properties: direct-direct blind transmittance, direct-reflected blind transmittance, direct blind reflectance, and direct blind absorptance. The direct-direct blind transmittance is defined as the fraction of direct sunlight that directly passes through the blind assembly without striking any blind slats. The direct-reflected blind transmittance is defined as the fraction of direct sunlight that indirectly passes through the blind assembly by reflections between the blind slats. The direct blind reflectance is defined as the fraction of direct sunlight that reflects from the blind assembly back to the outside. The direct blind absorptance is defined as the fraction of direct sunlight that is absorbed by the blind slats.

By definition, the direct-direct blind transmittance is identically the same as the opening ratio. Therefore, calculations described in Section A.3 are used to calculate the direct-direct blind transmittance by the ray-tracing blind model. Utilizing the MCRT algorithm as discussed in Section A.5, the direct-reflected blind transmittance can be determined as the accumulated ray intensity of the inside opening. Likewise, the direct blind reflectance can be determined as the accumulated ray intensity of the outside opening. Finally, the direct blind absorptance can simply be determined as the difference between one and the sum of all other blind optical properties.

It should be mentioned that, for blinds with flat slats, when the slat angle is zero, the direct-reflected blind transmittance must also include the fraction of direct sunlight that directly reflected from a slat edge (i.e. the upper slat edge in the model). The slat-edge reflection fraction can be calculated by multiplying the slat edge ratio and the solar reflectance of the slat edge. When both the slat angle and the profile angle are zero, the ray tracing process is unnecessary for the flat-slat blind model. For this special case, the direct-reflected blind transmittance is zero while the direct blind reflectance is equal to the slat-edge reflected fraction.

To check whether the ray-tracing blind model is correctly implemented, the direct blind absorptance may be calculated differently. The direct blind absorptance can alternatively be determined as the sum of the accumulated ray intensity of all blind slat surfaces (using the MCRT algorithm) and the fraction of direct sunlight that is initially absorbed by illuminated surface(s). The initial absorption fraction can generally be calculated as the sum of the product of the slat ratio and the solar absorptance of an illuminated surface.

APPENDIX B

NET-RADIATION OPTICAL BLIND MODEL FOR DIRECT SOLAR RADIATION

B.1 Overview

Like the ray-tracing optical blind model, the net-radiation blind model consists of two sub-models: one for blinds having non-zero-thickness flat slats and one for blinds having negligible-thickness curved slats. The net-radiation model also employs the same analytically derived formulations as described in Appendix A to determine how much the sunlight passes directly through the blind assembly, and how much the sunlight falls on blind slats. However, the model utilizes the net-radiation method, instead of the Monte-Carlo ray tracing technique, to deal with the sunlight that reflects from the blind slats. Detailed calculations required by the net-radiation model are described in the following sections. The calculation procedure used in the net-radiation blind model is summarized below.

- First, calculate essential information used to define the blind enclosure.
- Then, calculate limits of profile angle and determine calculation cases.
- Next, calculate ratios of sunlight passing directly through the blind and falling on slat surface(s).
- Then, determine blind enclosure surfaces and their view factors.

- Next, perform net-radiation calculations.
- Finally, calculate optical blind properties.

B.2 Common Calculations

The net-radiation blind model resembles the ray-tracing blind model in many aspects since both models utilize the same analytically derived formulations to determine how much the sunlight passes directly through the blind assembly, and how much the sunlight falls on blind slats. Therefore, calculations described in Sections A.2 to A.4 for the ray-tracing blind model are also used by the net-radiation blind model. However, it should be noted that the curved-slat blind sub-model of the net-radiation blind model was developed only for a positive angle κ. Therefore, the net-radiation curved-slat blind sub-model only uses calculations valid for the positive angle κ.

It should also be mentioned that, in the net-radiation blind model, if a blind slat is partially illuminated, the slat surface is subdivided into two surfaces: illuminated and shaded surfaces. Otherwise, there is no slat surface division. Figure B.1 illustrates the surface divisions for calculation cases in the flat-slat blind sub-model while Figures B.2 and B.3 illustrates those for calculation cases in the curved-slat blind sub-model (see Figures A-8, A-13, and A-14 for a comparison with the ray-tracing blind model). As shown, surface identification numbers and points used to define those surfaces for each case are given in the figures.

For the flat-slat blind sub-model, calculations described in Section A.2.2 can be used to determine points *A* to *F* used to define the blind enclosure. Calculations described in Section A.4.1 can be used to determine a boundary between illuminated and shaded slat surfaces (i.e. point *G* for Case 1, point *H* for Case 4, or point *I* for Case 5). Points *G* and *H* can then be related as follows:

$$H = \left(G_x + T\sin(\psi), G_y - S + T\cos(\psi)\right) \tag{B-1}$$

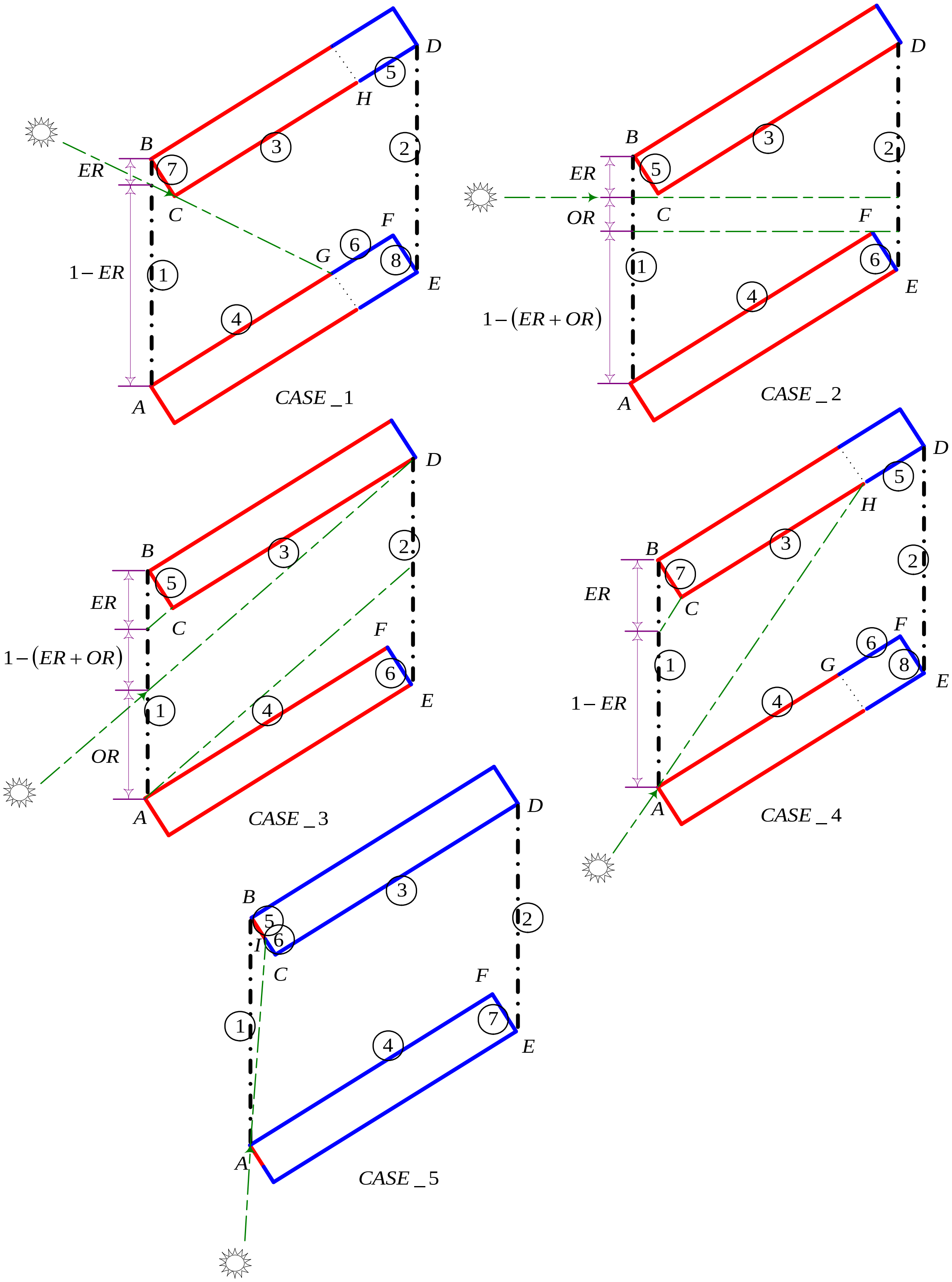

Figure B-1 Calculation Cases for the Flat-Slat Blind Model

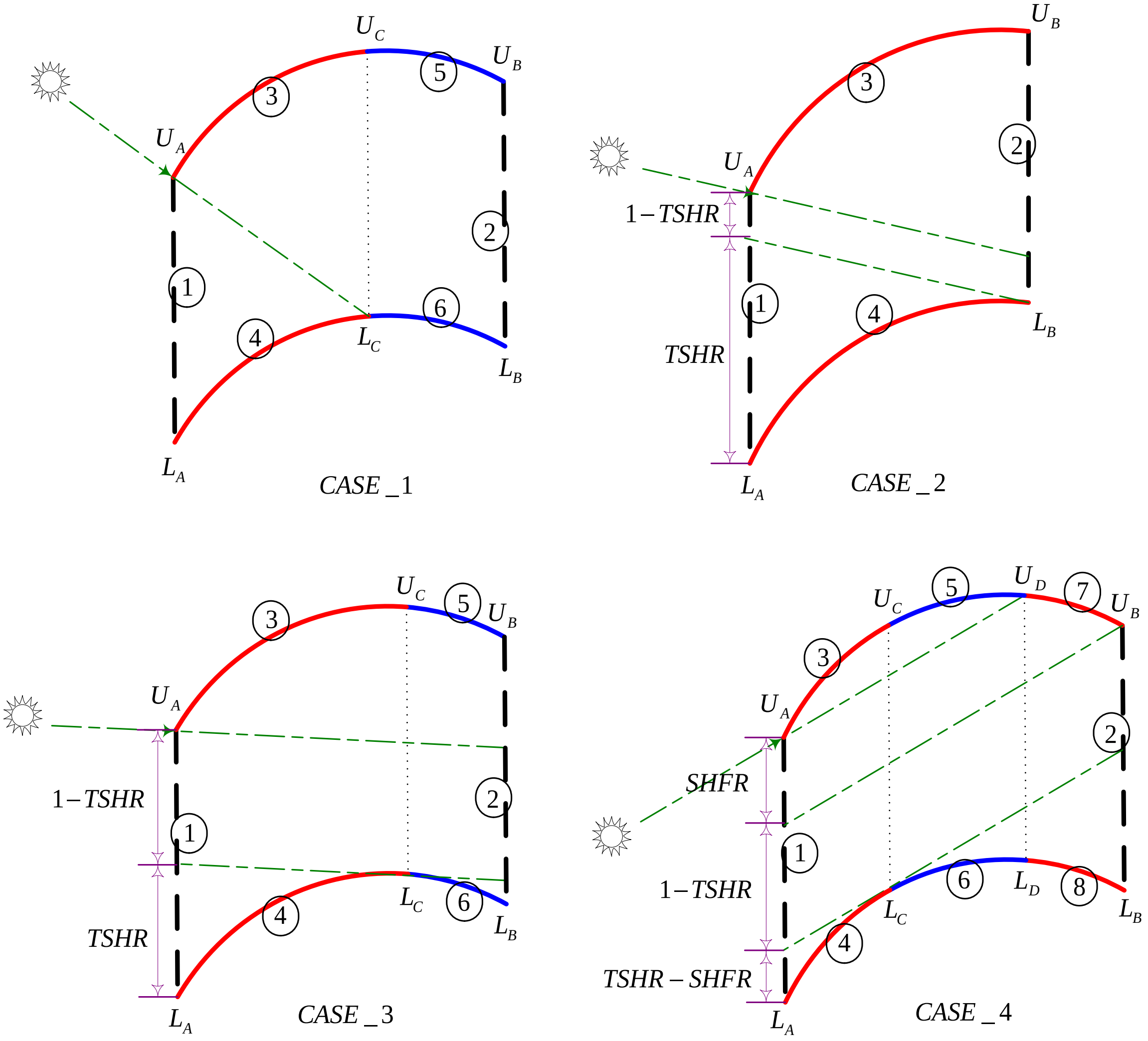

Figure B-2 Calculation Cases 1 to 4 for the Curved-Slat Blind Model

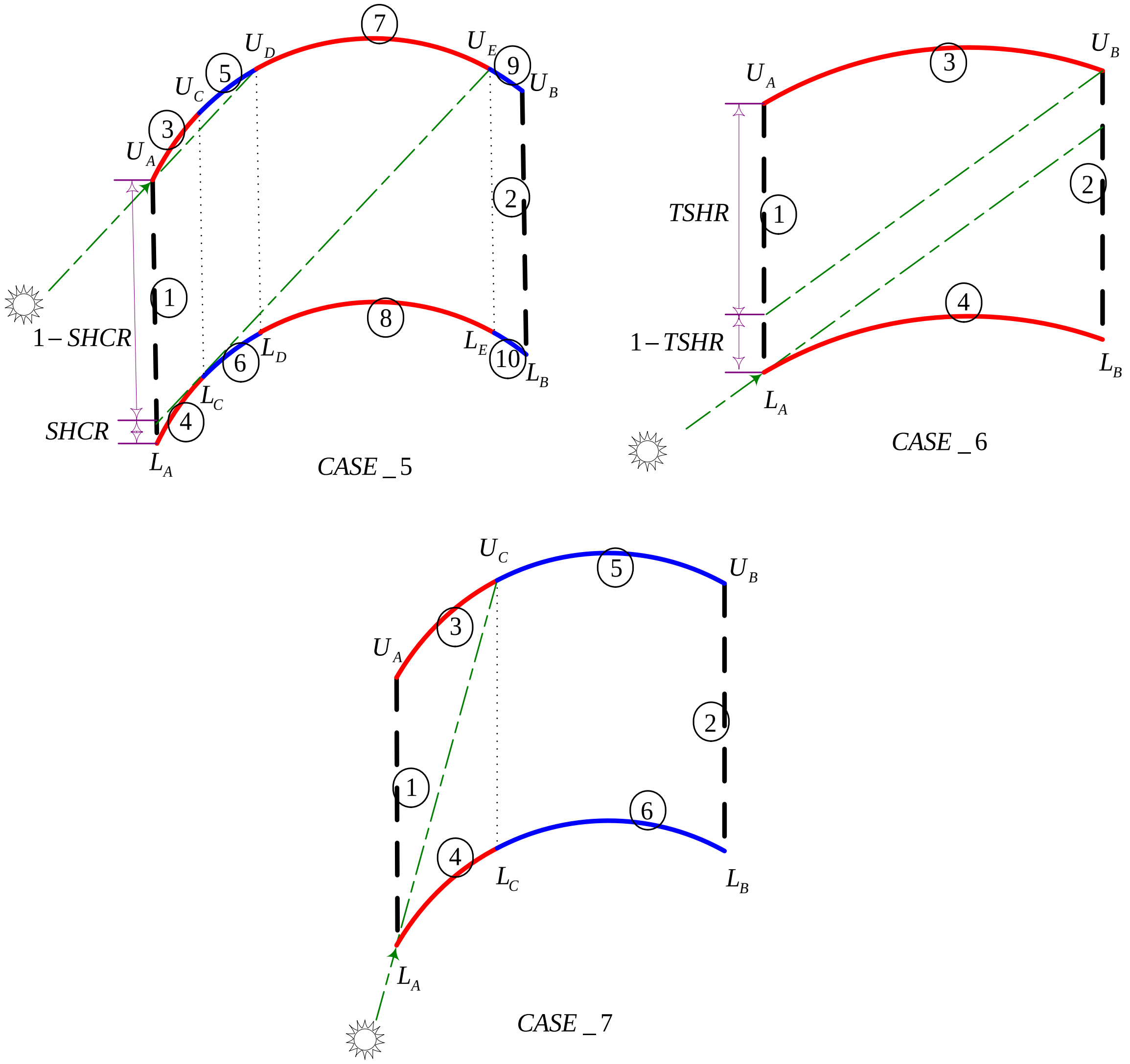

Figure B-3 Calculation Cases 5 to 7 for the Curved-Slat Blind Model

For the curved-slat blind sub-model, calculations described in Section A.2.3 can be used to determine points representing opening surfaces (i.e. U_A, U_B, L_A and L_B). Calculations described in Section A.4.2 can be used to determine a boundary between illuminated and shaded slat surfaces (e.g. point L_C for Cases 1, 3, 4 and 5). Then, the following relationship can be used to determine another boundary point having the same subscript on the opposite slat (i.e. point U_C):

$$U = \left(L_x, L_y - S\right) \tag{B-2}$$

B.3 Net-Radiation Method

To deal with the reflected radiation for blinds having purely diffuse reflecting slats, the net-radiation method is employed in the net-radiation blind model. To illustrate the use of the net-radiation method in the net-radiation blind model, Figure B-4 shows radiative energy balance on a non-opaque material. Let Q_n and Q_{n+1} be the net fluxes at which radiation impinges on and are absorbed by surfaces *n* and *n+1*, respectively. Then, the relationship between net flux (Q), radiosity (J), and irradiation (G) can be expressed by:

$$Q_n = G_n - J_n \tag{B-3a}$$

$$Q_{n+1} = G_{n+1} - J_{n+1} \tag{B-3b}$$

By definition, the radiosity can be written in terms of irradiation (G), emissive power (E), and surface radiative properties (ρ and τ) as:

$$J_n = R_n + E_n + T_{n+1} = \rho_n G_n + E_n + \tau_{n+1\rightarrow n} G_{n+1} \tag{B-4a}$$

$$J_{n+1} = R_{n+1} + E_{n+1} + T_n = \rho_{n+1} G_{n+1} + E_{n+1} + \tau_{n\rightarrow n+1} G_n \tag{B-4b}$$

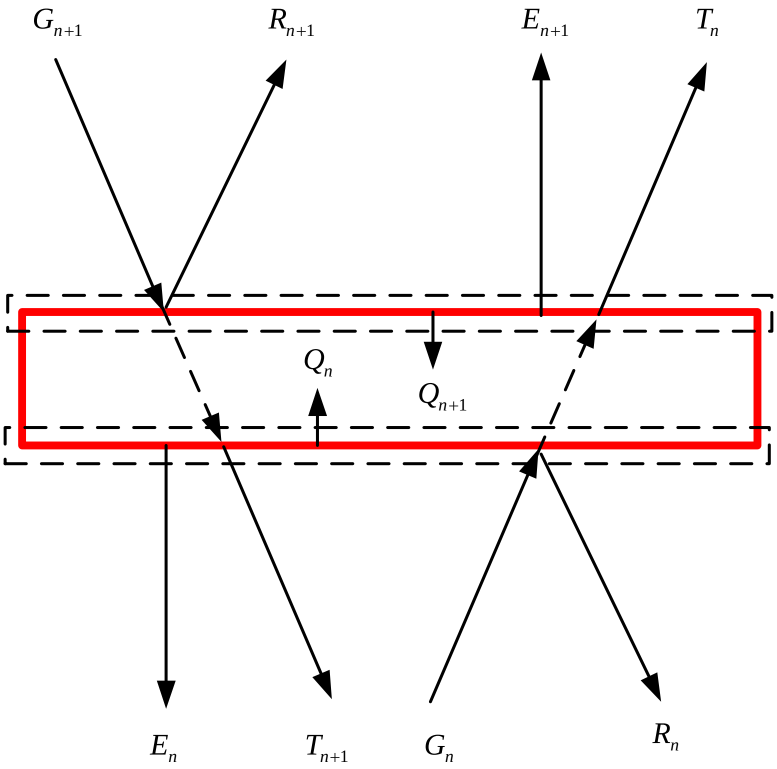

Figure B-4 Radiative Energy Balance on a Non-Opaque Material

Using the definition of view factor and rearranging the above equations, we have

$$J_n - \rho_n \sum_{i=1}^{N} F_{i\to n} J_i - \tau_{n+1\to n} \sum_{i=1}^{N} F_{i\to n+1} J_i = E_n \quad \text{(B-5a)}$$

$$J_{n+1} - \rho_{n+1} \sum_{i=1}^{N} F_{i\to n+1} J_i - \tau_{n\to n+1} \sum_{i=1}^{N} F_{i\to n} J_i = E_{n+1} \quad \text{(B-5b)}$$

Equation (B-5) can be written in a matrix form for all enclosure surfaces as

$$[A][J]=[E] \tag{B-6}$$

where [J] = vector of unknown radiosities,
[E] = vector of known emissive powers, and
[A] = matrix of known coefficients.

The matrix entries (or coefficients) of A can be expressed by

$$A_{r,c}=\delta_{r,c}-\rho_r F_{c\to r}-\tau_r F_{c\to r+1} \quad \text{for odd } r \text{ (i.e. r = 1, 3, 5, …)} \tag{B-7a}$$

$$A_{r,c}=\delta_{r,c}-\rho_r F_{c\to r}-\tau_r F_{c\to r-1} \quad \text{for even } r \text{ (i.e. r = 2, 4, 6, …)} \tag{B-7b}$$

where r = row index,
c = column index, and
$\delta_{r,c}$ = Kronecker delta (= 1 for $r = c$; and = 0, otherwise).

After solving the matrix equation, the net radiation flux incident on surface *n* can be determined by

$$Q_n=\sum_{i=1}^{N}F_{i\to n}J_i-J_n \tag{B-8}$$

To illustrate how the net-radiation method is being applied in the net-radiation blind model, let consider Calculation Case 3 for the curved-slat blind model shown in Figure B-2. As shown in the figure, some of solar radiation can be directly transmitted through the blind assembly and the lower slats of the blind are partially illuminated. For this example, the determination of reflected radiation can be considered as a problem of an enclosure with six surfaces: 1) opening on the outside, 2) opening on the inside, 3) illuminated upper slat, 4) illuminated lower slat, 5) shaded upper slat, and 6) shaded lower slat.

For surfaces in this example, ρ_1 and ρ_2 are equal to zero, ρ_3 and ρ_5 are equal to diffuse slat reflectance on the back side of the blind slats ($\rho_{df}^{sl,b}$), and ρ_4 and ρ_6 are equal to diffuse slat reflectance on the front side of the slats ($\rho_{df}^{sl,f}$). Also, τ_1 and τ_2 are equal to one, and τ_3 to τ_6 are equal to diffuse slat transmittance (τ_{df}^{sl}). In addition, E_3 is equal to beam radiation transmitted diffusely through the (translucent) blind slats ($LR \cdot \tau_{bm}^{sl}$)[1], E_4 is equal to beam radiation reflected diffusely from the blind slats ($LR \cdot \rho_{bm}^{sl,f}$), and all other emissive powers are equal to zero.

It can be noticed that J_1 and J_2 are equal to zero for the openings. This suggests that only four equations are required to be solved. Therefore, the problem reduces to

$$\begin{bmatrix} 1-\rho_{df}^{sl,b}F_{3-3}-\tau_{df}^{sl}F_{3-4} & -\rho_{df}^{sl,b}F_{4-3}-\tau_{df}^{sl}F_{4-4} & -\rho_{df}^{sl,b}F_{5-3}-\tau_{df}^{sl}F_{5-4} & -\rho_{df}^{sl,b}F_{6-3}-\tau_{df}^{sl}F_{6-4} \\ -\rho_{df}^{sl,f}F_{3-4}-\tau_{df}^{sl}F_{3-3} & 1-\rho_{df}^{sl,f}F_{4-4}-\tau_{df}^{sl}F_{4-3} & -\rho_{df}^{sl,f}F_{5-4}-\tau_{df}^{sl}F_{5-3} & -\rho_{df}^{sl,f}F_{6-4}-\tau_{df}^{sl}F_{6-3} \\ -\rho_{df}^{sl,b}F_{3-5}-\tau_{df}^{sl}F_{3-6} & -\rho_{df}^{sl,b}F_{4-5}-\tau_{df}^{sl}F_{4-6} & 1-\rho_{df}^{sl,b}F_{5-5}-\tau_{df}^{sl}F_{5-6} & -\rho_{df}^{sl,b}F_{6-5}-\tau_{df}^{sl}F_{6-6} \\ -\rho_{df}^{sl,f}F_{3-6}-\tau_{df}^{sl}F_{3-5} & -\rho_{df}^{sl,f}F_{4-6}-\tau_{df}^{sl}F_{4-5} & -\rho_{df}^{sl,f}F_{5-6}-\tau_{df}^{sl}F_{5-5} & 1-\rho_{df}^{sl,f}F_{6-6}-\tau_{df}^{sl}F_{6-5} \end{bmatrix} \cdot \begin{bmatrix} J_3 \\ J_4 \\ J_5 \\ J_6 \end{bmatrix} = \begin{bmatrix} LR \cdot \tau_{bm}^{sl} \\ LR \cdot \rho_{bm}^{sl,f} \\ 0 \\ 0 \end{bmatrix}$$

It is worth noting that, for this problem, the lower slat surfaces (surfaces 4 and 6) cannot view themselves (i.e. F_{4-4} and F_{6-6} are zero) while the upper slat surfaces (surfaces 3 and 5) can view themselves (i.e. F_{3-3} and F_{5-5} are not zero).

---

[1] For this case, *LR* is equal to *TSHR*, which can be calculated as described in Section A.3.2.

After obtaining the radiosities, the net radiation flux incident on surfaces of the enclosure can then be determined using Equation (B-8). Finally, blind optical properties can be calculated as a function of the net radiation flux incident on the enclosure surfaces. Calculations of the blind optical properties are presented in Section B.5. In the following sections, essential data required for the net-radiation calculations are summarized.

B.3.1 Calculations for Blinds with Flat Slats

This section summarizes essential data required by the flat-slat blind model. It should be noted that the emissive power terms are only given for those that are not zero. It should also be mentioned that Figure B-2 shows calculation cases when the slat angle is not zero. For zero slat angle cases, slat edges are not considered as parts of the blind enclosure in the net-radiation calculations. This means that the number of surfaces in each case for zero slat angle cases is less than that for non-zero slat angle cases by two. View factor calculations are described in detail in Section B.4.2.

Summary of Surface Radiative Properties:

- Slat reflectance of opening surfaces = zero
- Slat transmittance of opening surfaces = one
- Slat reflectance of upper slat surfaces = $\rho_{df}^{sl,b}$
- Slat transmittance of upper slat surfaces = τ_{df}^{sl}
- Slat reflectance of lower slat surfaces = $\rho_{df}^{sl,f}$
- Slat transmittance of lower slat surfaces = τ_{df}^{sl}
- Slat reflectance of slat edge surfaces = $\dfrac{\rho_{df}^{sl,b} + \rho_{df}^{sl,f}}{2}$
- Slat transmittance of slat edge surfaces = zero

Case 1 for $\varphi_1 < \varphi < +90°$:

- View factor case number = II for zero slat angle case
- View factor case number = IV for non-zero slat angle case
- $E_3 = (1 - ER) \cdot \tau_{bm}^{sl}$
- $E_4 = (1 - ER) \cdot \rho_{bm}^{sl,f}$
- $E_7 = ER \cdot \rho_{bm}^{sl,e}$ for non-zero slat angle case

Case 2 for $\varphi_2 \le \varphi \le \varphi_1$:

- View factor case number = I for zero slat angle case
- View factor case number = III for non-zero slat angle case
- $E_3 = (1 - ER - OR) \cdot \tau_{bm}^{sl}$
- $E_4 = (1 - ER - OR) \cdot \rho_{bm}^{sl,f}$
- $E_5 = ER \cdot \rho_{bm}^{sl,e}$ for non-zero slat angle case
- No net-radiation calculation required for $\varphi = \varphi_2$ and $\psi = 0$

Case 3 for $\varphi_3 \le \varphi < \varphi_2$:

- View factor case number = I for zero slat angle case
- View factor case number = III for non-zero slat angle case
- $E_3 = (1 - ER - OR) \cdot \rho_{bm}^{sl,b}$
- $E_4 = (1 - ER - OR) \cdot \tau_{bm}^{sl}$
- $E_5 = ER \cdot \rho_{bm}^{sl,e}$ for non-zero slat angle case

Case 4 for $\varphi_4 < \varphi < \varphi_3$:

- View factor case number = II for zero slat angle case
- View factor case number = IV for non-zero slat angle case

- $E_3 = (1 - ER) \cdot \rho_{bm}^{sl,b}$
- $E_4 = (1 - ER) \cdot \tau_{bm}^{sl}$
- $E_7 = ER \cdot \rho_{bm}^{sl,e}$ for non-zero slat angle case

Case 5 for $-90° < \varphi \le \varphi_4$ and $\psi \ne 0$:

- View factor case number = III for $\varphi = \varphi_4$
- View factor case number = V for $\varphi < \varphi_4$
- $E_5 = \rho_{bm}^{sl,e}$

B.3.2 Calculations for Blinds with Curved Slats

This section summarizes essential data required by the curved-slat blind model. Like the flat-slat blind model, the emissive power terms are only given for those that are not zero. Slat radiative properties are the same as those given for the flat-slat blind model except that there is no slat edge in the curved-slat blind model. Detailed calculations of view factors are described in Section B.4.3.

Case 1 for $\varphi_1 < \varphi < +90°$:

- View factor case number = II
- $E_3 = \tau_{bm}^{sl}$
- $E_4 = \rho_{bm}^{sl,f}$

Case 2 for $\varphi_2^* \le \varphi \le \varphi_1$ and $\omega_2 = 2\eta$:

- View factor case number = I
- $E_3 = LR \cdot \tau_{bm}^{sl}$
- $E_4 = LR \cdot \rho_{bm}^{sl,f}$

Case 3 for a) $\varphi_2 \leq \varphi \leq \varphi_1$ and $\omega_2 < 2\eta$, or b) $\varphi_2 \leq \varphi < \varphi_2^*$ and $\omega_2 = 2\eta$:

- View factor case number = II
- $E_3 = LR \cdot \tau_{bm}^{sl}$
- $E_4 = LR \cdot \rho_{bm}^{sl,f}$

Case 4 for a) $\varphi_3 < \varphi < \varphi_2$, or b) $\varphi = \varphi_3$ and $\omega_1 > 0$:

- View factor case number = III
- $E_3 = LR \cdot \tau_{bm}^{sl}$
- $E_4 = LR \cdot \rho_{bm}^{sl,f}$
- $E_7 = URB \cdot \rho_{bm}^{sl,b}$
- $E_8 = URB \cdot \tau_{bm}^{sl}$

Case 5 for $\varphi_4 < \varphi < \varphi_3$ and $\omega_1 > 0$:

- View factor case number = IV
- $E_3 = LR \cdot \tau_{bm}^{sl}$
- $E_4 = LR \cdot \rho_{bm}^{sl,f}$
- $E_7 = URB \cdot \rho_{bm}^{sl,b}$
- $E_8 = URB \cdot \tau_{bm}^{sl}$

Case 6 for $\varphi_4 \leq \varphi \leq \varphi_3$ and $\omega_1 = 0$:

- View factor case number = I
- $E_3 = URB \cdot \rho_{bm}^{sl,b}$
- $E_4 = URB \cdot \tau_{bm}^{sl}$

Case 7 for a) $-90° < \varphi \le \varphi_4$ and $\omega_1 > 0$, or b) $-90° < \varphi < \varphi_4$ and $\omega_1 = 0$:

- View factor case number = II
- $E_3 = \rho_{bm}^{sl,b}$
- $E_4 = \tau_{bm}^{sl}$

B.4 View Factors between Blind Enclosure Surfaces

View factors used in the net-radiation blind model are derived using the Crossed-Strings method [Modest 2003]. To determine view factors, distances between points representing blind enclosure surfaces are needed. In the next section, calculations of the distances between points are presented. Then, summaries of view factor calculations are given in the following sections.

B.4.1 Distance Calculations

A distance between two points required for the view factor calculations can be categorized into 3 groups: the straight distance, the curved distance, and the mixed distance. The straight distance is defined as the length of the straight line connecting the two points. The curved distance is defined as the distance measured along a curvature where the two points are on. The mixed distance is defined as a combination of the straight distance and the curved distance. For points *A* and *B* shown in Figure B-5, either the straight distance or the curved distance may be needed depending on which view factor is being considered. For points *A* and *D*, the mixed distance is typically required.

In the distance and view factor calculations, $\overline{A}\overline{B}$ denotes the straight distance for points *A* and *B*, $\widehat{A}\widehat{B}$ denotes the curved distance for points *A* and *B*, and $\overline{A}\widehat{D}$ denotes the mixed distance for points *A* and *D*. In the following calculations, it is assumed that points *A*, *B*, *C*, and *D* are already known. As shown in Figure B-5, points *A* and *B* are points on the upper curvature while point *D* is a point on the lower curvature. Point *C* is the center of the lower curvature.

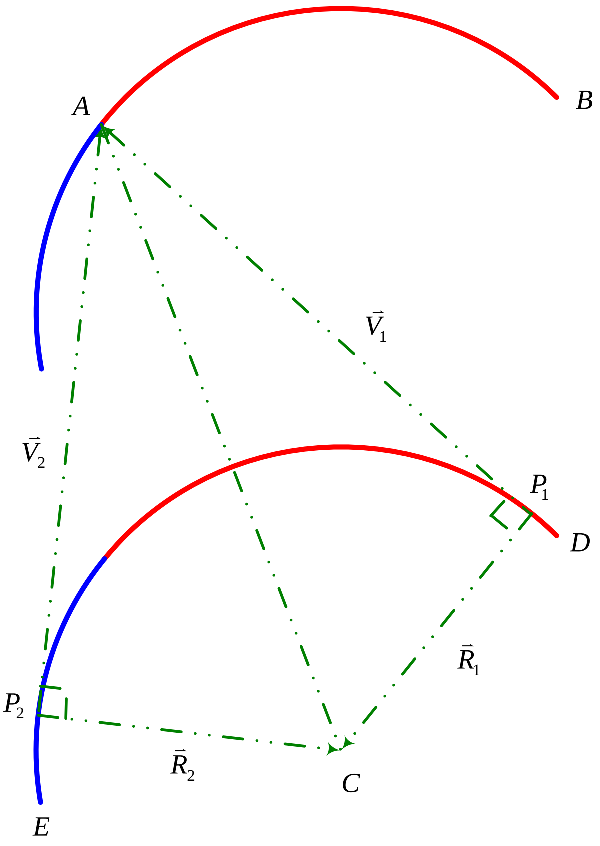

Figure B-5 Determinations of Points Required for Mixed Distance Calculation

Then, the straight distance for points *A* and *B* can simply be calculated by:

$$\overline{A}\overline{B} = \sqrt{\left(A_x - B_x\right)^2 + \left(A_y - B_y\right)^2} \quad \text{(B-9)}$$

For points *A* and *B*, the curved distance can be calculated by:

$$\widehat{A}\widehat{B} = 2R\angle AB \quad \text{(B-10)}$$

where R is the curvature radius, and $\angle AB$ is an angle difference of the two points on the curvature. The calculation procedure described in Appendix A (i.e. Equations (A-19) to (A-22)) can be used to determine an angle representing each point on a curvature.

For points *A* and *D*, it is essential to check whether the lower curvature has an effect in the calculation of the distance between the two points. If it does, point P_1 as shown in Figure B-5 will be within the distance between points *A* and *D*. As shown in the figure, point P_1 is a point on the lower curvature where a vector from the point to point *A* on the upper curvature is perpendicular to a vector from the point to the center of the lower curvature. To check if point P_1 is within the distance between points *A* and *D*, the straight distance for points *A* and P_1 can be calculated by:

$$\overline{A}\overline{P}_1 = \sqrt{\overline{A}\overline{C}^{\,2} - R^2} \tag{B-11}$$

Then, if $\overline{A}\overline{P}_1$ is greater than $\overline{A}\overline{D}$, point P_1 is not within the distance between points *A* and *D*. Therefore, the distance for points *A* and *D* can be calculated as the straight distance. This means that $\overline{A}\overset{\frown}{D}$ is equal to $\overline{A}\overline{D}$. Otherwise, the mixed distance for points *A* and *D* can be determined by:

$$\overline{A}\overset{\frown}{D} = \overline{A}\overline{P}_1 + \overset{\frown}{P}_1\overset{\frown}{D} \tag{B-12}$$

It is essential to determine the coordinate of point P_1 and its related angle before the calculation of $\overset{\frown}{P}_1\overset{\frown}{D}$ can be done. In the following calculations, point P_1 is referred to as a perpendicular point. The calculation procedure described below is used to determine two possible perpendicular points (i.e. points P_1 and P_2 shown in Figure B-5).

Let $\vec{V}$ be a unit vector from a perpendicular point P (e.g. either point P_1 or P_2) to the original point O (e.g. point A) and $\vec{R}$ be a unit vector from that perpendicular point to the curvature center C (e.g. point C). Then, we have

$$O_x - P_x = \overline{O}\overline{P} \cdot V_x \tag{B-13a}$$

$$O_y - P_y = \overline{O}\overline{P} \cdot V_y \tag{B-13b}$$

$$C_x - P_x = \overline{C}\overline{P} \cdot R_x \tag{B-14a}$$

$$C_y - P_y = \overline{C}\overline{P} \cdot R_y \tag{B-14b}$$

Subtracting Equation (B-13a) by Equation (B-14a) and Equation (B-13b) by Equation (B-14b), we get

$$\overline{O}\overline{P} \cdot V_x - \overline{C}\overline{P} \cdot R_x = O_x - C_x \tag{B-15a}$$

$$\overline{O}\overline{P} \cdot V_y - \overline{C}\overline{P} \cdot R_y = O_y - C_y \tag{B-15b}$$

Because $\vec{V}$ and $\vec{R}$ are perpendicular to each other, the dot product of the two vectors is equal to zero. This implies that $\vec{R} = \begin{bmatrix} V_y \\ -V_x \end{bmatrix}$ or $\vec{R} = \begin{bmatrix} -V_y \\ V_x \end{bmatrix}$. In Figure B-5, $\vec{R}_1 = \begin{bmatrix} V_{1,y} \\ -V_{1,x} \end{bmatrix}$ and $\vec{R}_2 = \begin{bmatrix} -V_{2,y} \\ V_{2,x} \end{bmatrix}$. Using these relations, we get

$$\vec{V}_1 = \begin{bmatrix} V_{1,x} \\ V_{1,y} \end{bmatrix} = \begin{bmatrix} \dfrac{\overline{OP}\left(O_x - C_x\right) + \overline{CP}\left(O_y - C_y\right)}{\overline{OP}^2 + \overline{CP}^2} \\ \dfrac{\overline{OP} \cdot V_{1,x} - \left(O_x - C_x\right)}{\overline{CP}} \end{bmatrix} \tag{B-16a}$$

$$\vec{V}_2 = \begin{bmatrix} V_{2,x} \\ V_{2,y} \end{bmatrix} = \begin{bmatrix} \dfrac{\overline{CP}\left(O_x - C_x\right) + \overline{OP}\left(O_y - C_y\right)}{\overline{OP}^2 + \overline{CP}^2} \\ \dfrac{\overline{OP} \cdot V_{1,y} - \left(O_y - C_y\right)}{\overline{CP}} \end{bmatrix} \tag{B-16b}$$

Knowing $\vec{V}_1$ and $\vec{V}_2$, the two possible perpendicular points (e.g. P_1 and P_2) can finally be determined using Equation (B-13). It is essential to calculate both perpendicular points since we do not know in advance which perpendicular point is the one we actually need. For instance, point P_2, not point P_1, would be the one we need if we want to determine the distance between points *A* and *E*.

After determining the two possible perpendicular points, we can determine which point is the one we need by checking (straight) distances between the two perpendicular points and the point of interest (e.g. point *D* for $\overline{A}\widehat{D}$). The perpendicular point with a shorter distance (e.g. point P_1 for $\overline{A}\widehat{D}$) would be the one.

B.4.2 Calculations for Blinds with Flat Slats

For the flat-slat blind model, only the straight distance is required in the view factor calculations. In the flat-slat blind model, the view factor calculations can be divided into five cases as shown in Figure B-6. Calculation Cases I and II are used for zero slat angle cases while Calculation Cases III to V are used for non-zero slat angle cases. The view factor calculations required for each case are summarized below.

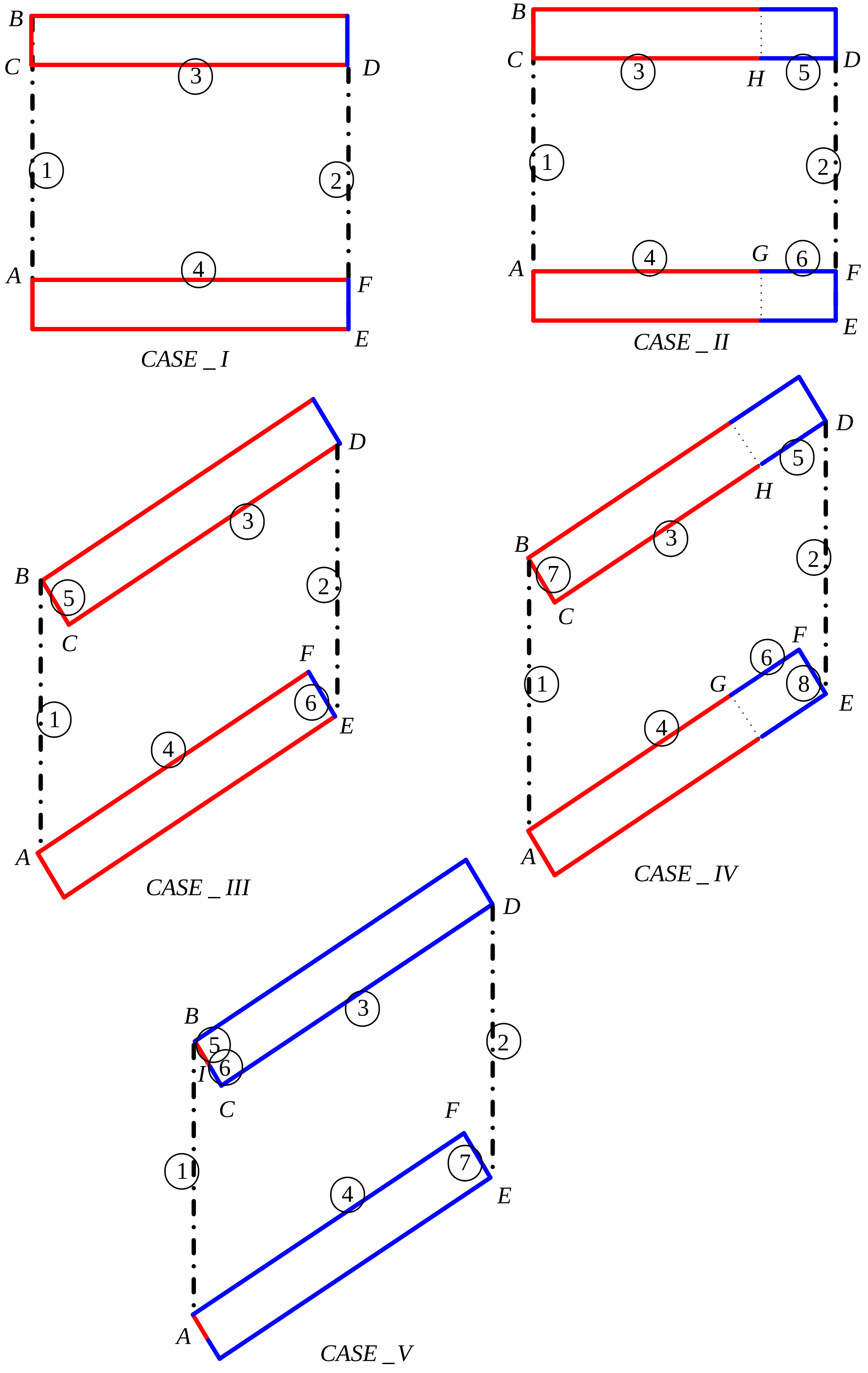

CASE _ I

CASE _ II

CASE _ III

CASE _ IV

CASE _ V

Figure B-6 View Factor Calculation Cases for the Flat-Slat Blind Model

Case I: 4-Surface Enclosure Domain (for $\psi = 0$)

$$F_{1-1} = 0\,;$$

$$F_{1-2} = \frac{\left(\overline{A}\overline{D} + \overline{C}\overline{F}\right) - \left(\overline{A}\overline{F} + \overline{C}\overline{D}\right)}{2\overline{A}\overline{C}}$$

$$F_{1-3} = \frac{\left(\overline{A}\overline{C} + \overline{C}\overline{D}\right) - \overline{A}\overline{D}}{2\overline{A}\overline{C}}\,;$$

$$F_{1-4} = F_{1-3}$$

$$F_{2-1} = F_{1-2}\,;$$

$$F_{2-2} = F_{1-1}$$

$$F_{2-3} = F_{1-4}\,;$$

$$F_{2-4} = F_{1-3}$$

$$F_{3-1} = \frac{\overline{A}\overline{C}}{\overline{C}\overline{D}} F_{1-3}\,;$$

$$F_{3-2} = F_{3-1}$$

$$F_{3-3} = 0\,;$$

$$F_{3-4} = \frac{\left(\overline{A}\overline{D} + \overline{C}\overline{F}\right) - \left(\overline{A}\overline{C} + \overline{D}\overline{F}\right)}{2\overline{C}\overline{D}}$$

$$F_{4-1} = F_{3-2}\,;$$

$$F_{4-2} = F_{3-1}$$

$$F_{4-3} = F_{3-4}\,;$$

$$F_{4-4} = F_{3-3}$$

Case II: 6-Surface Enclosure Domain (for $\psi = 0$)

$$F_{1-1} = 0\,;$$

$$F_{1-2} = \frac{\left(\overline{A}\overline{D} + \overline{C}\overline{F}\right) - \left(\overline{A}\overline{F} + \overline{C}\overline{D}\right)}{2\overline{A}\overline{C}}$$

$$F_{1-3} = \frac{\left(\overline{A}\overline{C} + \overline{C}\overline{H}\right) - \overline{A}\overline{H}}{2\overline{A}\overline{C}}\,;$$

$$F_{1-4} = F_{1-3}$$

$$F_{1-5} = \frac{\left(\overline{A}\overline{C} + \overline{C}\overline{D}\right) - \overline{A}\overline{D}}{2\overline{A}\overline{C}} - F_{1-3}\,;$$

$$F_{1-6} = F_{1-5}$$

$$F_{2-1} = F_{1-2}\,;$$

$$F_{2-2} = F_{1-1}$$

$$F_{2-3} = \frac{\left(\overline{D}\overline{F} + \overline{C}\overline{D}\right) - \overline{C}\overline{F}}{2\overline{D}\overline{F}} - F_{2-5}\,;$$

$$F_{2-4} = F_{2-3}$$

$$F_{2-5} = \frac{\left(\overline{D}\overline{F} + \overline{D}\overline{H}\right) - \overline{F}\overline{H}}{2\overline{D}\overline{F}}\,;$$

$$F_{2-6} = F_{2-5}$$

$$F_{3-1} = \frac{\overline{A}\overline{C}}{\overline{C}\overline{H}} F_{1-3}\,;$$

$$F_{3-2} = \frac{\overline{D}\overline{F}}{\overline{C}\overline{H}} F_{2-3}$$

$$F_{3-3} = 0\,; \qquad F_{3-4} = \frac{\left(\overline{AH} + \overline{CG}\right) - \left(\overline{AC} + \overline{GH}\right)}{2\overline{CH}}$$

$$F_{3-5} = 0\,; \qquad F_{3-6} = \frac{\left(\overline{CF} + \overline{GH}\right) - \left(\overline{CG} + \overline{FH}\right)}{2\overline{CH}}$$

$$F_{4-1} = F_{3-1}\,; \qquad F_{4-2} = F_{3-2}$$

$$F_{4-3} = F_{3-4}\,; \qquad F_{4-4} = F_{3-3}$$

$$F_{4-5} = F_{3-6}\,; \qquad F_{4-6} = F_{3-5}$$

$$F_{5-1} = \frac{\overline{AC}}{\overline{DH}} F_{1-5}\,; \qquad F_{5-2} = \frac{\overline{DF}}{\overline{DH}} F_{2-5}$$

$$F_{5-3} = 0\,; \qquad F_{5-4} = \frac{\overline{AG}}{\overline{DH}} F_{4-5}$$

$$F_{5-5} = 0\,; \qquad F_{5-6} = \frac{\left(\overline{DG} + \overline{FH}\right) - \left(\overline{DF} + \overline{GH}\right)}{2\overline{DH}}$$

$$F_{6-1} = F_{5-1}\,; \qquad F_{6-2} = F_{5-2}$$

$$F_{6-3} = F_{5-4}\,; \qquad F_{6-4} = F_{5-3}$$

$$F_{6-5} = F_{5-6}\,; \qquad F_{6-6} = F_{5-5}$$

Case III: 6-Surface Enclosure Domain (for $\psi \neq 0$)

$$F_{1-1'} = \frac{\left(\overline{AB} + \overline{AC}\right) - \overline{BC}}{2\overline{AB}}\,; \qquad F_{3-2'} = \frac{\left(\overline{CD} + \overline{DF}\right) - \overline{CF}}{2\overline{CD}}$$

$$F_{1-1} = 0\,; \qquad F_{1-2} = \left[\frac{\left(\overline{AD} + \overline{CF}\right) - \left(\overline{AF} + \overline{CD}\right)}{2\overline{AC}}\right] F_{1-1'}$$

$$F_{1-3} = \left[\frac{\left(\overline{AC} + \overline{CD}\right) - \overline{AD}}{2\overline{AC}}\right] F_{1-1'}\,; \qquad F_{1-4} = \left[\frac{\left(\overline{AC} + \overline{AF}\right) - \overline{CF}}{2\overline{AC}}\right] F_{1-1'}$$

$$F_{1-5} = \frac{\left(\overline{AB} + \overline{BC}\right) - \overline{AC}}{2\overline{AB}}\,; \qquad F_{1-6} = 0$$

$$F_{2-1} = F_{1-2}\,; \qquad F_{2-2} = F_{1-1}$$

$$F_{2-3} = F_{1-4}\,; \qquad F_{2-4} = F_{1-3}$$

$$F_{2-5} = F_{1-6}\,; \qquad F_{2-6} = F_{1-5}$$

$$F_{3-1} = \frac{\left(\overline{AC} + \overline{CD}\right) - \overline{AD}}{2\overline{CD}}\,; \qquad F_{3-2} = \left[\frac{\left(\overline{DE} + \overline{DF}\right) - \overline{EF}}{2\overline{DF}}\right] F_{3-2'}$$

$$F_{3-3} = 0\,; \qquad F_{3-4} = \frac{\left(\overline{AD} + \overline{CF}\right) - \left(\overline{AC} + \overline{DF}\right)}{2\overline{CD}}$$

$$F_{3-5} = 0\,; \qquad F_{3-6} = F_{3-2'} - F_{3-2}$$

$$F_{4-1} = F_{3-2}\,; \qquad F_{4-2} = F_{3-1}$$

$$F_{4-3} = F_{3-4}\,; \qquad F_{4-4} = F_{3-3}$$

$$F_{4-5} = F_{3-6}\,; \qquad F_{4-6} = F_{3-5}$$

$$F_{5-1} = \frac{\overline{AB}}{\overline{BC}} F_{1-5}\,; \qquad F_{5-2} = 0$$

$$F_{5-3} = 0\,; \qquad F_{5-4} = \frac{\left(\overline{AC} + \overline{BC}\right) - \overline{AB}}{2\overline{BC}}$$

$$F_{5-5} = 0\,; \qquad F_{5-6} = 0$$

$$F_{6-1} = F_{5-2}\,; \qquad F_{6-2} = F_{5-1}$$

$$F_{6-3} = F_{5-4}\,; \qquad F_{6-4} = F_{5-3}$$

$$F_{6-5} = F_{5-6}\,; \qquad F_{6-6} = F_{5-5}$$

Case IV: 8-Surface Enclosure Domain (for $\psi \neq 0$)

$$F_{1-1'} = \frac{\left(\overline{AB} + \overline{AC}\right) - \overline{BC}}{2\overline{AB}}\,; \qquad F_{1'-1} = \frac{\overline{AB}}{\overline{AC}} F_{1-1'}$$

$$F_{1'-4} = \frac{\left(\overline{AC} + \overline{AG}\right) - \overline{CG}}{2\overline{AC}}\,; \qquad F_{2-2'} = F_{1-1'}$$

$$F_{2'-2} = F_{1'-1}\,; \qquad F_{2'-5} = \frac{\left(\overline{DF} + \overline{DH}\right) - \overline{FH}}{2\overline{DF}}$$

$$F_{2'-6} = \frac{\left(\overline{DF} + \overline{FG}\right) - \overline{DG}}{2\overline{DF}}\,;$$

$$F_{3-2'} = \frac{\left(\overline{CH} + \overline{FH}\right) - \overline{CF}}{2\overline{CH}}$$

$$F_{4-1'} = \frac{\overline{AC}}{\overline{AG}} F_{1'-4}\,;$$

$$F_{5-2'} = \frac{\overline{DF}}{\overline{DH}} F_{2'-5}$$

$$F_{6-1'} = \frac{\left(\overline{CG} + \overline{FG}\right) - \overline{CF}}{2\overline{FG}}\,;$$

$$F_{7-1'} = \frac{\left(\overline{AC} + \overline{BC}\right) - \overline{AB}}{2\overline{BC}}$$

$$F_{8-2'} = F_{7-1'}$$

$$F_{1-1} = 0\,;$$

$$F_{1-2} = \left[\frac{\left(\overline{AD} + \overline{CF}\right) - \left(\overline{AF} + \overline{CD}\right)}{2\overline{AC}}\right] F_{1-1'}$$

$$F_{1-3} = \left[\frac{\left(\overline{AC} + \overline{CH}\right) - \overline{AH}}{2\overline{AC}}\right] F_{1-1'}\,;$$

$$F_{1-4} = F_{1-1'} \cdot F_{1'-4}$$

$$F_{1-5} = \left[\frac{\left(\overline{AC} + \overline{CD}\right) - \overline{AD}}{2\overline{AC}}\right] F_{1-1'} - F_{1-3}\,;$$

$$F_{1-6} = \left[\frac{\left(\overline{AC} + \overline{AF}\right) - \overline{CF}}{2\overline{AC}}\right] F_{1-1'} - F_{1-4}$$

$$F_{1-7} = \frac{\left(\overline{AB} + \overline{BC}\right) - \overline{AC}}{2\overline{AB}}\,;$$

$$F_{1-8} = 0$$

$$F_{2-1} = F_{1-2}\,;$$

$$F_{2-2} = 0$$

$$F_{2-3} = \left[\frac{\left(\overline{CD} + \overline{DF}\right) - \overline{CF}}{2\overline{DF}}\right] F_{2-2'} - F_{2-5}\,;$$

$$F_{2-4} = \left[\frac{\left(\overline{AF} + \overline{DF}\right) - \overline{AD}}{2\overline{DF}}\right] F_{2-2'} - F_{2-6}$$

$$F_{2-5} = F_{2-2'} \cdot F_{2'-5}\,;$$

$$F_{2-6} = F_{2-2'} \cdot F_{2'-6}$$

$$F_{2-7} = 0\,;$$

$$F_{2-6} = F_{1-7}$$

$$F_{3-1} = \frac{\left(\overline{AC} + \overline{CH}\right) - \overline{AH}}{2\overline{CH}}\,;$$

$$F_{3-3} = 0$$

$$F_{3-4} = \frac{\left(\overline{AH} + \overline{CG}\right) - \left(\overline{AC} + \overline{GH}\right)}{2\overline{CH}}\,;$$

$$F_{3-5} = 0$$

$$F_{3-6} = \frac{\left(\overline{CF} + \overline{GH}\right) - \left(\overline{CG} + \overline{FH}\right)}{2\overline{CH}}\,;$$

$$F_{3-7} = 0$$

```
If ( $\overline{DE}\sin(\psi) \le \overline{DH}$ ) Then
    $F_{3-2} = F_{3-2'}$
    $F_{3-8} = 0$
Else
    $F_{3-2} = F_{3-2'} \cdot F_{2'-2}$
    $F_{3-8} = F_{3-2'} - F_{3-2}$
End If
```

$$F_{4-1} = F_{4-1'} \cdot F_{1'-1}\,; \qquad F_{4-2} = \frac{\left(\overline{AG} + \overline{DG}\right) - \overline{AG}}{2\overline{AG}}$$

$$F_{4-3} = F_{3-4}\,; \qquad F_{4-4} = 0$$

$$F_{4-5} = \frac{\left(\overline{AD} + \overline{GH}\right) - \left(\overline{AH} + \overline{DG}\right)}{2\overline{AG}}\,; \qquad F_{4-6} = 0$$

$$F_{4-7} = F_{4-1'} - F_{4-1}\,; \qquad F_{4-8} = 0$$

$$F_{5-1} = \frac{\left(\overline{AH} + \overline{DH}\right) - \overline{AD}}{2\overline{DH}}\,; \qquad F_{5-2} = F_{5-2'} \cdot F_{2'-2}$$

$$F_{5-3} = 0\,; \qquad F_{5-4} = \frac{\overline{AG}}{\overline{DH}} F_{4-5}$$

$$F_{5-5} = 0\,; \qquad F_{5-6} = \frac{\left(\overline{DG} + \overline{FH}\right) - \left(\overline{DF} + \overline{GH}\right)}{2\overline{DH}}$$

$$F_{5-7} = 0\,; \qquad F_{5-8} = F_{5-2'} - F_{5-2}$$

$$F_{6-2} = \frac{\overline{DF}}{\overline{FG}} F_{2'-6}\,; \qquad F_{6-3} = \frac{\overline{CH}}{\overline{FG}} F_{3-6}$$

$$F_{6-4} = 0\,; \qquad F_{6-5} = F_{5-6}$$

$$F_{6-6} = 0\,; \qquad F_{6-8} = 0$$

```
If ( $\overline{AB}\sin(\psi) \le \overline{AG}$ ) Then
    $F_{6-1} = F_{6-1'}$
    $F_{6-7} = 0$
Else
    $F_{6-1} = F_{6-1'} \cdot F_{1'-1}$
    $F_{6-7} = F_{6-1'} - F_{6-1}$
End If
    $F_{7-1} = \frac{\overline{AB}}{\overline{BC}} F_{1-7}$;        $F_{7-2} = 0$
    $F_{7-3} = 0$;        $F_{7-5} = 0$
    $F_{7-7} = 0$;        $F_{7-8} = 0$
If ( $\overline{AB}\sin(\psi) \le \overline{AG}$ ) Then
    $F_{7-4} = F_{7-1'}$
    $F_{7-6} = 0$
Else
    $F_{7-4} = F_{7-1'} \cdot F_{1'-4}$
    $F_{7-6} = F_{7-1'} - F_{7-4}$
End If
    $F_{8-1} = 0$;        $F_{8-2} = \frac{\overline{DE}}{\overline{EF}} F_{2-8}$
    $F_{8-4} = 0$;        $F_{8-6} = 0$
    $F_{8-7} = 0$;        $F_{8-8} = 0$
```

If ($\overline{DE}\sin(\psi) \le \overline{DH}$) Then

$F_{8-5} = F_{8-2'}$

$F_{8-3} = 0$

Else

$F_{8-5} = F_{8-2'} \cdot F_{2'-5}$

$F_{8-3} = F_{8-2'} \cdot F_{8-5}$

End If

Case V: 7-Surface Enclosure Domain (for $\psi \neq 0$)

$$F_{1-1'} = \frac{(\overline{AB} + \overline{AC}) - \overline{BC}}{2\overline{AB}}; \qquad F_{1-1} = 0$$

$$F_{1-2} = \left[\frac{(\overline{AD} + \overline{CF}) - (\overline{AF} + \overline{CD})}{2\overline{AC}}\right] F_{1-1'}; \qquad F_{1-3} = \left[\frac{(\overline{AC} + \overline{CD}) - \overline{AD}}{2\overline{AC}}\right] F_{1-1'}$$

$$F_{1-4} = \left[\frac{(\overline{AC} + \overline{AF}) - \overline{CF}}{2\overline{AC}}\right] F_{1-1'}; \qquad F_{1-5} = \frac{(\overline{AB} + \overline{BI}) - \overline{AI}}{2\overline{AB}}$$

$$F_{1-6} = \frac{(\overline{AB} + \overline{BC}) - \overline{AC}}{2\overline{AB}} - F_{1-5}; \qquad F_{1-7} = 0$$

$$F_{2-1} = F_{1-2}; \qquad F_{2-2} = F_{1-1}$$

$$F_{2-3} = F_{1-4}; \qquad F_{2-4} = F_{1-3}$$

$$F_{2-5} = 0; \qquad F_{2-6} = 0$$

$$F_{2-7} = F_{1-5} + F_{1-6}$$

$$F_{3-2'} = \frac{(\overline{CD} + \overline{DF}) - \overline{CF}}{2\overline{CD}}; \qquad F_{3-1} = \frac{(\overline{AC} + \overline{CD}) - \overline{AD}}{2\overline{CD}}$$

$$F_{3-2} = \left[\frac{(\overline{DE} + \overline{DF}) - \overline{EF}}{2\overline{DF}}\right] F_{3-2'}; \qquad F_{3-3} = 0$$

$$F_{3-4} = \frac{\left(\overline{A}\overline{D} + \overline{C}\overline{F}\right) - \left(\overline{A}\overline{C} + \overline{D}\overline{F}\right)}{2\overline{C}\overline{D}};$$

$$F_{3-5} = 0$$

$$F_{3-6} = 0;$$

$$F_{3-7} = F_{3-2'} - F_{3-2}$$

$$F_{4-(5+6)} = F_{3-7};$$

$$F_{1'-(5+6)} = \frac{\left(\overline{A}\overline{C} + \overline{B}\overline{C}\right) - \overline{A}\overline{B}}{2\overline{A}\overline{C}}$$

$$F_{1'-5} = F_{1'-(5+6)} - \frac{\left(\overline{A}\overline{C} + \overline{C}\overline{I}\right) - \overline{A}\overline{I}}{2\overline{A}\overline{C}};$$

$$F_{4-1} = F_{3-2};$$

$$F_{4-2} = F_{3-1};$$

$$F_{4-3} = F_{3-4};$$

$$F_{4-4} = F_{3-3};$$

$$F_{4-5} = \frac{F_{1'-5}}{F_{1'-(5+6)}} F_{4-(5+6)};$$

$$F_{4-6} = F_{4-(5+6)} - F_{4-5};$$

$$F_{4-7} = 0$$

$$F_{5-1} = \frac{\overline{A}\overline{B}}{\overline{B}\overline{I}} F_{1-5};$$

$$F_{5-2} = 0$$

$$F_{5-3} = 0;$$

$$F_{5-4} = 1 - F_{5-1}$$

$$F_{5-5} = 0;$$

$$F_{5-6} = 0$$

$$F_{5-7} = 0$$

$$F_{6-1} = \frac{\overline{A}\overline{B}}{\overline{C}\overline{I}} F_{1-6};$$

$$F_{6-2} = 0$$

$$F_{6-3} = 0;$$

$$F_{6-4} = 1 - F_{6-1}$$

$$F_{6-5} = 0;$$

$$F_{6-6} = 0$$

$$F_{6-7} = 0;$$

$$F_{7-1} = 0$$

$$F_{7-2} = \frac{\overline{D}\overline{E}}{\overline{E}\overline{F}} F_{2-7};$$

$$F_{7-3} = 1 - F_{7-2}$$

$$F_{7-4} = 0;$$

$$F_{7-5} = 0$$

$$F_{7-6} = 0;$$

$$F_{7-7} = 0$$

B.4.3 Calculations for Blinds with Curved Slats

For the curved-slat blind model, all straight, curved and mixed distances are required in the view factor calculations. In the curved-slat blind model, the view factor calculations can be divided into four cases as shown in Figure B-7. The view factor calculations required for each case are summarized below.

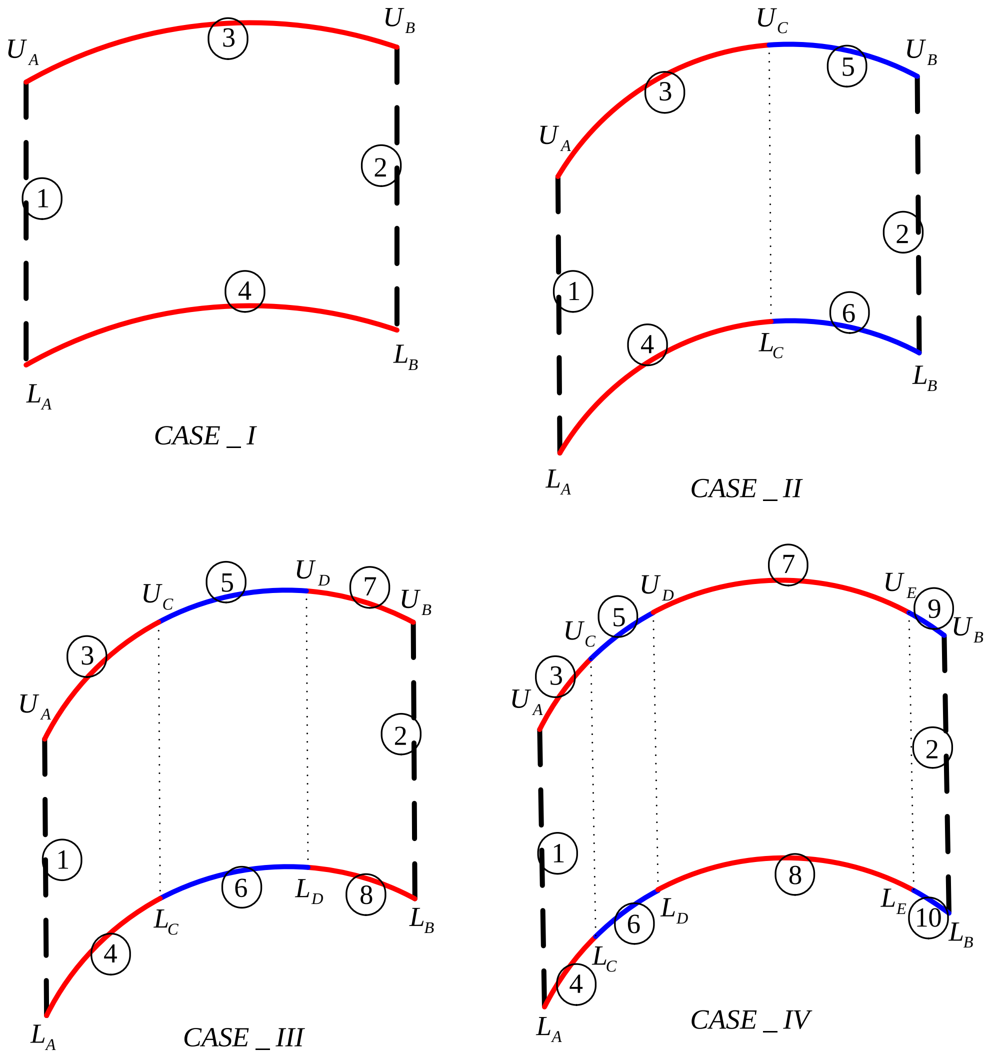

Figure B-7 View Factor Calculation Cases for the Curved-Slat Blind Model

Case I: 4-Surface Enclosure Domain

$$F_{1-1} = 0\,; \qquad F_{1-2} = \frac{\left(\overline{U}_A \widehat{L}_B + \overline{U}_B \widehat{L}_A\right) - \left(\widehat{L}_A \widehat{L}_B + \overline{U}_A \overline{U}_B\right)}{2\overline{U}_A \overline{L}_A}$$

$$F_{1-3} = \frac{\left(\overline{U}_A \overline{L}_A + \overline{U}_A \overline{U}_B\right) - \left(\overline{U}_B \widehat{L}_A\right)}{2\overline{U}_A \overline{L}_A}\,; \qquad F_{1-4} = \frac{\left(\overline{U}_A \overline{L}_A + \widehat{L}_A \widehat{L}_B\right) - \left(\overline{U}_A \widehat{L}_B\right)}{2\overline{U}_A \overline{L}_A}$$

$$F_{2-1} = F_{1-2}\,; \qquad F_{2-2} = 0$$

$$F_{2-3} = \frac{\left(\overline{U}_B \overline{L}_B + \overline{U}_A \overline{U}_B\right) - \left(\overline{U}_A \widehat{L}_B\right)}{2\overline{U}_B \overline{L}_B}\,; \qquad F_{2-4} = \frac{\left(\overline{U}_B \overline{L}_B + \widehat{L}_A \widehat{L}_B\right) - \left(\overline{U}_B \widehat{L}_A\right)}{2\overline{U}_B \overline{L}_B}$$

$$F_{3-1} = \frac{\overline{U}_A \overline{L}_A}{\widehat{U}_A \widehat{U}_B} F_{1-3}\,; \qquad F_{3-2} = \frac{\overline{U}_B \overline{L}_B}{\widehat{U}_A \widehat{U}_B} F_{2-3}$$

$$F_{3-3} = 1 - \frac{\overline{U}_A \overline{U}_B}{\widehat{U}_A \widehat{U}_B}\,; \qquad F_{3-4} = \frac{\left(\overline{U}_A \widehat{L}_B + \overline{U}_B \widehat{L}_A\right) - \left(\overline{U}_A \overline{L}_A + \overline{U}_B \overline{L}_B\right)}{2\widehat{U}_A \widehat{U}_B}$$

$$F_{4-1} = \frac{\overline{U}_A \overline{L}_A}{\widehat{L}_A \widehat{L}_B} F_{1-4}\,; \qquad F_{4-2} = \frac{\overline{U}_B \overline{L}_B}{\widehat{L}_A \widehat{L}_B} F_{2-4}$$

$$F_{4-3} = F_{3-4}\,; \qquad F_{4-4} = 0$$

Case II: 6-Surface Enclosure Domain

$$F_{1-1} = 0\,; \qquad F_{1-2} = \frac{\left(\overline{U}_A \widehat{L}_B + \overline{U}_B \widehat{L}_A\right) - \left(\widehat{L}_A \widehat{L}_B + \overline{U}_A \overline{U}_B\right)}{2\overline{U}_A \overline{L}_A}$$

$$F_{1-3} = \frac{\left(\overline{U}_A \overline{L}_A + \overline{U}_A \overline{U}_C\right) - \left(\overline{U}_C \widehat{L}_A\right)}{2\overline{U}_A \overline{L}_A}\,; \qquad F_{1-4} = \frac{\left(\overline{U}_A \overline{L}_A + \widehat{L}_A \widehat{L}_C\right) - \left(\overline{U}_A \widehat{L}_C\right)}{2\overline{U}_A \overline{L}_A}$$

$$F_{1-5} = \frac{\left(\overline{U}_A \overline{U}_B + \overline{U}_C \widehat{L}_A\right) - \left(\overline{U}_A \overline{U}_C + \overline{U}_B \widehat{L}_A\right)}{2\overline{U}_A \overline{L}_A}\,; \qquad F_{1-6} = \frac{\left(\overline{U}_A \overline{L}_A + \widehat{L}_A \widehat{L}_B\right) - \left(\overline{U}_A \widehat{L}_B\right)}{2\overline{U}_A \overline{L}_A} - F_{1-4}$$

$$F_{2-1} = F_{1-2}\,; \qquad F_{2-2} = 0$$

$$F_{2-3} = \frac{\left(\overline{U}_A \overline{U}_B + \overline{U}_C \widehat{L}_B\right) - \left(\overline{U}_A \widehat{L}_B + \overline{U}_B \overline{U}_C\right)}{2\overline{U}_B \overline{L}_B}\,; \qquad F_{2-4} = \frac{\left(\overline{U}_B \overline{L}_B + \widehat{L}_A \widehat{L}_B\right) - \left(\overline{U}_B \widehat{L}_A\right)}{2\overline{U}_B \overline{L}_B} - F_{2-6}$$

$$F_{2-5} = \frac{\left(\overline{U}_B\overline{L}_B + \overline{U}_B\overline{U}_C\right) - \left(\overline{U}_C\widehat{L}_B\right)}{2\overline{U}_B\overline{L}_B}; \qquad F_{2-6} = \frac{\left(\overline{U}_B\overline{L}_B + \widehat{L}_B\widehat{L}_C\right) - \left(\overline{U}_B\widehat{L}_C\right)}{2\overline{U}_B\overline{L}_B}$$

$$F_{3-1} = \frac{\overline{U}_A\overline{L}_A}{\widehat{U}_A\widehat{U}_C}F_{1-3}; \qquad F_{3-2} = \frac{\overline{U}_B\overline{L}_B}{\widehat{U}_A\widehat{U}_C}F_{2-3}$$

$$F_{3-3} = 1 - \frac{\overline{U}_A\overline{U}_C}{\widehat{U}_A\widehat{U}_C}; \qquad F_{3-4} = \frac{\left(\overline{U}_A\widehat{L}_C + \overline{U}_C\widehat{L}_A\right) - \left(\overline{U}_A\overline{L}_A + \overline{U}_C\overline{L}_C\right)}{2\widehat{U}_A\widehat{U}_C}$$

$$F_{3-5} = \frac{\left(\overline{U}_A\overline{U}_C + \overline{U}_B\overline{U}_C\right) - \overline{U}_A\overline{U}_B}{2\widehat{U}_A\widehat{U}_C}; \qquad F_{3-6} = \frac{\left(\overline{U}_A\widehat{L}_B + \overline{U}_C\overline{L}_C\right) - \left(\overline{U}_A\widehat{L}_C + \overline{U}_C\widehat{L}_B\right)}{2\widehat{U}_A\widehat{U}_C}$$

$$F_{4-1} = \frac{\overline{U}_A\overline{L}_A}{\widehat{L}_A\widehat{L}_C}F_{1-4}; \qquad F_{4-2} = \frac{\overline{U}_B\overline{L}_B}{\widehat{L}_A\widehat{L}_C}F_{2-4}$$

$$F_{4-3} = F_{3-4}; \qquad F_{4-4} = 0$$

$$F_{4-5} = \frac{\left(\overline{U}_B\widehat{L}_A + \overline{U}_C\overline{L}_C\right) - \left(\overline{U}_C\widehat{L}_A + \overline{U}_B\widehat{L}_C\right)}{2\widehat{L}_A\widehat{L}_C}; \qquad F_{4-6} = 0$$

$$F_{5-1} = \frac{\overline{U}_A\overline{L}_A}{\widehat{U}_B\widehat{U}_C}F_{1-5}; \qquad F_{5-2} = \frac{\overline{U}_B\overline{L}_B}{\widehat{U}_B\widehat{U}_C}F_{2-5}$$

$$F_{5-3} = \frac{\widehat{U}_A\widehat{U}_C}{\widehat{U}_B\widehat{U}_C}F_{3-5}; \qquad F_{5-4} = \frac{\widehat{L}_A\widehat{L}_C}{\widehat{U}_B\widehat{U}_C}F_{4-5}$$

$$F_{5-5} = 1 - \frac{\overline{U}_B\overline{U}_C}{\widehat{U}_B\widehat{U}_C}; \qquad F_{5-6} = \frac{\left(\overline{U}_B\widehat{L}_C + \overline{U}_C\widehat{L}_B\right) - \left(\overline{U}_B\overline{L}_B + \overline{U}_C\overline{L}_C\right)}{2\widehat{U}_B\widehat{U}_C}$$

$$F_{6-1} = \frac{\overline{U}_A\overline{L}_A}{\widehat{L}_B\widehat{L}_C}F_{1-6}; \qquad F_{6-2} = \frac{\overline{U}_B\overline{L}_B}{\widehat{L}_B\widehat{L}_C}F_{2-6}$$

$$F_{6-3} = \frac{\widehat{U}_A\widehat{U}_C}{\widehat{L}_B\widehat{L}_C}F_{3-6}; \qquad F_{6-4} = 0$$

$$F_{6-5} = F_{5-6}; \qquad F_{6-6} = 0$$

Case III: 8-Surface Enclosure Domain

$$F_{1-1}=0\,;$$

$$F_{1-2}=\frac{\left(\overline{U}_A\widehat{L}_B+\overline{U}_B\widehat{L}_A\right)-\left(\widehat{L}_A\widehat{L}_B+\overline{U}_A\overline{U}_B\right)}{2\overline{U}_A\overline{L}_A}$$

$$F_{1-3}=\frac{\left(\overline{U}_A\overline{L}_A+\overline{U}_A\overline{U}_C\right)-\left(\overline{U}_C\widehat{L}_A\right)}{2\overline{U}_A\overline{L}_A}\,;$$

$$F_{1-4}=\frac{\left(\overline{U}_A\overline{L}_A+\widehat{L}_A\widehat{L}_C\right)-\left(\overline{U}_A\widehat{L}_C\right)}{2\overline{U}_A\overline{L}_A}$$

$$F_{1-5}=\frac{\left(\overline{U}_A\overline{U}_D+\overline{U}_C\widehat{L}_A\right)-\left(\overline{U}_A\overline{U}_C+\overline{U}_D\widehat{L}_A\right)}{2\overline{U}_A\overline{L}_A}\,;$$

$$F_{1-6}=\frac{\left(\overline{U}_A\overline{L}_A+\widehat{L}_A\widehat{L}_D\right)-\left(\overline{U}_A\widehat{L}_D\right)}{2\overline{U}_A\overline{L}_A}-F_{1-4}$$

$$F_{1-7}=\frac{\left(\overline{U}_A\overline{U}_B+\overline{U}_D\widehat{L}_A\right)-\left(\overline{U}_A\overline{U}_D+\overline{U}_B\widehat{L}_A\right)}{2\overline{U}_A\overline{L}_A}\,;$$

$$F_{1-8}=\frac{\left(\overline{U}_A\overline{L}_A+\widehat{L}_A\widehat{L}_B\right)-\left(\overline{U}_A\widehat{L}_B\right)}{2\overline{U}_A\overline{L}_A}-F_{1-4}-F_{1-6}$$

$$F_{2-1}=F_{1-2}\,;$$

$$F_{2-2}=0$$

$$F_{2-3}=\frac{\left(\overline{U}_A\overline{U}_B+\overline{U}_C\widehat{L}_B\right)-\left(\overline{U}_A\widehat{L}_B+\overline{U}_B\overline{U}_C\right)}{2\overline{U}_B\overline{L}_B}\,;$$

$$F_{2-4}=\frac{\left(\overline{U}_B\overline{L}_B+\widehat{L}_A\widehat{L}_B\right)-\left(\overline{U}_B\widehat{L}_A\right)}{2\overline{U}_B\overline{L}_B}-F_{2-6}-F_{2-8}$$

$$F_{2-5}=\frac{\left(\overline{U}_B\overline{U}_C+\overline{U}_D\widehat{L}_B\right)-\left(\overline{U}_C\widehat{L}_B+\overline{U}_B\overline{U}_D\right)}{2\overline{U}_B\overline{L}_B}\,;$$

$$F_{2-6}=\frac{\left(\overline{U}_B\overline{L}_B+\widehat{L}_B\widehat{L}_C\right)-\left(\overline{U}_B\widehat{L}_C\right)}{2\overline{U}_B\overline{L}_B}-F_{2-8}$$

$$F_{2-7}=\frac{\left(\overline{U}_B\overline{L}_B+\overline{U}_B\overline{U}_D\right)-\left(\overline{U}_D\widehat{L}_B\right)}{2\overline{U}_B\overline{L}_B}\,;$$

$$F_{2-8}=\frac{\left(\overline{U}_B\overline{L}_B+\widehat{L}_B\widehat{L}_D\right)-\left(\overline{U}_B\widehat{L}_D\right)}{2\overline{U}_B\overline{L}_B}$$

$$F_{3-1}=\frac{\overline{U}_A\overline{L}_A}{\widehat{U}_A\widehat{U}_C}F_{1-3}\,;$$

$$F_{3-2}=\frac{\overline{U}_B\overline{L}_B}{\widehat{U}_A\widehat{U}_C}F_{2-3}$$

$$F_{3-3}=1-\frac{\overline{U}_A\overline{U}_C}{\widehat{U}_A\widehat{U}_C}\,;$$

$$F_{3-4}=\frac{\left(\overline{U}_A\widehat{L}_C+\overline{U}_C\widehat{L}_A\right)-\left(\overline{U}_A\overline{L}_A+\overline{U}_C\overline{L}_C\right)}{2\widehat{U}_A\widehat{U}_C}$$

$$F_{3-5}=\frac{\left(\overline{U}_A\overline{U}_C+\overline{U}_C\overline{U}_D\right)-\overline{U}_A\overline{U}_D}{2\widehat{U}_A\widehat{U}_C}\,;$$

$$F_{3-6}=\frac{\left(\overline{U}_A\widehat{L}_D+\overline{U}_C\overline{L}_C\right)-\left(\overline{U}_A\widehat{L}_C+\overline{U}_C\widehat{L}_D\right)}{2\widehat{U}_A\widehat{U}_C}$$

$$F_{3-7}=\frac{\left(\overline{U}_A\overline{U}_D+\overline{U}_B\overline{U}_C\right)-\left(\overline{U}_A\overline{U}_B+\overline{U}_C\overline{U}_D\right)}{2\widehat{U}_A\widehat{U}_C}\,;$$

$$F_{3-8}=\frac{\left(\overline{U}_A\widehat{L}_B+\overline{U}_C\widehat{L}_D\right)-\left(\overline{U}_A\widehat{L}_D+\overline{U}_C\widehat{L}_B\right)}{2\widehat{U}_A\widehat{U}_C}$$

$$F_{4-1}=\frac{\overline{U}_A\overline{L}_A}{\widehat{L}_A\widehat{L}_C}F_{1-4}\,;$$

$$F_{4-2}=\frac{\overline{U}_B\overline{L}_B}{\widehat{L}_A\widehat{L}_C}F_{2-4}$$

$$F_{4-3} = F_{3-4}; \qquad F_{4-4} = 0$$

$$F_{4-5} = \frac{\left(\overline{U}_C \overline{L}_C + \overline{U}_D \widehat{L}_A\right) - \left(\overline{U}_C \widehat{L}_A + \overline{U}_D \widehat{L}_C\right)}{2\widehat{L}_A \widehat{L}_C}; \qquad F_{4-6} = 0$$

$$F_{4-7} = \frac{\left(\overline{U}_B \widehat{L}_A + \overline{U}_D \overline{L}_C\right) - \left(\overline{U}_B \widehat{L}_C + \overline{U}_D \widehat{L}_A\right)}{2\widehat{L}_A \widehat{L}_C}; \qquad F_{4-8} = 0$$

$$F_{5-1} = \frac{\overline{U}_A \overline{L}_A}{\widehat{U}_C \widehat{U}_D} F_{1-5}; \qquad F_{5-2} = \frac{\overline{U}_B \overline{L}_B}{\widehat{U}_C \widehat{U}_D} F_{2-5}$$

$$F_{5-3} = \frac{\widehat{U}_A \widehat{U}_C}{\widehat{U}_C \widehat{U}_D} F_{3-5}; \qquad F_{5-4} = \frac{\widehat{L}_A \widehat{L}_C}{\widehat{U}_C \widehat{U}_D} F_{4-5}$$

$$F_{5-5} = 1 - \frac{\overline{U}_C \overline{U}_D}{\widehat{U}_C \widehat{U}_D}; \qquad F_{5-6} = \frac{\left(\overline{U}_C \widehat{L}_D + \overline{U}_D \widehat{L}_C\right) - \left(\overline{U}_C \overline{L}_C + \overline{U}_D \overline{L}_D\right)}{2\widehat{U}_C \widehat{U}_D}$$

$$F_{5-7} = \frac{\left(\overline{U}_B \overline{U}_D + \overline{U}_C \overline{U}_D\right) - \overline{U}_B \overline{U}_C}{2\widehat{U}_C \widehat{U}_D}; \qquad F_{5-8} = \frac{\left(\overline{U}_C \widehat{L}_B + \overline{U}_D \overline{L}_D\right) - \left(\overline{U}_C \widehat{L}_D + \overline{U}_D \widehat{L}_B\right)}{2\widehat{U}_C \widehat{U}_D}$$

$$F_{6-1} = \frac{\overline{U}_A \overline{L}_A}{\widehat{L}_C \widehat{L}_D} F_{1-6}; \qquad F_{6-2} = \frac{\overline{U}_B \overline{L}_B}{\widehat{L}_C \widehat{L}_D} F_{2-6}$$

$$F_{6-3} = \frac{\widehat{U}_A \widehat{U}_C}{\widehat{L}_C \widehat{L}_D} F_{3-6}; \qquad F_{6-4} = 0$$

$$F_{6-5} = F_{5-6}; \qquad F_{6-6} = 0$$

$$F_{6-7} = \frac{\left(\overline{U}_B \widehat{L}_C + \overline{U}_D \overline{L}_D\right) - \left(\overline{U}_B \widehat{L}_D + \overline{U}_D \widehat{L}_C\right)}{2\widehat{L}_C \widehat{L}_D}; \qquad F_{6-8} = 0$$

$$F_{7-1} = \frac{\overline{U}_A \overline{L}_A}{\widehat{U}_B \widehat{U}_D} F_{1-7}; \qquad F_{7-2} = \frac{\overline{U}_B \overline{L}_B}{\widehat{U}_B \widehat{U}_D} F_{2-7}$$

$$F_{7-3} = \frac{\widehat{U}_A \widehat{U}_C}{\widehat{U}_B \widehat{U}_D} F_{3-7}; \qquad F_{7-4} = \frac{\widehat{L}_A \widehat{L}_C}{\widehat{U}_B \widehat{U}_D} F_{4-7}$$

$$F_{7-5} = \frac{\widehat{U}_C \widehat{U}_D}{\widehat{U}_B \widehat{U}_D} F_{5-7}; \qquad F_{7-6} = \frac{\widehat{L}_C \widehat{L}_D}{\widehat{U}_B \widehat{U}_D} F_{6-7}$$

$$F_{7-7} = 1 - \frac{\overline{U}_B \overline{U}_D}{\widehat{U}_B \widehat{U}_D}\,;$$

$$F_{7-8} = \frac{\left(\overline{U}_B \widehat{L}_D + \overline{U}_D \widehat{L}_B\right) - \left(\overline{U}_B \overline{L}_B + \overline{U}_D \overline{L}_D\right)}{2\widehat{U}_B \widehat{U}_D}$$

$$F_{8-1} = \frac{\overline{U}_A \overline{L}_A}{\widehat{L}_B \widehat{L}_D} F_{1-8}\,;$$

$$F_{8-2} = \frac{\overline{U}_B \overline{L}_B}{\widehat{L}_B \widehat{L}_D} F_{2-8}$$

$$F_{8-3} = \frac{\widehat{U}_A \widehat{U}_C}{\widehat{L}_B \widehat{L}_D} F_{3-8}\,;$$

$$F_{6-4} = 0$$

$$F_{8-5} = \frac{\widehat{U}_C \widehat{U}_D}{\widehat{L}_B \widehat{L}_D} F_{5-8}\,;$$

$$F_{8-6} = 0$$

$$F_{8-7} = F_{7-8}\,;$$

$$F_{8-8} = 0$$

Case IV: 10-Surface Enclosure Domain

$$F_{1-1} = 0\,;$$

$$F_{1-2} = \frac{\left(\overline{U}_A \widehat{L}_B + \overline{U}_B \widehat{L}_A\right) - \left(\widehat{L}_A \widehat{L}_B + \overline{U}_A \overline{U}_B\right)}{2\overline{U}_A \overline{L}_A}$$

$$F_{1-3} = \frac{\left(\overline{U}_A \overline{L}_A + \overline{U}_A \overline{U}_C\right) - \left(\overline{U}_C \widehat{L}_A\right)}{2\overline{U}_A \overline{L}_A}\,;$$

$$F_{1-4} = \frac{\left(\overline{U}_A \overline{L}_A + \widehat{L}_A \widehat{L}_C\right) - \left(\overline{U}_A \widehat{L}_C\right)}{2\overline{U}_A \overline{L}_A}$$

$$F_{1-5} = \frac{\left(\overline{U}_A \overline{U}_D + \overline{U}_C \widehat{L}_A\right) - \left(\overline{U}_A \overline{U}_C + \overline{U}_D \widehat{L}_A\right)}{2\overline{U}_A \overline{L}_A}\,;$$

$$F_{1-6} = \frac{\left(\overline{U}_A \overline{L}_A + \widehat{L}_A \widehat{L}_D\right) - \left(\overline{U}_A \widehat{L}_D\right)}{2\overline{U}_A \overline{L}_A} - F_{1-4}$$

$$F_{1-7} = \frac{\left(\overline{U}_A \overline{U}_E + \overline{U}_D \widehat{L}_A\right) - \left(\overline{U}_A \overline{U}_D + \overline{U}_E \widehat{L}_A\right)}{2\overline{U}_A \overline{L}_A}\,;$$

$$F_{1-8} = \frac{\left(\overline{U}_A \overline{L}_A + \widehat{L}_A \widehat{L}_E\right) - \left(\overline{U}_A \widehat{L}_E\right)}{2\overline{U}_A \overline{L}_A} - F_{1-4} - F_{1-6}$$

$$F_{1-9} = \frac{\left(\overline{U}_A \overline{U}_B + \overline{U}_E \widehat{L}_A\right) - \left(\overline{U}_A \overline{U}_E + \overline{U}_B \widehat{L}_A\right)}{2\overline{U}_A \overline{L}_A}$$

$$F_{1-10} = \frac{\left(\overline{U}_A \overline{L}_A + \widehat{L}_A \widehat{L}_B\right) - \left(\overline{U}_A \widehat{L}_B\right)}{2\overline{U}_A \overline{L}_A} - F_{1-4} - F_{1-6} - F_{1-8}$$

$$F_{2-1} = F_{1-2}\,;$$

$$F_{2-2} = 0$$

$$F_{2-3} = \frac{\left(\overline{U}_A\overline{U}_B + \overline{U}_C\widehat{L}_B\right) - \left(\overline{U}_A\widehat{L}_B + \overline{U}_B\overline{U}_C\right)}{2\overline{U}_B\overline{L}_B}$$

$$F_{2-4} = \frac{\left(\overline{U}_B\overline{L}_B + \widehat{L}_A\widehat{L}_B\right) - \left(\overline{U}_B\widehat{L}_A\right)}{2\overline{U}_B\overline{L}_B} - F_{2-6} - F_{2-8} - F_{2-10}$$

$$F_{2-5} = \frac{\left(\overline{U}_B\overline{U}_C + \overline{U}_D\widehat{L}_B\right) - \left(\overline{U}_C\widehat{L}_B + \overline{U}_B\overline{U}_D\right)}{2\overline{U}_B\overline{L}_B}; \quad F_{2-6} = \frac{\left(\overline{U}_B\overline{L}_B + \widehat{L}_B\widehat{L}_C\right) - \left(\overline{U}_B\widehat{L}_C\right)}{2\overline{U}_B\overline{L}_B} - F_{2-8} - F_{2-10}$$

$$F_{2-7} = \frac{\left(\overline{U}_B\overline{U}_D + \overline{U}_E\widehat{L}_B\right) - \left(\overline{U}_D\widehat{L}_B + \overline{U}_B\overline{U}_E\right)}{2\overline{U}_B\overline{L}_B}; \quad F_{2-8} = \frac{\left(\overline{U}_B\overline{L}_B + \widehat{L}_B\widehat{L}_D\right) - \left(\overline{U}_B\widehat{L}_D\right)}{2\overline{U}_B\overline{L}_B} - F_{2-10}$$

$$F_{2-9} = \frac{\left(\overline{U}_B\overline{L}_B + \overline{U}_B\overline{U}_E\right) - \left(\overline{U}_E\widehat{L}_B\right)}{2\overline{U}_B\overline{L}_B}; \qquad F_{2-10} = \frac{\left(\overline{U}_B\overline{L}_B + \widehat{L}_B\widehat{L}_E\right) - \left(\overline{U}_B\widehat{L}_E\right)}{2\overline{U}_B\overline{L}_B}$$

$$F_{3-1} = \frac{\overline{U}_A\overline{L}_A}{\widehat{U}_A\widehat{U}_C}F_{1-3}; \qquad F_{3-2} = \frac{\overline{U}_B\overline{L}_B}{\widehat{U}_A\widehat{U}_C}F_{2-3}$$

$$F_{3-3} = 1 - \frac{\overline{U}_A\overline{U}_C}{\widehat{U}_A\widehat{U}_C}; \qquad F_{3-4} = \frac{\left(\overline{U}_A\widehat{L}_C + \overline{U}_C\widehat{L}_A\right) - \left(\overline{U}_A\overline{L}_A + \overline{U}_C\overline{L}_C\right)}{2\widehat{U}_A\widehat{U}_C}$$

$$F_{3-5} = \frac{\left(\overline{U}_A\overline{U}_C + \overline{U}_C\overline{U}_D\right) - \overline{U}_A\overline{U}_D}{2\widehat{U}_A\widehat{U}_C}; \qquad F_{3-6} = \frac{\left(\overline{U}_A\widehat{L}_D + \overline{U}_C\overline{L}_C\right) - \left(\overline{U}_A\widehat{L}_C + \overline{U}_C\widehat{L}_D\right)}{2\widehat{U}_A\widehat{U}_C}$$

$$F_{3-7} = \frac{\left(\overline{U}_A\overline{U}_D + \overline{U}_C\overline{U}_E\right) - \left(\overline{U}_A\overline{U}_E + \overline{U}_C\overline{U}_D\right)}{2\widehat{U}_A\widehat{U}_C}; \quad F_{3-8} = \frac{\left(\overline{U}_A\widehat{L}_E + \overline{U}_C\widehat{L}_D\right) - \left(\overline{U}_A\widehat{L}_D + \overline{U}_C\widehat{L}_E\right)}{2\widehat{U}_A\widehat{U}_C}$$

$$F_{3-9} = \frac{\left(\overline{U}_A\overline{U}_E + \overline{U}_B\overline{U}_C\right) - \left(\overline{U}_A\overline{U}_B + \overline{U}_C\overline{U}_E\right)}{2\widehat{U}_A\widehat{U}_C}; \quad F_{3-10} = \frac{\left(\overline{U}_A\widehat{L}_B + \overline{U}_C\widehat{L}_E\right) - \left(\overline{U}_A\widehat{L}_E + \overline{U}_C\widehat{L}_B\right)}{2\widehat{U}_A\widehat{U}_C}$$

$$F_{4-1} = \frac{\overline{U}_A\overline{L}_A}{\widehat{L}_A\widehat{L}_C}F_{1-4}; \qquad F_{4-2} = \frac{\overline{U}_B\overline{L}_B}{\widehat{L}_A\widehat{L}_C}F_{2-4}$$

$$F_{4-3} = F_{3-4}; \qquad F_{4-4} = 0$$

$$F_{4-5} = \frac{\left(\overline{U}_C\overline{L}_C + \overline{U}_D\widehat{L}_A\right) - \left(\overline{U}_C\widehat{L}_A + \overline{U}_D\widehat{L}_C\right)}{2\widehat{L}_A\widehat{L}_C}; \qquad F_{4-6} = 0$$

$$F_{4-7} = \frac{\left(\overline{U}_E \widehat{L}_A + \overline{U}_D \widehat{L}_C\right) - \left(\overline{U}_E \widehat{L}_C + \overline{U}_D \widehat{L}_A\right)}{2\widehat{L}_A \widehat{L}_C}; \quad F_{4-8} = 0$$

$$F_{4-9} = \frac{\left(\overline{U}_B \widehat{L}_A + \overline{U}_E \widehat{L}_C\right) - \left(\overline{U}_B \widehat{L}_C + \overline{U}_E \widehat{L}_A\right)}{2\widehat{L}_A \widehat{L}_C}; \quad F_{4-10} = 0$$

$$F_{5-1} = \frac{\overline{U}_A \overline{L}_A}{\widehat{U}_C \widehat{U}_D} F_{1-5}; \qquad F_{5-2} = \frac{\overline{U}_B \overline{L}_B}{\widehat{U}_C \widehat{U}_D} F_{2-5}$$

$$F_{5-3} = \frac{\widehat{U}_A \widehat{U}_C}{\widehat{U}_C \widehat{U}_D} F_{3-5}; \qquad F_{5-4} = \frac{\widehat{L}_A \widehat{L}_C}{\widehat{U}_C \widehat{U}_D} F_{4-5}$$

$$F_{5-5} = 1 - \frac{\overline{U}_C \overline{U}_D}{\widehat{U}_C \widehat{U}_D}; \qquad F_{5-6} = \frac{\left(\overline{U}_C \widehat{L}_D + \overline{U}_D \widehat{L}_C\right) - \left(\overline{U}_C \overline{L}_C + \overline{U}_D \overline{L}_D\right)}{2\widehat{U}_C \widehat{U}_D}$$

$$F_{5-7} = \frac{\left(\overline{U}_C \overline{U}_D + \overline{U}_D \overline{U}_E\right) - \overline{U}_C \overline{U}_E}{2\widehat{U}_C \widehat{U}_D}; \qquad F_{5-8} = \frac{\left(\overline{U}_C \widehat{L}_E + \overline{U}_D \overline{L}_D\right) - \left(\overline{U}_C \widehat{L}_D + \overline{U}_D \widehat{L}_E\right)}{2\widehat{U}_C \widehat{U}_D}$$

$$F_{5-9} = \frac{\left(\overline{U}_B \overline{U}_D + \overline{U}_C \overline{U}_E\right) - \left(\overline{U}_B \overline{U}_C + \overline{U}_D \overline{U}_E\right)}{2\widehat{U}_C \widehat{U}_D}; \quad F_{5-10} = \frac{\left(\overline{U}_C \widehat{L}_B + \overline{U}_D \overline{L}_E\right) - \left(\overline{U}_C \widehat{L}_E + \overline{U}_D \widehat{L}_B\right)}{2\widehat{U}_C \widehat{U}_D}$$

$$F_{6-1} = \frac{\overline{U}_A \overline{L}_A}{\widehat{L}_C \widehat{L}_D} F_{1-6}; \qquad F_{6-2} = \frac{\overline{U}_B \overline{L}_B}{\widehat{L}_C \widehat{L}_D} F_{2-6}$$

$$F_{6-3} = \frac{\widehat{U}_A \widehat{U}_C}{\widehat{L}_C \widehat{L}_D} F_{3-6}; \qquad F_{6-4} = 0$$

$$F_{6-5} = F_{5-6}; \qquad F_{6-6} = 0$$

$$F_{6-7} = \frac{\left(\overline{U}_E \widehat{L}_C + \overline{U}_D \overline{L}_D\right) - \left(\overline{U}_E \widehat{L}_D + \overline{U}_D \widehat{L}_C\right)}{2\widehat{L}_C \widehat{L}_D}; \quad F_{6-8} = 0$$

$$F_{6-9} = \frac{\left(\overline{U}_B \widehat{L}_C + \overline{U}_E \overline{L}_D\right) - \left(\overline{U}_B \widehat{L}_D + \overline{U}_E \widehat{L}_C\right)}{2\widehat{L}_C \widehat{L}_D}; \quad F_{6-10} = 0$$

$$F_{7-1} = \frac{\overline{U}_A \overline{L}_A}{\widehat{U}_D \widehat{U}_E} F_{1-7}; \qquad F_{7-2} = \frac{\overline{U}_B \overline{L}_B}{\widehat{U}_D \widehat{U}_E} F_{2-7}$$

$$F_{7-3} = \frac{\widehat{U}_A \widehat{U}_C}{\widehat{U}_D \widehat{U}_E} F_{3-7}; \qquad F_{7-4} = \frac{\widehat{L}_A \widehat{L}_C}{\widehat{U}_D \widehat{U}_E} F_{4-7}$$

$$F_{7-5} = \frac{\widehat{U}_C \widehat{U}_D}{\widehat{U}_D \widehat{U}_E} F_{5-7};$$

$$F_{7-6} = \frac{\widehat{L}_C \widehat{L}_D}{\widehat{U}_D \widehat{U}_E} F_{6-7}$$

$$F_{7-7} = 1 - \frac{\overline{U}_D \overline{U}_E}{\widehat{U}_D \widehat{U}_E};$$

$$F_{7-8} = \frac{\left(\overline{U}_E \widehat{L}_D + \overline{U}_D \widehat{L}_E\right) - \left(\overline{U}_E \overline{L}_E + \overline{U}_D \overline{L}_D\right)}{2\widehat{U}_D \widehat{U}_E}$$

$$F_{7-9} = \frac{\left(\overline{U}_D \overline{U}_E + \overline{U}_B \overline{U}_E\right) - \left(\overline{U}_B \overline{U}_D\right)}{2\widehat{U}_D \widehat{U}_E};$$

$$F_{7-10} = \frac{\left(\overline{U}_D \widehat{L}_B + \overline{U}_E \overline{L}_E\right) - \left(\overline{U}_D \widehat{L}_E + \overline{U}_E \widehat{L}_B\right)}{2\widehat{U}_D \widehat{U}_E}$$

$$F_{8-1} = \frac{\overline{U}_A \overline{L}_A}{\widehat{L}_D \widehat{L}_E} F_{1-8};$$

$$F_{8-2} = \frac{\overline{U}_B \overline{L}_B}{\widehat{L}_D \widehat{L}_E} F_{2-8}$$

$$F_{8-3} = \frac{\widehat{U}_A \widehat{U}_C}{\widehat{L}_D \widehat{L}_E} F_{3-8};$$

$$F_{8-4} = 0$$

$$F_{8-5} = \frac{\widehat{U}_C \widehat{U}_D}{\widehat{L}_D \widehat{L}_E} F_{5-8};$$

$$F_{8-6} = 0$$

$$F_{8-7} = F_{7-8};$$

$$F_{8-8} = 0$$

$$F_{8-9} = \frac{\left(\overline{U}_B \widehat{L}_D + \overline{U}_E \overline{L}_E\right) - \left(\overline{U}_B \widehat{L}_E + \overline{U}_E \widehat{L}_D\right)}{2\widehat{L}_D \widehat{L}_E};$$

$$F_{8-10} = 0$$

$$F_{9-1} = \frac{\overline{U}_A \overline{L}_A}{\widehat{U}_B \widehat{U}_E} F_{1-9};$$

$$F_{9-2} = \frac{\overline{U}_B \overline{L}_B}{\widehat{U}_B \widehat{U}_E} F_{2-9}$$

$$F_{9-3} = \frac{\widehat{U}_A \widehat{U}_C}{\widehat{U}_B \widehat{U}_E} F_{3-9};$$

$$F_{9-4} = \frac{\widehat{L}_A \widehat{L}_C}{\widehat{U}_B \widehat{U}_E} F_{4-9}$$

$$F_{9-5} = \frac{\widehat{U}_C \widehat{U}_D}{\widehat{U}_B \widehat{U}_E} F_{5-9};$$

$$F_{9-6} = \frac{\widehat{L}_C \widehat{L}_D}{\widehat{U}_B \widehat{U}_E} F_{6-9}$$

$$F_{9-7} = \frac{\widehat{U}_D \widehat{U}_E}{\widehat{U}_B \widehat{U}_E} F_{7-9};$$

$$F_{9-8} = \frac{\widehat{L}_D \widehat{L}_E}{\widehat{U}_B \widehat{U}_E} F_{8-9}$$

$$F_{9-9} = 1 - \frac{\overline{U}_B \overline{U}_E}{\widehat{U}_B \widehat{U}_E};$$

$$F_{9-10} = \frac{\left(\overline{U}_B \widehat{L}_E + \overline{U}_E \widehat{L}_B\right) - \left(\overline{U}_B \overline{L}_B + \overline{U}_E \overline{L}_E\right)}{2\widehat{U}_B \widehat{U}_E}$$

$$F_{10-1} = \frac{\overline{U}_A \overline{L}_A}{\widehat{L}_B \widehat{L}_E} F_{1-10};$$

$$F_{10-2} = \frac{\overline{U}_B \overline{L}_B}{\widehat{L}_B \widehat{L}_E} F_{2-10}$$

$$F_{10-3} = \frac{\widehat{U}_A \widehat{U}_C}{\widehat{L}_B \widehat{L}_E} F_{3-10}; \qquad F_{10-4} = 0$$

$$F_{10-5} = \frac{\widehat{U}_C \widehat{U}_D}{\widehat{L}_B \widehat{L}_E} F_{5-10}; \qquad F_{10-6} = 0$$

$$F_{10-7} = \frac{\widehat{U}_D \widehat{U}_E}{\widehat{L}_B \widehat{L}_E} F_{7-10}; \qquad F_{10-8} = 0$$

$$F_{10-9} = F_{9-10}; \qquad F_{10-10} = 0$$

B.5 Blind Solar-Optical Properties

Similar to the ray-tracing blind model, the net-radiation blind model determines four blind solar-optical properties: direct-direct blind transmittance, direct-reflected blind transmittance, direct blind reflectance, and direct blind absorptance. In existing optical blind models [DOE 2006; Pfrommer et al. 1996], these four optical properties are often referred to as direct-to-direct blind transmittance (τ^{bl}_{bm-bm}), direct-to-diffuse blind transmittance (τ^{bl}_{bm-df}), direct-to-diffuse blind reflectance (ρ^{bl}_{bm-df}), and direct-to-diffuse blind absorptance (α^{bl}_{bm-df}), respectively. The four blind optical properties can simply be calculated by:

$$\tau^{bl}_{bm-bm} = OR \tag{B-17}$$

$$\tau^{bl}_{bm-df} = Q_2 \tag{B-18}$$

$$\rho^{bl}_{bm-df} = Q_1 \tag{B-19a}$$

$$\alpha^{bl}_{bm-df} = 1 - \tau^{bl}_{bm-bm} - \tau^{bl}_{bm-df} - \rho^{bl}_{bm-df} \tag{B-20}$$

where OR is the opening ratio, and Q_1 and Q_2 are net radiation fluxes incident on the outside and the inside openings, respectively. Calculations of OR are discussed in Section A.3 whereas calculations of Q_1 and Q_2 are presented in Section B.3.

Equations (B-17) to (B-20) are applicable to both the flat-slat and the curved-slat blind sub-models. For the flat-slat blind model with zero slat angle cases, however, the direct blind reflectance is determined slightly different. This is due to the fact that reflected radiation due to sunlight incident on slat edges only goes back to the outside; hence, the slat edges are not considered as parts of the blind enclosure in the net-radiation calculations. Therefore, to account for this reflected radiation, the direct blind reflectance for the flat-slat blind model with zero slat angle cases can be calculated by:

$$\rho_{bm-df}^{bl} = Q_1 + ER \cdot \rho_{bm}^{sl,e} \tag{B-19b}$$

When both the slat angle and the profile angle are zero, there is no need for the net-radiation calculations for the flat-slat blind model. For this special case, both Q_1 and Q_2 are zero; hence, the direct-reflected blind transmittance is zero while the direct blind reflectance is equal to the product of the slat edge ratio and the slat edge reflectance (i.e. the second term on the right hand side of Equation (B-19b)).

Like the ray-tracing blind model, to check whether the net-radiation blind model is correctly implemented, the direct blind absorptance can be determined differently. The direct blind absorptance can alternatively be calculated by summing all net radiation fluxes absorbed by the blind slat surfaces and the fraction of direct sunlight that is initially absorbed by illuminated slat surface(s).

APPENDIX C

OPTICAL BLIND MODEL FOR DIFFUSE SOLAR RADIATION

C.1 Overview

The diffuse blind model adapts a concept proposed by Parmelee and Aubele [1952] to estimate blind optical properties for diffuse solar radiation. In an analysis of the diffuse solar radiation, a hemisphere is placed in front of a plane parallel to a blind assembly (the blind assembly plane shown in Figure C-1). The diffuse blind model assumes that there are only two sources of the diffuse solar radiation: the sky and the ground. As illustrated in Figure C-1, a part of the hemisphere above the horizontal plane represents the sky while the other part below the horizontal plane represents the ground. Both the sky and the ground are subdivided into a number of small patches as shown in the figure. Then, the diffuse solar radiation leaving each patch is treated as direct solar radiation emitted from the center of the patch to the center of the hemisphere where the blind assembly is located. Consequently, a model used to predict optical blind properties for the direct solar radiation can be utilized to predict optical blind properties for the diffuse solar radiation. The diffuse blind model assumes that blind slats behave like diffuse-reflecting surfaces for the diffuse solar radiation although they may behave otherwise for the direct solar radiation. Therefore, the net-radiation blind model described in Section B is employed by the diffuse blind model. It should be noted that the diffuse blind model is applicable when the blind assembly plane is vertical as well as when the plane is inclined. The model is also applicable to both isotropic and anisotropic diffuse radiance distributions.

C.2 Diffuse Irradiance on Blind Assembly

Fundamentally, the irradiance (or radiative heat flux; units in W/m² or Btu/h·ft²) on a small surface located at the center of a hemisphere (δI) due to radiance (or radiative intensity; units in W/m²·sr or Btu/h·ft²·sr) from a small patch of the hemisphere can be given by

$$\delta I = R(\theta_p, \varphi_p) \cdot \cos(\theta_i) \cdot \delta\Omega \tag{C-1}$$

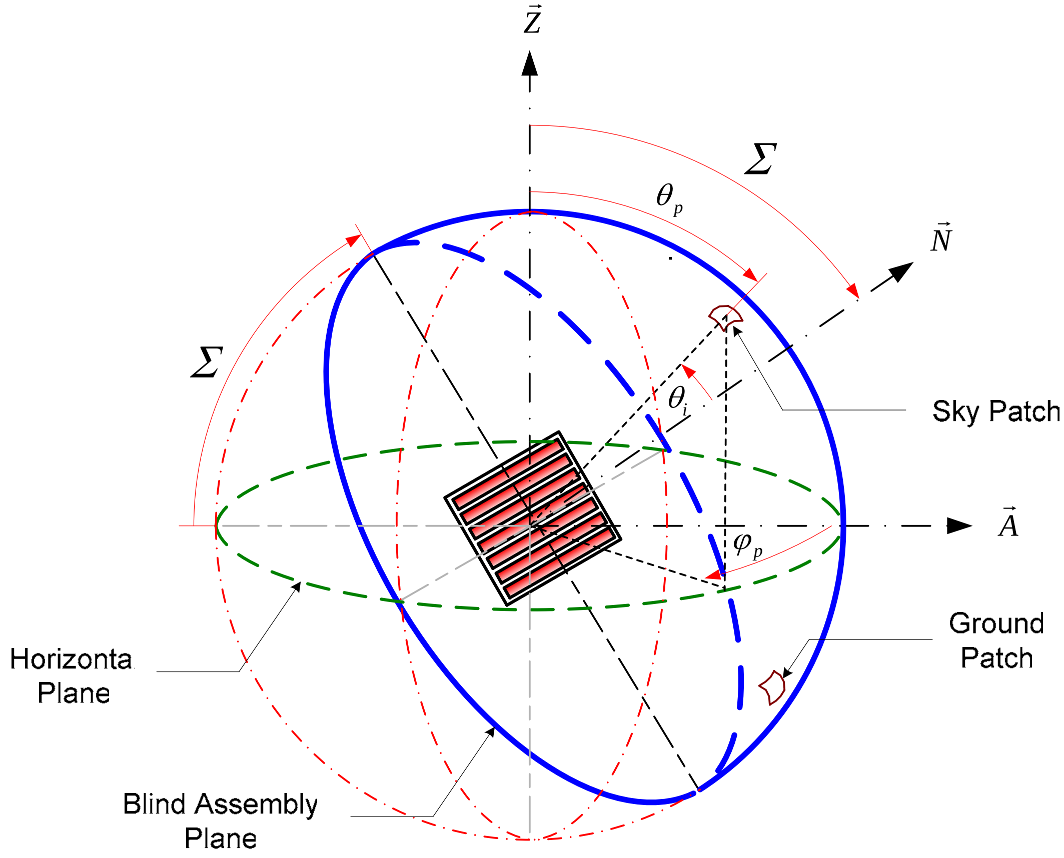

Figure C-1 Half Sphere Representing Sky and Ground in Front of the Blind Assembly where $R(\theta_p, \varphi_p)$ is the radiance of the small patch centered at the zenith angle (θ_p) and the azimuth angle (φ_p); θ_i is an angle of incidence, the angle between a line from the hemisphere center to the patch center and a line normal to the surface; and Ω is a solid angle (unit in steradian). Figure C-1 illustrates how the zenith angle, the azimuth angle, and the angle of incidence are defined. According to Figure C-1, $\vec{Z}$ is the zenith (or vertical) direction, $\vec{A}$ the surface-azimuth direction, and $\vec{N}$ the surface normal direction. The range of the zenith angle is from 0 to π in radians (or from 0 to 180 in degrees). The range of the azimuth angle is from -π to π in radians (or from -180 to 180 in degrees). Figure C-1 shows a positive azimuth angle. The range of the incidence angle is from 0 to π/2 in radians (or from 0 to 90 in degrees).

Referring to Figure C-1, the solid angle can be expressed as a function of the zenith angle and the azimuth angle as follows:

$$\delta\Omega = \sin(\theta_p) \cdot \delta\theta_p \cdot \delta\varphi_p \tag{C-2}$$

Also, the angle of incidence can be related to the zenith angle and the azimuth angle as follows:

$$\cos(\theta_i) = \cos(\theta_p) \cdot \cos(\Sigma) + \sin(\theta_p) \cdot \sin(\Sigma) \cdot \cos(\varphi_p) \tag{C-3}$$

where Σ is the surface tilt angle measured from the horizontal plane as shown in Figure C-1. The range of the surface tilt angle is from 0 to π in radians (or from 0 to 180 in degrees).

Then, the diffuse irradiance due to the radiance from the sky ($R_{sky}(\theta_p,\varphi_p)$) on an arbitrarily inclined surface, with the surface tilt angle less than or equal to π/2, can be calculated by

$$I_{df-sky} = \int_{-\pi}^{\pi}\int_{0}^{\theta_0} R_{sky}(\theta_p,\varphi_p)\cdot\sin(\theta_p)\cdot\cos(\theta_i)\cdot\delta\theta_p\cdot\delta\varphi_p \qquad \text{(C-4)}$$

For $-\pi/2 \le \varphi_p \le \pi/2$, the zenith angle limit (θ_0) is equal to π/2. Otherwise, the zenith angle limit can be determined by solving Equation (C-3) for the zenith angle (θ_p) when the cosine of the angle of incidence is zero [Gueymard 1987]. The solution yields

$$\theta_0 = \tan^{-1}\left[-\frac{1}{\tan(\Sigma)\cdot\cos(\varphi_p)}\right] \qquad \text{(C-5)}$$

The diffuse irradiance due to the radiance from the ground ($R_{gnd}(\theta_p,\varphi_p)$) on the same inclined surface can be calculated by

$$I_{df-gnd} = \int_{-\pi/2}^{\pi/2}\int_{\pi/2}^{\pi+\theta_0} R_{gnd}(\theta_p,\varphi_p)\cdot\sin(\theta_p)\cdot\cos(\theta_i)\cdot\delta\theta_p\cdot\delta\varphi_p \qquad \text{(C-6)}$$

where the zenith angle limit is obtained using Equation (C-5).

For the surface tilt angle greater than π/2, Equations (C-4) and (C-6) may also be used to predict the diffuse irradiance on the surface due to the radiance from the sky and from the ground, respectively. However, the limits of the azimuth angle used in Equation (C-4) are from -π/2 to π/2 while the limits of the azimuth angle used in Equation (C-6) are from -π to π. The limits of the zenith angle used in Equation (C-4) are from the zenith angle limit (θ_0) to π/2 whereas the limits of the zenith angle used in Equation (C-6) are from π+θ_0 to π. For the diffuse sky irradiance, Equation (C-5) is used to determine the zenith angle limit. For the diffuse ground irradiance, the zenith angle limit is equal to -π/2 when $-\pi/2 \leq \varphi_p \leq \pi/2$. Otherwise, Equation (C-5) is used to determine the zenith angle limit.

For an isotropic sky, the sky radiance is constant and the sky diffuse irradiance can be determined analytically resulting in the following familiar formula of the isotropic diffuse sky model:

$$I_{df-sky}^{iso} = \pi \cdot R_{sky,cont} \cdot \left[\frac{1+\cos(\Sigma)}{2}\right] = I_{df,hor} \cdot \left[\frac{1+\cos(\Sigma)}{2}\right] \tag{C-7}$$

where $R_{sky,cont}$ is the constant sky radiance and $I_{df,hor}$ is the diffuse irradiance on a horizontal plane of the isotropic sky.

Likewise, if we assume that both direct and diffuse solar radiation reflect isotropically from the ground (i.e. an isotropic ground), the ground diffuse irradiance can be expressed analytically by:

$$I_{df-gnd}^{iso} = \pi \cdot R_{gnd,cont} \cdot \left[\frac{1-\cos(\Sigma)}{2}\right] = \rho_{gnd} \cdot I_{tot,hor} \cdot \left[\frac{1-\cos(\Sigma)}{2}\right] \tag{C-8}$$

where $R_{gnd,cont}$ is the constant ground radiance, ρ_{gnd} is the ground reflectance and $I_{tot,hor}$ is the total irradiance on a horizontal plane.

If the sky and the ground are considered to be anisotropic, the knowledge of sky and ground radiance distributions is essential in order to solve Equations (C-4) and (C-6). A literature search on the subject found several available models for predicting sky radiance distribution [Brunger and Hooper 1993; Igawa et al. 2004; Vida et al. 1999], but found no existing model for calculating ground radiance distribution. It is worth noting that building energy simulation tools commonly predict diffuse solar irradiance on outside surfaces of a building without the knowledge of diffuse radiance distributions although the programs may not assume isotropic diffuse radiance distributions. Anisotropic sky diffuse models typically employed in these programs, such as Perez's model [Perez et al. 1990], are categorized as slope irradiance models [Vartiainen 2000], which usually yield the prediction of the sky diffuse irradiance on an inclined surface directly but provide no information about the radiance of the sky.

C.3 Blind Solar-Optical Properties

Since the diffuse blind model considers two sources of the diffuse solar radiation, the diffuse blind model predicts two sets of blind diffuse solar-optical properties: one for sky diffuse radiation and one for ground diffuse radiation. Each set consists of three optical properties: diffuse blind transmittance, diffuse blind reflectance, and diffuse blind absorptance. The diffuse blind transmittance can be determined by:

$$\tau_{df}^{bl} = \frac{\iint \left[\tau_{bm-bm}^{bl} + \tau_{bm-df}^{bl}\right] \cdot R_{df}\,(\theta_p, \varphi_p) \cdot \sin(\theta_p) \cdot \cos(\theta_i) \cdot \delta\theta_p \cdot \delta\varphi_p}{I_{df}} \tag{C-9}$$

Equation (C-9) shows a general formula for a diffuse blind transmittance. Limits of the two integrations, the diffuse radiance, and the diffuse irradiance depend on the source of diffuse solar radiation considered. As previously mentioned, the net-radiation blind model described in detail in Appendix B is employed to predict the direct blind transmittance and the direct-reflected blind transmittance. The two direct blind transmittances are dependent on the profile angle, which is subsequently a function of the zenith angle (θ_p) and the azimuth angle (φ_p). The profile angle can be calculated as described in Chapter 4.

Similarly, the diffuse blind reflectance can be determined by

$$\rho_{df}^{bl} = \frac{\iint \rho_{bm-df}^{bl} \cdot R_{df}(\theta_p, \varphi_p) \cdot \sin(\theta_p) \cdot \cos(\theta_i) \cdot \delta\theta_p \cdot \delta\varphi_p}{I_{df}} \tag{C-10}$$

where the direct blind reflectance is also determined by the net-radiation blind model.

Finally, the diffuse blind absorptance can simply be calculated by

$$\alpha_{df}^{bl} = 1 - \left(\tau_{df}^{bl} + \rho_{df}^{bl}\right) \tag{C-11}$$

A numerical integration method is essential for solving Equations (C-9) and (C-10). Utilizing the calculations described above, the diffuse blind model is applicable to a slat-type blind installed on a vertical plane as well as on an inclined plane. The vertical blind assembly is a special case where the upper half of the hemisphere represents the sky while the lower half of the hemisphere represents the ground. The diffuse blind model is also applicable to both isotropic and anisotropic diffuse radiance distributions. However, the model will depend on the availability and the accuracy of radiance distribution models selected.

APPENDIX D

OPTICAL FENESTRATION MODEL

In this appendix, an optical fenestration model for predicting overall optical properties of a fenestration system containing a slat-type blind is presented. The model is based on the multi-layer optical calculations where the overall optical properties are determined as a function of optical properties of the fenestration system's individual components. The model was specifically developed to be consistent with a newly developed optical blind model presented in Chapter 5 so the model is slightly different from those given in the literature [DOE 2006; ISO 2000; Klems 2002; van Dijk and Goulding 1996; Wright and Kotey 2006]. To be consistent with the new optical blind model, the model treats direct and diffuse components of incident solar radiation separately. Also, the model treats direct and diffuse components of transmitted solar radiation due to incident direct solar radiation separately. In addition, the model treats diffuse solar radiation from the sky and the ground separately.

The optical fenestration model presented here is applicable to the fenestration system consisting of any number of glazing layers with one blind layer. The model requires spectrally-averaged optical properties of the glazing and the blind as input data. Optical properties of the glazing can be obtained using glazing models [Finlayson et al. 1993; Rubin et al. 1998; Wright 1998] and/or window computer programs [LBL 1994, 2001; van Dijk and Goulding 1996; Wright and Sullivan 1995]. Optical properties of the blind are determined using the newly developed blind model presented in Chapter 5.

In the following calculations, the overall optical properties denoted by "*sys*" are given in terms of separated blind optical properties and glazing optical properties. The blind optical properties denoted by '*bl*' are optical properties of the blind layer alone while the glazing optical properties denoted by '*gl*' are optical properties of the whole glazing system in the absence of the blind. For the fenestration system containing an interior blind, overall optical properties including system transmittances (τ^{sys}), system absorptances of the glass layers ($\alpha^{sys,gl}$), and system absorptances of the blind layer ($\alpha^{sys,bl}$) can then be determined by

$$\tau^{sys}_{bm-bm}(\theta,\phi)=\tau^{gl}_{bm}(\theta)\cdot\tau^{bl}_{bm-bm,f}(\phi) \tag{D-1}$$

$$\tau^{sys}_{bm-df}(\theta,\phi)=\tau^{gl}_{bm}(\theta)\left[\tau^{bl}_{bm-df,f}(\phi)+\frac{\rho^{bl}_{bm-df,f}(\phi)\cdot\rho^{gl}_{df,b}\cdot\tau^{bl}_{df,f}}{1-\rho^{gl}_{df,b}\cdot\rho^{bl}_{df,f}}\right] \tag{D-2}$$

$$\alpha^{sys,gl,n}_{bm-df}(\theta,\phi)=\alpha^{gl,n}_{bm,f}(\theta)+\frac{\tau^{gl}_{bm}(\theta)\cdot\rho^{bl}_{bm-df,f}(\phi)\cdot\alpha^{gl,n}_{df,b}}{1-\rho^{gl}_{df,b}\cdot\rho^{bl}_{df,f}},\ (n = 1 \text{ to } N) \tag{D-3}$$

$$\alpha^{sys,bl}_{bm-df}(\theta,\phi)=\tau^{gl}_{bm}(\theta)\left[\alpha^{bl}_{bm-df,f}(\phi)+\frac{\rho^{bl}_{bm-df,f}(\phi)\cdot\rho^{gl}_{df,b}\cdot\alpha^{bl}_{df,f}}{1-\rho^{gl}_{df,b}\cdot\rho^{bl}_{df,f}}\right] \tag{D-4}$$

$$\tau^{sys}_{sky-df}=\tau^{gl}_{df}\left[\tau^{bl}_{sky-df,f}+\frac{\rho^{bl}_{sky-df,f}\cdot\rho^{gl}_{df,b}\cdot\tau^{bl}_{df,f}}{1-\rho^{gl}_{df,b}\cdot\rho^{bl}_{df,f}}\right] \tag{D-5}$$

$$\alpha^{sys,gl,n}_{sky-df}=\alpha^{gl,n}_{df,f}+\frac{\tau^{gl}_{df}\cdot\rho^{bl}_{sky-df,f}\cdot\alpha^{gl,n}_{df,b}}{1-\rho^{gl}_{df,b}\cdot\rho^{bl}_{df,f}},\ \text{(for glass layer } n = 1 \text{ to } N) \tag{D-6}$$

$$\alpha^{sys,bl}_{sky-df}=\tau^{gl}_{df}\left[\alpha^{bl}_{sky-df,f}+\frac{\rho^{bl}_{sky-df,f}\cdot\rho^{gl}_{df,b}\cdot\alpha^{bl}_{df,f}}{1-\rho^{gl}_{df,b}\cdot\rho^{bl}_{df,f}}\right] \tag{D-7}$$

$$\tau^{sys}_{gnd-df}=\tau^{gl}_{df}\left[\tau^{bl}_{gnd-df,f}+\frac{\rho^{bl}_{gnd-df,f}\cdot\rho^{gl}_{df,b}\cdot\tau^{bl}_{df,f}}{1-\rho^{gl}_{df,b}\cdot\rho^{bl}_{df,f}}\right] \tag{D-8}$$

$$\alpha^{sys,gl,n}_{gnd-df}=\alpha^{gl,n}_{df,f}+\frac{\tau^{gl}_{df}\cdot\rho^{bl}_{gnd-df,f}\cdot\alpha^{gl,n}_{df,b}}{1-\rho^{gl}_{df,b}\cdot\rho^{bl}_{df,f}},\ (n = 1 \text{ to } N) \tag{D-9}$$

$$\alpha^{sys,bl}_{gnd-df} = \tau^{gl}_{df}\left[\alpha^{bl}_{gnd-df,f} + \frac{\rho^{bl}_{gnd-df,f}\cdot\rho^{gl}_{df,b}\cdot\alpha^{bl}_{df,f}}{1-\rho^{gl}_{df,b}\cdot\rho^{bl}_{df,f}}\right] \tag{D-10}$$

In the above formulations, the parentheses after the optical properties indicate that those properties are dependent on the profile angle (ϕ) and/or the angle of incidence (θ). The calculations account for both the blind and the glazing having different front- and back-side optical properties. The denotation '*f*' refers to radiation incident on the side of each particular layer closest to the outside while the denotation '*b*' refers to radiation incident on the side of the layer closest to the inside. It is assumed that radiation is diffusely reflected from the blind layer although the blind slats are non-purely diffuse reflecting surfaces (i.e. blind optical properties for direct solar radiation determined using the ray-tracing blind model). Therefore, hemispherical diffuse blind properties (τ^{bl}_{df}, ρ^{bl}_{df}, and α^{bl}_{df}) are required for the optical fenestration model in addition to direct, sky-diffuse, and ground-diffuse blind properties. The diffuse blind model described in Appendix C can also be used to obtain the hemispherical diffuse blind properties where isotropic radiance distribution (of the hemisphere over the blind) is assumed.

For the fenestration system containing an exterior blind, the overall optical properties can be determined by

$$\tau^{sys}_{bm-bm}(\theta,\phi) = \tau^{gl}_{bm}(\theta)\cdot\tau^{bl}_{bm-bm,f}(\phi) \tag{D-11}$$

$$\tau^{sys}_{bm-df}(\theta,\phi) = \tau^{gl}_{df}\left[\frac{\tau^{bl}_{bm-bm,f}(\phi)\cdot\rho^{gl}_{bm,f}(\theta)\cdot\rho^{bl}_{bm-df,b}(\phi)+\tau^{bl}_{bm-df,f}(\phi)}{1-\rho^{gl}_{df,f}\cdot\rho^{bl}_{df,b}}\right] \tag{D-12}$$

$$\begin{aligned}\alpha^{sys,gl,n}_{bm-df}(\theta,\phi) &= \tau^{bl}_{bm-bm,f}(\phi)\cdot\alpha^{gl,n}_{bm,f}(\theta)\\ &+\alpha^{gl,n}_{df,f}\left[\frac{\tau^{bl}_{bm-bm,f}(\phi)\cdot\rho^{gl}_{bm,f}(\theta)\cdot\rho^{bl}_{bm-df,b}(\phi)+\tau^{bl}_{bm-df,f}(\phi)}{1-\rho^{gl}_{df,f}\cdot\rho^{bl}_{df,b}}\right],\ (n = 1 \text{ to } N)\end{aligned} \tag{D-13}$$

$$\alpha_{bm-df}^{sys,bl}(\theta,\phi)=\alpha_{bm-df,f}^{bl}(\phi)+\tau_{bm-bm,f}^{bl}(\phi)\cdot\rho_{bm,f}^{gl}(\theta)\cdot\alpha_{bm-df,b}^{bl}(\phi)$$

$$+\rho_{df,f}^{gl}\cdot\alpha_{df,b}^{bl}\left[\frac{\tau_{bm-bm,f}^{bl}(\phi)\cdot\rho_{bm,f}^{gl}(\theta)\cdot\rho_{bm-df,b}^{bl}(\phi)+\tau_{bm-df,f}^{bl}(\phi)}{1-\rho_{df,f}^{gl}\cdot\rho_{df,b}^{bl}}\right] \tag{D-14}$$

$$\tau_{sky-df}^{sys}=\frac{\tau_{sky-df,f}^{bl}\cdot\tau_{df}^{gl}}{1-\rho_{df,f}^{gl}\cdot\rho_{df,b}^{bl}} \tag{D-15}$$

$$\alpha_{sky-df}^{sys,gl,n}=\frac{\tau_{sky-df,f}^{bl}\cdot\alpha_{df,f}^{gl,n}}{1-\rho_{df,f}^{gl}\cdot\rho_{df,b}^{bl}},\ (n = 1 \text{ to } N) \tag{D-16}$$

$$\alpha_{sky-df}^{sys,bl}=\alpha_{sky-df,f}^{bl}+\frac{\tau_{sky-df,f}^{bl}\cdot\rho_{df,f}^{gl}\cdot\alpha_{df,b}^{bl}}{1-\rho_{df,f}^{gl}\cdot\rho_{df,b}^{bl}} \tag{D-17}$$

$$\tau_{gnd-df}^{sys}=\frac{\tau_{gnd-df,f}^{bl}\cdot\tau_{df}^{gl}}{1-\rho_{df,f}^{gl}\cdot\rho_{df,b}^{bl}} \tag{D-18}$$

$$\alpha_{gnd-df}^{sys,gl,n}=\frac{\tau_{gnd-df,f}^{bl}\cdot\alpha_{df,f}^{gl,n}}{1-\rho_{df,f}^{gl}\cdot\rho_{df,b}^{bl}},\ (n = 1 \text{ to } N) \tag{D-19}$$

$$\alpha_{gnd-df}^{sys,bl}=\alpha_{gnd-df,f}^{bl}+\frac{\tau_{gnd-df,f}^{bl}\cdot\rho_{df,f}^{gl}\cdot\alpha_{df,b}^{bl}}{1-\rho_{df,f}^{gl}\cdot\rho_{df,b}^{bl}} \tag{D-20}$$

For the fenestration system containing the interior blind, only front-side blind optical properties (those denoted by '*f*') are required. However, back-side blind optical properties (those denoted by '*b*') are also needed for the fenestration system containing the exterior blind. It should be noted that the profile angles are the same for direct radiation incident on the front (from the sun) and on the back (from the glazing) sides of the blind assembly. However, the slat angles are opposite. Therefore, if the slat angle specified for determining the front-side blind optical properties is positive, the slat angle specified for obtaining the back-side blind optical properties would be negative.

For the fenestration system containing a between-pane blind, Equations (D-1) to (D-20) can be utilized to calculate its overall optical properties. In the first step of the calculations, the fenestration system is subdivided into 2 sub-systems. The first sub-system consists of all glazing layers closer to the outside than the blind layer while the second sub-system consists of the blind layer and all remaining glazing layers (i.e. glazing layers closer to the inside than the blind layer). A glazing model (i.e. a fenestration model for the glazing system) is used to calculate overall optical properties of the first sub-system whereas the glazing model along with Equations (D-11) to (D-20) are used to calculate overall optical properties of the second sub-system. In the second (final) step of the calculations, Equations (D-1) to (D-10) are then employed to calculate overall optical properties of the fenestration system containing the between-pane blind. In the second step, the overall optical properties of the first sub-system are used in place of glazing optical properties while overall optical properties of the second sub-system are used in place of blind optical properties.

APPENDIX E

DERIVATIONS OF CONDUCTION TERMS FOR HB THERMAL FENESTRATION MODEL

This appendix provides derivations of conduction terms used in the HB thermal fenestration model. The HB thermal fenestration model is described in detail in Chapter 6. Section E.1 shows derivations of the conduction terms for a glazing layer, which are used for the fenestration layers *1* to *L-1* modeled by the HB thermal fenestration model. Section E.2 shows derivations of the conduction terms for a combined glazing and blind layer, which are used for the fenestration layer *L* modeled by the HB thermal fenestration model.

E.1 Conduction Terms for Glazing Layer

For an individual glazing layer, it can be assumed that (1) shortwave radiation (including solar radiation and shortwave radiation from lights) is absorbed uniformly along the thickness of the glazing layer, and (2) thermal storage of the glazing layer is negligible. Figure E-1 illustrates the conduction in a glazing layer with uniform solar absorption. For this case, conduction in the glazing layer can be modeled using an equation for 1-D heat conduction with a heat generation term as follows:

$$k_g \frac{d^2T(x)}{dx^2} + \frac{q''_{swr,g}}{t_g} = 0 \qquad \text{(E-1)}$$

where x = distance along the thickness of the glazing layer (ft, m),

$T(x)$ = temperature along the thickness of the glazing layer (°F, K),

k_g = thermal conductivity of the glazing layer (Btu/h·ft·°F, W/m·K),

t_g = thickness of the glazing layer (ft, m), and

$q''_{swr,g}$ = shortwave radiation absorbed by the glazing layer (Btu/h·ft², W/m²).

According to Incropera and DeWitt [2002], a general solution of Equation (E-1) can simply be expressed as:

$$T(x) = -\frac{q''_{swr,g}}{t_g \cdot k_g}\frac{x^2}{2} + B_1 x + B_2 \tag{E-2}$$

where B_1 and B_2 are the constants of integration, which are dependent on boundary conditions.

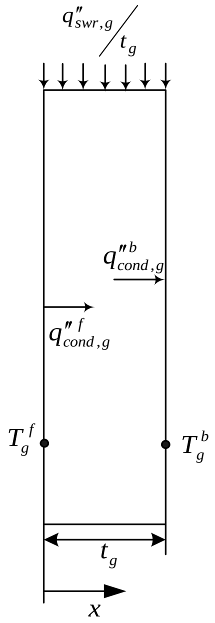

Figure E-1 Conduction in a Glazing Layer with Uniform Solar Absorption

The HB thermal fenestration model requires the conduction terms be expressed as a function of surface temperatures. Therefore, first applying the boundary condition at $x = 0$ where $T(0) = T_g^f$, we get $B_2 = T_g^f$. Then, applying the boundary condition at $x = t_g$ where $T(t_g) = T_g^b$, we get

$$B_1 = -\left(\frac{T_g^f - T_g^b}{t_g} - \frac{q''_{swr,g}}{2 \cdot k_g} \right) \tag{E-3}$$

Equation (E-2), which describes the temperature distribution along the thickness of the glazing layer, thus becomes

$$T(x) = -\frac{q''_{swr,g}}{t_g \cdot k_g} \frac{x^2}{2} - \left(\frac{T_g^f - T_g^b}{t_g} - \frac{q''_{swr,g}}{2 \cdot k_g} \right) x + T_g^f \tag{E-4}$$

Then, the conduction term at $x = 0$, $q''^{f}_{cond,g}$, can be related to the surface temperatures as given below:

$$q''^{f}_{cond,g} = -k_g \left. \frac{dT(x)}{dx} \right|_{x=0} \tag{E-5a}$$

$$q''^{f}_{cond,g} = -k_g \cdot \left. \left\{ -\frac{q''_{swr,g}}{t_g \cdot k_g} \cdot x - \left(\frac{T_g^f - T_g^b}{t_g} - \frac{q''_{swr,g}}{2 \cdot k_g} \right) \right\} \right|_{x=0} \tag{E-5b}$$

$$q''^{f}_{cond,g} = \frac{k_g}{t_g} \left(T_g^f - T_g^b \right) - \frac{q''_{swr,g}}{2} \tag{E-5c}$$

$$q''^{f}_{cond,g} = c_g \cdot \left(T_g^f - T_g^b \right) - \frac{q''_{swr,g}}{2} \tag{E-5d}$$

where c_g is the thermal conductance of the glazing layer (Btu/h·ft²·°F, W/m²·K), which is the ratio of the glazing thermal conductivity to the glazing thickness.

The conduction term at $x = t_g$, $q''^{b}_{cond,g}$, can be obtained similarly resulting in the following equation:

$$q''^{f}_{cond,g} = c_g \cdot \left(T_g^f - T_g^b\right) + \frac{q''_{swr,g}}{2} \tag{E-6}$$

E.2 Conduction Terms for Combined Glazing and Blind Layer

As discussed in Chapter 6, the HB thermal fenestration model treats the innermost glazing layer and the interior blind as a single layer. By combining the glazing layer and the blind layer into a single layer, the total heat transfer from the back (real) surface of the innermost glazing layer to the (imaginary) plane parallel to the interior blind is treated as the equivalent conduction heat transfer through the combined glazing and blind layer. The total heat transfer includes convection and radiation and accounts for thermal interactions between the window and the blind. For the conduction modeling purposes, the combined glazing and blind layer is modeled as two homogeneous sub-layers having perfect thermal contact. The first sub-layer represents the glazing layer alone while the second sub-layer represents the blind layer and the air gap between the glazing and the blind layers. It is assumed that shortwave radiation (including solar and shortwave from lights) absorbed by the glazing layer is distributed uniformly along the thickness of the glazing layer (the first layer) whereas the shortwave radiation absorbed by the blind layer is all distributed to the back surface of the combined air and blind layer (the second sub-layer). It is also assumed that the thermal storage effect in both sub-layers is negligible. Figure E-2 illustrates the conduction modeling of the combined glazing and blind layer.

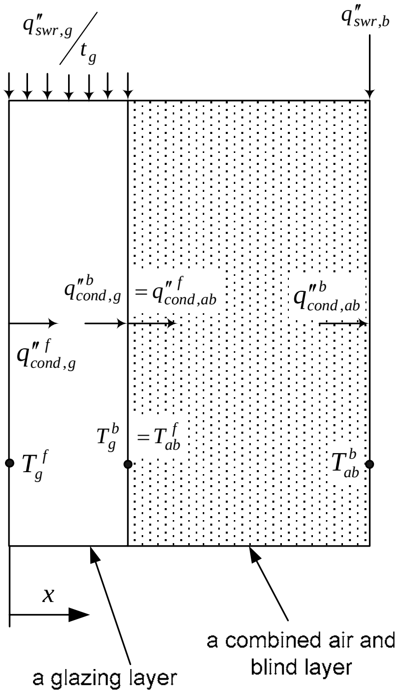

Figure E-2 Conduction Modeling of the Combined Glazing and Blind Layer

Equations (E-5d) and (E-6) used for the glazing layer can also be utilized for the conduction terms of the first sub-layer of the combined glazing and blind layer. For the second sub-layer, the conduction terms can be given by:

$$q''^{f}_{cond,ab} = c_{ab} \cdot \left(T^{f}_{ab} - T^{b}_{ab}\right) \tag{E-7}$$

$$q''^{b}_{cond,ab} = c_{ab} \cdot \left(T^{f}_{ab} - T^{b}_{ab}\right) + q''_{swr,b} \tag{E-8}$$

where c_{ab} = the thermal conductance of the second layer (Btu/h·ft²·°F, W/m²·K),

$q''_{swr,b}$ = shortwave radiation absorbed by the blind layer (Btu/h·ft², W/m²), and

T^{b}_{ab} = temperature of a fictitious surface representing the back surface of the combined glazing and blind layer (°F, K).

With perfect thermal contact, the back surface temperature of the first layer (T_g^b) and the front surface temperature of the second layer (T_{ab}^f) are the same. Also, the conduction through the back surface of the first layer is the same as the conduction through the front surface of the second layer. Equating Equations (E-6) and (E-7), we can then obtain the common temperature (i.e. the back surface temperature of the first layer and the front surface temperature of the second layer) as a function of the front surface temperature of the first layer (T_g^f) and the back surface temperature of the second layer (T_{ab}^b) as follows:

$$T_g^b = T_{ab}^f \quad = \quad \frac{c_g}{c_g + c_{ab}} T_g^f + \frac{c_{ab}}{c_g + c_{ab}} T_{ab}^b + \frac{1}{c_g + c_{ab}} \frac{q''_{swr,g}}{2} \qquad \text{(E-9)}$$

By substituting the common temperature in Equations (E-5d) and (E-8), the conduction terms for the combined glazing and blind layer can then be given as:

$$q''^{f}_{cond,g} \quad = \quad \frac{c_g \cdot \left(c_g + c_{ab} - 1\right)}{c_g + c_{ab}} T_g^f - \frac{c_g \cdot c_{ab}}{c_g + c_{ab}} T_{ab}^b - \frac{\left(c_g + c_{ab} + 1\right)}{c_g + c_{ab}} \frac{q''_{swr,g}}{2} \qquad \text{(E-10)}$$

$$q''^{b}_{cond,ab} \quad = \quad \frac{c_g \cdot c_{ab}}{c_g + c_{ab}} T_g^f - \frac{c_{ab} \cdot \left(1 - c_g - c_{ab}\right)}{c_g + c_{ab}} T_{ab}^b + \frac{c_g}{c_g + c_{ab}} \frac{q''_{swr,g}}{2} + q''_{swr,b} \qquad \text{(E-11)}$$

As previously mentioned in Chapter 6, using thermo-physical properties of the glass, the thermal conductance of the first layer can simply be determined as the ratio of the glazing thermal conductivity to the glazing layer thickness. On the other hand, the (equivalent) thermal conductance of the second layer (i.e. c_{ab}) must be experimentally determined using the proposed experimental method presented in Chapter 6.

Using the indexing convention presented in Chapter 6 for the combined glazing and blind layer, Equations (E-10) and (E-11) become:

$$q''^{f}_{cond,L} = \frac{c_L \cdot (c_L + c_{L+1} - 1)}{c_L + c_{L+1}} T^{f}_{s,L} - \frac{c_L \cdot c_{L+1}}{c_L + c_{L+1}} T^{b}_{s,L} - \frac{(c_L + c_{L+1} + 1)}{c_L + c_{L+1}} \frac{q''_{swr,L}}{2} \tag{E-12}$$

$$q''^{b}_{cond,L} = \frac{c_L \cdot c_{L+1}}{c_L + c_{L+1}} T^{f}_{s,L} - \frac{c_{L+1} \cdot (1 - c_L - c_{L+1})}{c_L + c_{L+1}} T^{b}_{s,L} + \frac{c_L}{c_L + c_{L+1}} \frac{q''_{swr,L}}{2} + q''_{swr,L+1} \tag{E-13}$$

VITA

Chanvit Chantrasrisalai

Candidate for the Degree of

Doctor of Philosophy

Thesis: OPTICAL AND THERMAL FENESTRATION MODELS FOR BUILDING COOLING LOAD CALCULATIONS

Major Field: Mechanical Engineering

Biographical:

Education:
- Received Bachelor of Engineering degree in Mechanical Engineering from Chulalongkorn University, Thailand in 1992.
- Received Master of Science degree in Architectural Engineering from University of Kansas, Kansas in 2000.
- Completed the requirements for the Doctor of Philosophy degree in Mechanical Engineering at Oklahoma State University, Oklahoma in May 2007.

Experience:
- Employed as a mechanical engineer for 49 Engineering Consultants Limited, Thailand from 1992 to 1997.
- Employed as a research assistant for Energy Research Center, University of Kansas, Kansas from 1998 to 1999.
- Employed as a research assistant for School of Mechanical and Aerospace Engineering, Oklahoma State University, Oklahoma from 2000 to 2007.

Professional Memberships: American Society of Heating, Refrigerating, and Air Conditioning Engineers (ASHRAE) and International Building Performance Simulation Association - USA Affiliate (IBPSA-USA)

Name: Chanvit Chantrasrisalai Date of Degree: May, 2007

Institution: Oklahoma State University Location: Stillwater, Oklahoma

Title of Study: OPTICAL AND THERMAL FENESTRATION MODELS FOR BUILDING COOLING LOAD CALCULATIONS

Pages in Study: 319 Candidate for the Degree of Doctor of Philosophy

Major Field: Mechanical Engineering

Scope and Method of Study: The objective of this study was to enhance the modeling of fenestration systems containing shading devices for building thermal load and energy calculations. The focus was on the simulation of the fenestration system containing a slat-type blind. Two optical models were developed: one for predicting the blind optical properties (called the comprehensive blind model) and one for predicting the overall optical properties of the fenestration system. An in situ experimental method was also developed to measure solar-optical properties of installed fenestration systems. Two thermal models were also developed: one suitable for the Heat Balance load calculation method and one suitable for the Radiant Time Series load calculation method. The thermal models are applicable to the fenestration system containing the interior blind only. In addition, an experimental method was developed to measure the thermal parameters required by the thermal models.

Findings and Conclusions: The comprehensive blind model was compared to existing optical blind models (the Parmelee and Pfrommer models) and was compared with measured data obtained by the in situ experimental method. Overall, the comprehensive blind model consistently agreed quite well with measured data for diffusely reflecting blinds. The comprehensive blind model had slightly better agreements with measured diffuse solar transmittance than both the Parmelee and Pfrommer models did. For total solar transmittance, the comprehensive blind model showed better agreements with measured data than the Pfrommer model did. The comprehensive blind model agreed significantly better with measured total solar transmittance than the Parmelee model did when a large amount of direct solar radiation was directly transmitted without any reflections. However, the Parmelee model tended to do slightly better when a large amount of direct solar radiation was transmitted by reflections. In summary, the comprehensive blind model has been both verified and experimentally validated.

A limited set of experiments were conducted to demonstrate the feasibility of supporting the thermal models with measured data. An uncertainty analysis was used to estimate the accuracy of the experimental results. Good agreements between calculated and measured surface temperatures were used to support the validity of primary experimental measurements. Good agreements between measured data and published numerical results were then used to demonstrate that the proposed experimental method can capture the effect of an experimental variable on the thermal parameters. In addition, the evaluation of the experimental variable effects was used to provide information useful for the development of empirical correlations of the thermal parameters.

ADVISOR’S APPROVAL: Dr. Daniel E. Fisher